CRANFIELD UNIVERSITY

SCHOOL OF MECHANICAL ENGINEERING

DEPARTMENT OF TURBOMACHINERY
AND
ENGINEERING MECHANICS

PhD THESIS

Academic Year 1997 - 1998

DAVID UZO MBA

CONDITION MONITORING OF SLOW SPEED ROTATING MACHINERY USING STRESS WAVES

Supervisor: Dr. R. H. Bannister

JUNE 1998

ABSTRACT

Condition monitoring through the use of vibration analysis is an established and effective technique for detecting loss of mechanical integrity of a wide range and classification of rotating machinery. Equipment rotating at low rotational speeds present an increased difficulty to the maintenance engineer, since conventional vibration measuring equipment is not capable of measuring the fundamental frequency of operation, also, component distress at low operational speeds does not necessarily show an obvious change in vibration signature.

This thesis presents a study of high frequency stress wave analysis as a means of detecting early stages of loss of mechanical integrity in slow speed machinery, the first of its kind. Investigations were centred on the Rotating Biological Contactor (RBC) which is used for sewage treatment in small communities and rotates between 0.6 to 1 revolutions per minute.

The mechanism of stress wave generation was the relative movements between mating components that were experiencing loss of mechanical integrity, for instance, the loss of tightening torque between clamped components. Development of the stress wave monitoring technique was accomplished by firstly, simulating a variety of mechanical faults on the test-rig, and secondly, by numerous 'on-site' tests on operational RBCs and their bearings. In application of this technique to operational RBCs and bearings, as well as cataloguing evidence of mechanical deficiencies associated with RBCs operated within the Severn Trent Water region, the author inspected 261 RBCs and covered over 35,000 miles, contributing to the uniqueness of this research programme.

This research has provided Severn Trent Water limited with a PC-based monitoring system comprising an AE transducer, pre/post amplifiers, ADC board and software on which all diagnosis was undertaken. Furthermore, during the process of investigating reasons for the mechanical failures of the RBC, technical information was uncovered thereby assisting Severn Trent Water in perusing a more robust design of RBC. Moreover this work has assisted Severn Trent Water to maintain that envious reputation that over a number of years not one of the RBC sewage treatment works has failed its consent level as set by the Environmental Agency.

ACKNOWLEDGEMENTS

I would like to express my gratitude and appreciation to Dr. R. H. Bannister, for his superb advice and guidance throughout this research program, and, for the immense support on other related projects. I would also like to thank the departmental support team of Mrs. S. Jones and Mrs. I. Howes.

Many thanks to Mr. G. E. Findlay, of Severn Trent Water Engineering, for giving me the opportunity to undertake this research program.

My warmest gratitude and appreciation to my partner Rebecca and daughter Shamar, for their understanding and enormous support. Also, to David and Ailsa Cregan, and my family, for their encouragement.

I dedicate this thesis to the memory of Mrs. Cynthia Davies, whose strength and courage I can only aspire to.

CONTENTS

Abstract.......... i
Acknowledgements.......... ii
Contents.......... iii
List of figures.......... ix
List of photographs.......... xii
List of tables.......... xiv
Glossary of terms.......... xv
Glossary of equations.......... xvii

1 Introduction.......... **1**

1.1 The Rotating Biological Contactor (RBC).......... 1
1.2 Historical background.......... 1
1.3 Process description.......... 2
1.4 RBC size.......... 3
1.5 Rotational speed.......... 3
1.6 Advantages and disadvantages of the RBC.......... 3
1.7 Types of RBCs.......... .4
1.7.1 Design I.......... 4
1.7.2 Design II.......... 5
1.7.2.1 The shaft.......... 5
1.7.2.2 The bearings.......... 5
1.7.2.3 The shaft clamp.......... 6
1.7.2.4 The media support structure.......... 6
1.7.2.5 The media packs.......... 7
1.8 Condition monitoring of RBCs.......... 9

2 Mechanical integrity of RBCs.......... **12**

2.1 Introduction.......... 12
2.2 Description of mechanical deficiencies on RBCs.......... 12
2.2.1 Shaft failure.......... 12
2.2.2 Bearing failure.......... 13
2.2.3 Media support structure failure.......... 13
2.2.3.1 The radial arms 13

2.2.3.2 The outer circumferential rim........................ 15
2.2.3.3 The through-rods.. 16
2.2.3.4 The through-rod clamps................................. 17
2.2.4 The media panels... 20
2.2.5 Motor and gearbox unit...................................... 20
2.3 Conclusion.. 21

3 Design inadequacies of RBCs...................................... 22

3.1 Introduction.. 22
3.2 Designing against fatigue.. 22
3.3 Corrosion fatigue... 23
3.4 Low frequency corrosion fatigue.................................. 24
3.4.1 Initiation of cracks.. 24
3.4.2 Hydrogen embrittlement...................................... 25
3.4.3 Examples of the effect of low frequency loading on crack growth rates, fatigue life and fretting in corrosive environments.................... 27
3.5 Effects of plating on the endurance of steel.................... 29
3.6 Influence of biomass on fatigue strength........................ 31
3.7 Operating performance of the biofilm............................ 31
3.8 The effect of the biofilm on the mechanical integrity of RBCs.... 32
3.9 Microbiologically Influenced Corrosion (MIC).................. 33
3.9.1 Effect of MIC on mild and stainless steels................ 33
3.10 Bearing failures... 34
3.11 Detailed finite element analysis of RBC structures............ 35
3.12 Conclusion... 35

4 Condition monitoring.. 36

4.1 Condition monitoring of low-speed rotating machinery........ 36
4.2 Problems with low-speed rotating machinery..................... 36
4.2.1 Summary.. 39
4.3 Literature review of low-speed vibration monitoring........... 39
4.3.1 Conclusion... 42
4.4 Acoustic emissions (AE).. 42
4.4.1 Stress waves (SW).. 43
4.4.2 Stress waves propagation and attenuation................. 44

4.4.3 Types of stress waves.. 44
4.4.4 Acoustic emission transducers........................... 45
4.4.5 Advantages and disadvantages of stress waves......... 45
4.5 Application of acoustic emission to condition monitoring of low-speed machinery.................................... 45

5 Experimental procedure and apparatus..................................... 48

5.1 Introduction.. 48
5.2 Test-rig.. 48
5.3 Simulation of mechanical defects.............................. 50
5.3.1 Frame looseness.. 50
5.3.2 Broken support-rod rubbing..................................... 51
5.3.3 Media movement.. 53
5.4 Data acquisition.. 53
5.4.1 The transducer.. 54
5.4.2 The pre-amplifier.. 55
5.4.3 The post-amplifier... 55
5.4.4 The Analogue-to-Digital Converter............................ 56
5.4.5 Signal generator.. 58
5.4.6 The computer.. 58.
5.5 Calibration.. 59
5.5.1 Pre/Post amplifiers and ADC board.......................... 59
5.5.2 Transducers.. 61
5.5.3 Electronic noise... 63

6 Signal Processing.. 64

6.1 Introduction.. 64
6.2 Time and frequency domain recognition and classification features.. 64
6.3 Linear prediction and Auto-Regressive modelling............... 65
6.3.1 AR coefficient and Model order determination.. 72
6.4 Application of parametric modelling to signal classification.. 74
6.5 Recognition and classification techniques........................ 74
6.5.1 Cluster analysis.. 75
6.5.1.1 Separation measurement.................................. 75

6.5.2 Principal component analysis.. 76
6.5.3 Neural networks.. 76
6.6 Features extraction parameters for classification of detected stress wave signatures.. 76
6.6.1 Time and frequency domain classification features.. 77
6.7 Pre-processing of collected data.. 80
6.7.1 Digital filters.. 80
6.7.2 The median filter.. 80

7 Experimental results and discussions.. 82

7.1 Introduction.. 82
7.2 Position of AE transducer.. 82
7.3 Attenuation characteristics of the test-rig.. 87
7.4 Simulation results.. 90
7.4.1 Frame looseness.. 90
7.4.2 Broken support-rod rubbing.. 92
7.4.3 Media movement.. 92
7.5 Classification for identification.. 92
7.6 AR model order determination.. 93
7.7 Effective source classification parameter.. 94
7.8 Severity classification.. 96
7.9 Classification of simulations arising from mechanical faults to the test-rig.. 104
7.10 Severity of simulations.. 106
7.11 Other observations.. 106

8 RBC site recordings.. 108

8.1 Introduction.. 108
8.2 Attenuation tests on a real sized RBC.. 109
8.3 Background noise measurements.. 111
8.4 On-site RBC fault detection.. 113
8.4.1 STW Billesdon.. 114
8.4.2 STW Illmington.. 118
8.4.3 STW Hamstall Ridware.. 123
8.4.4 STW Defford.. 126
8.4.5 STW Flyford Flavell.. 131

8.5 List of other RBCs monitored with results.............. 133

9 RBC bearings.. 134

9.1 Introduction... 134
9.2 Condition monitoring of bearings.. 134
  9.2.1 Bearing element passing frequencies........................ 135
  9.2.2 Resonance of bearing elements.................................. 137
  9.2.3 Acoustic emissions.. 137
9.3 On-site measurements of stress waves from operational RBC bearings.. 138
  9.3.1 Position of sensor.. 138
  9.3.2 Background noise.. 139
9.4 On-site bearing fault detection.. 141
  9.4.1 STW Willoughby.. 141
  9.4.2 STW Stiperstone... 145
  9.4.3 STW Ashover... 150
  9.4.4 STW Snailbeach.. 152
  9.4.5 STW Penybontfawr.. 155
  9.4.6 STW Hamstall Ridware.. 157
  9.4.7 Other RBC locations.. 159
9.5 List of other bearings monitored with results...................... 160

10 Discussions.. 161

11 Conclusions.. 166

12 Recommendations.. 171

References.. 172

APPENDIX

Appendix A...

7.3 Attenuation tests for placement of receiving transducer............... 182
7.4 Attenuation of test-rig.. 183
7.5 Attenuation of test-rig.. 184

Appendix B **Signal processing procedure...........**

1 Time/Frequency domain feature extraction algorithm............ 185
2 AR coefficients extraction algorithm................................ 186
3 Sub-routine program for time/frequency domain feature extraction program... 188
4 Sub-routine program for AR coefficient extraction program.. 200
5 Algorithms used for computation of attenuation characteristics of the test-rig.. 204
6 Cluster algorithm used for classification of features........... 212
7 The median filter algorithm.. 218

LIST OF FIGURES

Figure **page**

1.1 Stages in assembly of design II RBCs.. 6
1.2 Stages in assembly of design II RBCs.. 7
1.3 Stages in assembly of design II RBCs.. 8
1.4 Stages in assembly of design II RBCs.. 8

3.1 Corrosion fatigue data of 13% Cr steel.. 24
3.2 Fatigue crack growth rate of high strength 4340M steel..................... 27
3.3 Fretting fatigue data of carbon steels.. 28
3.4 Corrosion fatigue data of SUS403 stainless steel............................... 28

4.1 Comparison of vibration displacement, velocity and acceleration....... 37

5.1 Test-rig layout... 50
5.2 Squirrel cage for fractured through-rod simulation.............................. 51
5.3 Simulation of media movement... 53
5.4 Data acquisition set-up... 53
5.5 Frequency response of sensor provided by supplier............................ 54
5.6 Layout of ADC interface software, written by D.Mba......................... 57
5.7 Amplitude response of amplifiers and ADC.. 59
5.8 Pulse input with its corresponding frequency spectrum....................... 60
5.9 Zoomed diagram of figure 5.8... 60
5.10 Response of ADC boards to pulse input.. 61
5.11 Amplitude response of sensor.. 62
5.12 Back-to-Back response of sensor... 62
5.13 Comparison of calibration results with calibration chart..................... 63

6.1 Forward linear predictor.. 66
6.2 The prediction-error filter.. 69
6.3 The Auto-Regressive model.. 72
6.4 An example of median filtering... 81

7.1 Predetermined positions on test-rig... 83
7.2 Typical response to excitation at a fixed location................................ 85

7.3a Comparison of relative energy levels........ 86
7.3b Comparison of maximum amplitude values........ 86
7.4 Attenuation characteristics of test-rig........ 88
7.5 Frequency attenuation characteristics for varying discontinuities........ at similar distances from the sensor. 89
7.6 Typical response to simulated frame looseness........ 91
7.7 Typical response to simulated frame looseness........ 91
7.8 Typical response to broken through-rod simulations........ 92
7.9 AR model order determination........ 94
7.10 Classification based on AR coefficients........ 95
7.11 Classification based on time and frequency characteristics........ 95
7.12 Bursts generated at three different positions on the test-rig........ 96
7.13 Severity classification based on AR coefficients........ 97
7.14 Severity classification based on time/frequency parameters........ 97
7.15 Responses to varying amplitudes at position P8........ 98
7.16 Severity measurements at position P8........ 99
7.17 Classification based on AR coefficients........ 100
7.18 Classification based on time and frequency characteristics........ 100
7.19a Responses to varying pulse input duration's at position P12........ 102
7.19b Frequency responses of various pulse input duration's........ 102
7.19c Signatures generated at position P8 with different pulse duration's........ 103
7.19d Signatures generated at position P8 with different pulse duration's........ 103
7.20a Classification of simulation results based on AR coefficients........ 105
7.20b Classification of simulations based on time/freq. characteristics........ 105
7.21 Severity of simulations........ 106
7.22 Bursts indicative of continued rubbing/sliding of mating parts........ 107

8.1 Relative attenuation based on energy levels........ 110
8.2 Relative attenuation based on maximum amplitude........ 110
8.3 Background noise from STW Moreton Morrell........ 112
8.4 Background noise from STW Beckford........ 112
8.5 Dendogram of background noise at STW Moreton Morrell........ 113
8.6 Classification of stress waves at STW Billesdon, 3/12/97........ 114
8.7 Stress waves detected at STW Billesdon........ 115
8.8 Stress wave bursts associated with cluster 1........ 116
8.9 Stress wave bursts associated with cluster 2........ 116
8.10 Background noise from STW Illmington........ 118
8.11 Classification of stress wave bursts at STW Illmington, 31/10/96........ 119
8.12 Stress waves detected at STW Illmington........ 119

8.13 Stress waves detected at STW Illmington... 120
8.14 Stress waves detected at STW Illmington... 121
8.15 Rejected stress wave bursts at STW Hamstall Ridware........................ 123
8.16 Classification of stress waves detected at STW Hamstall Ridware....... 124
8.17 Stress waves detected at STW Hamstall Ridware................................ 124
8.18 Stress waves detected at STW Hamstall Ridware................................ 125
8.19 Stress waves detected at STW Hamstall Ridware................................ 125
8.20 Classification of stress waves detected at STW Defford...................... 127
8.21 Stress waves detected at STW Defford.. 128
8.22 Stress waves detected at STW Defford.. 128
8.23 stress waves detected at STW Flyford Flavell..................................... 131
8.24 Typical stress waves at STW Flyford Flavell....................................... 132

9.1 Background noise of SKF bearings... 139
9.2 Background noise of Split Cooper bearing.. 140
9.3 Dendogram of background noise at STW Tregynon............................. 141
9.4 Typical signature of rejected stress wave bursts.................................. 142
9.5 Classification of stress waves at STW Willoughby, 1/4/97..................... 143
9.6 Stress waves detected at STW Willoughby.. 143
9.7 Stress waves detected at STW Willoughby.. 144
9.8 Classification of stress waves at STW Stiperstone, 18/8/97.................. 146
9.9 Stress waves detected at STW Stiperstone.. 146
9.10 Stress waves detected at STW Stiperstone.. 147
9.11 Stress waves detected at STW Stiperstone.. 147
9.12 Stress waves detected at STW Stiperstone.. 148.
9.13 Classification of stress waves at STW Ashover, 16/10/97...................... 150
9.14 Typical stress waves detected at STW Ashover, before and after filtering.. 151
9.15 Classification of stress waves at STW Ashover, after filtering................ 151
9.16 Classification of stress waves at STW Snailbeach, 18/8/97.................... 153
9.17 Stress waves detected at STW Penybontfawr....................................... 153
9.18 Stress waves detected at STW Penybontfawr....................................... 154
9.19 Classification of stress waves at STW Penybontfawr, 13/5/97................ 155
9.20 Stress waves detected at STW Penybontfawr....................................... 156
9.21 Stress waves detected at STW Penybontfawr....................................... 156
9.22 Classifcation of stress waves at STW Hamstall Ridware, 3/6/97........... 158
9.23 Stress waves detected at STW Hamstall Ridware................................ 158

LIST OF PHOTOGRAPHS

Photograph **page**

1.1 RBC sited at STW Kirkby, 1/12/97 2
1.2 Klargester manufactured GRP RBC 5
1.3 Cambridge manufactured RBC. STW Upton Snodbury, 12.11.96 9

2.1 Scored shaft 13
2.2 Fractured cage 13
2.3 Fractured radial arms 14
2.4 Radial arm movement 14
2.5 Radial arm movement 14
2.6 Fractured media support structure 15
2.7 Galvanic corrosion 16
2.8 Fractured through rod 16
2.9 Fractured 'U' strap 17
2.10 Fractured 'U' bolt 17
2.11 Loose 'U' strap 18
2.12 Fretting of 'U' bolt 18
2.13 Axial movement of through rods 19
2.14 Fractured 'U' strap bolt 19
2.15 Galvanic corrosion 19
2.16 GRP media degradation 20
2.17 HD Polypropylene media degradation 20

3.1 Corrosion of a galvanised steel structure 30

5.1 The Test-rig 49
5.2 Squirrel cage 51
5.3 Effect of rubbing on the cut faces 52

8.1 Placement of sensor on stub shaft, STW Illmington 108
8.2 Cambridge RBC in storage depot, STW Ladywood 109
8.3 Radial arm/shaft clamp movement 117
8.4 Radial arm/outer-rim movement 117
8.5 Media segment movement 122

8.6 Rotational and axial through rod movement.. 122
8.7 Loose 'U' bolt detected at STW Hamstall Ridware, 3/6/97................ 126
8.8 Movement of radial arms.. 129
8.9 Fractured section of the outer circumferential rim.............................. 130
8.10 Fractured radial arm and 'U' bolt... 130

9.1 Split Cooper bearing housing... 138
9.2 SKF bearing housing.. 138
9.3 Willoughby RBC.. 142
9.4 Placement of sensor... 142
9.5 Excessive gap between rollers.. 145
9.6 Cage fragments.. 145
9.7 Scored stub shaft.. 149
9.8 Part of fractured cage... 149
9.9 Severely worn roller... 149
9.10 Uneven wear across rollers.. 154
9.11 Misalignment... 154
9.12 Cage wear.. 157
9.13 Cage wear.. 157
9.14 Uneven wear across rollers at STW Rushbury, 23/4/97........................... 159

LIST OF TABLES

Table **page**

7.1 List of discontinuities.......... 83
7.2 Distance of predetermined positions from sensor.......... 84

Appendix A

7.3 Attenuation tests for placement of receiving transducer.......... 182
7.4 Attenuation of test-rig.......... 183
7.5 Attenuation of test-rig.......... 184

8.1 List of discontinuities.......... 109
8.2 List of other RBCs monitored with results.......... 133

9.1 List of other bearings monitored with results.......... 159

GLOSSARY OF TERMS

Aerobic :	A condition in which bacteria will grow in or on the surface of a simple solid medium exposed to air.
Anaerobic :	A condition in which bacteria will **not** grow in or on the surface of a simple solid medium freely exposed to air.
BOD :	Biological oxygen demand. This measures the amount of oxygen used in aerobic biological decay of organic matter. It is an aid to how much oxygen would be used if wastewater were diluted into fresh water.
DO :	Dissolved oxygen.
Facultative :	Bacteria that can grow in either the presence or absence of free oxygen. An example would be a facultative anaerobe, which prefers anaerobic conditions, but can live in some other condition, such as aerobic, if necessary.
HE :	Hydrogen Embrittlement
Heterotroph :	Organisms that depend upon organic substances for their nutritional needs.
HSLA :	High Strength Low Alloyed
Hz	Number of cycles per second
K-means	Distance between the centriod of groups
MIC :	Microbiologically influenced Corrosion.
SCC	Stress corrosion cracking
Sessile :	Bacteria that attach itself to a surface and grow.
SOB :	Sulphide Oxidising Bacteria.

Substrate : The specific substance upon which an enzyme acts.

SRB : Sulphate reducing bacteria.

GLOSSARY OF EQUATIONS

Ni	Number of cycles to crack initiation
Np	Number of cycles for crack propagation
N	Number of cycles to failure
$\mathbf{K_{Ic}}$	Fracture toughness of a material
$\mathbf{K_{Iscc}}$	Static stress corrosion initiation intensity factor
$\mathbf{K_{fcc}}$	Dynamic stress corrosion intensity factor
$\mathbf{\Delta K}$	Stress intensity range ,defined as $\Delta K = [K_{max} - K_{min}]$ in one load cycle
$\mathbf{K_{th}}$	Threshold stress intensity factor
$\mathbf{K_{max}}$	Applied intensity factor
da/dN	Crack growth rate per cycle
R	Stress ratio, defined as min stress/max stress per load cycle
$\tilde{x}$ **(n)**	Forward linear prediction based on a time series x(n-1), x(n-2),...,x(n-M)
x(n)	Actual process value at time n
e_M **(n)**	Forward prediction error
h(k)	Coefficients that define the impulse response of the filter
ε	Mean-square value of e_M (n)
P	Mean-squared value of the desired response.

$\mathbf{R(k)}$	Correlation between the desired response and the input signal for lag (k)
$\mathbf{M}$	Model order number
$\mathbf{K}$	Number of lags for computing correlation's
$\mathbf{R(m-k)}$	Auto-correlation function of the input signal for a lag of (m-k)
$\mathbf{h_0(k)}$	Optimum filter coefficients
$\mathbf{a}_{M}$	Optimum coefficients defined by $\left\{\begin{array}{ll} 1, & m=0 \\ -h_0(m), & m=1,\ldots,M \\ 0, & m>M \end{array}\right\|$
$\varepsilon_{\min}$	Minimum mean-squared value
σ^2	Variance
Δ_M	Incremental step in model order number
$\mathbf{D_{ij}}$	Euclidean distance
$\mathbf{X_{ik}}$	The value of the k^{th} variable for the i^{th} entry

CHAPTER 1

INTRODUCTION

The Environment Act 1995 merged the National River Authority (NRA) with other Pollution Control Bodies and created a new statutory body called the Environmental Agency (EA). The EA is an independent body responsible, as far as sewage treatment is concerned, for setting discharge consent standards, for monitoring compliance to these standards and for prosecuting offenders. This meant that the privatised Water companies, who had inherited a considerable number of old sewage treatment works, had to update and improve their works to achieve higher effluent standards.

Currently Severn Trent Water Limited (STW) operates over 1000 sewage treatment works, approximately 70% of which serve a population of less than 2000 [1]. In order to meet the demands set by the EA at a competitive cost, STW have selected Rotating Biological Contactors (RBC) for sewage treatment in sparsely populated areas.

1.1 The Rotating Biological Contactor (RBC)

The RBC can be used for sewage treatment in areas having a population of up to 5000 [2,3,..]. They consists of corrugated plastic discs attached together to form a media pack as illustrated in photograph 1.1. The plastic discs, also referred to as media panels, are held within an enclosed basin tank and submerged by about 40% of their height. Wastewater passes through the basin as the disks slowly rotate, at approximately 1 rev/min, exposing the biological growth, which develops on the surface of the disks alternately to the wastewater, and to oxygen in the air. The RBC operates continuously throughout its life as a break in operation will necessitate attention by the operator to maintain consent standards, often at higher costs. Typically, a media pack, consisting of a collection of media panels, represents one stage of the treatment process. The RBC in photograph 1.1 consists of three media packs.

1.2 Historical background

The principal of the RBC originated in the early part of the century, however, it was not until 1960 that the first commercial system was installed in West Germany. Thereafter, RBC units have been operated across the globe, e.g. USA, Austria, UK, Spain, etc. By

1978, there were over 1000 units in operation within Europe, probably expanding to several time this number at present.

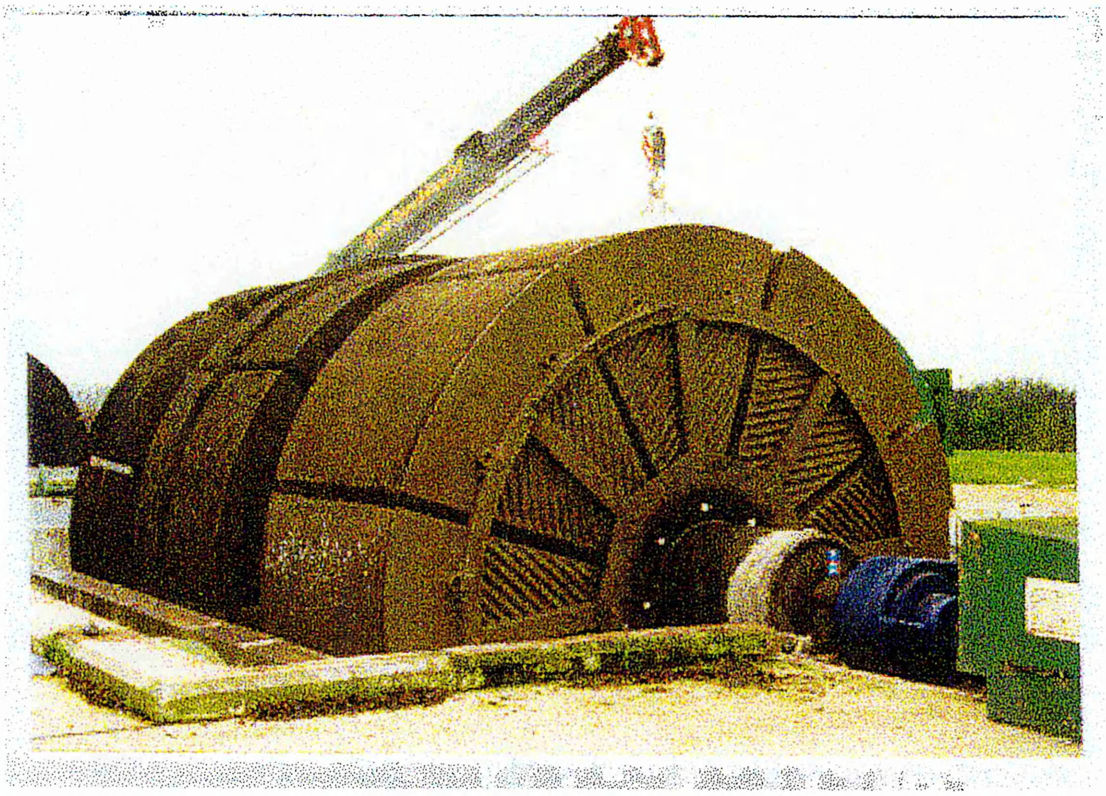

Photograph 1.1 **RBC sited at STW Kirkby, 1/12/97**

The commercial viability of the systems in the 1960's and early 70's was deemed to be very poor as flat expanded polystyrene sheets were being used for the media panels. With the development of polymers came the introduction of thin, corrugated sheets of high-density polyethylene in 1972. This meant that the available surface area over a given length of shaft was increased dramatically, improving the performance of the RBC and its relative cost effectiveness. As a result, installations of RBCs increased considerably, but wider applications were limited due to mechanical breakdowns.

1.3 Process description

In operation, biological growths (biomass) become attached to the surfaces of the media panels and eventually form a slime layer of the entire wetted surface. As the RBC rotates, the biomass is exposed alternately to the sewage liquor and to oxygen in the air, ensuring aerobic conditions are maintained for the survival of the biomass. Organisms in the developed biomass remove both dissolved oxygen and organic materials from the wastewater, effectively cleaning the settled sewage. Shearing forces are exerted on the biomass as it passes through the wastewater, causing any excess biomass to be stripped from the media panel, thus controlling the depth to which the biomass can grow. In a well-operated system there exists a continual cycle of film growth followed by biomass stripping.

The first stage in a system, operating within the proper organic loading range, exhibits a characteristic brownish-grey biomass colour, decreasing in thickness with succeeding stages. The terminal nitrifying stages normally have a characteristic reddish-bronze colour. In lightly loaded nitrifying stages, the biomass growth may not be uniform and patches of bare media become visible.

1.4 RBC size

The size of RBC is dependent upon the population it serves, settled sewage strength and the EA consent. Size usually refers to the diameter of the unit; however, other factors influencing its size are the number of media packs, the number of media panels held within each pack and the total surface area of the media panels. STW operate RBCs with diameters ranging from 1 to 3.6 meters, having 2 to 5 media packs with shaft lengths of 1 to 8 meters. The entire unit is enclosed to maintain optimum biomass operation temperatures and prevent external interference.

1.5 Rotational speed

Essential to the biological process is the requirement for oxygen to be transferred from the atmosphere into the biofilm. The faster the rate of rotation of the media panels, the greater the rate of aeration, however, there is an upper limit when the peripheral velocity prevents the biomass film adhering to the surface. For this reason peripheral speeds are set at approximately 0.25m/sec, corresponding to between 0.6 and 1.5 rev/min.

1.6 Advantages and disadvantages of the RBC

Compared with conventional sewage treatment works, the RBC has the following advantages [4]:

i) Integral RBCs are much more compact than percolating filters.
ii) RBCs require negligible hydraulic head compared with percolating filters.
iii) RBCs do not, as a rule, require recirculation at times of low flow.
iv) Problems of seasonal shedding of biomass from percolating filters are reduced in the semi-controlled environment of the RBC.

v) Power requirements are much less.
vi) Fly nuisance and odour are contained.
vii) RBCs are environmentally non-intrusive.

Furthermore, in a report undertaken by Northwest Water [6] on the cost effectiveness of RBCs in relation to other prefabricated aeration plants, it was concluded that RBCs had much lower operational costs.

Disadvantages include:
i) Relatively high capital costs of equipment.
ii) Oxygen deficiencies in the sewage liquor.
iii) **Mechanical failures**. The mechanical deficiencies associated with RBCs have limited their applicability to several users.

1.7 Types of RBCs

There are two distinct designs operated by Severn Trent Water Limited:

1.7.1. Design I

Designed and built before the mid 1980's, the RBC consisted of continuous corrugated or fan shaped Glass Reinforced plastic (GRP) media panels which are cemented directly onto the main shaft. Spacing between the panels is achieved by using axial location strips and spacers, thereby fixing the distance between individual media panels and allowing for efficient biomass growth, see photograph 1.2. This particular design of RBC is no longer used due to cost implications.

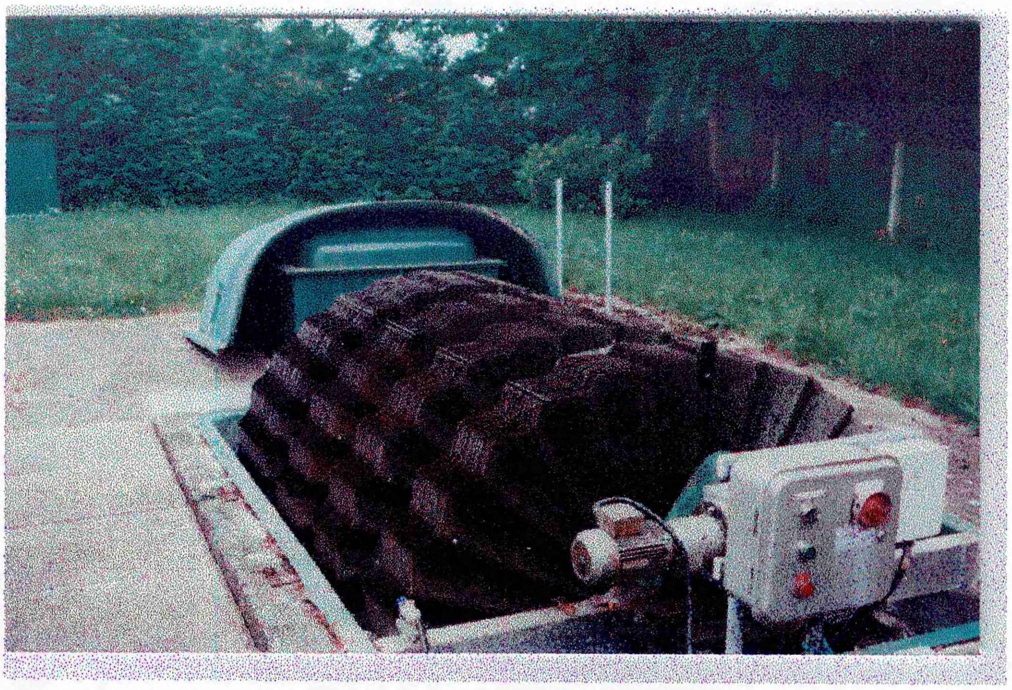

Photograph 1.2 **Klargester manufactured GRP RBC**

1.7.2 Design II

Designed and built from the early 1980's, the RBC consists of a stainless or galvanised steel structure supporting high-density polypropylene media panels. The size and material type of components used for this design are dependent on the RBC size and manufacturer. There are over five manufacturers in the U.K, each having characteristic design features, though the design outlays are very similar. The components of this design are :

1.7.2.1 The Shaft

The shaft is of galvanised steel and, depending on manufacturer, could have a GRP overlay to prevent corrosion. Stub shafts, shot blasted and zinc sprayed, are welded or bolted onto the end of the shaft and serve to rest the entire unit onto bearings. See stage 1 of figure 1.1.

1.7.2.2 The Bearings

Two bearings are used to support the shaft. Within the Severn Trent region, two types are commonly used, the SKF and the Split Cooper bearings. See stage 2 of figure 1.1.

1.7.2.3 The Shaft Clamp

Fixed onto the shaft are a series of shaft clamps. The media support structure is fixed onto these clamps and two clamps are used for each media pack, see stage 3 of figure 1.1. Depending on manufacturer, these clamps are either of a hub design or welded onto the shaft.

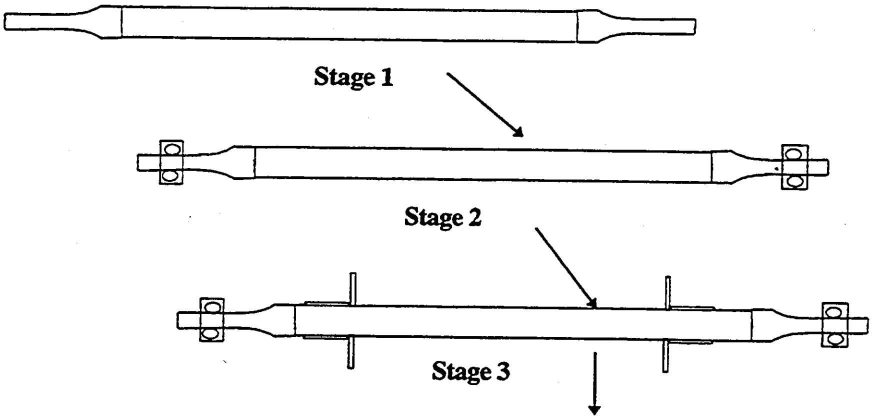

Figure 1.1 Stages in the assembly of design II RBCs.

1.7.2.4 The Media Support Structure

The media support structure consists of between 4 to 12 equal media segments, dependent on RBC size. Each segment consists of:

Radial Arms : The radial arms are bolted onto the shaft clamp, stage 4 of figure 1.2.

The Outer Circumferential Rim : The rim acts as a bridge between adjacent radial arms and serve to support some of the through rods, see stage 5 of figure 1.2. The rim is located at the extreme outer radius of the radial arm.

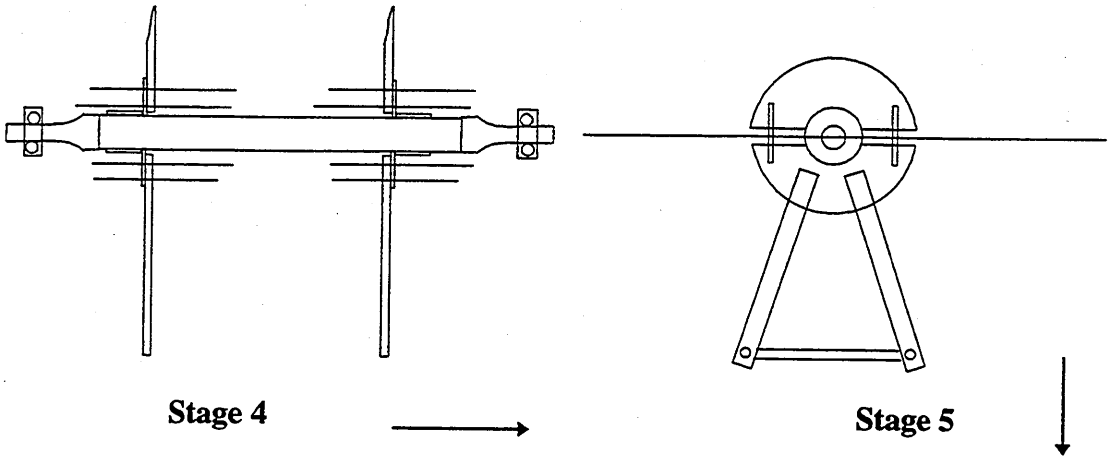

Figure 1.2 **Stages in the assembly of design II RBCs.**

<u>The Through rods</u> : The through rods are of steel hollow tube and serve to locate and support the media panels. The rods bridge opposite support structures at varying heights and there can be between 2 to 4 through rods on each media segment, stage 6 of figure 1.3.

<u>The Through Rod Clamps</u>

These clamps fix the through rods onto the outer circumferential rim. There are various types in use depending on the manufacturer: 'U' bolts are a typical example, see stage 7 of figure 1.3.

1.7.2.5 The Media Panels

These are corrugated high-density polypropylene, approximately 0.9mm thick, and they serve to support the biomass. The type of corrugation is dependent on manufacturer, stage 8 of figure 1.4.

Photograph 1.3 shows the assembled RBC.

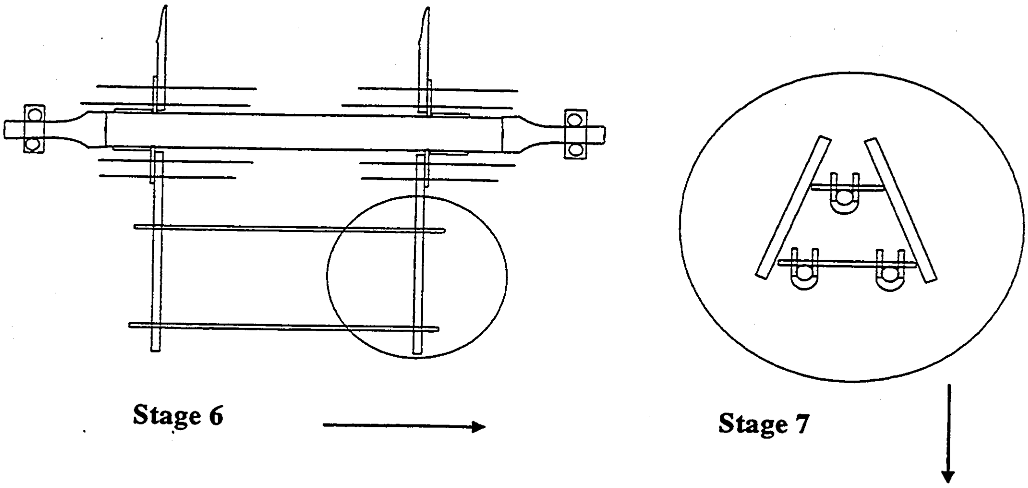

Figure 1.3 Stages in the assembly of design II RBCs.

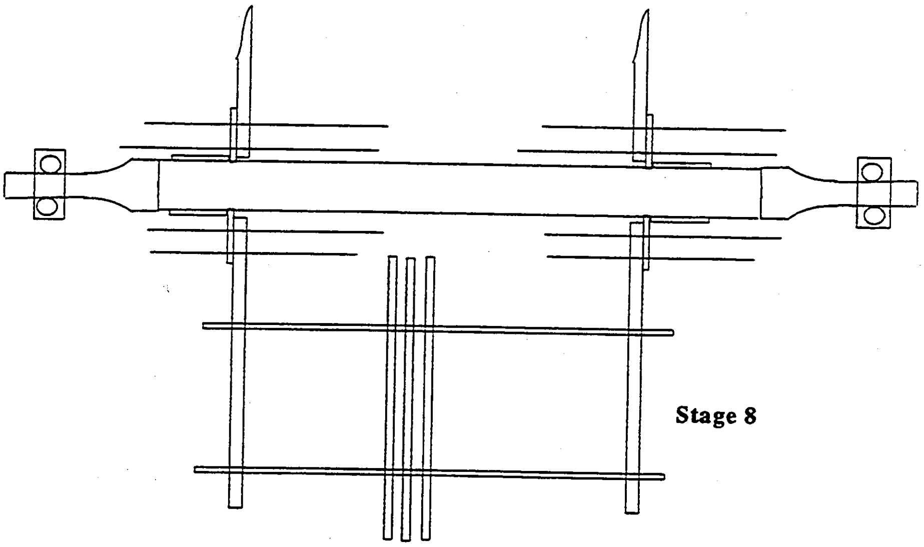

Figure 1.4 Stages in the assembly of design II RBCs.

Photograph 1.3 **Cambridge manufactured RBC.**
STW Upton Snodbury, 12/11/96

1.8 Condition monitoring of RBCs

Whilst it is recognised that the RBC is very effective in sewage treatment, Severn Trent Water Limited, and indeed several other water authorities in the U.K and aboard, have experienced mechanical failures well before their expiry dates. This will result in Severn Trent Water adopting alternative methods whilst the plant is out of operation. These alternative methods can cost several thousand pounds in total, more importantly is the interruption to routine operations. Failure to meet consent standards set by the EA may result in heavy fines on STW Limited.

In an in-depth investigation into the design, operation and maintenance of RBCs [5] it was concluded that while improvements in the design of RBCs can result in more robust units, the loss of mechanical integrity of these units is common and unpredictable. Typical failures reported by Brenner include shaft breakage, stub shaft damage, media degradation and damage, and bearing failure. Any one, or combination, of these faults will require prompt replacement. Based on this report, and experience with sudden loss of operation, Severn Trent Water Limited have taken a number of steps to prevent this from happening on their plants and consequently extend the operational life of their units. However, to date, none of the RBC sewage treatment works has failed to meet the consent level set by the Environmental Agency.

One of the steps taken is the development of a condition monitoring system for their RBCs, and this thesis outlines the foundation on which a such a system can be developed. The second involved commissioning a mechanical design audit of all RBCs operated within the Severn Trent Water region. These steps are the first of their kind in the history of RBCs and are a major step towards understanding and tackling the mechanical deficiencies of RBCs. The results of the audit will put STW at the forefront of RBC design, not only by setting design standards that most Water companies would probably adopt, but also by significantly increasing the applicability of RBCs within their region. Furthermore, the improved RBC design will revolutionise applicability of RBCs to high flow/highly populated regions. This thesis also highlights reasons for mechanical deficiencies, with significant evidence, and contributes technical information to the setting of design standards for future RBCs.

Condition monitoring through the use of vibration analysis is an effective technique for detecting loss of mechanical integrity of a wide range and classification of rotating machinery. Moreover, it is noted for its cost effectiveness, though there could be a limited time between detection and failure. The magnitude and frequency of vibration measured at any point in a machine will depend on a wide variety of factors, such as speed, magnitude of driving force, stiffness of machine and supporting structure, natural frequencies of the structure and component parts and the direction and position of measurement.

Equipment rotating at low rotational speeds presents an increased difficulty to the maintenance engineer, since conventional vibration measuring equipment is not capable of measuring the fundamental frequency of operation, also, component distress at low operational speeds does not necessarily show an obvious change in vibration signature. To date, not much effort has been concentrated on the condition monitoring of low speed rotating machinery and this is reflected in the number of applications and publications. Nevertheless, there are many other applications in the Petrochemical, Coal and Mining, Textiles, Metals and Paper Industries where low speed machinery is an integral part of the production process.

An alternative to vibration analysis is acoustic emissions (AE). It offers opportunities to gain information on structural integrity of a given plant in different phases of its useful operational life, independent of rotational speed. The driving force behind all AE activity is the release of energy generated by material deformation and flaw growth at an atomic scale. These waves propagate in all directions, at the velocity of sound, and cover a broad frequency range of between 20KHz to several Mega-Hertz. At such high frequencies the background noise of operating machinery is filtered out, overcoming a major drawback with conventional vibration monitoring. Whilst there are several advantages to acoustic emissions, see section 4.4.6, it is still relatively new. The correlation between the AE signal and wear is still to be established. Moreover, the small number of people who can analyse collected data to interpret the machine health limits the widespread use of acoustic analysis. This is often based on some knowledge of the machine characteristics and there might not always be the opportunity to undertake tests prior to monitoring.

The attempted application of AE technology to condition monitoring of low speed machinery, presented in this thesis, is the first of its kind. The condition monitoring system will be based on unknown characteristics of the machines, whilst ensuring minimal training for site maintenance personnel.

The development of this system involved:

i Demonstrating that stress wave signals, generated from rubbing of mating surfaces, are detectable over a range of distances and interfaces.
ii Determining the best position for location of the transducer.
iii Development of an acquisition system to capture stress waves emitted.
iv Simulation of operational faults on a test rig.
v Development of signal processing techniques to classify, locate and measure severity of mechanical faults simulated on the test-rig.
vi Obtaining 'on-site' measurements and correlating these results with the test rig. Also, to verify the effectiveness of the signal processing techniques already developed.
vii Specification of sensors, measuring equipment and processing techniques that would allow for easy operational use.

The last developmental step highlights the philosophy that must be adopted, not only for this project, but also for all condition monitoring systems if they are to be widely accepted as a cost-effective tool. The philosophy of **simplicity and availability** must be considered during all stages of development.

CHAPTER 2

MECHANICAL INTEGRITY OF RBCs

2.1 Introduction

In the past, Severn Trent Water Limited (STW) used the G90, conditions of contract agreed with the IMechE for water industry plant installations, in awarding projects for RBC sewage treatment works. It became apparent that a small number of RBCs, installed under these terms of contract, experienced mechanical failures. Cranfield University was invited to firstly, develop a condition monitoring system for this class of RBC, and secondly, investigate reasons for such deficiencies. Due to the proactive approach adopted by STW, they have at all times being able to meet sewage discharge compliance and react positively to manufacturer shortcomings. This chapter highlights mechanical problems associated with STW RBCs, whilst the following two chapters discuss the reasons for the mechanical breakdowns and explains why these deficiencies are best monitored by studying the resulting stress waves emitted from a failing component.

2.2 Description of Mechanical deficiencies on RBCs

The following mechanical deficiencies have been observed:

2.2.1 Shaft failure

Fracture of the shaft has been experienced on several RBCs, which can result in complete collapse of the unit. This mode of failure is considered to be the most severe form of mechanical breakdown, because the replacement costs are greatest, for instance, the cost involved in replacing a complete RBC of medium size can be in the order of £50,000. Usually, however, once shaft failure has occurred the complete RBC unit is replaced as the media panels are usually damaged beyond repair.

2.2.2 Bearing failure

Bearing failures occur regularly on RBCs and can result in loss of operation for at least two weeks. Observations to date suggest that failure is as a result of either grease contamination or lack of lubricant. Both of these can result in cage failure, severe pitting in the rolling elements or even wear of the elements. Moreover, damage to the raceways have been observed which take the form of severe scoring, again suggesting that lubrication is the initial cause of bearing failure. Photographs 2.1 and 2.2 illustrate this type of failure.

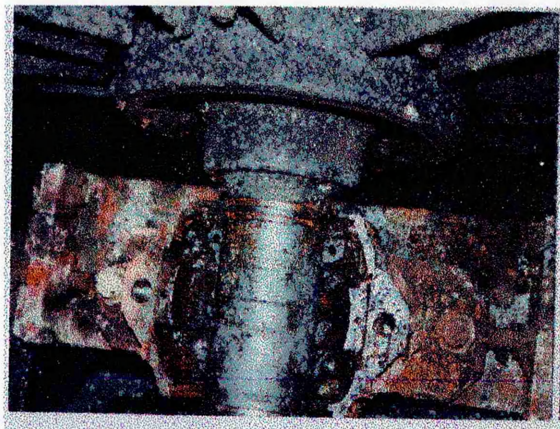

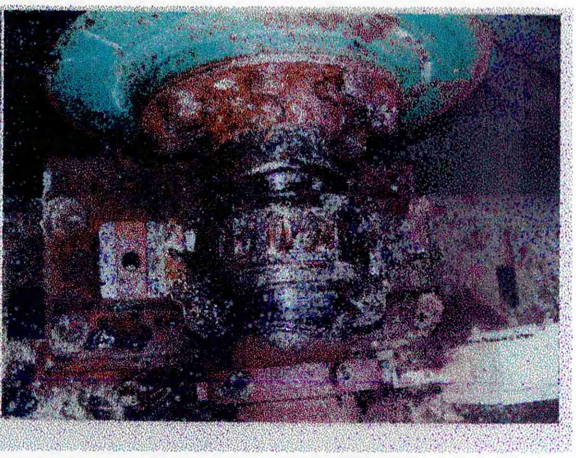

Source : **STW Langar, 17/6/97** **STW Stiperstones, 19/8/97**

Photograph 2.1 Scored shaft **Photograph 2.2 Fractured cage**

2.2.3 Media Support Structure failure

2.2.3.1 The Radial arms

Fatigue failure of the radial arms has been experienced, see photograph 2.3. Fracture of a radial arm will cause in additional stresses to be distributed across the media support structure, thereby acting as a catalyst for complete collapse.

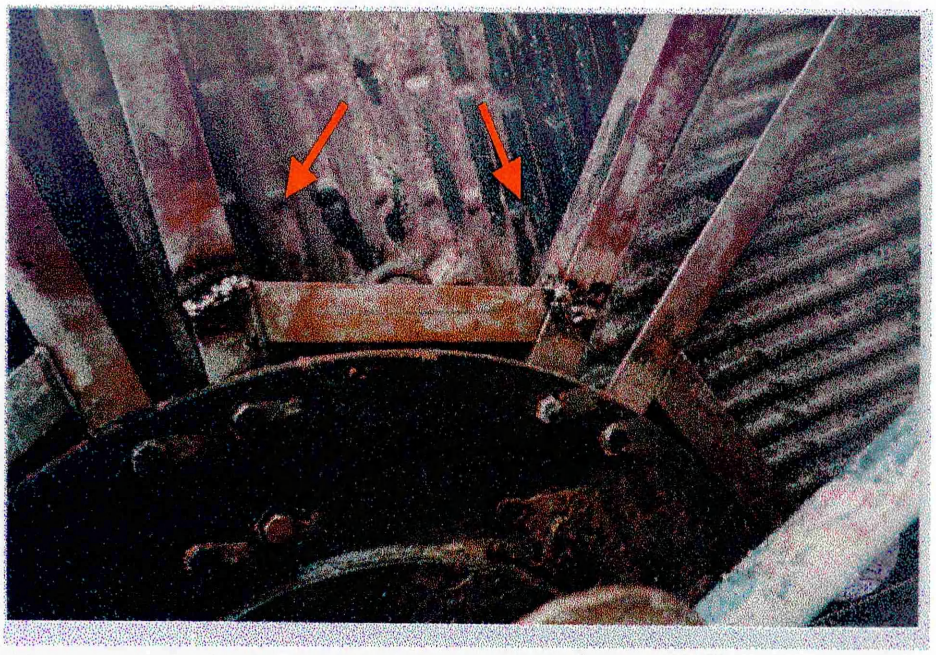

Source : STW Hoton, 18/9/97

Photograph 2.3 Fractured radial arms

Moreover, as a result of inadequate design, the radial arms have been known to become loose in the region where they are bolted to the shaft clamp and outer circumferential rim, see photographs 2.4 and 2.5. The loose radial arms will cause in circumferential movement of the media segment, thereby giving rise to additional stresses on the media support structure. Also, loose radial arms have caused fretting between the shaft clamp and the arms.

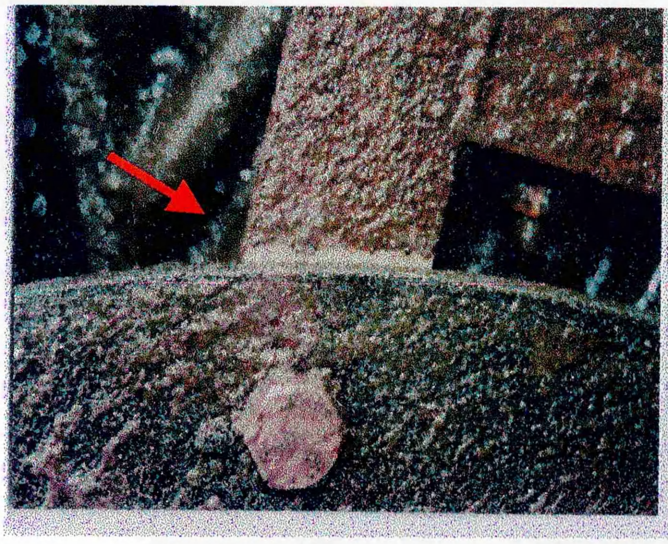

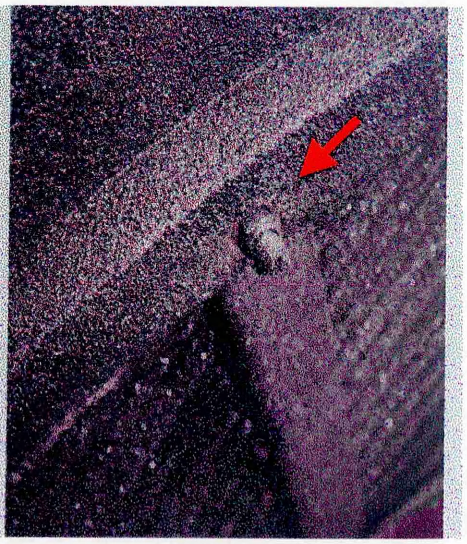

Source : STW Hoton, 18/9/97

STW Langar, 26/9/97

Photograph 2.4 Radial arm movement

Photograph 2.5 Radial arm movement

2.2.3.2 The Outer Circumferential rim

Fatigue failure of this structure has been experienced, particularly on the larger RBCs, see photograph 2.6. Once part of the circumferential rim has fractured, additional stresses will be re-distributed across the media support structure resulting in catastrophic failures as suggested in the opening paragraph of this chapter.

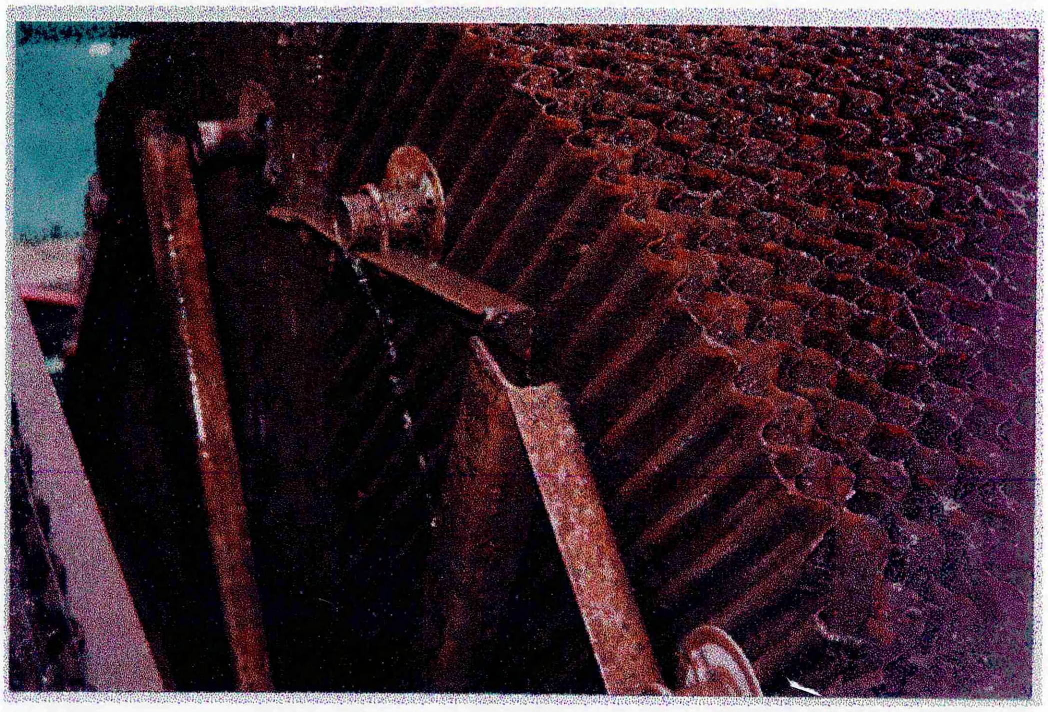

Source : STW Knowbury

Photograph 2.6 Fractured media support structure

Also, galvanic corrosion of the circumferential rim has been experienced. Using two different materials combined with some form of electrolyte, which in this application is the sewage liquor, causes bimetallic corrosion. For example, a galvanised steel circumferential outer rim supporting a stainless steel through rod will most certainly experience galvanic corrosion. Typical galvanic corrosion is illustrated in photograph 2.7.

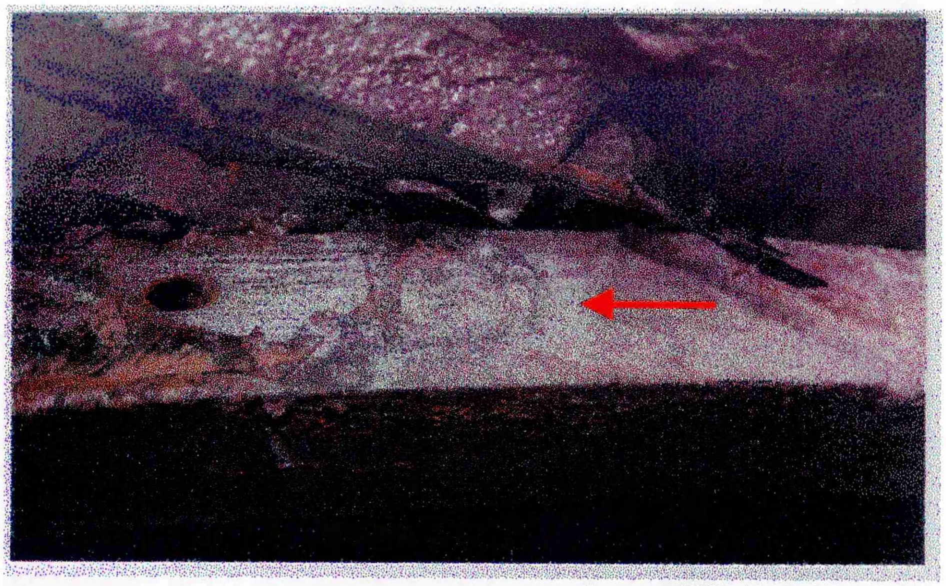

Source : STW Trefeglwys, 2/7/97

Photograph 2.7 Galvanic corrosion

2.2.3.3 The Through rods

The through rods are an essential component to the operation of RBCs, as they support the media pack. There have been many reported cases of through rod fracture, see photograph 2.8. Once fracture occurs, not only is the load redistributed between other through rods within the segment, but also the rigidity of the media pack is lost, resulting in severe damage to the media panels. The increased loads on other through-rods within the segment will accelerate fatigue fracture.

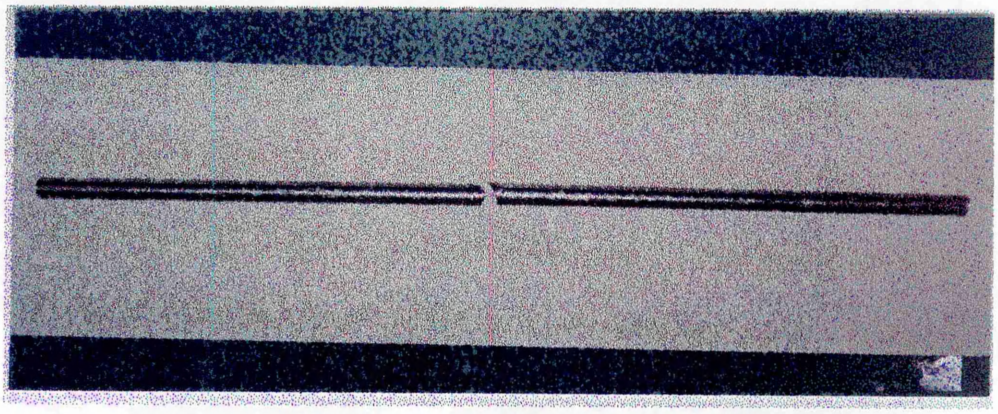

Source : STW Avening, 19/8/97, Photographed at Cranfield University

Photograph 2.8 Fractured through rod

2.2.3.4 The Through rod clamps

There are various types being used. The most troublesome are the 'U' bolts and 'U' straps. Their mechanical deficiencies can be classified into four groups:

i) Fractured ’U’ bolt or ’U’ strap

The 'U' bolts or straps used to clamp the through rod onto the media pack support frame have fractured on several RBCs. Photographs 2.9 and 2.10 illustrate this mechanism of failure. Fracture was as a direct result of large bending moments being reacted back onto the support frame, in addition to built-in stresses during the manufacture of the 'U' bolt or strap. This type of fracture has a domino effect, whereby the load is transferred onto adjacent end clamps/straps thereby dramatically reducing the service life of the unit.

Source : STW Trefeglwys, 2/7/97

Photograph 2.9 Fractured ‘U’ strap

STW Condover, 2/10/97

Photograph 2.10 Fractured ‘U’ bolt

ii) Loose 'U' bolts and 'U' straps

Loose 'U' bolts and straps have been detected; photograph 2.11 illustrates a typical loose strap on polypropylene media panels. This is as a result of loss of tightening torque. Furthermore, it was noted on a few RBCs that polymer sheeting was used to make up dimensional discrepancies between the ‘U’ shaped straps and the media pack support frame. Over the passage of time creep of the polymer will result in loss of clamping efficiency of the ‘U’ strap.

Loss of clamping efficiency resulting from fretting between the 'U' strap/bolt and the through rods has been observed, which will give rise to premature fracture and/or looseness, see photograph 2.12.

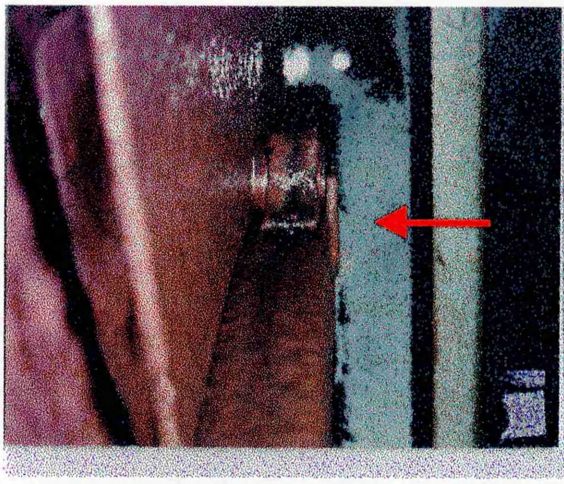

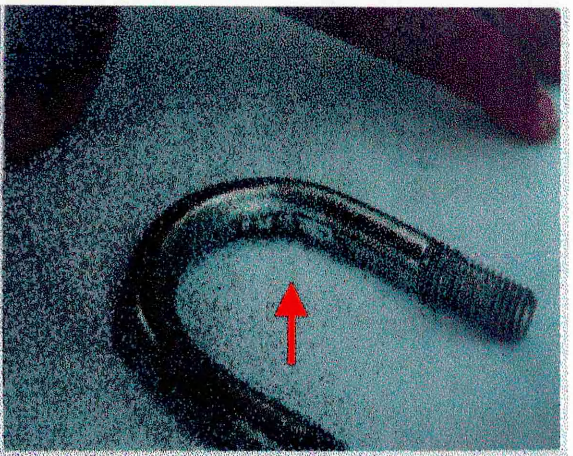

Source : **STW Kelstedge, 21/8/96** **STW Abberley Common, 4/11/97**

Photograph 2.11 Loose 'U' strap

Photograph 2.12 Fretting of 'U' bolt

Axial movement of the through rods has been observed on a number of the larger RBCs. If this axial movement is allowed to continue then the through rod will eventually come into contact with the GRP basin resulting in substantial damage to the RBC but perhaps more importantly, the GRP basin will have to be replaced resulting in many months of down time. If this type of failure is allowed to go undetected and damage does occur tanking costs to remove the sewage can be very high, thereby adding to the replacement costs. Axial movement of the through rod is illustrated in photograph 2.13.

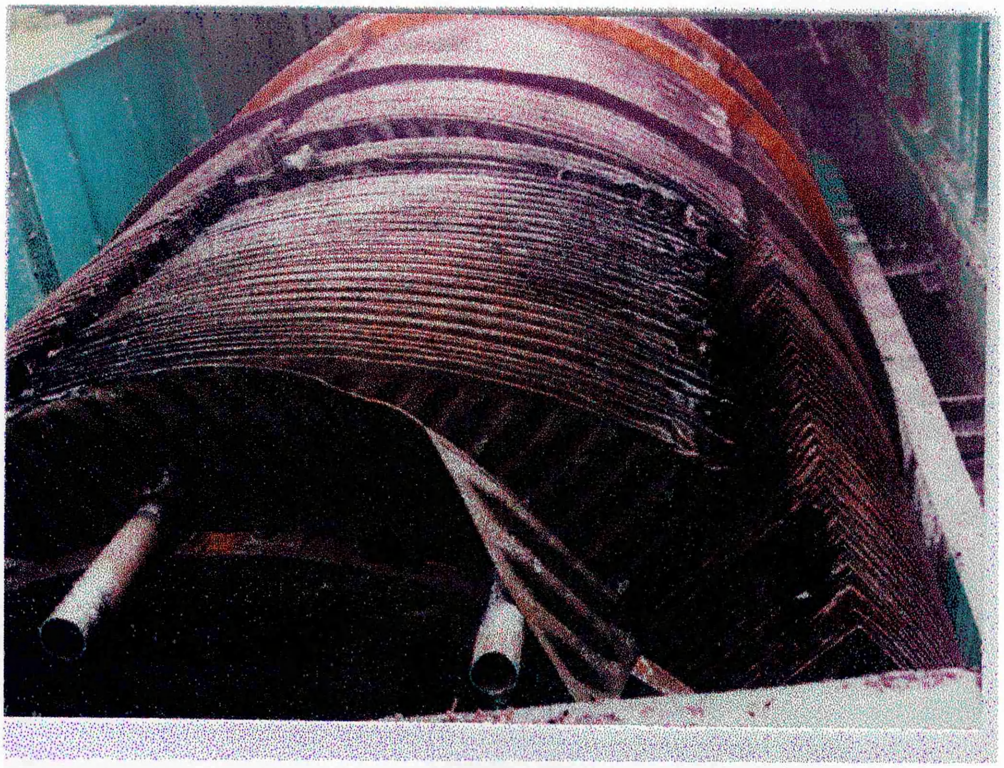

Source : STW Trefeglwys, 2/7/97

Photograph 2.13 Axial movement of through rods

iii) Fractured 'U' strap bolt

In addition to fractured straps it is also possible for the bolts securing the straps to suffer from bending fatigue and or galvanic corrosion. Typical failures are shown in photographs 2.14 and 2.15 respectively.

Source : STW Penkridge Bank, 12/2/97

Photograph 2.14 Fractured 'U' strap bolt

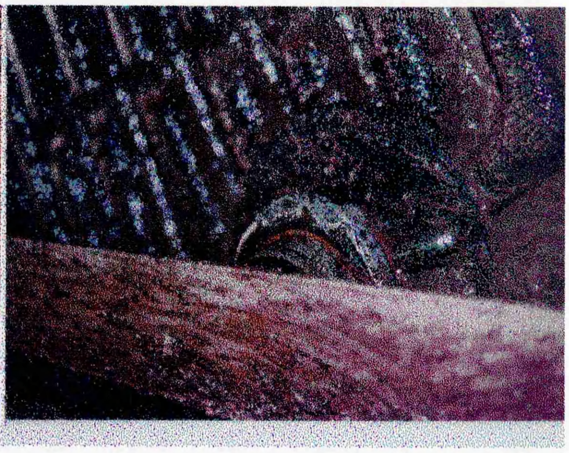

STW Chaddesley Corbert, 14/5/97

Photograph 2.15 Galvanic corrosion

2.2.4 The Media panels

Media panel degradation resulting from hydrolysis of the GRP media, or tearing of the polypropylene panels in the vicinity of the through rods, have been observed on a large number of RBCs. Photographs 2.16 and 2.17 illustrate this form of damage. Further, on GRP media panels there has been evidence of what can only be described as brittleness of the media, no doubt caused by water absorption, see photograph 2.16. Regrettably, this type of degradation cannot be avoided, moreover, it is not possible to improve the mechanical strength of these media panels.

Source : STW Woodseeves, 15/5/97 **STW Kelstedge, 21/8/96**

Photograph 2.16 GRP media degradation

Photograph 2.17 HD Polypropylene media degradation

2.2.5 Motor and gearbox unit

Most RBCs within STW employ a Helical-Bevel motor and gear system. However certain manufacturers use a drive system which consists of a pinion wheel driving a larger gear wheel. In order to achieve a low rotational speed of one revolution per minute, the gear ratio between the pinion wheel and the larger driven gear wheel results in a tooth contact ratio of exactly one. Moreover, most RBCs of this construction use only seven teeth on the pinion wheel, which is well below gear design recommendations. The deeper implications of using a tooth contact ratio of exactly one, is that any slight wear will result in a tooth contact ratio of less than one, giving rise to a circumferential jerking motion of the RBC rotor. Such jerking action produces unacceptable inertia loading on both the gears and the media pack support structure. Unfortunately, this type of drive is un-lubricated, which again causes accelerated wear. Both wheels are of fabricated construction, therefore susceptible to alignment difficulties.

On RBCs with this arrangement, severe grooving was found to have taken place on the side of the segmental gear wheel plates, this was as a direct result of misalignment problems. Moreover, it was noted that severe wear had also taken place on the contacting face of the gear tooth, resulting from high contact pressures and the unavoidable sliding that takes place between tooth pairs. As a direct result of the above wearing action, a jerking action of the entire RBC was visible. This jerking action causes the rotor to be rapidly accelerated, resulting in acceleration forces being reacted back onto the gear drive unit. Eventually, this will lead to failure of the motor/gear drive unit.

2.3 Conclusion

It is evident that there is a wide range of mechanical deficiencies associated with RBCs. The fundamental design errors associated with these deficiencies are discussed in the next chapter. From the catalogue of defects the following faults were evident:

i) The mechanical integrity and clamping efficiency of the 'U' bolts and 'U' straps used to clamp the outer through rods onto the outer circumferential rim was poor.
ii) In a number of cases different materials were used adjacent to each other, thereby causing galvanic corrosion.
iii) The mechanical integrity of the media support structure was poor.
iv) Bolts clamping the radial spider arms to the shaft clamp and outer circumferential rim had worked loose, possibly caused by undersized bolts or incorrect bolt tightening torque.
v) On some RBCs the motor/gearbox system was of poor design.

CHAPTER 3

DESIGN INADEQUACIES OF RBCs

3.1 Introduction

A requirement for supplying RBCs to STW is that the units installed have an operational life of 20 years. However, this requirement is rarely achieved as mechanical deficiencies have affected all manufacturers and suppliers to STW. From the previous chapter it is apparent that the mechanical faults catalogued are as a consequence of three major design deficiencies:

i Inadequate clamping design for the through rods
ii Inadequate fatigue strength of the support structure, through rods and through rod clamps.
iii Disregard for the influence of galvanic corrosion.

3.2 Designing against fatigue

Fatigue failures of all components of the RBC have been experienced, suggesting that the designers have used inappropriate fatigue data. Designing against fatigue calls for an understanding of how materials behave under a particular stress mode. For example, the stressed component could be loaded either in bending, axial loading, torsion, or a combination of all three. Therefore, whenever using fatigue data, it is prudent to establish the mode of loading for which the fatigue data was obtained. It is also vital that the loading frequency of the data to be used is comparable to the actual application. Most fatigue tests are conducted on specimens which have a good surface finish, usually obtained by grinding or polishing. The effect of a polished surface finish is to give improved fatigue endurance limits. Therefore, it is important to make some allowances if the surface of the designed component is of a lesser quality.

An understanding of the loading on RBC components is vital in determining its life. STW have specified that RBCs be designed to cater for a maximum biomass growth of 3mm. However, on several RBCs, bridging of biomass has been observed and this results in growths exceeding 5mm. Bridging must be avoided, as it results in loss of effective surface area for treatment and increases the loading on the support structure by several multiples. However, estimating anticipated biomass growth is extremely difficult as it depends on the strength of sewage liquor. It has recently been suggested by Mr. E. Findlay, Principal engineer, STW, that all future RBCs be designed to cater for a biomass growth of 5mm. More recent investigations suggest this is marginally generous in the vast majority of cases and compensates where the biomass growth is substantially higher. To complicate matters further, Bannister, et. al. [7] have shown the load distribution on the through rods within a segment to be dependent on the angular position of the high-density polypropylene media panels and not to be equally divided between the through rods in that segment. This was attributed to the corrugations on the media panels causing a variation in stiffness at various angles of rotation.

Codes of practice for corrosion control are well documented within STW. For example, steelworks below the water level should, where possible, be hot dip galvanised or of stainless steel. Whilst this is good practice in the fight against corrosion, it might not be the right material for the application. Moreover, it is extremely difficult to predict the corrosive properties of various metals when continuously exposed to sewage liquor, as the chemical composition of the liquor will vary from site to site. Furthermore, the influence of ground water, which can infiltrate sewage pipes, could cause wider variations in the chemical composition.

Whilst it could be argued that these specifications may restrict suppliers of RBCs from using other materials which they feel might improve the mechanical performance, evidence suggests otherwise. At present no manufacturer takes account of two vital issues; firstly, the angular variation in load on the through rods, and secondly, the effect of low-loading frequency on the corrosion fatigue strength, to which the mechanical inadequacies are attributed.

3.3 Corrosion fatigue

This is defined as the resistance of a metal and its alloys to the formation and development of cracks, which lead to final fracture under the effect of a corrosive environment. The total corrosion fatigue life of a metal can be divided into three stages: crack initiation, crack growth and final fracture. This relationship can be represented with the aid of fatigue and kinetic fracture diagrams. In an inert environment, e.g. air, initiation of fatigue cracks at initially plain surfaces may account for 90% of the total life of the material. However, in a corrosive environment, the greater part of the fatigue life is occupied by the crack growth stage, even in very smooth specimens. A figure of between 22-25% of the total life for crack initiation in a corrosive environment has been experimentally proven [8], though Parkins [10] quoted a value of less than 10%.

The major effect of corrosion on the material endurance curve is that fatigue limits are removed so that a finite lifetime exists at any stress. An example of the effects of a corrosive environment on the fatigue life of stainless steel is shown in figure 3.1.

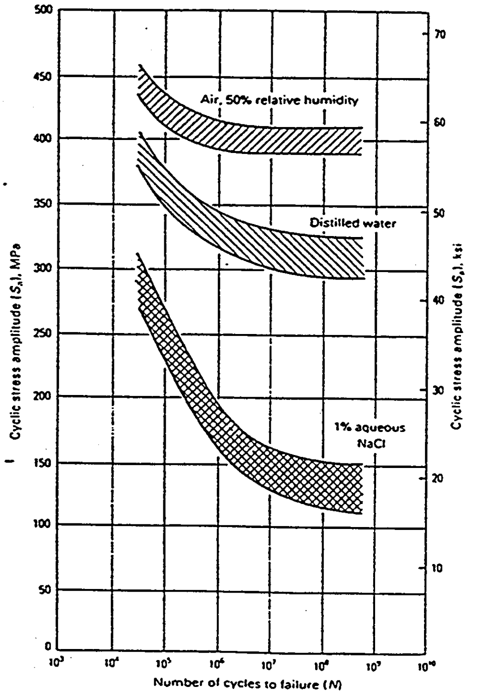

Source : Reference 35, loading frequency 50Hz

Figure 3.1 Corrosion fatigue data of 13% Cr steel

3.4 Low frequency corrosion fatigue

Most of the published corrosion fatigue data is based on tests carried out at loading frequencies of 50Hz and over. At much lower loading frequencies, less than 3Hz, there is a significant drop in the corrosion fatigue life. Several factors are responsible for this phenomena, more significant is the early initiation of cracks and faster propagation due to Hydrogen Embrittlement. Other factors include anodic dissolution, absorption strength reduction, induced wedge effect, loading waveform and microbiological influenced corrosion (see section 3.9).

3.4.1 Initiation of cracks

The widely held view is that pitting, developed over a range of chemical and electrochemical conditions with or without the influence of cyclic loading, may serve to accelerate the fatigue initiation process through a purely mechanical notch effect. This view was supported by Komai [11], who investigated crack initiation in seawater and observed that cracks were initiated at the bottom of corrosion pits. However as Szklarska-Simalowska and others [9,12] discovered, this may not always be the case. A study of pit initiation in 18Cr austentic stainless steels and 18-8 stainless steels exposed to MgCl solutions showed cracks to initiate from a smooth surface, as opposed to the general view that cracks form from pits. It was concluded that cracks nucleated at fissures in the semi-protective layer of corrosion products.

Whatever the case, crack initiation is achieved above certain threshold stress intensity values, K_{Iscc}, on surface flaws. This is represented on kinetic fracture diagrams and is an essential parameter of the system material-environment since it allows for computation of allowable stresses in structures that contain crack-like flaws of certain size, e.g., coarse surface finish. It is widely acknowledged that the K_{th} value for which cracks will grow in most steels lies between 5 - 10 Mpa.m$^{1/2}$: for example a type 4340 steel has a K_{Iscc} value of 6 Mpa.m$^{1/2}$ when immersed in water, see figure 3.2.

However, Komai [8] showed that on HT 50 and 80 steels, tested in synthetic seawater at a frequency of 0.167Hz, crack initiation at the bottom of corrosion pits occurred at a stress intensity factor of 1.65 and 1.55 MPa.m$^{1/2}$ respectively. These values suggest crack initiation at a much earlier stage when loading at low frequencies in corrosive environments. Knowledge of the physical-chemical nature of stress-corrosion fracture is especially important for the case of cracks growing at such low magnitudes of stress intensity values. The dominating factors in this case are anodic dissolution, adsorption strength reduction and more importantly, hydrogen Embrittlement.

3.4.2 Hydrogen Embrittlement

Hydrogen Embrittlement (HE) is defined as the hydrogen-caused reduction of the load bearing and/or the mechanical energy absorption ability of a metallic alloy. It is now known that most metals and alloys suffer, in some degree, a loss in mechanical strength caused by the presence of hydrogen [13]. Further, it plays a significant role in enhanced crack propagation.

A characteristic of hydrogen embrittlement (HE) mechanism, is that it is independent of the environment outside the crack. The required pH values and potentials are generated within the crack to make thermodynamically possible the discharge of hydrogen ions together with their subsequent absorption through the interior surfaces of the crack. The transfer of hydrogen ions, protons, from the crystal lattice to interfaces i.e., flaw surface, void, ...etc., leads to the formation of molecular hydrogen. This is a spontaneous process and is thermodynamically inevitable. As hydrogen penetrates into microvoids in the steel, it produces a pressure which leads to the formation of stresses in the lattice, distortion of the metal or part of it (blistering) and the formation of discontinuities. When a critical concentration of hydrogen accumulates, a separate microcrack is immediately formed that subsequently merges with the main crack. The most common models of HE assume that the dissolved hydrogen diffuses into the zone with a triaxial state of stress just ahead of the crack tip, and consequently is responsible for the loss of strength of the metal. This is one of the several theories on the mechanism of HE on most metals, Oriani [13] covers the various theories established to date.

Several authors [9,14,15,16,17,18,19,20,21,22,23,...] have shown that by **reducing the frequency of loading the crack propagation rate increases** and it is attributed to HE. The widely held mechanism for this is that, at high loading frequencies, the electrolyte near the tip of the crack is stirred better and acidification at the tip is prevented. As a result the rate of hydrogen absorption and anodic dissolution decreases. Since the frequency of cyclic loading is high, the rate of movement of the triaxially stressed region is much greater than that of hydrogen diffusion; therefore, a great number of hydrogen atoms will fail to keep pace with the triaxially stressed region. Under these conditions crack growth was governed by mechanical factors only. However, when the frequency of loading is low and the rate of movement of the triaxially stressed region is less than that of hydrogen diffusion, a great number of hydrogen atoms can follow this zone and facilitate the initiation of a mircocrack in the region of triaxial stresses ahead of the crack tip. The growth of the micro crack depends on the time within which hydrogen passes through the zone of triaxial stresses.

Low frequency loading also affects the fretting fatigue of two mating components. Fretting fatigue is often found in machine components which are clamped together and are not intended to undergo relative movement, as with structural components of RBCs. Endo et al. [24] investigated the effects of frequency on the fretting fatigue life of carbon steels. Bending and twisting tests were carried out on two smooth carbon steels with yields strengths of 285MPa (0.34%C) and 430 MPa (0.53%C) at a loading frequency of between 3 to 30Hz. It was concluded that fatigue strength decreased by 40% in the presence of fretting at a loading frequency of 30Hz and by a further 15% at 3Hz, see figure 3.3.

3.4.3 Examples of the effect of low frequency loading on crack growth rates, fatigue life and fretting in corrosive environments

The graphs in figures 3.2 to 3.4 highlight the effects of low frequency on fatigue in a corrosive environment. All tests were carried out under rotating bending with smooth specimens.

i) Crack growth rate

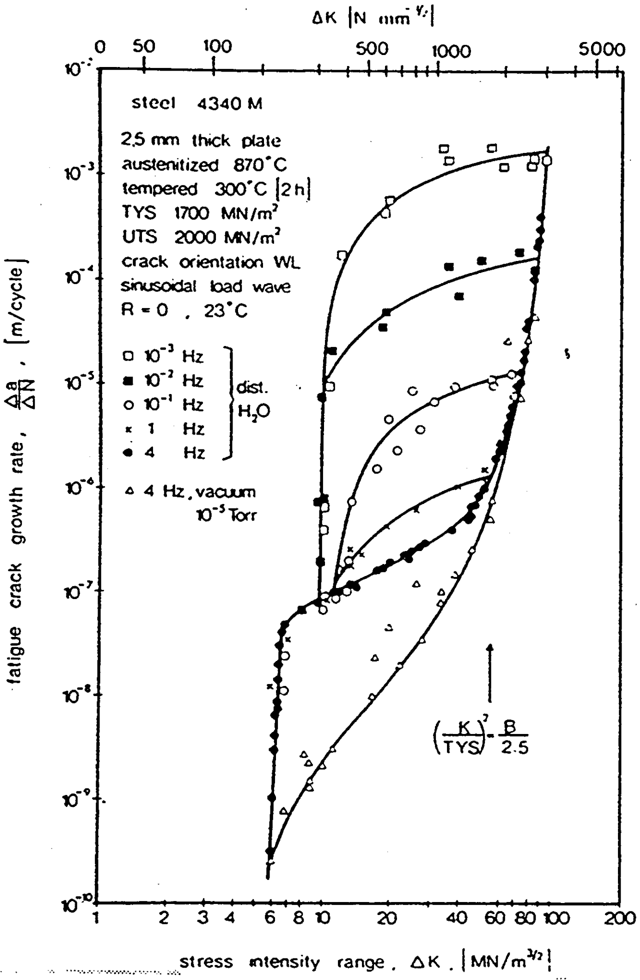

Source : Reference 15

Figure 3.2 Fatigue crack growth rate of high strength 4340M steel

ii) Fretting fatigue life

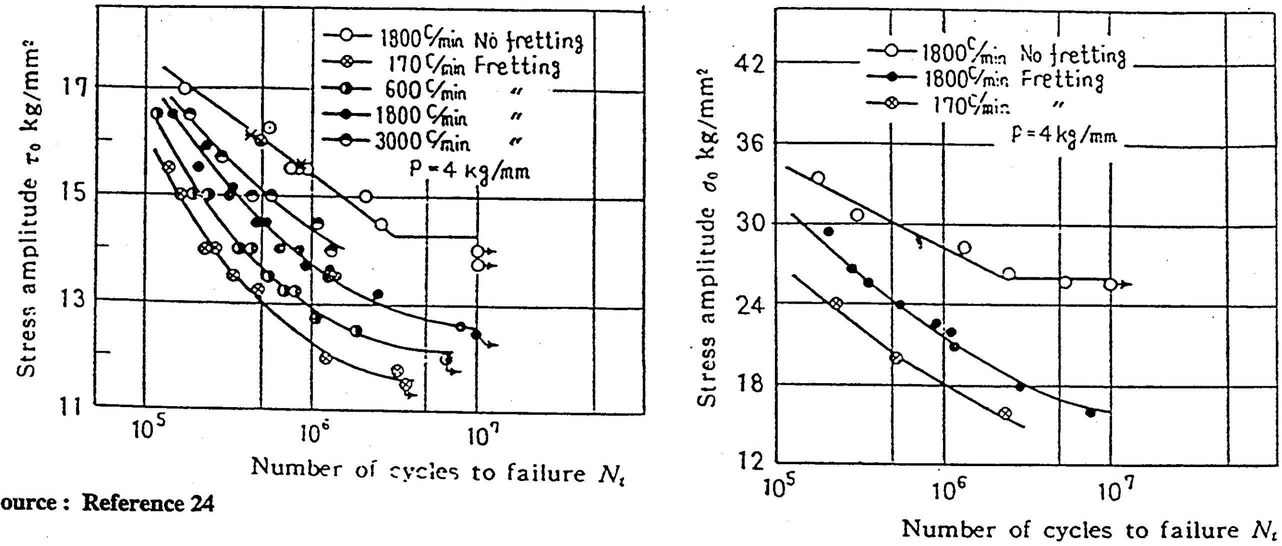

Source : Reference 24

Figure 3.3 Fretting fatigue data of carbon steels

iii) Corrosion fatigue life

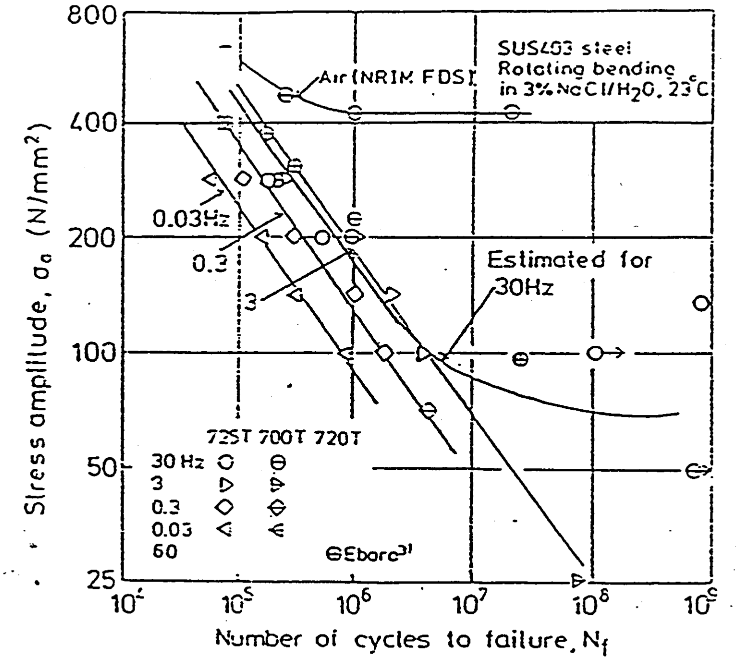

Source : Reference 25

Figure 3.4 Corrosion fatigue data of SUS403 stainless steel

3.5 Effects of plating on the endurance of steel

France and Swanger [26] studied the effects of hot-dip zinc coatings on steel and concluded that the endurance limit was reduced by the brittle iron-zinc alloy layer in which cracks form and propagate through the steel. It was noted that the endurance limit dropped by as much as 40%, dependent on hardness, whereas the same steels electroplated with zinc were unharmed. Forsam et. al., Dolan, et. al., and Watt [27,28,29] also concluded that hot-dip galvanising could lower the fatigue limit of steels in air by up to 33% of its original value.

These authors accounted for this on the basis that for electroplating with zinc, the substrate steel surface remained smooth prior to electro-depositing, but hot dip galvanising requires pickling of the surface of the substrate. Therefore, cracks in the brittle zinc layer on the hot-dip galvanised specimens could progress unhampered owing to the intimate bond between the coating and steel. Also, the brittle intermediate layer of diffused zinc and iron (intermetallic compound) may crack at stress levels less than the fatigue limit of the plate or substrate, thus producing cracks which propagated through the steel, even though the corrosive medium had not made a direct contact with the underlying steel. With the electroplated zinc coating, there existed sufficient ductility to deform about the bottom of the advancing crack, thus reducing the stress concentration. Also, the sharp boundary between the electrolytic zinc deposit and steel helped to retard cracking.

Zeevalkink, et. al. [30] showed that some commercially electroplated zinc coatings, which were prickled prior to plating, reduced the corrosion fatigue life by 29% of the value in air. With the pickled bath, there is always the possibility of the presence of some entrapped hydrogen in the outer layers of the steel, unless the material is annealed to expel the gases. The presence of the gas in the steel tends to make the surface more brittle, hence more susceptible to cracking (HE).

Forsman's [29] investigation into the effects of hot galvanising and zinc electrolytic on a wide range of steels under different environments stumbled upon the effect of low frequency of loading. The majority of the samples were tested at a loading frequency of 50Hz, though a couple of samples were tested at a frequency 15Hz. Seawater tests at the latter frequency, on zinc electrolytic platings, showed a marked reduction in corrosion fatigue strength of up to 63% of its value in air. This was in contrast to reductions of between 0 - 7% on tests with the same specimen at the higher loading frequency. Forsman concluded *"The low values obtained from the tests on plate material with electrolytic zinc coatings seem to indicate the great importance of the time factor"*. This would suggest that the rate of loading has a significant effect on the integrity of electroplated coating.

There is evidence on RBCs to suggest that zinc plated steels provide inadequate protection against the corrosive sewage liquor. On a few sites there has been evidence of corrosion and flaking of the zinc coating, see photograph 3.1. Moreover, the severity was dependent on the amount of oxygen in the stage of the RBC unit; i.e., more corrosion was evident in the nitrifying packs, due to relatively lower oxygen concentrations in the liquor. Since there is relatively much less loading in the nitrifying packs, it is safe to say that the corrosion of the zinc-plated structure was purely due to the aggressive properties of the sewage liquor. At the time of writing this thesis, information regarding the thickness of zinc plating used was still awaited.

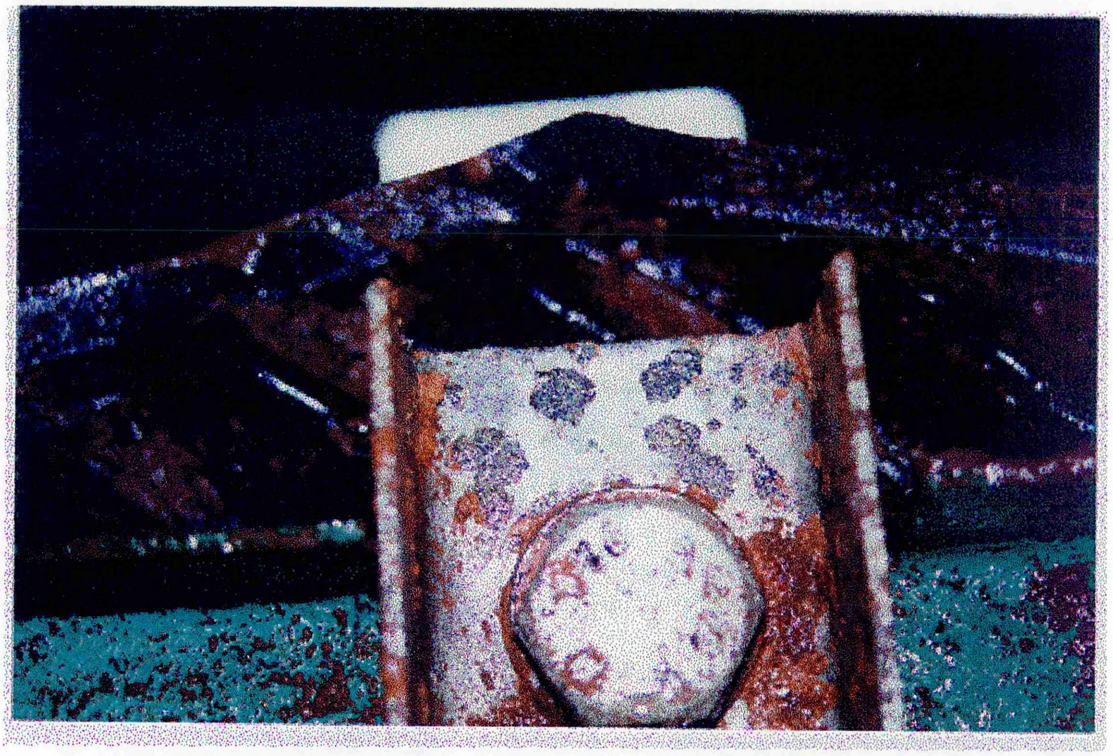

Source: STW Hollinwood Whixall, 2/9/97

Photograph 3.1 Corrosion of a galvanised steel structure

3.6 Influence of biomass on fatigue strength

The previous sections highlighted the effects of low frequency loading and corrosion on fatigue life of metals. Another influence on the fatigue strength of RBCs is the biomass growth.

Sewage treatment by the RBC is achieved by the biofilm attached to high-density polyethylene media discs. The biofilm removes dissolved and particulate contaminants and helps determine the water quality by influencing the dissolved oxygen content and by serving as a sink for toxic materials. At any point during the development of a biofilm, portions of the biofilm shear away and re-enter the bulk liquid. This detachment is a continuous removal process of the biofilm and is dependent on hydrodynamic conditions (shearing). Further, sloughing, which refers to random massive removal of biofilm due to nutrient/oxygen depletion deep within the biofilm, also occurs [31]. Although most of the biofilm is on the media panels, the support structure of the RBC is also covered with biomass.

In analysing the mechanical integrity of the RBC, it is necessary to consider the physical mass transfer of organics and nutrients from the bulk liquid into the biofilm, and the transfer of oxygen from the atmosphere into the biofilm and bulk liquid and how they might affect the underlying structural materials.

3.7 Operating performance of the biofilm

When the media is exposed to the atmosphere, the liquid film boundary at the air interface immediately becomes saturated with dissolved oxygen (DO). This saturation in turn results in an increase in the mass of oxygen that diffuses into the biofilm. When the media is submerged, oxygen transfer can occur either into or out of the biofilm depending on bulk liquid DO levels and the degree of mixing of the liquid film with the bulk liquid.

The overall performance of the biofilm is influenced by both the mass transfer and biological kinetic considerations. Kornegay et. al. [32] reported that substrate removal rate became constant after the biofilm reached a certain thickness and that further increases in film thickness need not result in increased rates of substrate removal under constant-defined feed conditions.

Active biomass depth has been estimated by several investigators to be between **20-600μm** [33,34,35,37]. However, the uneven biomass surface makes the definition of active biomass depth somewhat imprecise. Nonetheless, where active depths are compared to biofilm thickness, it is clear that, in the first stages of a highly loaded RBC, there consist large amounts of biomass not contributing to the removal of organic materials in the influent wastewater. Therefore the first stages of the RBC system are **biologically, and** hence **mechanically, overloaded.**

3.8 The effect of the biofilm on the mechanical integrity of RBCs

When sulphide is present, either in the influent wastewater or by its production deep within the biofilm, sulphide oxidising bacteria (SOB) such as **Beggiatoa** will grow on the biofilm surface. The production of sulphide within the biofilm is due to oxygen depletion. Beggiatoa will compete with heterotrophic organisms for oxygen and space on the media surface and in extreme cases they will take over the first stage of an overloaded RBC, shifting the load to the next stage and progressively taking over the system.

Microorganisms within the biofilm will respond to their environmental surroundings and this environment is continually changing. Surampalli et al.[37] reported that due to low DO conditions, Beggiatoa growth increased significantly during the summer months and slowly disappeared as the DO levels increased during the winter months. The report stated that *"the observed phenomenon of low DO conditions in the summer was due to higher biological reaction rate and lower saturation DO concentration levels. Therefore, the rate of oxygen used by the biomass increased, and the ability to transfer oxygen decreased at the high summer wastewater temperatures"*. This would suggest that during the summer months there is a higher probability of Beggiatoa growth.

Several authors [38,39,40,37,41] have sighted structural and operational problems on RBCs with heavy biomass growth, due to the presence of Beggiatoa. They sighted failures of the shaft and media. Further, it was reported that the use of supplemental air eliminated Beggiatoa growth and established a thinner active biomass, implying less stress on load-carrying structural members of an RBC. This can be achieved by pumping air into the sewage liquor. Another advantage of the supplemental air was to improve the organic removal rates. The reduction of the biofilm thickness was accomplished in two ways: firstly, the increase in bulk liquid DO levels, as a result of increased turbulence, resulted in a decrease of nuisance organisms. Secondly, as the bubbles rose through the media, they stripped excess biofilm growth. None of the above authors, nor anyone else to date, has linked the nuisance organisms to microbiologically influenced corrosion (MIC) of the RBC structure.

Another method to help reduce biomass growth is to increase the rotational speed, thereby increasing the shearing force acting to strip excessive biomass growths.

3.9 Microbiologically Influenced Corrosion (MIC)

It is well documented that microbiologically influenced corrosion leads to rapid material deterioration. Microorganisms can accelerate and control corrosion reactions by several mechanisms, one of which is the formation of aggressive metabolites such as sulphides and organic and inorganic acids.

The most widely acknowledged corrosive organism is the sulphate-reducing bacteria (SRB). These are anaerobic organisms which have a comparatively restricted nutritional spectrum and tend to grow in association with other microbial and macrobial forms. Such micro- and marco-bial communities create anaerobic conditions by the removal of oxygen from the system and the generation of the necessary nutrients as end products of their own metabolism [42,43]. Beggiatoa is one type of organism that can provide nutrients for SRB and/or create conditions conducive for SRB. This is facilitated by the thick biofilm preventing diffusion of oxygen into the active film layer; furthermore, outward diffusion of metabolites and corrosion products can become impeded, thus allowing areas within the biofilm to become anaerobic.

Once SRB growth has started, the production of H_2S occurs and concentrations of the gas can rapidly be produced, typically with a doubling concentration approximately every 10 - 15hrs [44]. The effect of SRB and SOB on steels is brought about by enhanced corrosion and hydrogen embrittlement. Although the mechanistic role of hydrogen sulphide in promoting the entry of hydrogen into iron based alloys has not been determined with certainty, the fact that hydrogen embrittlement occurs in sulphide-containing environments is unquestionable.

3.9.1 Effect of MIC on mild and stainless steels

MIC is localised corrosion that can appear as pitting, crevice corrosion, under-deposit corrosion or stress-corrosion cracking. Pits associated with MIC often have small surface openings with a larger subsurface cavity. It has been reported [45,46] that SRB cultures initiated pitting and intergranular corrosion on AISI 304L, 430, 409, 316L and 316 Stainless steels. Wagner et al. [47] reported that SRB produce open pitting or gouging on stainless steel while Borenstein [48] reported substrate tunnelling has been observed along ferrite stringers in weld areas of stainless steel. Tatnall's [107] review of case studies reported severe pitting of stainless and galvanised steels as a result of coexistence of SRB, SOB and iron reducing bacteria.

Kilgallon [49] investigated crack propagation rates and fatigue failure of two HSLA steels with yield strengths of 500MPa (SE500) and 690MPa (DSE690) and noted that sulphides produced as a by-product of SRB activity were responsible for enhanced absorption of hydrogen into the steel (HE). This resulted in higher corrosion fatigue crack growth rates.

Hoyt [50] investigated the corrosion fatigue strength of a nickel silicon steel in two aqueous environments at different frequencies. The aqueous media A contained a quantity of hydrogen sulphide, while B was water. The tests were undertaken at loading frequencies of 30Hz and 0.6Hz. The results show that hydrogen sulphide plays a significant role in reducing the corrosion fatigue strength of a metal at low frequencies of loading.

3.10 Bearing failures

Investigations into bearing failures on RBCs revealed the main reason to be as a result of selection of an inappropriate grade of grease. Failure of this type could be accelerated with poor installation.

All failed bearings were lubricated with grease having a base oil viscosity of between 73 to 150 cSt (Centistoke). For such slow speeds as the RBC, the minimum viscosity should be 1000 sCt at 40^0C. Since the elastrohydrodyanmic film thickness is a function of viscosity, a low viscosity could result in metal to metal contact within a bearing, accelerating bearing failure [51].

Also, it was noted on several RBCs that the level of grease filled about 50% of the housing. Whilst this practice is adequate for medium to high-speed bearings, it is inadequate for the low speeds of RBCs. It is recommended that the housing be **completely** filled with the specified type of grease mentioned above. Further, none of the bearings used on RBCs had grease escape or discharge values. Escape valves should be fitted to the underside of the housing, opposite to the lubrication entry point. This has the advantage of ensuring the passage of fresh grease across the bearing and will prevent grease build-up within the housing.

3.11 Detailed Finite Element Analysis of RBC structures

A detailed stress analysis was undertaken by Cranfield University consultants on the structures of various RBC suppliers to STW. The results compared favourably with the low-frequency corrosion fatigue limits already highlighted. However, details of this investigation have been restricted by STW Limited.

3.12 Conclusion

The fatigue strength of metals is reduced in a corrosive environment and reduced even further at low frequencies of loading. Evidence showing these effects has been presented. These factors have the effect of removing any fatigue limits, consequently, under these circumstances every structural component will fail. The operating history of RBCs has proved this point. The codes of practice for corrosion control set by STW have been shown to be in appropriate for the application of RBCs. Galvanised and zinc-plated steels are susceptible to low-frequency corrosion fatigue.

It would appear that most RBCs are biologically overloaded and there exists a high probability of Beggiatoa growth. There is strong evidence to suggest that Beggiatoa growth will be accompanied by SRB, moreover, the by-product of SRB metabolism has been shown to enhance corrosion and hydrogen absorption in a wide range of steels.

The evidence presented in this chapter has highlighted the factors responsible for the mechanical failures on RBCs and has necessitated the development of a condition monitoring system.

CHAPTER 4

CONDITION MONITORING

To ensure optimal performance, minimum operating and maintenance costs, Severn Trent Water Limited require a low cost monitoring system with easy readout indicators. This will allow the maintenance engineer to diagnose impending failure at an early stage.

4.1 Condition monitoring of low-speed rotating machinery

There is no universally accepted criterion at which machines are classified as slow-speed. However, it is generally accepted that 600 rpm is the minimum speed for intermediate-speed classification [52] and any speed below this could be classified as low-speed. Generally, low-speed machines are massive in size and consequently when defects begin to occur the resulting vibration is often very low and serious faults can go undetected.

It is well known that low-speed machines make great demands on both the analyst and vibration diagnostic instrumentation. This is primarily because standard predictive maintenance measuring instruments are inappropriate for low speeds. Furthermore, normal vibration severity charts only apply to rotating machines over 600 rpm and there is no information on specifying spectral alarm levels for low-speed machinery.

4.2 Problems with low-speed rotating machinery

The main problems with vibration analysis of low-speed machinery can be divided into four sections :

i) Optimum vibration parameter for low-frequency measurements, Acceleration, Velocity or Displacement ?

The most widely used parameter for measuring vibration is acceleration, however, acceleration decreases with reductions in rotational speed. Figure 4.1 shows the relationship between displacement, velocity and acceleration as they vary with rotational speed. It is evident that acceleration is the most sensitive parameter for analysing vibration levels at high rotational speeds (>60,000 rpm), whilst displacement is best suited for low rotational speed analysis (<600 rpm). Velocity provides a flat response for a broad speed range, and it is not surprising therefore that this parameter is widely used for setting alarm levels of machinery rotating between 600 to 60,000 rpm. A displacement of 10.0 mils (peak - peak) and a peak velocity of 0.314 in/sec (7.98 mm/sec) describe a somewhat "equivalent alarm vibration level" for such speeds. However, at 60 rpm where a peak velocity of 0.341 in/sec (7.98 mm/sec) is equivalent to a displacement of 100mils, it is more approiate to use displacement as a measuring parameter for setting severity levels compared with velocity.

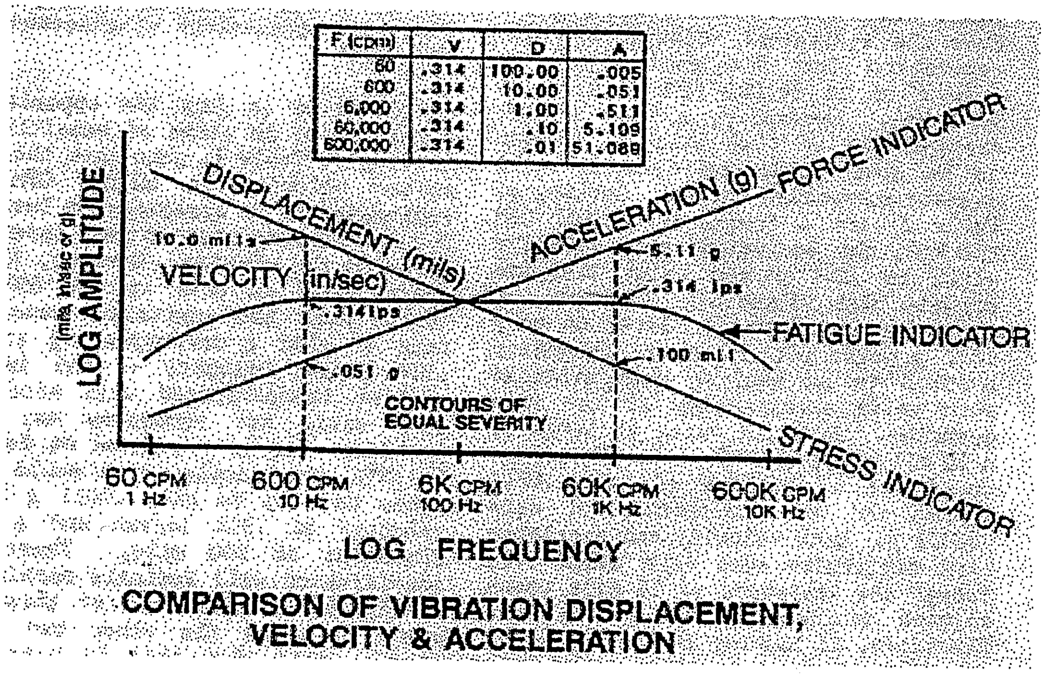

F (cpm)	V	D	A
60	.314	100.00	.005
600	.314	10.00	.051
6,000	.314	1.00	.511
60,000	.314	.10	5.109
600,000	.314	.01	51.088

Source : reference 53

Figure 4.1 Comparison of vibration displacement, velocity and Acceleration.

ii) Instrument limitations for low-frequency analysis

In general, spectrum analysers and data collectors are not designed for analysing machinery at low rotational speeds. On typical spectrum analysers noise will be seen in the first 4 FFT lines, assuming a 400-line resolution is employed, camouflaging actual vibration data in this low-frequency range. In order to combat the inherent low-frequency instrument noise problem, many data collectors and spectrum analysers are fitted with high pass roll-off filters at approximately 5Hz. Unfortunately, the filters will also suppress actual vibration signals within this frequency range. For example, a high pass filter at 5Hz, implies that the fundamental frequency of operation on machines rotating at below 300 rpm will not be detectable with conventional analysers.

As mentioned in the previous section, a more suitable parameter for measuring low-rotational speeds is either velocity or displacement. In order to read velocity or displacement spectra with a conventional accelerometer, integration and double integration of acceleration will be required. Integration can be achieved either digitally or by analog integration. Analog integration will distort and attenuate lower-frequency components due to high pass filtering necessary for the integrator. Further, it will also be accompanied by the integration or double integration of noise.

With digital integration, the problems of accompanied noise integration is more evident. The Schottky, i.e, the reciprocal of frequency, is the major contributor to noise levels [54]. The reciprocal of frequency (1/f) varies as $f^{1.5}$ with single integration to velocity and $f^{2.5}$ with double integration to displacement. For example, a decrease in frequency from 600 to 60, a factor of 10, would see an increase in noise of a factor of 31.6 in velocity units and 316 displacement units. This large noise increase is commonly called the "Ski-Slope" and can easily camouflage low-vibration signatures.

iii) Sensor requirements for low frequency analysis.

The frequency response of the sensor and analyser must be considered when taking low-frequency measurements. All sensors have roll-off filters which affect the magnitude of signals detected within the roll-off frequency range. Moreover, for any sensor there is a frequency at which the signal developed by the vibration cannot be reliably separated from the non-vibration signal, such as electrical noise generated within the measuring system. It is widely accepted [54,55,56] that for low-speed vibration monitoring a shear mode sensor with a sensitivity greater than 500mV/g should be employed. The shear mode sensor, unlike compression sensors, is less prone to the effect of temperature transients, which result in an increase in background noise with increasing temperatures. Whilst temperature transients can affect the performance of accelerometers, these effects are not considered in this thesis since all RBCs operate at ambient or near ambient temperatures.

If the frequency of interest is within the roll-off frequency of both the sensor or analyser, then the signal will be attenuated according to the roll-off charateristics of the measuring equipment. For example, if within the frequency range of interest the data collector/analyser and measuring sensor had roll-off attenuation rates of 50% and 30% respectively, the resultant amplitude of the required signal would be 35% (0.5 x 0.7 x 100) of its original value.

A further example; if the sensor had a sensitivity of 500mV/g, a 10mil peak-peak alarm level at 1 rpm should correspond to 0.0000014g's. This will generate an amplitude of 0.000007V on the measuring transducer. A typical 8 bit, 2.5V peak-peak, ADC board which has an absolute amplitude resolution of 0.009765V, will not be able to detect this signal. A 16bit board with the same peak-peak range will have an absolute resolution of 0.000038V, this also will not be able to detect the fault signal. A 22-bit A/D board will be required to detect the fault. However, at this level of signal magnitude a considerable amount of electronic noise will exist. Moreover, there are no 22-bit ADC boards avaliable on the open market.

iv) Coupling between the sensor and the data collector

Murphy [54] suggested that a strong magnetic clamp be used to attach the sensor to the machine, thus avoiding the rocking effects as would be experienced with a hand held probe, thereby reducing unwanted noise at very low frequencies. By contrast, Robinson [52] suggests the use of a coaxial cable, to minimise any electrical noise pickup and avoid hanging cables which would avoid tribo-electric effects at low-frequencies.

4.2.1 Summary

It is evident that displacement is the best parameter for measuring vibrations of low-speed rotating machinery. Regrettably however, measuring displacement is made difficult as a result of the low frequency noise associated with both the sensor and measuring instrumentation.

4.3 Literature review of low-speed vibration monitoring

The four points highlighted in the previous section make vibration monitoring of low-speed rotating machinery practically impossible, though some attempts have been made. Much of the work to date has concentrated on monitoring both rolling element and plain journal bearings. Kuboyama [57] summarises the difficulty with monitoring low speed rotating machinery, by stating that *"At over 100 rpm, it is easy to diagnose the condition of degradation and damage using vibration analysis. This is because vibrations have a great amount of energy and occur over a short period. On the other hand, with a rotating machine working at less than 100 rpm, it is difficult to diagnose damage or degradation because of the small amount of energy and the vibrations occur over a longer period"*. Furthermore, the vibration could be camouflaged by background noise. Kuboyama suggests several techniques for monitoring low-speed (1 rpm) bearings:

The Peak Level Differential Method (PLD) :
This technique was applied to rolling element bearings whereby Kuboyama considered signatures generated from a number of bearings of the same type and size. Noise was rejected by band pass filtering of the bearings natural frequencies.

Acceleration peaks exceeding pre-set threshold levels were held by what Kuboyama referred to as a "peak picker". The peak level differentials between both bearings and the number of occurrences were calculated, when values exceeded a certain criteria the bearing was judged to have sustained damage. This technique required the comparison of two bearings and was applied to pinch roller bearings which were operated at 1rpm. Kuboyama claimed successful detection of flaking on the surface of the inner race on one of the bearings, however, he does not specify the type of measuring equipment, nor characteristics of the sensor used. It is the opinion of this author that with all the associated problems of low-speed vibration monitoring, it would seem unlikely for this detection to have been accomplished. Moreover, in his conclusion Kuboyama states that *" these techniques have not yet been applied because of technical difficulties".*

Other methods employed by Kuboyama included the Self-Correlation method, Cycle Histogram method and Fe Content Detector.

Penter [58] investigated monitoring of a gearbox at low rotational speeds using temperature measurements, debris and vibration analysis. The gearbox was run to destruction for 2600 hours (69 days) under 1.5 x full load ratings with contaminants added to the lubricant. The major defects were contact fatigue of the bevel pinion, fatigue failure of the shaft and outer race bearing damage. Penter noted that temperature measurements and debris analysis could not provide adequate warning before a failure.

Penter stated that hand held vibration monitoring instruments failed to give a clear indication of any failures. However, some success was achieved with a wide-band spectral analyser (0 - 10KHz). Signatures detected with this analyser were averaged to suppress non-synchronous information. Monitoring was achieved by examining energy levels, first and second order vibration levels, low-frequency modulation and general signal deterioration. Also, changes in the frequency domain, as a function of time, were observed. Penter concluded that this technique of vibration analysis could provide up to 30 days warning for certain faults. However, the speed of the gearbox was not provided, therefore, Penter's definition of low speed is unknown.

Canada et. al. [59] developed a Slow Speed Technology (SST) system for measuring vibrations on low-speed machinery. It was based on separating electronic noise of the sensor, with a specified level of statistical confidence, from the captured data. Furthermore, the adjusted data was then corrected for the distortion introduced by the analog integrator, i.e., introducing a gain to compensate for the roll-off characteristics of the integrator. This method was shown to give improved performances when compared to digital integration.

Robinson et. al [52] proposed a new methodology for vibration monitoring of low speed machinery, however the proposed technique is similar to the PLD method developed by Kuboyama. It involved segmenting the signal into time intervals, dependent on the sampling frequency, and obtaining peak values for continuing time intervals until the desired number are captured for processing. Peak values can be obtained using analogue circuitry or digitally. Processing peak values, however, involves spectral and waveform analysis. Comparisons of the peak value method with enveloping (demodulation) were made. Enveloping involves high pass filtering, rectification (half or full wave), and low pass filtering to separate the assumed low-frequency modulating signal from the high-frequency carrier. The spectrum of the enveloped signal shows whether the vibration signal is random in terms of amplitude and phase, or whether there is a repetitive machine-speed related signature present. The proposed new method replaced the rectification process in demodulation with the peak value.

Direct comparisons of the peak value and enveloping on similar signals shows peak value results to be independent of speed of the machinery or analysing bandwidth. In contrast, enveloping was dependent on the speed of the machine, as well as analysing bandwidth. The sensitivity of the enveloping technique decreases rapidly with decreasing machine speed and becomes unreliable for low-speed machines. Field measurements using low-frequency accelerometers on bearings rotating at 2 rpm showed that the peak value technique detected inner race defects one month prior to failure. In this author's experience, bearing damage at this stage of supposedly early detection could have been detected with the human ear or a microphone 10 meters from the bearing. The failure, mentioned by Robinson is undefined. It is the present author's belief that catastrophic failure of low-speed bearings on heavily loaded machines does not occur. Whilst the bearing components could be badly damaged, the shaft will continue to rotate and even use the bearing housing for support. A loss of operation will occur if the scored shaft/stub shaft should break or misalignment of the bearing causes the drive unit to breakdown. The latter was experienced on an RBC located at STW Langar. Robinson's field results are viewed with scepticism.

Mechefske et. al [60] used parametric models (Auto-regressive, AR) of amplitude demodulated vibration signals to generate frequency spectra on low speed (<100rpm) roller bearings with defects. This has the advantage of using much shorter data lengths. Differences in frequency spectra between good and faulty conditions were used to identify bearing defects. Szrom [108] claimed successful detection of bearing defects at speeds as low as 48 rpm using a velocity-based vibration sensor.

4.3.1 Conclusion

It is apparent that condition monitoring of low-speed machinery using vibration analysis is fraught with difficulties and where there has been claims of success, the period between detection and failure was about 30 days. This period is too short for adequate plans of replacement or repair, particularly for large low-speed machines. Furthermore, some of the authors in the previous section failed to specify the equipment used for experiments.

4.4 Acoustic emissions (AE)

As detailed in chapter 2, mechanical deficiencies of RBCs result in rubbing between mating components. The relative movement between mating parts is very slow, approximately in the order of 0.05m/sec, therefore, vibration monitoring of these deficiencies cannot be accomplished. With acoustic emissions offering opportunities to gain information on structural integrity in different phases of its useful operational life, Sato [61] suggests that the study of the release of AE elastic waves emitted from moving parts offers a more robust method of detection. Equally important is that the generation of acoustic emissions is independent of rotational and/or relative velocities.

Acoustic emission is a naturally occurring phenomenon within materials. Historically AE is defined as the resulting transient elastic wave generated when strain energy is released suddenly within a material. This is due to microstructure changes, i.e., dislocations, crack generation and propagation, friction phenomena within a crack, plastic deformation, fracture of brittle inclusions, formation and growth of twins, fibre breakage, phase (martensitic) transformation, etc... These changes can be generated internally or externally and cover a broad frequency range between 20 KHz to several Mega-Hertz. This thesis concentrates on the elastic waves generated by the rubbing of metal components, covering a frequency range of 100KHz to 1Mega-Hertz.

The application of the acoustic emission technique in research and industry is well-documented [56,62]. In most applications of this technique, the material under investigation has to be adequately loaded. When the sample is loaded and producing AE, unloaded, and then reloaded in the same direction of the original load, AE activity often does not begin until the previously achieved stress is reached and passed. This phenomenon is known as the Kaiser effect.

Studies in tribology bear resemblance to the presented investigations on rubbing faces of RBCs. Boness et. al. [63,64] investigated wear between loaded metal surfaces in relative motion, with or without lubrication, and concluded that AE can be used to determine the onset and the rate of wear between components. The source of AE activity was attributed to the breaking of surface asperities and the formation and destruction of the friction contact. The latter is similar to the 'slip-stick' mechanism of frictional movement under constant running conditions [65,66]. Boness used sensors with a frequency range of between 60KHz to 4 MHz, furthermore, pre-amplification of between 40 to 80dB was employed. Sarychev [64] noted that the strength of AE depended on; sliding velocity, friction coefficient of mating surfaces, contact pressure and the height of roughness asperities.

Whilst it is generally agreed that interpretation of AE signals can be difficult, especially under multiple source generation, rms. (root mean square) values have been found to give a good correlation between wear and AE activity. Other parameters used for AE characterisation of wear mechanisms include total count, count rate, amplitude distribution, the first four statistical moments and AE energy. It may be concluded that the process of rubbing between loose contact faces of an RBC will generate AE activity. **The application of AE analysis to the monitoring of such low-speed machines as RBCs is the first of its kind.**

Investigations [65,66] to understand the 'slip-stick' process of sliding friction discovered that at a velocity below the 'critical velocity', the motion of a body sliding under friction proceeded in a discontinuous or stick-slip form. A typical example being the tool feed drives for machines. This motion proceeds as jerks, i.e., the surfaces initially stick together until, as a result of gradually increasing pull, there is a sudden break with a very rapid slip. The surfaces stick again and this process is repeated indefinitely. In the event of slip-stick motion the acoustic emissions activity will be high.

4.4.1 Stress waves (SW)

Stress waves and acoustic emissions have always been referred to hand-in-hand, however, this author will differentiate between the two for the purpose of this research.

Whilst AE are generated within the material, stress waves will be defined as the transient elastic waves generated on the surface of a material as a result of friction between two mating parts. The breaking of surface irregularities or asperities and relative motion of entrapped broken debris will result in the generation of stress waves.

Stress waves are similar to Rayleigh waves in their generation, though the present author believes that stress waves will consist of a mixture of Rayliegh and Lamb waves. Furthermore, it is the belief of the author that, like AE, a type of Kaiser effect can exist with stress wave emission. With the passage of time, friction between mating surfaces will lead to wear, resulting in SW activity as surface asperities as broken. Surface asperities will eventually be smoothened. In this event friction between the entrapped debris and the mating surfaces will be the source of stress waves. As the wear increases, looseness between the mating parts will increase and entrapped debris will filter out between the mating parts, in this event stress wave generation will diminish considerably unless the mating parts are constantly forced together, e.g., the raceway and rollers in a bearing. If the latter is not the case then regeneration will occur after re-tightening of mating parts, and the process of friction has restarted. However, the author has no evidence to prove the existance of a Kaiser effect.

4.4.2 Stress wave propagation and attenuation

Stress waves, like AE, propagate in all directions. Factors that affect propagation include attenuation, interfaces, reflections, material absorption and impedance. High-frequency stress waves are rapidly attenuated while low-frequency stress waves can be detected at longer distances from the source. The attenuation coefficient is given as:

$$\alpha = \frac{20}{x} \mathrm{LOG} \frac{A_0}{A_1} \tag{4.1}$$

where α is the attenuation coefficient in dB/m, the magnitude of a signal at a point is A_0 and the magnitude reduces to A_1 at a distance x (m).

4.4.3 Types of Stress waves

Acoustic emissions and SW can be either of Burst and Continuous emission. Burst emission refers to high amplitude waves that are well separated from noise and each other, i.e., they are singularly distinguishable from other bursts. AE from crack growth is a typical example. Continuous emissions are of low energy and are not singularly distinguishable. Dislocation movement in metals is a typical example. In certain instances, burst emissions can become continuous when the burst rate is very high and the time lapse between bursts is very short.

4.4.4 Acoustic emission transducers

Stress waves can be measured with standard AE transducers. There are various types of transducers, resonant or wide-band, depending on application. Wide-band sensors have a flat response over a wide frequency range but are less sensitivity than resonant transducers.

4.4.5 Advantages and disadvantages of Stress waves

Advantages and disadvantages of stress waves are identical to AE. Advantages include:

i It can be used continuously during operation of machinery.
ii Only a small surface of the structure is needed to analyse the complete structure.
iii AE provides source location capabilities
iv Due to the high frequency range associated with AE, background noise of operation will be filtered out.

Disadvantages include:
i There does not exist a definite correlation between AE and wear. Therefore experiments for the application must be undertaken prior to application.
ii Attenuation due to transmission length.
ii Since AE is wide-band frequency and therefore contains low energy levels, the signals could be masked in low ambience background noise. Therefore steps must be taken to reduce interference from noise within the system.

4.5 Application of acoustic emissions to condition monitoring of low-speed machinery

Sato [61] investigated the use of AE to monitor seal rubbing on large steam turbines. Results showed an increase in the output signal amplitude with the generation of rubbing. During real tests on steam turbines it proved difficult to judge rubbing phenomena solely on amplitude changes due to high background noise. However, Sato used the spectrum of the envelope waveform and showed that rotational frequencies of the turbine were generated with rubbing. The above-mentioned procedure was also successful in detecting bearing tilt under considerable background noise. Since Sato employed enveloping, there was no advantage to using high frequencies. Liu [72] also successfully correlated AE generation to rubbing phenomena on real gas turbine generators.

Further, Sato investigated low-speed bearing damage by simulating metal wipe in journal bearings at 5.5 rpm. It was observed that acoustic bursts were generated as a result of slight metallic contact. The amplitude of the waveform became larger with increasing metal wear. However, no evidence was presented showing the correlation between increased AE strength and wear.

Rogers [73] applied AE analysis to condition monitoring of off-shore cranes. He stated *"because of the slow rotational speed of the crane, application of conventional vibration analysis (0-20KHz) was of limited value for on-line condition monitoring".* AE resonant transducers between 100KHz to 300 KHz were found to be informative for on-line monitoring of bearings using kurtosis at different frequency bands. Balderstone [74] reiterated the successful application of resonant AE transducers to detect incipient failures in bearings.

McFadden et. al. [75] explored the use of acoustic emission transducers for the monitoring of rolling element (angular contact) bearings at speeds varying from 10 to 1850 rpm. The sensors were placed on the bearing housing. A fault, simulated by a fine scratch on the inner raceway, formed the basis of this experiment. It was commented that the AE transducer, with a frequency response beyond 300KHz, failed to perform as expected at the higher end of the rotational speed range (850 rpm) and was inferior to the conventional high-frequency accelerometer. However, at low rotational speeds (10 rpm) the AE transducer appeared to respond to minute strains (local distortions) of the bearing housing caused by the concentrated loading of each ball in the bearing. These minute strains appeared as spurious spikes superimposed on the ball pass frequency. Measurements with conventional strain gauges failed to detect the strain on the bearing housing. The ball pass frequency was detected with a fault signature superimposed onto the original signal in the time domain.

It was concluded that at low speeds with steady loads, base bending/strain of the bearing housing could enable the AE transducer to detect signatures from very small defects in rolling element bearings, while at higher speeds base bending appears as low frequency noise. It is the view of the present author that the experimental tests reported were vague. Even more questionable is how the ball pass frequency, which is less than 0.6Hz, was detected with a sensor having a resonance of between 200KHz to 300KHz.

Smith [76] was involved in the experiment mentioned above. In a separate paper, Smith reiterated the difficulties with vibration analysis at low speeds. However, Smith confirmed the findings of McFadden, stating " *the form of response of the AE sensor was puzzling since the transducer was responding to once-per-ball distorting in the casing at frequencies as low as 1Hz. AE transducers are not supposed to respond to frequencies as low as these*".

It is the present author's view that the distress waveform presented by McFadden could be mistaken for spurious electrical spikes being superimposed on the ball pass frequency. Median filtering of this signature would have removed such spikes, see section 6.7.

The preceding chapters present the successful applications of stress waves to the detection of mechanical deficiencies on RBC structures and bearings, the first of its kind.

CHAPTER 5

EXPERIMENTAL PROCEDURE AND APPARATUS

5.1 Introduction

Ideally, experimental tests should be carried out on real sized machines operating under real loading conditions. This criterion is never achieved, mainly due to availability, cost and time. The latter is even more relevant at the very low rotational speeds of RBCs. The simulation and monitoring of a crack growth and/or the process of loss of tightening torque will take a considerable period to achieve under true loading conditions. Therefore a test-rig was built that allowed the introduction of known mechanical deficiencies. Investigations were centred on the stress waves generated by rubbing of mating components. Such rubbing could be as a result of miniature movements, e.g., the loss of tightening torque between bolted components or the rubbing of a fractured/cracked face under alternating stress.

5.2 Test-rig

A test rig was built to simulate some of the mechanical defects that were reported by Brenner [5]. The faults simulated were:

i Frame looseness, a result of loss of tightening torque
ii Rubbing of a broken support rod
iii Media movement as a result of creep

The rig consisted of two sections. The top half, seen in figure 5.1 and photograph 5.1, is equivalent to a pie section of an RBC, with 4 radial rams, 4 support rods and a media sheet. This section was equivalent to the smaller size of RBC in operation. The counter balance weights on the bottom half allowed the media structure to be balanced about the shaft, thereby eliminating movement of any structure during rotation, e.g. movement of gears. This was intended to help eliminate unwanted acoustic bursts. Materials used were of mild steel and the motor/gear box unit was a KA96R62 Helical-Bevel geared motor, providing a rotational speed of 1.12rev/min.

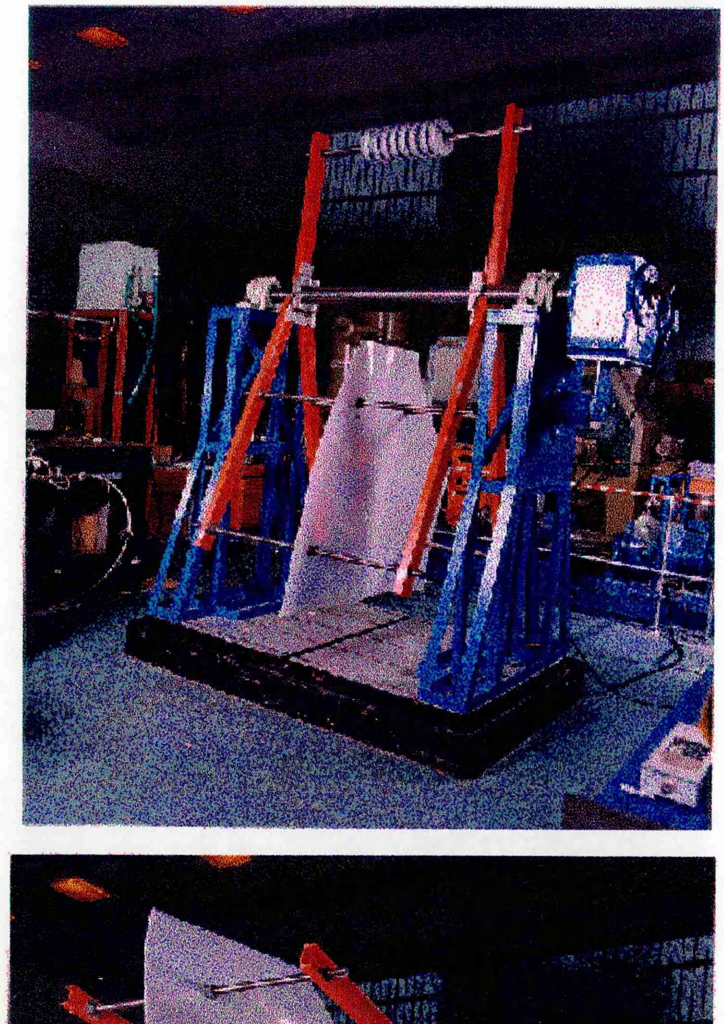

Photograph 5.1 The Test-rig

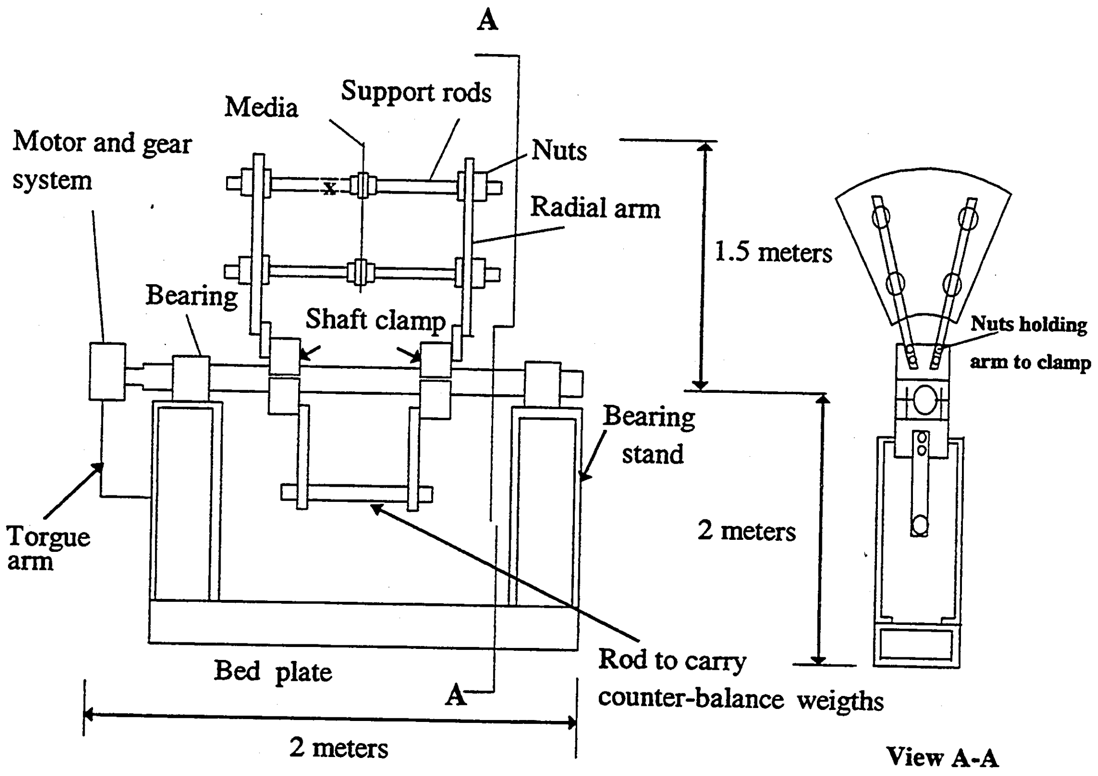

Figure 5.1 Test-rig layout

5.3 Simulation of mechanical defects

Responses for each simulation was recorded whilst the rig was operating with a mass loading equivalent to 5mm biomass growth, as discussed in section 3.2.

5.3.1 Frame looseness

Frame looseness was simulated by a reduction of the tightening torque holding the radial arms onto the shaft clamp plate, thereby creating relative movement between the mating parts. The initial tightening torque was 100 Nm. Frame looseness was achieved by loosening the bolts by approximately a quarter of a revolution from the initial tightened position. Three sub-simulations were performed :

i The looseness of the entire structure (loosening of the bolts holding the four radial arms onto the shaft clamps) causing rubbing between all radial arms and shaft clamp plates. This resulted in slight jerks as the structure moved from top dead centre onto its downward phase and vice versa.

ii Just one of the radial arms was loosened. This resulted only in minute rubbing movements, which were not visible to the naked eye. Each of the four radial arms was loosened in turn.

iii Two radial arms sharing the same support rods were loosened at the same time. as in sub-simulations ii, no visible movements resulted.

5.3.2 Broken support-rod rubbing

Simulation was achieved by cutting the cross-section of a support rod into a cup/cone shape, which is typical of a fatigue fracture. The two halves were held together by a squirrel cage frame, as illustrated in figure 5.2 and photograph 5.2.

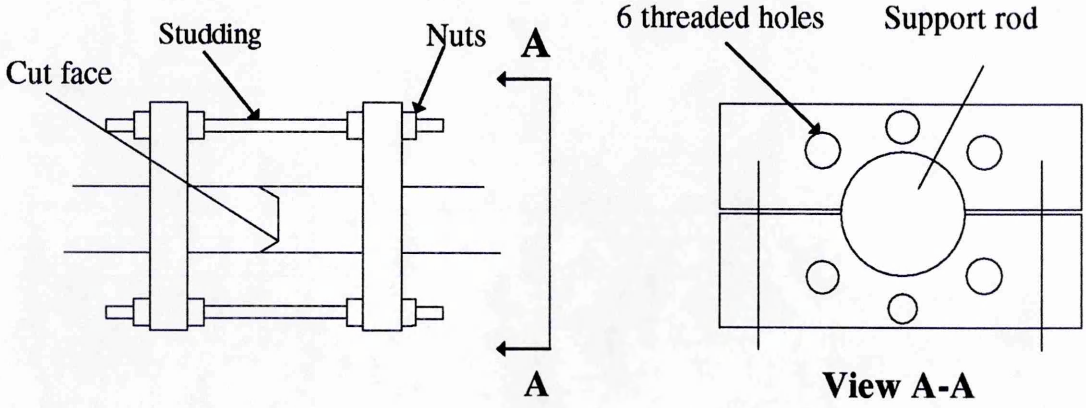

Figure 5.2 Squirrel cage for fractured through-rod simulation

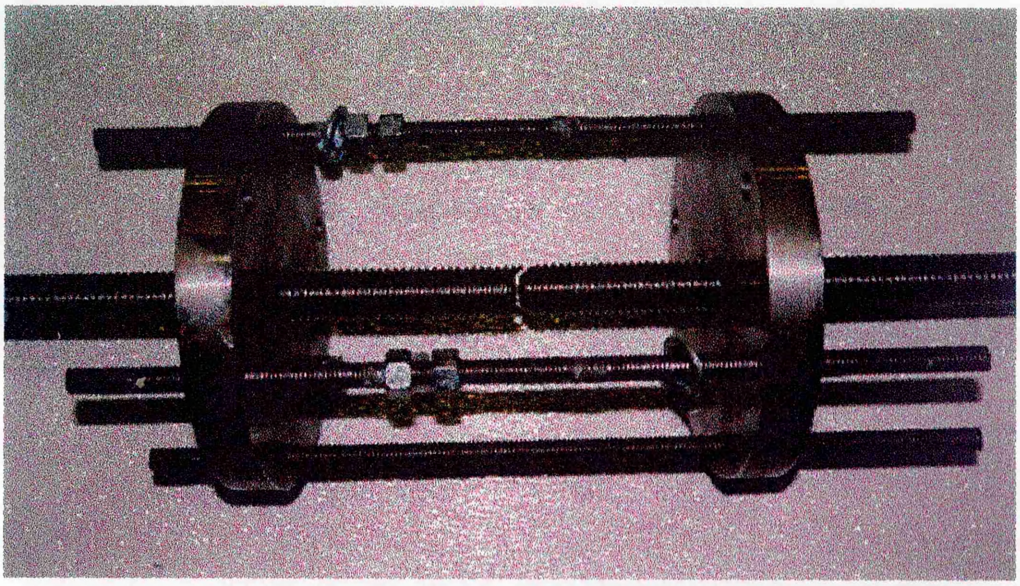

Photograph 5.2 Squirrel cage

This method of crack simulation has also being used by researchers studying the dynamic behaviour of cracked shafts. Placing weights either side of the cracked assembly simulated loading of the biomass. The assembly was put into one of the outer through-rod positions. During rotation the cut faces of the through-rods were forced to rub against each other, which caused surface asperities to be broken, thereby releasing acoustic energy. Photograph 5.3 shows the effect of rubbing on the cut faces, with evidence of wear. The importance of this particular aspect of the research programme was to simulate slip velocities in the order of 0.05m/sec.

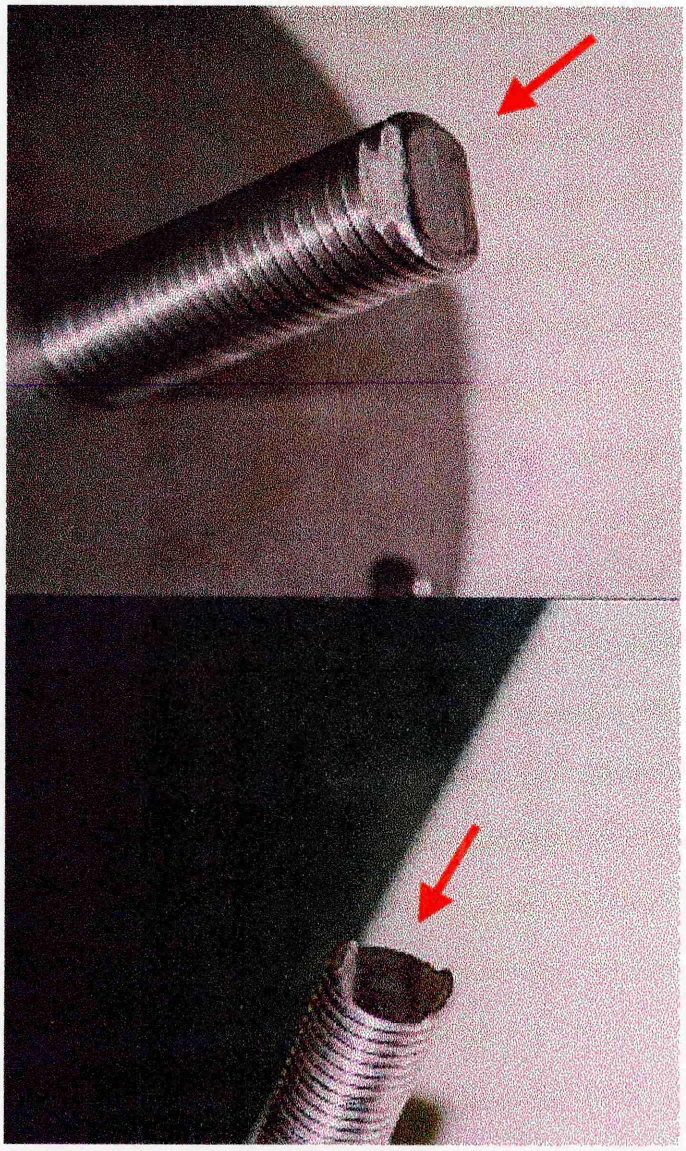

Photograph 5.3 Effect of rubbing on the cut faces

5.3.3 Media movement

A single sheet of high-density polyethylene, 1.5mm thick, was used to simulate media movement. By increasing the diameter and length of the holes through which the support rods run, movement of the plastic sheet about the support rods was created. The single media sheet was placed halfway along its support rods with an equivalent 5mm-biomass growth, see figure 5.3 and photograph 5.1.

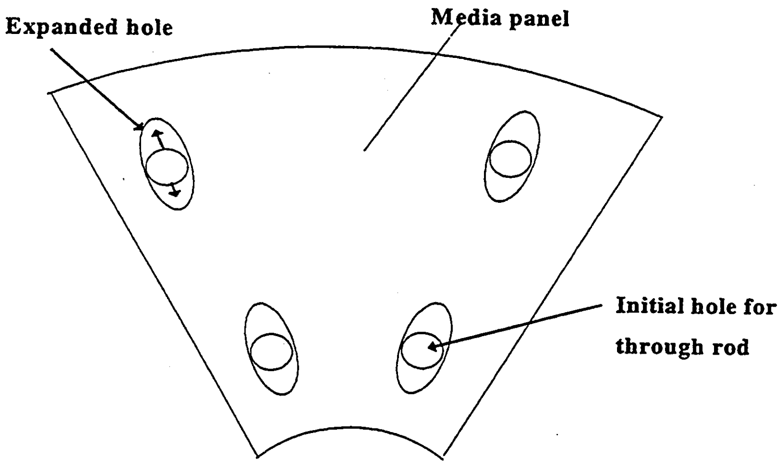

Figure 5.3 Simulation of media movement

5.4 Data acquisition

A schematic diagram of the data acquisition system used throughout all experiments and 'on-site' tests is shown in figure 5.4.

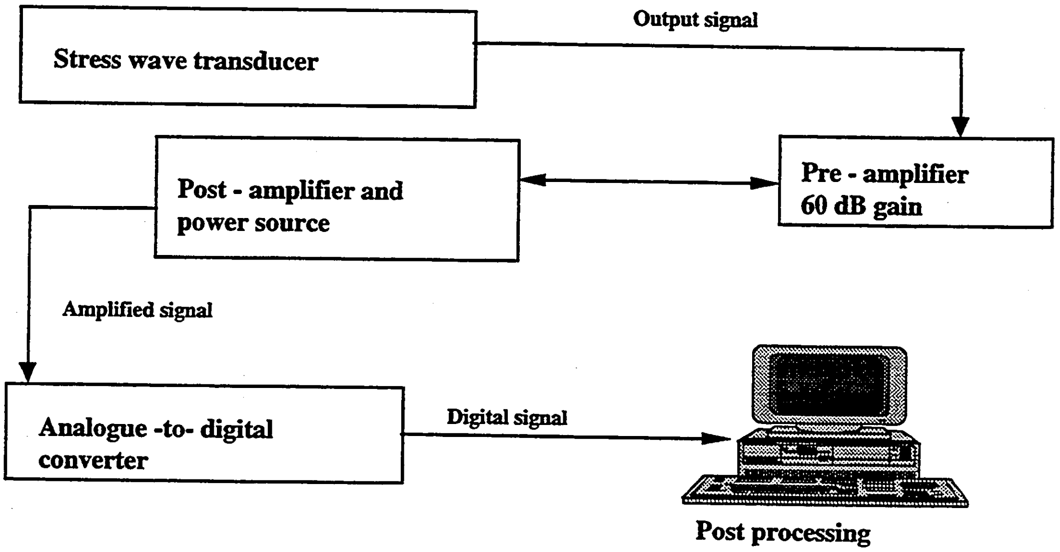

Figure 5.4 Data acquisition set-up

5.4.1 The Transducer

A commercially available piezo-electric type sensor, with a relatively flat frequency response of between 100KHz to 1000KHz at an operating temperature range of -65°C to 177°C, was used. The calibrated chart of the WD sensor supplied by Physical Acoustics Corporation is shown in figure 5.5.

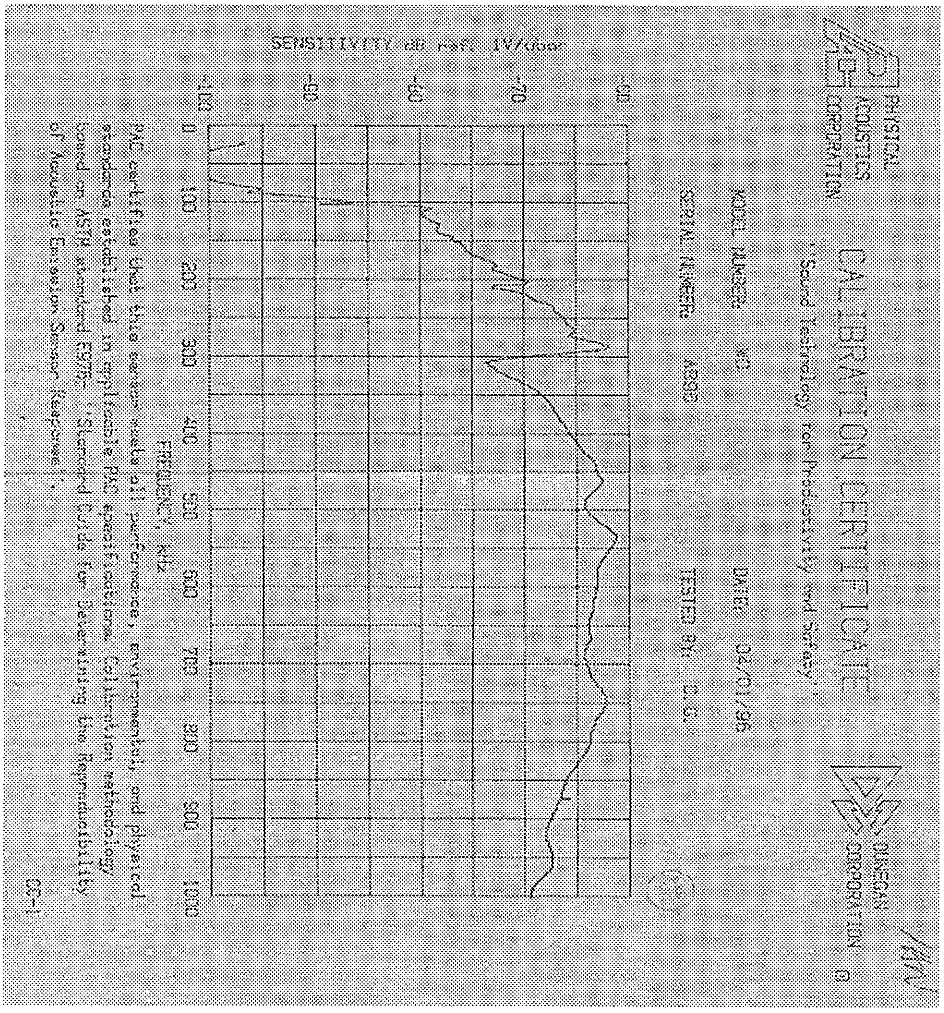

PHYSICAL ACOUSTICS CORPORATION

CALIBRATION CERTIFICATE

"Sound Technology for Productivity and Safety"

MODEL NUMBER: WD

DATE: 04/01/96

SERIAL NUMBER: AE93

TESTED BY: C.G.

DUNEGAN CORPORATION ®

PAC certifies that this sensor meets all performance, environmental, and physical standards established in applicable PAC specifications. Calibration methodology based on ASTM standard E976 - "Standard Guide for Determining the Reproducibility of Acoustic Emission Sensor Response".

CC-1

Figure 5.5 Frequency response of sensor provided by supplier

The transducer has a differential connection that provides common mode rejection of unwanted signals in environments of high electromagnetic interference. The selection of this type of transducer was primary for the following reasons:

i It was in keeping with the philosophy of availability and simplicity.

ii Since the resonance characteristics of the machines with varying structural sizes are unknown, it seemed prudent to use a sensor with a wide frequency range.

iii The true frequency characteristics of the sensor are readily available. Whilst resonant transducers have been designed at Cranfield University [77] for specific applications, calibration of these to transient and continuous stress waves are not adequate. The typical back-back and lead fracture calibration techniques only give approximations of the transfer functions. Realistically, these transfer functions should only be used as a measure of sensor deterioration and not sensor calibration. Commercially available sensors are calibrated to various standards dependent on application. For instance, Physical Acoustics Corporation calibrate their sensors to the U.S National Institute of Standards and Technology (NIST). Therefore, the true frequency characteristics are known, aiding selection.

The drawback with wide band transducers is that they are less sensitive than resonant type transducers.

5.4.2 The Pre-amplifier

The pre-amplifier used on all experimental and 'on-site' tests was the Physical Acoustics Corporation type 1220A, specifically designed for acoustic emission measurements. It has a bandwidth of between 20KHz to 1.2MHz, a 20V peak-peak, extremely low noise specification (< 2 µV) and a 40/60 dB switchable gain control. The pre-amplifier was powered by the post-amplifier.

5.4.3 The Post-amplifier

This delivers the 28V power needed for the pre-amplifier. The AE1A system, produced by Physical Acoustics Corporation, also has a 0-41dB gain switchable in 3dB steps. It is ideal for driving long coaxial cables, which could result in some attenuation in signal strength.

5.4.4 The Analogue-to-Digital Converter

A dual channel analogue to digital converter (ADC), R2000 Rapid systems, was used for data acquisition on laboratory experiments. The system provided the following features:

i Sampling rates of between 1Hz to 20MHz
ii 64 Kbytes memory capability per channel
iii 100% pre- and post-trigger capability
iv Selectable gain range of between 0.256 to 1280 Volts
v An 8-bit resolution capacity
vi Selection of analogue and digital triggering
vii Choices of automatic or manual data collection. In automatic mode an internal clock controls the sequence whilst in manual mode, the sequence is controlled by triggering.
viii An accompanying oscilloscope software. This allowed for easy set-up and acquisition control.

For 'on-site' recordings, it was hoped that data covering one complete revolution of the RBC could be collected and saved to disk, thereby allowing a detailed analysis. In order to specify the sensor and analytical procedure that will provide effective and realistic results, it is imperative that a complete investigation of all stress waves generated, either as a result of mechanical deficiencies or purely operational noise, is undertaken. With such a detailed analysis the final equipment specification to be provided could allow for a 'purely' analogue system thereby reducing, as far as possible, the training required for usage.

At a sampling rate of between 4 and 6 MHz, and a rotational speed of 1 rpm, a minimum buffer memory capacity of 240 Mbytes will be required to capture all the stress wave data in one revolution. It is recognised that there are limitations in buffer memory on the market today. The maximum available on ADC boards in the market was 2048Kbytes, produced by 'Kiethley instruments'. However, the continuous recording of large segments of data can alleviate this problem to a degree. Therefore, within cost restraints, a 'Kiethley Instruments' DAS-4101/256K ADC board was purchased for 'on-site' data measurements. This increased the buffer memory relative to the Rapid system by a factor of four, ensuring larger data segments could be recorded. A further reason for acquisition of a new board was that other researchers required use of the Rapid system, and it would have been unfair to restrict their use.

The board was fitted into a computer, thereby keeping the entire acquisition system within one unit. This ADC board had the following features:

i Sampling rate of between 500KHz to 64MHz.
ii 256 Kbytes of memory per channel.
iii Selectable gain of between 0.1 to 4 Volts.
iv An 8-bit resolution capability.
v Dual channel capability
vi Accompanying Scope software

The scope™ software provided to drive the 'Kietley' ADC board could only display and save 16 Kbytes of data per acquisition, limiting full usage of the boards buffer memory. Furthermore, the software did not allow for continuous recordings. To overcome this problem, Kietley Instruments in the United States, provided an interactive programme/software called 'Testpoint' which allowed continuous recording and display of 256 Kbytes of data. At the time of writing this thesis, this was the only software capable of displaying 256 Kbytes of data at once. A picture of the interface, written by the author and used to drive the ADC board, is shown in figure 5.6.

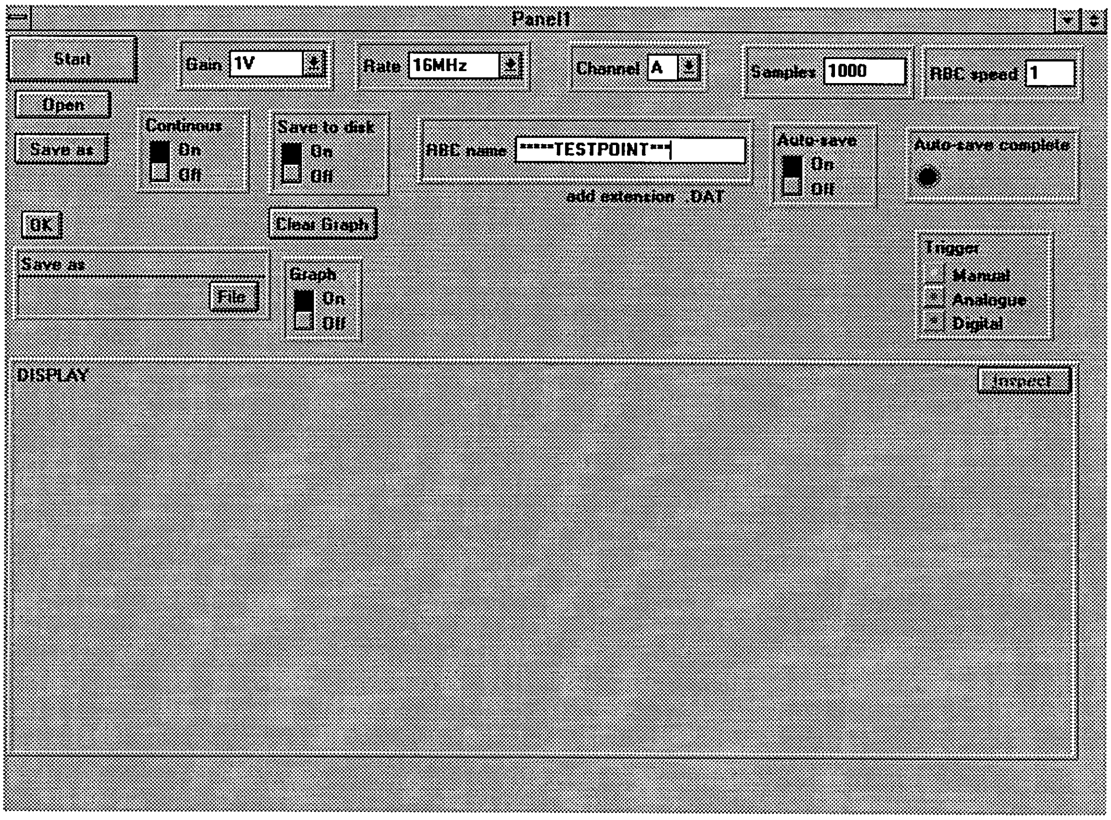

Gain 1V
Rate 16MHz
Channel A
Samples 1000
RBC speed 1
RBC name *****TESTPOINT***
add extension .DAT

Figure 5.6 Layout of ADC interface software, written by D. Mba

The drawback with segmented data acquisition was that a time delay existed between acquisitions and data transfer to hard disk. This is an inherent problem due to differences in buffer and computer speeds and can only be reduced by using faster computers and ADC boards. As a result of differences in speed, large segments of data will go unrecorded during one revolution of the RBC.

To overcome this, the time to acquire and record a segment of 256,000 data points was measured using the ADC's digital clock.. This was achieved by measuring the time to collect digital information, together with the time to transfer this data to the hard disk. By measuring the time to do both of these operations and knowing the time for the rotor to complete one revolution, it was possible to deduce the number of times necessary for the ADC to gather sufficient information describing one revolution. The net result was that more than one revolution would be required to obtain complete stress wave data recording over one revolution, dependent on sampling rate. This was implemented by setting a time delay after one revolution from the initial measuring point, equivalent to the time for acquisition and recording. By repeating this procedure over successive revolutions until the time delay between successive acquisitions was covered, data for an entire revolution was recorded.

5.4.5 Signal Generator

A Hewlett Packard model 8111a pulse/function signal generator was used for attenuation tests on the test rig. The generator could provide different waveforms and pulses with a maximum amplitude of 16.67 volts and varying pulse widths of between 25ns and 100ms. Furthermore, differing number of pulses could be generated simultaneously.

5.4.6 The Computer

A Viglen 133 MHz Pentium computer, with 1.6 Gbytes of hard disk memory was used for data acquisition and analysis. An external compact drive was used for additional memory storage, thus freeing space on the hard disk.

5.5 Calibration

5.5.1 Pre/Post amplifiers and ADC board

Whilst it is recognised that each of these components have specifications ensuring broad band characteristics in the frequency range of interest, between 100KHz to 1000KHz, it was thought prudent to calibrate these components whilst operating as a system. Two calibration tests were carried out. The first was a simple amplification test, where sine waves of varying frequencies at a constant amplitude were passed through the pre- / post-amplifiers and the ADC board. The amplitude response for varying frequencies is shown in figure 5.7.

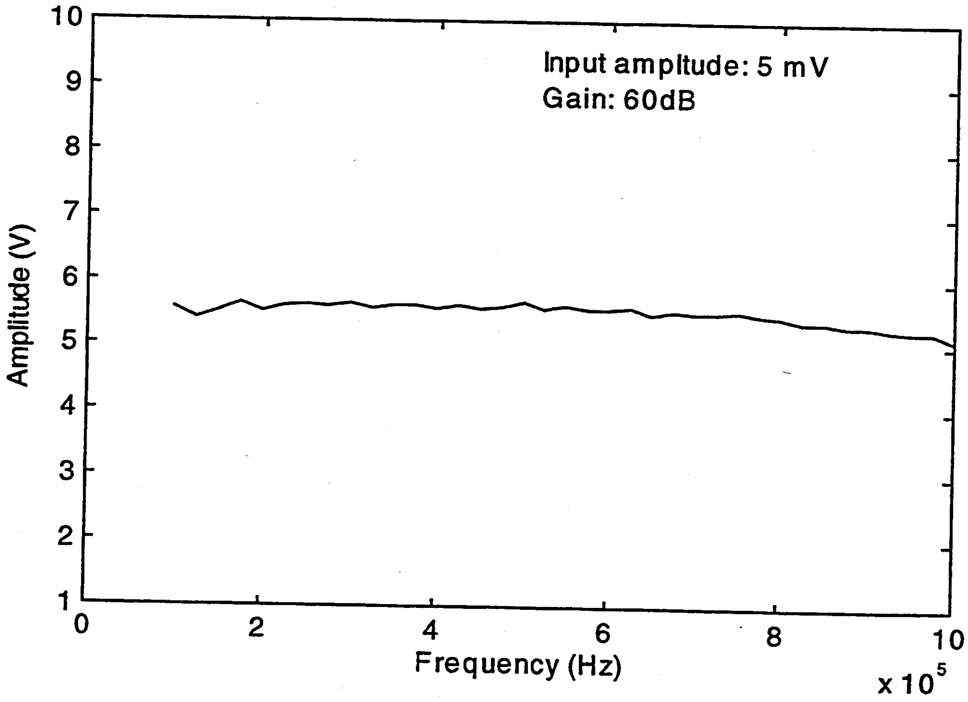

Figure 5.7 **Amplitude response of amplifiers and ADC**

In the second test, a pulse of width 100ns was put through the system. The time and frequency responses of the input pulse can be seen figures 5.8 and 5.9

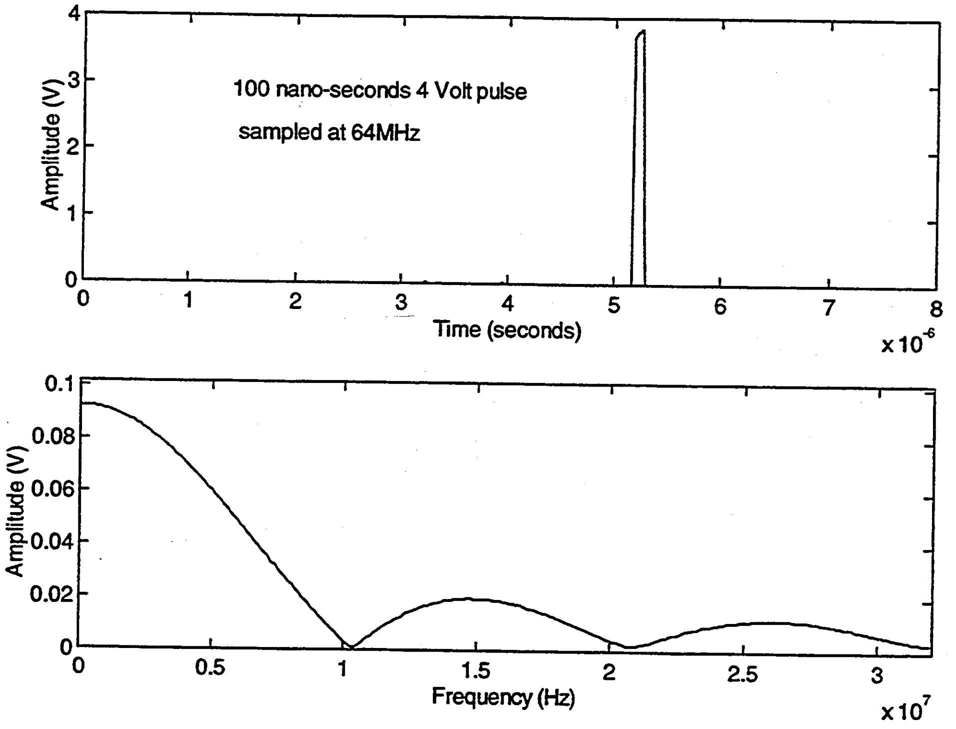

Figure 5.8 **Pulse input with its corresponding frequency spectrum**

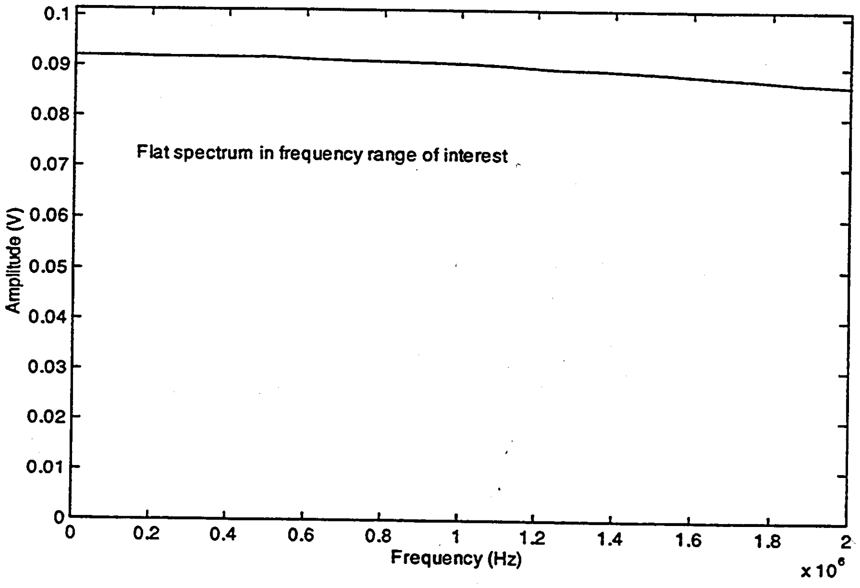

Figure 5.9 Zoomed diagram of figure 5.8

The response of the ADC boards to the input pulse showed a phase change of 180^0, see figure 5.10. The frequency response of both tests showed a relatively flat frequency response within the frequency range of interest. The response of the 'Kietley

Instruments' ADC board was sampled at 64 MHz, while the Rapid system was sampled at the maximum 20 MHz. The amplitude of the input pulse was 4mV, and a gain of 60 dB was applied.

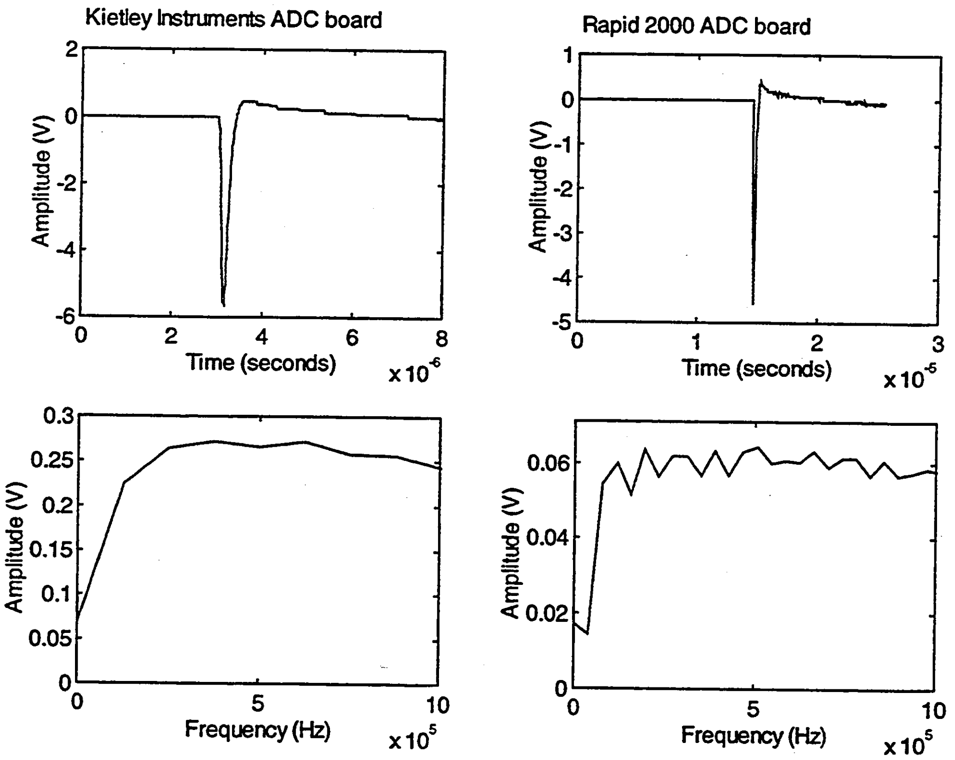

Figure 5.10 Response of ADC boards to pulse input

5.5.2 Transducers

Although the manufacturers had already supplied the calibration chart, it was thought prudent to cross-check the characteristics of the transducer. The principal of 'reciprocity' for piezoelectric sensors implies that such sensors can be used as emitters and receivers. Therefore, if the spectral resonance of the emitting transducer is known, the characteristics of the receiving transducers can be determined. For this test, two identical wide-band (WD) sensors were used. The sensors were fixed back-to-back, with a thin layer of acoustic gel between faces, thus minimising as far as possible any effect of the acoustic path between the emitting and receiving sensors. The response spectrum, comprising a composite output that represents the sum of both transducer transfer function, will be the resonance of a single transducer applied twice.

Two tests were performed. First was the simple amplification test, as described earlier. The signal generator, connected to one of the transducers, was used to excite the other. The amplitude response for varying frequencies is shown in figure 511.

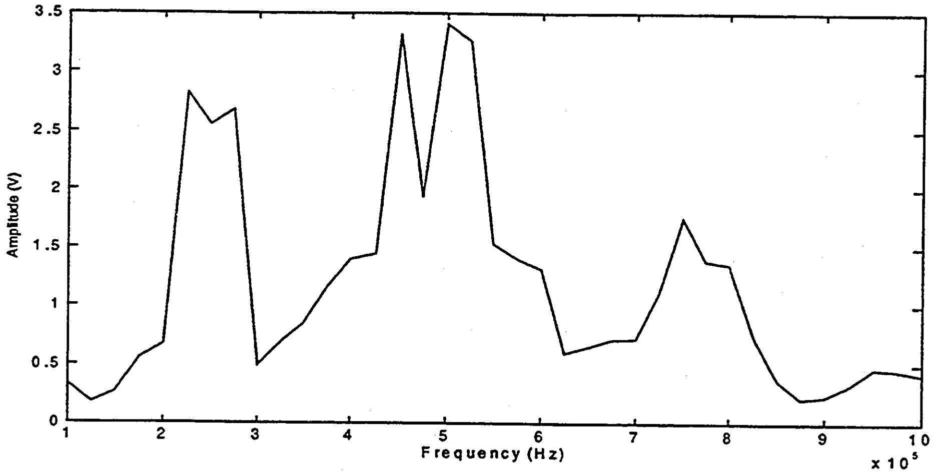

Figure 5.11 Amplitude response of sensor

The second test involved putting a 100ns pulse through the emitting transducer. The response with the corresponding frequency spectrum is shown in figure 5.12.

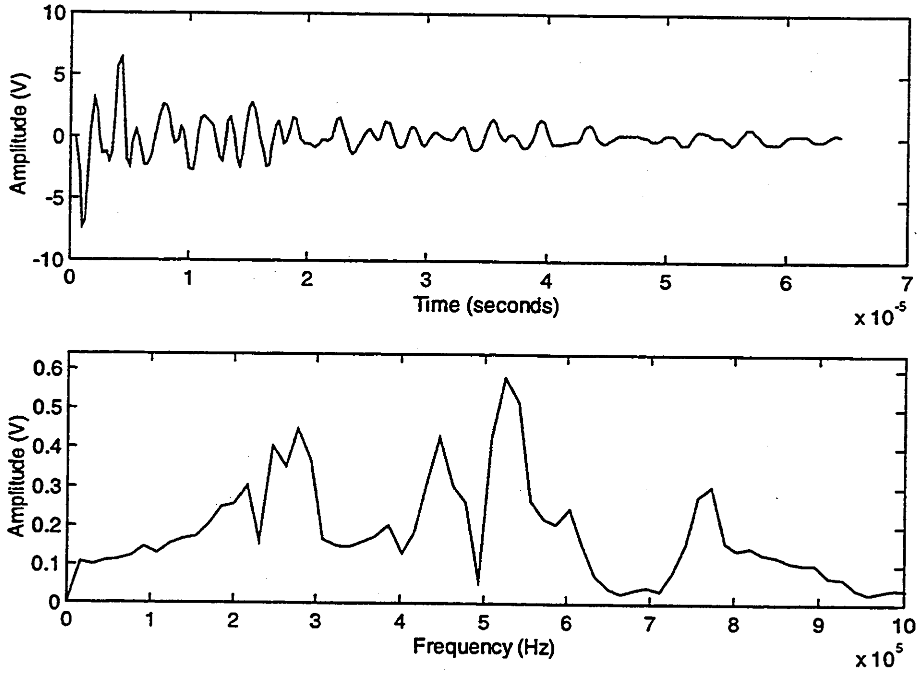

Figure 5.12 Back-to-Back response of sensor

A comparison between the two test results and the calibration chart provided by the manufacturer is shown in figure 5.13.

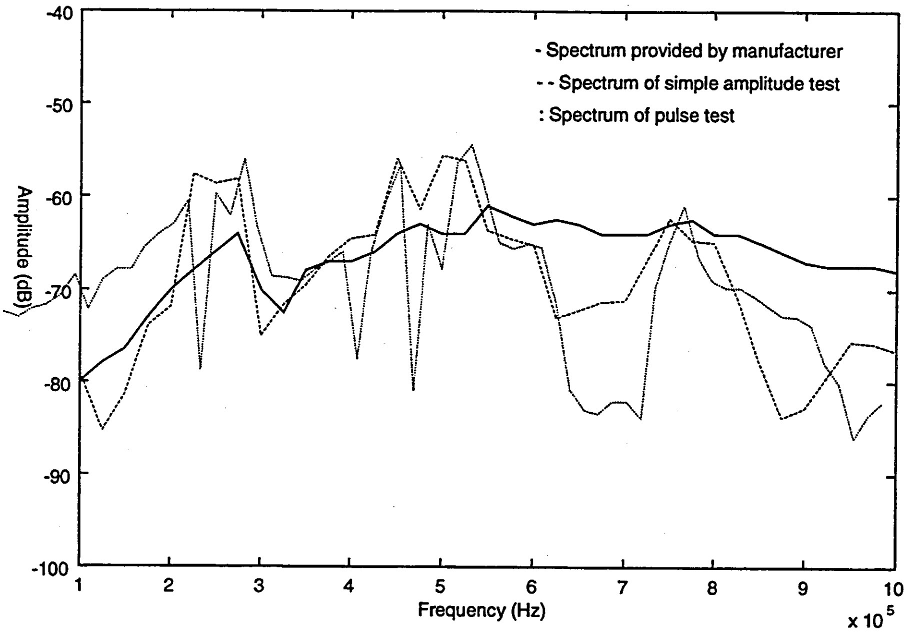

Figure 5.13 Comparison of calibration result with calibration chart.

The results of the two tests compare favourably with the calibration chart supplied by the manufacturer. It must be pointed out that these calibration tests undertaken are crude and a variance to the supplied chart is expected. The experimental spectra were superimposed onto figure 5.13.

5.5.3 Electronic noise

It was observed that the electronic noise, with 60dB amplification, had a peak voltage of approximately 30 and 50 mV on the Rapid and Kiethley ADC systems respectively.

CHAPTER 6

SIGNAL PROCESSING

6.1 Introduction

Signal processing is at the heart of all condition monitoring systems and the numerous algorithms employed have been widely discussed. The techniques used are dependent on application and rarely interchangeable between size and classification of different machines

A mechanical fault present on an RBC will result in the generation of stress waves, see section 4.4. It is imperative that the distress signatures are separated from other sources of emission and this is effectively achieved by extracting and classifying certain features of each signature. This chapter covers a brief review of classification techniques that have been successfully employed, a description of these techniques and finally a detailed listing of features to be extracted for classification of signatures generated from defective RBCs.

6.2 Time and frequency domain recognition and classification features

Features extracted from a signature in the time and frequency domain can provide adequate information about its source and strength. Much work has been undertaken in this field, a few of which are highlighted.

Belchamber et. al. [78] used principal component analysis (PCA) and hierarchical dendrograms to effectively differentiate and classify AE bursts from ten polymers and composites. Analysis was based on five features of the original signal and included peak amplitude, variance, half-life, median frequency and inter-quartile spread of features. Chan et. al. [79] successfully used thirty features, including shape factors, time domain, pulse information, partial energy distribution in different frequency bands and correlation coefficients, to classify AE signals generated during welding. Three pattern recognition techniques were employed: linear discriminant function classification, minimum distance and K-nearest neighbour classification.

Murthy et. al. [80] reviewed works on pattern recognition concepts to AE signal analysis and suggested the use of both time and frequency domain features for complete and effective classification. This was successfully encompassed by Liang et.al. [81] whilst monitoring punch-stretching processes using AE.

Generally, time and frequency domain features employed include :

Time domain	Frequency domain
Duration	Maximum amplitude
Counts per event	Mean
Peak amplitude per event	Median
rms. per event	Standard deviation
Standard deviation per event	Energy and statistical moments at differing frequency bands
Rise and fall time per event	
Energy per event	
Gap between events	
Correlation coefficients	
1st to 4th statistical moments	

Whilst these features have been used successfully, several parameters could be required to define the stress wave signatures with all its reflections. This can result in lengthy computations; moreover, the effectiveness of these parameters for classification of stress waves is unknown. It was therefore thought prudent to seek alternative parameters to provide, firstly, relative comparisons, and secondly, a more computationally efficient feature classification algorithm.

Claims that the shape of a burst [82] can be represented by a few Auto-Regressive (AR) coefficients have been made, see section 6.4. The computation of these coefficients is deduced from linear prediction.

6.3 Linear prediction and Auto-Regressive modelling

For a finite set of sample values of a stationary process, an attempt can be made to estimate a single value of the measured process some time into the future. This prediction is defined as linear if it is achieved by performing a linear filtering operation on a given set of measured samples [83,84].

Given a time series $x(n-1), x(n-2),...,x(n-M)$ obtained from a stationary process of zero mean, the forward linear prediction problem makes use of these sets of data to predict $\tilde{x}(n)$. If $x(n)$ denotes the actual process value at time n, the forward prediction error is defined as :

$$e_M(n) = x(n) - \tilde{x}(n) \qquad (6.1)$$

The subscript M in the forward prediction error emphasises that M sample values of the process were used to make the prediction. The signal produced at the filter output can be expressed as the convolution sum, see figure 6.1.

$$\tilde{x}(n) = \sum_{k=1}^{M} h(k)\, x(n-k) \qquad (6.2)$$

where $h(1), h(2),...,h(M)$ are the coefficients that define the impulse response of the filter.

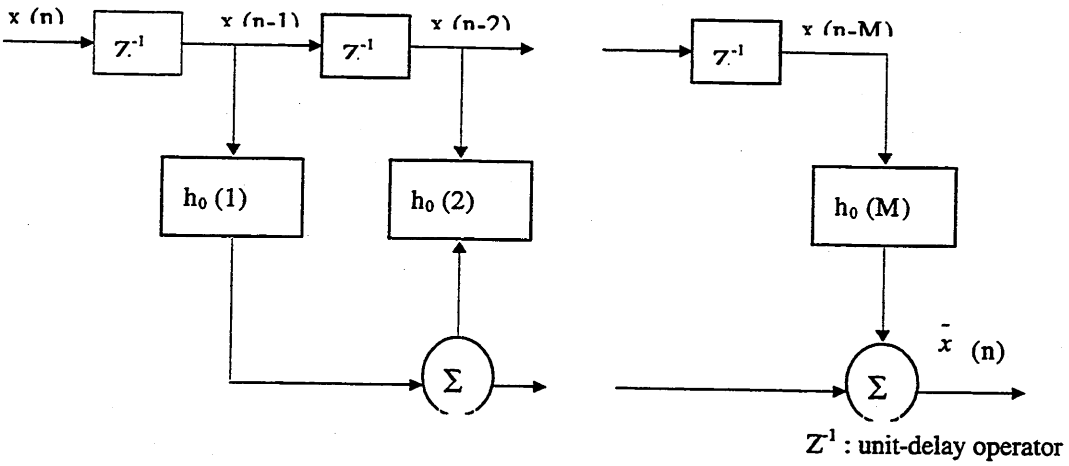

Figure 6.1 **Forward linear predictor**

The filter can be optimised by minimising the mean-square value of the error signal $e_M(n)$ (Wiener theory). The mean-square value of the error signal is given as:

$$\varepsilon = E[e_M^2(n)] \qquad (6.3)$$

where E is the expectation operator. Substituting (6.1) into (6.3)

$$\varepsilon = E[x^2(n)] - 2E[x(n)\,\tilde{x}(n)] + E[\tilde{x}^2(n)] \qquad (6.4)$$

and substituting equation (6.2) into (6.4)

$$\varepsilon = E[x^2(n)] - 2\sum_{k=1}^{M} h(k)\, E[x(n).\, x(n-k)] + \sum_{k=1}^{M}\sum_{m=1}^{M} h(k)h(m)\, E[x(n-k).\, x(n-m)] \qquad (6.5)$$

Assuming that the input signal and the desired response are stationary, the following interpretations can be deduced :

1 The expectation $E[x^2(n)]$ is equal to the mean-square value of the desired response $x(n)$.

$$P = E[x^2(n)] \qquad (6.6)$$

For a zero mean process, $E[x^2(n)] = \sigma^2$

2 The expectation $E[x(n).\, x(n-k)]$ is equal to the correlation between the desired response $x(n)$ and the input signal for a lag of k.

$$R(k) = E[x(n)\, x(n-k)], \qquad k = 1, 2, \ldots, M \qquad (6.7)$$

which implies

$$\sum_{k=1}^{M} h(k)\, E[x(n)\, x(n-k)] = \sum_{k=1}^{M} h(k)\, R(k) \qquad (6.8)$$

For $k = 0$ in equation (6.7),

$R(0) = E[x^2(n)] = P$, as defined in equation (6.6)

3 The expectation $E[x(n-k).\, x(n-m)]$ is equal to the auto-correlation function of the input signal for a lag of $(m-k)$.

$$R(m-k) = E[x(n-k)\, x(n-m)], \quad k, m = 1, 2, \ldots, M \qquad (6.9)$$

which implies

$$\sum_{k=1}^{M} \sum_{m=1}^{M} h(k).h(m)\, E\,[x\,(n\text{-}k)\, x(n\text{-}m)\,] = \sum_{k=1}^{M} \sum_{m=1}^{M} h(k).h(m)\;\; R(m - k) \tag{6.10}$$

Substituting equations (6.6), (6.8) and (6.10) into (6.5), the expression for the mean square error is :

$$\varepsilon = P - 2\sum_{k=1}^{M} h(k)\;\; R\,(k) \;+\; \sum_{k=1}^{M} \sum_{m=1}^{M} h(k).h(m)\;\; R(m - k) \tag{6.11}$$

Equation (6.11) states that the mean squared error is a second-order function of the filter coefficients. The mean squared error attains its minimum value when the derivatives with respect to the filter coefficients are equal to zero.

$$\frac{\partial \varepsilon}{\partial h(k)} = -2R\,(k) \;+\; 2\sum_{m=1}^{M} h(m)\;\; R(m - k) \tag{6.12}$$

Setting this result to zero we may obtain the optimum values of the individual filter coefficients, which are now denoted as $h_0(1)$, $h_0(2)$,...,$h_0\,(M)$. Therefore,

$$\sum_{m=1}^{M} h_0(m)\;\; R(m - k) \;=\; R\,(k), \qquad\qquad k = 1, 2,..., M \tag{6.13}$$

with $R(k) = E\,[x(n).\, x(n\text{-}k)\,]$, (6.7), and $R(m - k) \;= E\,[x\,(n\text{-}k).\; x(n\text{-}m)\,]$, (6.9)

We observe that we only need to know the auto-correlation of the input process for different lags in order to solve equation (6.13) for the one-step predictor coefficient, see matrix form of equation (6.13) at (6.22). This type of filter whose impulse response, $h_0(m)$, is defined by equations (6.13) is optimised in the mean-square sense.

By introducing a new set of filter coefficients defined by :

$$a_M(m) \;=\; \left\{\begin{array}{ll|} 1, & m = 0 \\ -h_0(m), & m = 1, \ldots, M \\ 0, & m > M \end{array}\right. \tag{6.14}$$

equation (6.13) can be expressed as

$$\sum_{m=0}^{M} a_M(m)\ R(m-k) = 0 \qquad k = 1,2,\ldots, M \tag{6.15}$$

The forward-prediction error, given in equation (6.1) can be expressed as:

$$e_M(n) = x(n) - \sum_{k=1}^{M} h_o(k)\, x(n-k) \tag{6.16a}$$

or

$$e_M(n) = \sum_{k=0}^{M} a_M(k)\ x(n-k) \tag{6.16b}$$

The equation in (6.16b) is known as the prediction-error filter and states that the forward prediction error at the filter output is produced by convolving the filter input with the impulse response of the filter, see figure 6.2. An important property of this filter is that it can **'whiten' any stationary input process** represented by the sequence $x(n-1)$, $x(n-2),\ldots, x(n-M)$, provided that the order number, M, is sufficiently large.

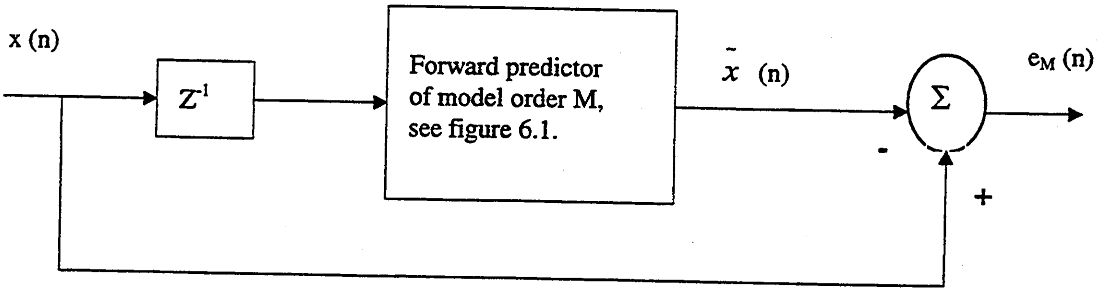

Figure 6.2 **The prediction-error filter**

We may express the minimum mean-square value of equation (6.11) as

$$\varepsilon_{min} = P - 2\sum_{k=1}^{M} h_o(k)\ R(k) + \sum_{k=1}^{M}\ \sum_{m=1}^{M} h_o(k).h_o(m)\ R(m-k) \tag{6.17}$$

$$= P - \sum_{k=1}^{M} h_o(k)\left[2R(k) + \sum_{m=1}^{M} h_o(m)\, R(m-k) \right] \tag{6.18}$$

Substituting equation (6.13) into (6.18),

$$\varepsilon_{min} = P - \sum_{k=1}^{M} h_o(k)\ R(k) \qquad (6.19)$$

since P = $E\,[\,x^2(n)\,] = R(0)$

$$\varepsilon_{min} = R(0) - \sum_{k=1}^{M} h_o(k)\ R(k) \qquad (6.20)$$

Equation's (6.15) and (6.20) can be written as a set of M+1 simultaneous equations as:

$$\sum_{m=0}^{M} a_M(m)R(m-k) = \begin{cases} \varepsilon_{\min}, & \mathrm{k}=0 \\ 0, & \mathrm{k}=1,2,\ldots,\mathrm{M} \end{cases} \qquad (6.21)$$

Equation (6.13) can be expressed in the matrix form as:

$$\begin{bmatrix} \mathrm{R}(0) & \mathrm{R}(-1) & \ldots & \mathrm{R}(\mathrm{M}-1) \\ \mathrm{R}(1) & \mathrm{R}(0) & \ldots & \mathrm{R}(\mathrm{M}-2) \\ & & & \\ \mathrm{R}(\mathrm{M}-1) & \mathrm{R}(\mathrm{M}-2) & \ldots & \mathrm{R}(0) \end{bmatrix} \begin{bmatrix} h_o(1) \\ h_o(2) \\ \\ h_o(M) \end{bmatrix} = - \begin{bmatrix} \mathrm{R}(1) \\ \mathrm{R}(2) \\ \\ \mathrm{R}(\mathrm{M}) \end{bmatrix} \qquad (6.22)$$

Multiplying these matrix equations and moving the right side to the left yields:

$$\begin{array}{lllll} R(1) & + \; R(0)h_0(1) & + \; R(-1)\,h_0(2) & + \ldots + R(M-1)\,h_0(M) & = 0 \\ R(2) & + \; R(1)\,h_0(1) & + \; R(0)\,h_0(2) & + \ldots + R(M-2)\,h_0(M) & = 0 \\ \vdots & \quad \vdots & \quad \vdots & \qquad \vdots & \\ R(M) & + \; R(M-1)\,h_0(1) & + \; R(M-2)\,h_0(2) & + \ldots + R(M)\,h_0(M) & = 0 \end{array}$$

Equation (6.22) can be augmented to incorporate the variance, σ^2, of ε_{min} . Thus

$$\begin{bmatrix} R(0) & R(-1) & \dots & R(M-1) \\ R(1) & R(0) & \dots & R(M-2) \\ R(2) & R(1) & \dots & R(M-3) \\ & & & \\ R(M-1) & R(M-2) & \dots & R(0) \end{bmatrix} \begin{bmatrix} 1 \\ a_M(1) \\ a_M(2) \\ \\ a_M(M) \end{bmatrix} = \begin{bmatrix} \sigma^2 \\ 0 \\ 0 \\ \\ 0 \end{bmatrix} \qquad (6.23)$$

From equation (6.23) it can be noted that the optimum coefficients are determined by the set of (M+1) auto-correlation function values of the input process for lags 0, 1, 2, ..., M.

Forward linear prediction and Auto-Regressive (AR) modelling of a stationary discrete-time stochastic process are related to each other. A stationary random process $x(n)$ may be described as an AR process of order M if its sample $x(n)$ at time n is regressed on M past samples, $x(n-1), x(n-2),..., x(n-M)$. This is expressed as:

$$x(n) = \sum_{k=1}^{M} h_0(k)\, x(n-k) + W(n) \qquad (6.24)$$

where $W(n)$ is a white noise process of zero mean and variance σ^2 and serves as the input.

From equation (6.24), it is observed that the summation on the right hand side represents the forward linear prediction of $\bar{x}(n)$, see figure 6.3. Therefore, we can conclude that the AR process of order M includes a forward linear predictor of order M in its feed-back path. Consequently, the AR model is referred to as the inverse filter. Given a set of optimum coefficients, $a_M(m)$, and a white-noise process $W(n)$ of zero mean and variance σ^2, we can generate the AR process $x(n)$.

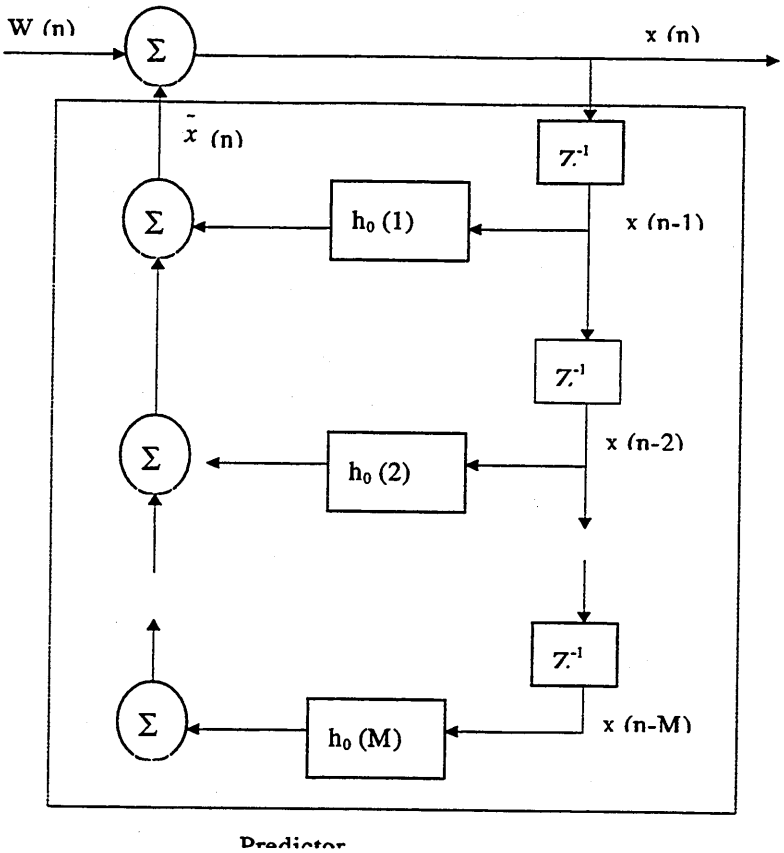

Figure 6.3 **The Auto-Regressive model**

From figure 6.3 it is evident that **the shape of the filter output, *x(n)*, is determined by the optimum AR coefficients, *$h_0(M)$*.** These coefficients were derived for stress wave signatures on mechanically deficient RBCs and used classification. This particular technique has not been used for analysis of stress wave signatures.

6.3.1 AR coefficients and Model order determination

Determining the model order is an important decision. As stated in section 6.3, the shape of the signature can be represented by AR coefficients as long as the model order, M, is sufficiently large. The Levinson-Durbin algorithm provides the most efficient solution to computing the parameters of equation (6.23) [84]. The AR coefficients are computed recursively and proceeds by setting the model order number, *M*, to zero. The values computed are used to determine the coefficients for the order, $M + 1$. This process is continued until the desired order is reached. This incremental step can be represented by :

$$\Delta_M = \sum_{m=0}^{M} a_M(m)\, R\,(M+1-m) \qquad (6.25)$$

Since the correlation matrix is symmetric, $R(M+1-m) = R(m-M-1)$.

$$\Rightarrow \qquad \Delta_M = \sum_{m=0}^{M} a_M(m)\, R\,(m-M-1) \qquad (6.26)$$

Equation (6.21) can be rewritten to include (6.26)

$$\sum_{m=0}^{M} a_M(m) R(m-k) = \begin{cases} \varepsilon_{\min}, & k=0 \\ 0, & k=1,2,\ldots,M \\ \Delta_m, & k=M+1 \end{cases} \qquad (6.27)$$

The Levinson-Durbin algorithm computes the parameter sets $[a_{11}, \sigma^2_1]$, $[a_{21}, a_{22}, \sigma^2_2]$, $[a_{31}, a_{32}, a_{33}\ \sigma^2_3]$, ... , $[a_{M1}, a_{M2}, \ldots, a_{MM}, \sigma^2_M]$. For $M= 0$, $a_0(0) = 1$ and $\varepsilon_{min} = \sigma^2$. The recursive algorithm is initialised by setting the model order $M = 1$. Thus

$$a_{11} = -R(1)/R(0) \qquad \text{and} \qquad \sigma^2_1 = (1 - |a_{11}|^2)\, R(0)$$

and the recursion for $m = 2, 3, \ldots, M$ is given as

$$a_{mm} = -\left[R(m) + \sum_{1}^{m-1} a_{m-1,1} R(m-1) \right] \Big/ \sigma^2_{m-1} \qquad (6.28)$$

$$a_{mi} = a_{m-1,i} + a_{mm} a_{m-1,m-i} \qquad (6.29)$$

and

$$\sigma^2_m = (1 - |a_{mm}|^2)\, \sigma^2_{m-1} \qquad (6.30)$$

In computing the AR coefficients for a model order M, the Levinson-Durbin algorithm also provides the AR parameters for all lower order models. This is a useful property when there is no information on the ideal model order to use [84]. Thus at the point when the variance of the minimum mean-squared error, σ^2_m , does not change would indicate the correct model order, see section 7.6. The procedure for computation of AR coefficients by the Levinson-Durbin algorithm is intended to provide an overview, and the reader is referred to numerous textbooks on Adaptive filters for further details [83,109].

6.4 Application of parametric modelling to signal classification

Chen and Bodenstien [85,86,87] investigated characterisation, segmentation and classification of transient, non-stationary, underwater AE events and showed that a low order AR model provided effective feature sets for cluster analysis and event classification. Chen accomplished segmentation and extraction of transient events from non-events by segmenting the data and employing the likelihood ratio of AR coefficients between adjacent segments. It was claimed to be successful for signal-to-noise ratios of 0.1. The model employed by Chen was referred to as the invariant model and was based on the assumption of local stationarity of the segmented time series.

The alternative to this model is the time variant model, which always follows the local properties of the non-stationary signal. The size of the data produced is a multiple of the data length and the model order number. This can make for complicated feature characterisation and so primary feature reduction is necessary [88]. Charbonnier [89] showed the adaptive recursive algorithm to be a powerful approach for detecting abrupt changes in time varying AR models. This type of modelling leads to an improved accuracy of parametric estimation methods [90].

Masayasu et. al.[91] used auto-regressive model coefficients as features for successful classification of failure mechanisms of composites using cluster analysis. Mechefske [60] used AR coefficients for fault detection on bearings at speeds of 60 rpm. This was accomplished by generating and comparing frequency spectra on short vibration data lengths.

Oksa's [82] philosophy to burst recognition and source location is very similar to that adopted for this research. His work involved the study of bursts associated with loose parts on nuclear power plants. Oksa states *"it is known from experience that, for a given sensor, the shape of the responses to bursts vary with location, but remain remarkably similar for the fixed location"*. Source location of loose parts was achieved with a single sensor. The frequency range of emitted bursts was not stated but this author believes the frequency range of interest does not exceed 20KHz. By the use of Levinson's forward linear prediction algorithm, Oksa showed that the shape of the bursts could be represented by a set of auto-regressive (AR) coefficients.

6.5 Recognition and classification techniques

There are various techniques by which classification can be achieved. Three main techniques include: cluster analysis, principal component analysis and neural networks.

6.5.1 Cluster analysis

The purpose of cluster analysis is to place similar objects into groups or classes. There are two approaches to cluster analysis: hierarchical and non-hierarchical methods. Non-hierarchical methods, which include optimisation - partitioning, density and clumping methods, are difficult to interpret. Hierarchical methods, such as dendrograms, have their origins in numerical taxonomy (Biology and Zoology) and are routinely used for identification and classification.

Different statistical methods can be applied to measure the separation between sample points, such as distance or similarity measures. Furthermore, different hierarchical clustering techniques can be applied to interpret the distance or similarity between groups of data [92], these include Nearest or Furthest Neighbour (single linkage), Centriod, Median, Group Average and Wards Method. Comparisons of these clustering techniques can be found in numerous textbooks [92,93,...]. Where no prior knowledge of groups is known, Centriod and Ward methods can produce better classification results than the single linkage method, which has a characteristic of forming long chains, making interpretation difficult.

As with each hierarchical technique, i.e., Centriod, Median, ..., the distance/similarity between groups is defined as the distance/similarity between groups of centriods, medians, ..., depending on which technique is employed. The procedure of linkage fuses groups with the smallest distance/similarity first, gradually building up to encompass all groups. The completed dendogram has a tree like structure.

6.5.1.1 Separation measurement

The most common **distance measure** used is the Euclidean distance, defined by the distance between objects i and j :

$$D_{ij} = (X_i - X_j)^T.(X_i - X_j) \qquad or \qquad D_{ij} = (\sum_{k=1}^{m} (X_{ik} - X_{jk})^2)^{1/2} \qquad (6.25)$$

Where X_{ik} is the value of the kth variable for the ith entity and ^{T} is the transpose.

Since Euclidean distance is not a scalar invariant, distances can be badly distorted by a simple change of scales. The lack of scale invariance has led to the suggestion that the data be standardised (by dividing each variable by its standard deviation) before computing the Euclidean distance. In this way the relative distances are preserved. To overcome the disadvantage of scale invariance, the Mahalanhois distance can be used. This has the advantage of explicitly accounting for any correlation's that might exist between the variables. Moreover it is scale invariant.

The **similarity coefficient** measures the relationship between two individuals, given the values of a set of 'p' variants common to both. In general, similarity coefficients have the value in the range 0 to 1. Allied to measurement of similarity is the question of weighting of variables, i.e. giving differential weights to the variables which are thought by the investigator to be most important for the purposes of classification [92]. It is perfectly possible to arrange for certain variables to be weighted so that agreement with respect to these properties counts for more than agreement on others, though various authors question the validity of such a procedure.

6.5.2 Principal Component analysis

This is a method of displaying, and effectively reducing, multivariant data. By projecting two principal components onto a plane, visual interpretations can be made. The principal components are the eigenvectors of the variance\covariance matrix, and hence are orthogonal and equal in number to the original variables. The first principal component expresses the direction of the biggest variance in the data, the second principal component the next, and so on. Principal components themselves are linear combinations of the original variables and yield valuable information about their relative discriminating power [94].

6.5.3 Neural Networks

Neural networks have been widely discussed. There is no evidence to suggest algorithms employed for training with a specific machine can be used on different machines. Since RBCs have structures of different shapes, sizes, materials, as well as initial assembly conditions and wear rates, it was thought prudent to use other classification techniques whilst observing developments in this field.

6.6 Features extraction parameters for classification of detected stress wave signatures

It is widely acknowledged that bursts generated from a given location will produce the same complex response for a given sensor at a fixed location. The complex signal detected will be a function of the velocity of stress waves, attenuation, reflections and surface absorption properties. These features can aid in source location, as the shape and frequency content could vary form source to source. Therefore, time/frequency domain features and AR coefficients were extracted and applied to simulated distress signatures. This was intended to give an indication of relative classification performance.

In application of the time/frequency domain extraction, the signature in the time domain was divided into a number of equal sections and the extraction algorithm was applied to each section. This was undertaken to enhance the definition of each burst shape. Typically, each burst over 16,000 data points was divided into sixteen sections, while bursts below 5000 data points were divided into eight sections.

The Levinson-Durbin algorithm was applied for computing the AR coefficients of stress waves detected.

The classification of computed time/frequency domain features and AR coefficients employed the clustering technique of hierarchical dendrograms with Euclidean distance measures of group centriods. The algorithm used for clustering is known as the K-means method and is defined as the distance between the Centroid of the group. The computing software used was MATLAB.

6.6.1 Time and frequency domain classification features

Since there is no prior knowledge of the best descriptors to use with regard to the generated stress wave, as many features as possible derived form the original signal should be used for classification. A listing with brief descriptions of the time and frequency features extracted is detailed below.

<u>**Time domain features**</u>

1 Mean, $\bar{x}$

2 Median.

3 Maximum amplitude.

4 Standard deviation, σ, given as :

$$\sigma = \surd(\frac{1}{N}(x_i - \bar{x})^2) \qquad (6.26)$$

The standard deviation is an indicator of the closeness of the values in a sample to the mean.

5 Variance, also expressed a σ^2.

6 The Skew is a measure of symmetry and is defined as the third moment about the mean, expressed as :

$$\text{Skew} = \frac{1}{N}\sum_{i=1}^{N} [(x_i - \bar{x})/\sigma]^3 \qquad (6.27)$$

A positive skew implies a distribution with an assymmetric tail extending out towards the positive axis of x. A negative skew implies a distribution with an asymmetric tail extending out towards the negative axis of x. A symmetric distribution will have a skew of zero.

7 The Kurtosis is a measure of peakness of a sample and is defined as the fourth moment about the mean, expressed as :

$$\text{Kurtosis} = \frac{1}{N}\sum_{i=1}^{N} [(x_i - \bar{x})/\sigma]^4 \qquad (6.28)$$

8 Root Mean Square value, R.M.S., is a measure of the energy of a signal and is expressed as :

$$V_{r.m.s} = \sqrt{(\frac{1}{N}\sum_{i=1}^{N} x^2(t))} \qquad (6.29)$$

9 Crest factor, defined as the ratio of the peak to the r.m.s. voltage.

10 Total energy, E_T, defined as the area under the squared amplitude of the time domain signal and expressed as :

$$E_T = \int_0^T x^2(t)\,dt \qquad (6.30)$$

where T is the duration of the signal.

11 Total energy, E_{TP}, of the positive values of $x(t)$ at ten thresholds. The thresholds are defined in increasing steps of 0.1 multiples of the maximum positive $x(t)$. This computation generates ten features.

12 Total energy, E_{TN}, of the negative values of $x(t)$ at ten thresholds. The thresholds are defined in increasing steps of 0.1 multiples of the maximum negative value of $x(t)$. This computation generates ten features.

13 The count at different amplitude levels can aid in shape description of the signature. The thresholds, or amplitude levels, are defined in increasing steps of 0.1 multiples of the maximum of $x(t)$, starting at 0.1 to 0.9.

14 Rise time, R_T, defined as the time from when the signal crosses a set level to reach the peak amplitude of $x(t)$. For feature extraction, five peaks with corresponding rise times were computed.

Frequency domain features

The most common method of obtaining the frequency spectrum of a finite length of data is by the use of the Fast Fourier Transform, FFT. It is a very efficient algorithm for the computation of frequency components and is based on the Fourier series. The Fourier series allows a periodic function to be represented as an infinite sum of its harmonic components.

$$f(t) = a_o + \sum_{n=1}^{\infty} [a_n cos(nwt) + b_n sin(nwt)] \qquad (6.31)$$

The determination of the coefficients, instantaneous amplitudes, a_o, a_n and b_n represent the central problem of Fourier analysis and are widely discussed in numerous text books [96]. The Fourier transform of $f(t)$ can be expressed as

$$f(w) = \int_{-\infty}^{\infty} f(t)e^{-iwt}.dt \qquad (6.32)$$

The features extracted include :

1 The spectrum energy, E_F, is defined as the total area under the amplitude spectrum of a transient signal and is expressed as :

$$E_F = \sum_{i=1}^{n-1} A_i \qquad (6.33)$$

The above expression was used for a frequency range of between 100KHz to the nyphist frequency, where A_i = spectral amplitudes.

2 Total energy, E_{FP}, at ten thresholds in increasing steps of 0.1 multiples of the maximum A_i. This computation generates ten features.

3 The maximum amplitude value can provide information of the characteristics of the sensor and system. Excitation at various positions in a large structure can yield different system characteristics. Therefore, three maximum values, and corresponding frequency values, were extracted.

4 The median frequency is the frequency that divides the area of the spectrum into two equal parts.

A total of seventy-one time and frequency domain features were computed for each section of data, generating one thousand, one hundred and thirty six (1136) features for a typical signature of 16,384 data points.

6.7 Pre-processing of collected data

Prior to feature extraction the signatures were band-pass and median filtered. Band-pass filtering was applied for time and frequency feature extraction.

6.7.1 Digital filters

Captured data was band-pass filtered between 100KHz and 1000KHz. There are various types of digital filters available to the user. The Infinite Impulse Response (IIR) filters meet specifications with a much lower filter order than a Finite Impulse Response (FIR) filter. IIR filters include the Butterworth, Chebyshev types I and II, Elliptic and Bessel filters [95,96], each having its own characteristics. For analysis of signatures in this thesis, the elliptic filter was chosen as not only could the pass-band and stop band ripples be set but also this filter has the steepest roll-off characteristics. This is advantageous when designing band-pass filters, ensuring minimal interference from frequency components outside the region of interest. The only disadvantage is the equiripple in both pass and stop-bands, though by specifying adequate attenuation's for these characteristics, the equiripple can be reduced. To overcome the phase distortions associated with IIR filters, 'Matlab' provides a non-causal zero-phase filtering option, 'filtfilt', which was used on all data that had to be filtered.

6.7.2 The Median filter

Application of the median filter was primarily to remove any spurious spikes within the captured data. The success of median filters is based on two main important properties, edge preservation and efficient attenuation of impulsive noise, both properties that cannot be achieved by traditional linear filtering techniques. Impulsive noise or noise spikes can be removed irrespective of their magnitude [97], but they cannot be designed by specifying frequency domain requirements. It is important that a low order is used otherwise real signal impulses could become distorted, so a compromise must be reached. All signatures displayed in this thesis and used for data analysis were passed through a 5th order median filter. An example of its application can be seen in figure 6.4.

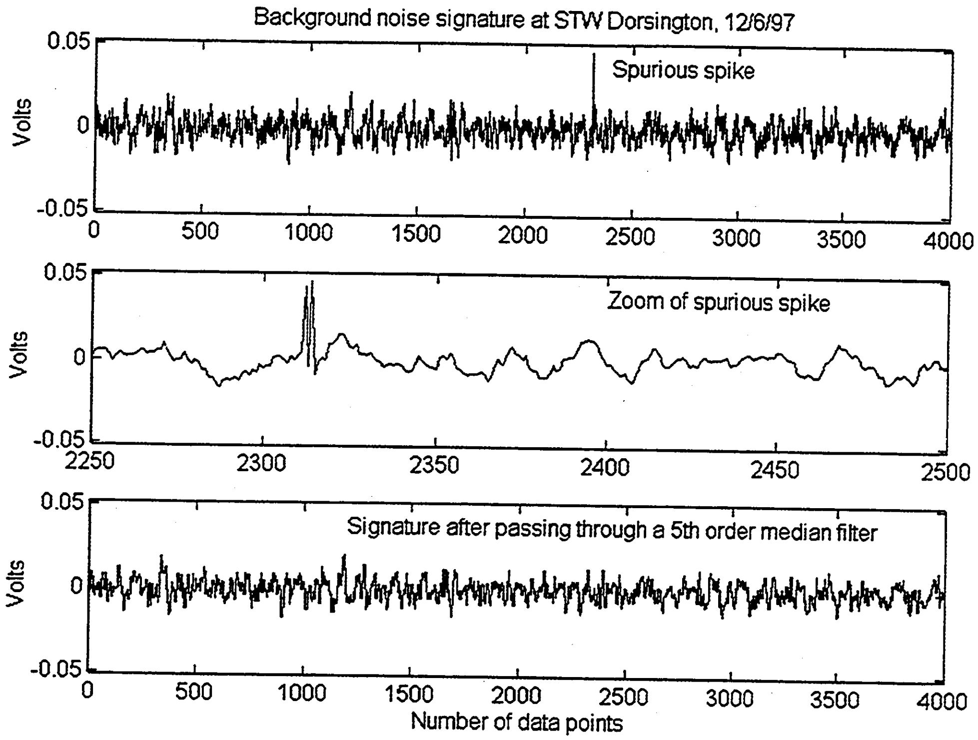

Figure 6.4 An example of median filtering

CHAPTER 7

EXPERIMENTAL RESULTS AND DISCUSSIONS

7.1 Introduction

Prior to simulations, attenuation tests were undertaken on the test-rig to investigate its attenuation characteristics and to determine the optimum position for placement of the AE transducer. Whilst there was access to any position on the test-rig for placement of the transducer, there is only access to the bearings, stub shaft and gearbox on operational RBCs. Moreover, it is standard practice to place the transducer on a non-rotating member of the machine, usually its bearing housing. It was therefore thought helpful to undertake attenuation tests to determine the best position for transducer placement. The transducer was placed on the stub shaft end and on the bearing housing. It was held in both positions by a magnetic clamp.

7.2 Position of AE transducer

To determine the optimum position for the AE transducer two tests were undertaken. Firstly, a pulse of width 100ns and amplitude of 16.67 volts was put through the test-rig at predetermined positions, see figure 7.1. Two identical sensors were used, one for exciting the structure, the other for 'listening'.

The second test involved pressing lead, 0.5mm 2H, obliquely against the surface at the same predetermined positions until fracture. This test is widely known as the Nielson source test. Due to the simplicity and repeatability in generating AE signals it was also used for evaluating source identification techniques. Paint was scraped off the surface of the predetermined positions, thereby exposing the bare metal surface for contact with the exciting transducer and pencil lead. Table 7.1 lists the number of discontinuities the stress wave must travel through from varying positions to reach the sensor. A discontinuity is defined as an interface, for instance, the interface between the shaft clamp and the shaft is defined as one discontinuity. Both tests were sampled at 5MHz.

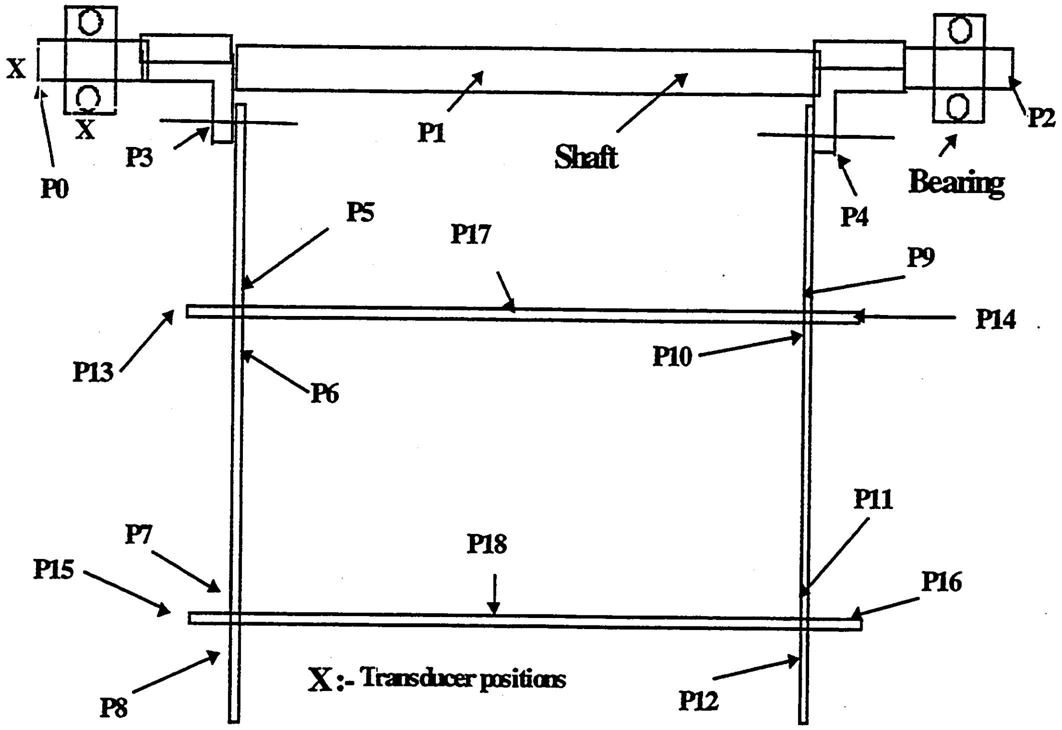

Figure 7.1 Predetermined positions on test-rig

Table 7.1 **List of discontinuities**

Discontinuity number	Interface positions at:	
	Bearing	**Stub shaft**
1	Bearing housing to transducer	Shaft to transducer
2	Outer race to bearing housing	Shaft clamp to shaft
3	Roller elements to outer race	Radial arm to shaft clamp
4	Inner race to roller elements	Support rod nuts to radial arm
5	Shaft to inner race of bearing	Support rod to support rod nuts
6	Shaft clamp to shaft	
7	Radial arm to shaft clamp	
8	Support rod nuts to radial arm	
9	Support rod to support rod nuts	

Table 7.2 lists the distance of the sensor from the predetermined input positions, with the number of associated discontinuities.

Table 7.2 **Distance of predetermined positions from sensor**

Position	**Distance from sensor (mm)**	**Number of discontinuities from :**	
		Bearing	**Stub shaft**
P0	25	5	1
P1	1000	5	1
P2	2000	5	1
P3	425	6	2
P4	1325	6	2
P5	800	7	3
P6	1000	7	3
P7	1420	7	3
P8	1670	7	3
P9	1620	7	3
P10	1800	7	3
P11	2280	7	3
P12	2450	7	3
P13	1000	9	5
P14	1810	9	5
P15	1725	9	5
P16	2490	9	5
P17	1400	9	5
P18	2220	9	5

Typical responses for the Nielson source test with the receiving sensor at two positions is shown in figure 7.2. The signatures displayed were distinct, indicative of the different transmission paths. A relative comparison of energy levels and maximum amplitudes with the sensor on the bearing housing and the stub shaft are shown in figure 7.3. Furthermore, relative attenuation rates of the detected signatures were computed, see table 7.3 of appendix A. Each graph of figure 7.3 has the same number of discontinuities.

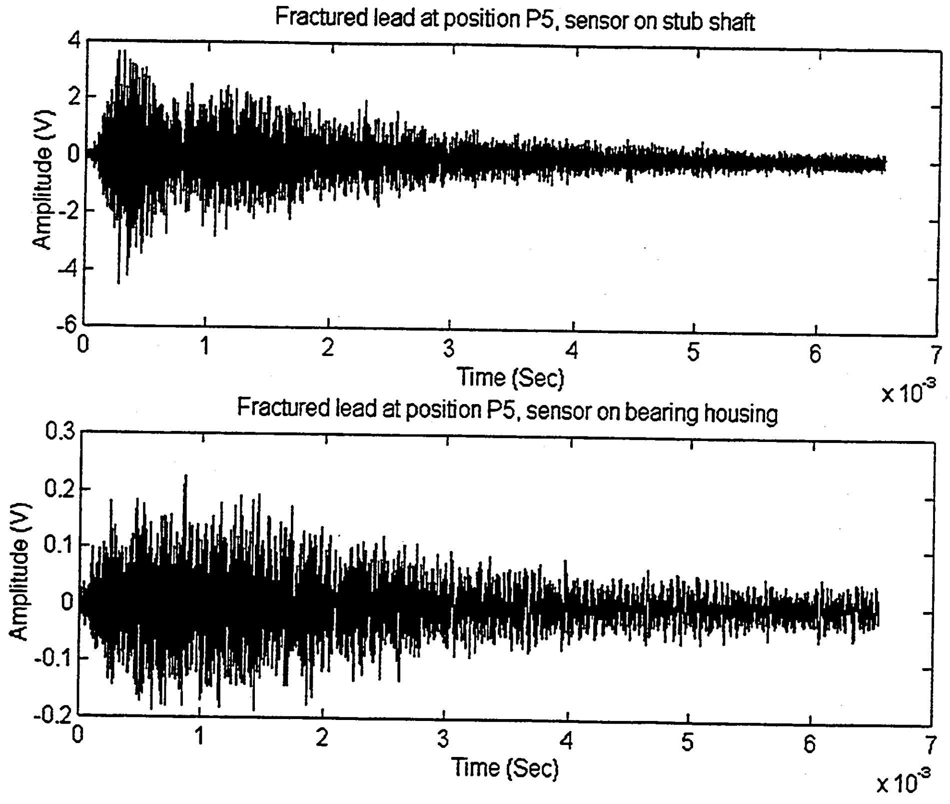

Figure 7.2 **Typical response to excitation at a fixed location**

Legend for figure 7.3

ls	- Nielson source test with sensor on stub shaft
lb	- Nielson source test with sensor on bearing housing
ps	- pulse input with sensor on stub shaft
pb	- pulse input with sensor on bearing housing

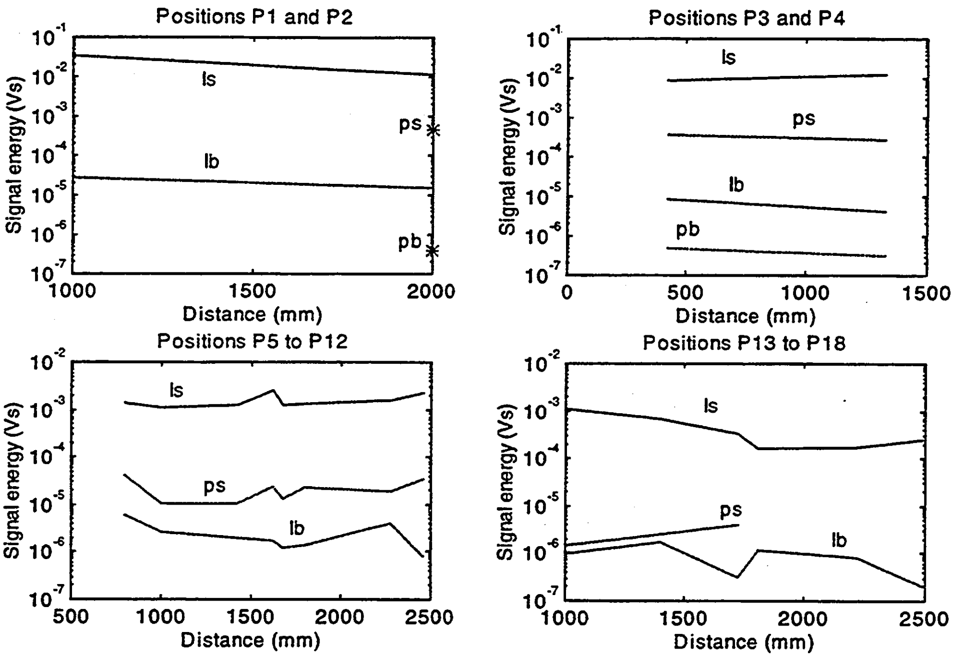

Figure 7.3 (a) Comparison of relative energy levels

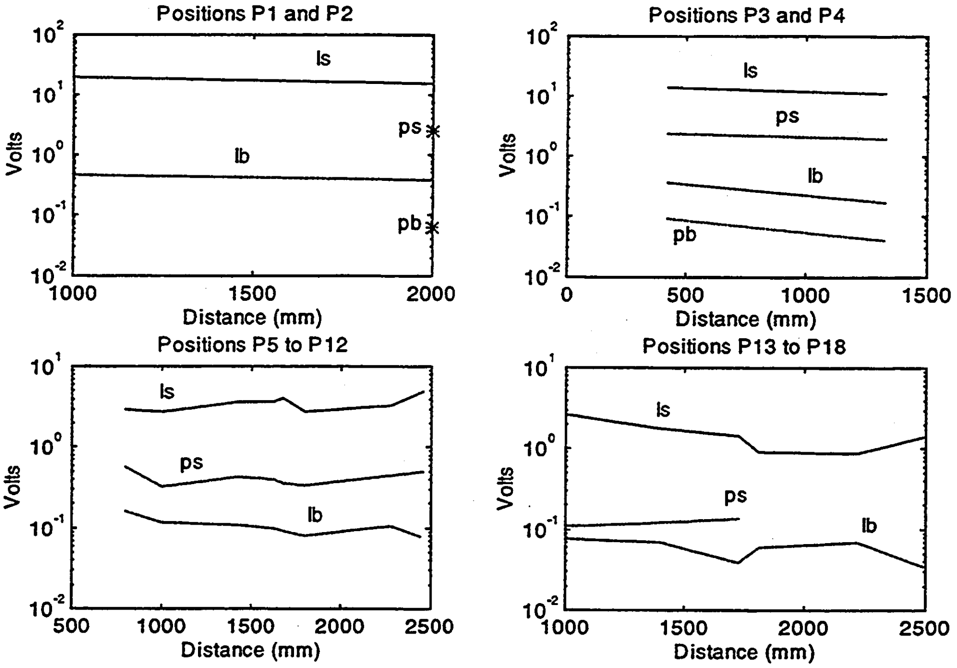

Figure 7.3 (b) Comparison of maximum amplitude values

Pulse inputs could not be accomplished at positions P1, P17 and P18, as these surfaces were curved and the sensor could not be rested squarely against them. Results of the

Nielson source tests (table 7.3, appendix A) show an average relative attenuation of approximately 57dB and 29dB for energy levels and maximum amplitude respectively. These results are within 6dB of pulse input tests, emphasising the repeatability of the Nielson source test. It was concluded that the best position for the transducer was on the stub shaft, and all subsequent tests were conducted with the transducer in this position.

An important point to consider is that the best transmission path to the transducer placed on the bearing house will occur when one of the rollers is under maximum Hertizan stress, i.e., making direct contact between opposite raceways. Therefore, as the rollers move in and out of this position, a significant amount of information will be attenuated and/or completely lost due to negligible contact. For the experiment undertaken above, great care was taken to ensure the maximum transmissibility to the bearing housing. Also, the sensor was positioned on the bottom half of the housing.

Undetected responses for pulse inputs between positions P5 and P16 with the sensor on the bearing housing was not unexpected. For instance, application of the 30dB relative amplitude attenuation on a detected signature of amplitude 0.71V (see P5 on table 7.3, with sensor on stub shaft) will result in a signature of amplitude 0.022V. This signature will be camouflaged within the electronic noise of the system, and therefore, be undetectable by conventional triggering.

7.3 Attenuation characteristics of the test-rig

The attenuation properties of the test-rig based on the Nielson source tests are shown in figure 7.4 and detailed in tables 7.4 and 7.5 of appendix A. The frequency attenuation characteristics for fixed distances are shown in figure 7.5. All analysis was based on 16384 data points.

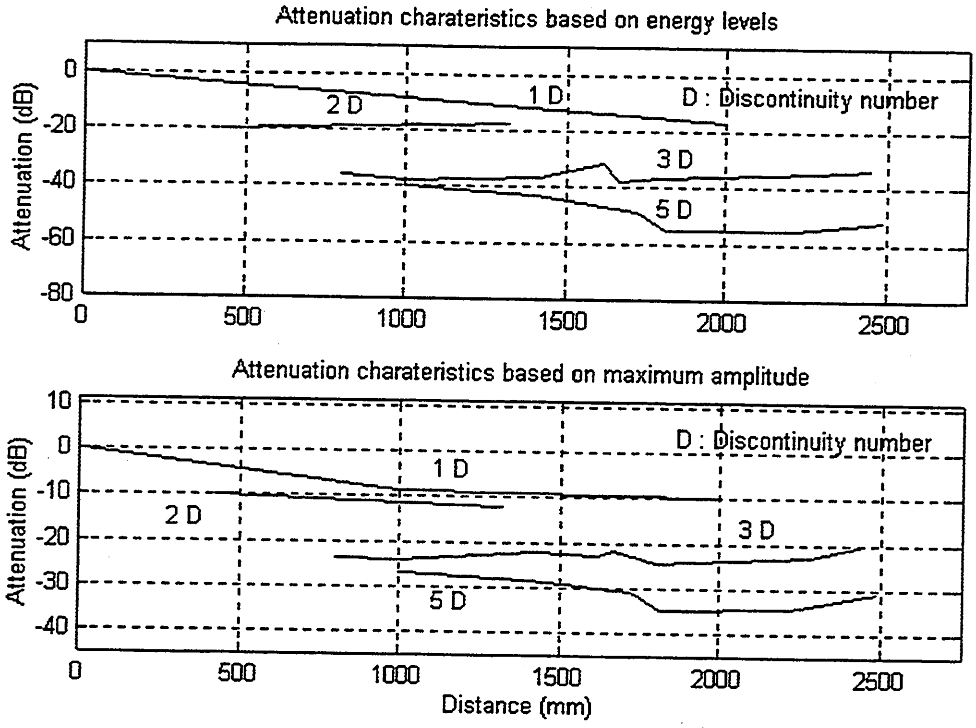

Figure 7.4 Attenuation characteristics of test-rig.

The reference used for attenuation calculations was the signal input at position P0 and the relative attenuation was computed by :

$$dB = 20*log(Pi/P0)_{i=1:18} \qquad (7.1)$$

Whilst it is evident that the attenuation increases with increasing discontinuity, the attenuation for each discontinuity does not follow theoretical expectations. For instance, the amplitude at 2- and 3-discontinuities appears to remain at the same level and not decrease with increasing distance. There are thought to be two reasons for this :

i) There is no guarantee that the strength and contact angle of the lead on the metal surface will be the same for each position.

ii) There are positions with similar distances and discontinuities but quite different transmission paths. For instance, positions P8 and P9 are at similar distances from the sensor, but have quite different transmission paths. Furthermore, energies generated from P8 will be dissipated through the through-rods in its path. This difference in transmission paths will result in different amplitude and energy levels for almost identical distances. Positions P14/P15 provide another example. These explanations also apply to figures 7.3a and 7.3b.

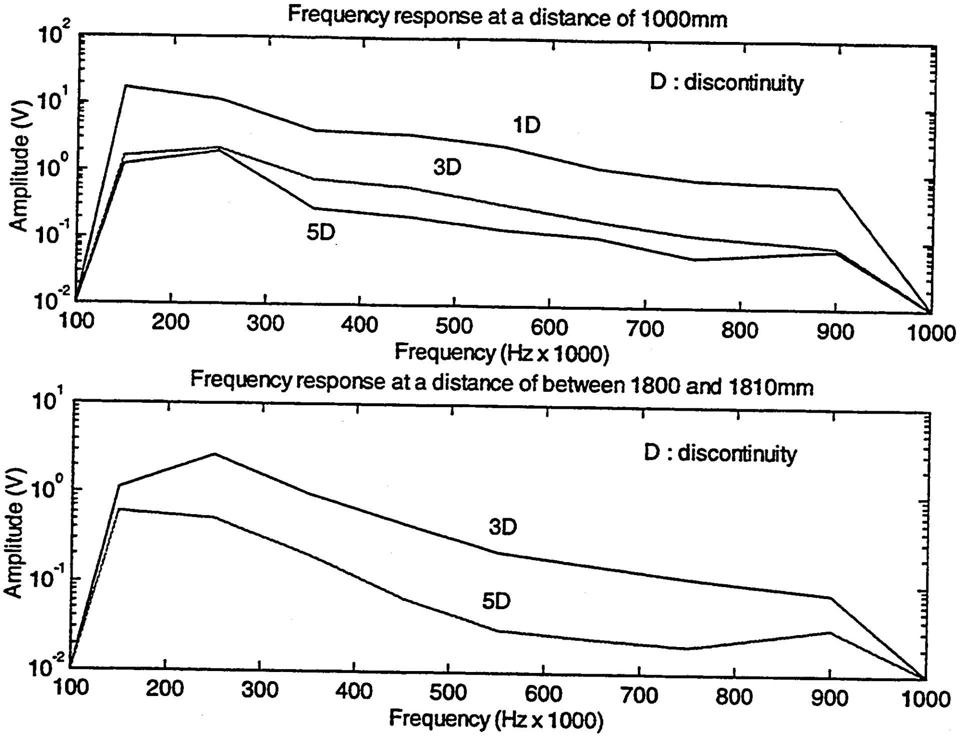

Figure 7.5 **Frequency attenuation characteristics for varying discontinuities at similar distances from the sensor.**

Figure 7.5 shows that the higher frequencies attenuate faster. However, the frequency attenuation rates remained relatively constant irrespective of the number of discontinuities and frequency. The reduction in strength with increasing discontinuity is attributed to attenuation.

Based on these results an estimate on the longest distance at which stress wave activity can be detected was calculated. Assuming the worst attenuation case of 5-discontinuities, the computed amplitude attenuation between 1000mm and 2000mm was approximately 8dB, see figure 7.4 and table 7.5. Furthermore, at a distance of 1000mm with 5-discontinuities, an attenuation of 27dB was obtained. Using the maximum amplitude value of a signature associated with the Nielson source technique as the reference (position P0 in table 7.5), it would require an attenuation of 61dB for signatures generated by this technique to be undetectable above the electronic noise of the ADC board. This would correspond to a distance of 5 meters having 5-discontinuities, assuming an attenuation of 8dB/meter after a distance of 1000mm. Whilst this is a very crude approximation of the attenuation properties, since the rate of attenuation with increasing distance is not linear, it does suggest that stress wave activity can be detected over considerable distances with several discontinuities. This provided encouragement prior to simulations and 'on-site' recordings.

7.4 Simulation results

Simulations were undertaken with the sensor fixed to the stub shaft end. Since the machine was rotating at 1.12 rpm, there was negligible dynamic force on the face of the sensor. However it was observed that there were restrictions in the number of revolutions for which data could be collected unimpeded. After about five revolutions twisting of the sensor cable resulted in generation of acoustic bursts. Although this could be overcome by setting higher trigger levels, it was thought unwise as lower level signatures with relevant information could go undetected. Moreover, until 'on-site' recordings had been taken, it was not possible to determine what trigger levels might be used. Therefore, after five revolutions the sensor cable was disconnected from the pre-amplifier and unwound.

The time and frequency spectra of simulation results are displayed in figures 7.6 to 7.8. All signatures were band-pass filtered between 100KHz to 1000KHz.

7.4.1 Frame looseness

Responses for stress waves were obtained as a result of rubbing between the radial arms and shaft clamps. These were detected for all three simulations (see section 5.3) and typical results with corresponding frequency spectra can be seen in figures 7.6 and 7.7. The results shown in figure 7.6 are typical for all radial arms loosened singularly and in pairs. The observed duration for stress wave bursts generated from simulated frame looseness was over 2msec, whilst their frequency content ranged from 100KHz to 750KHz. The sampling rate used on simulations of frame looseness was 10MHz.

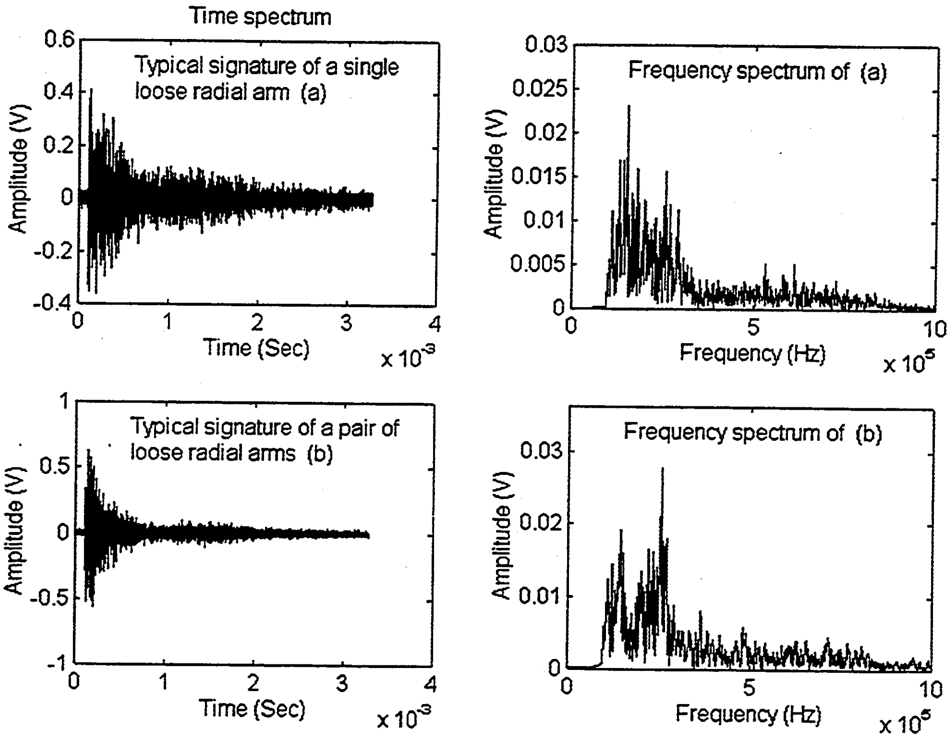

Figure 7.6 **Typical response to simulated frame looseness.**

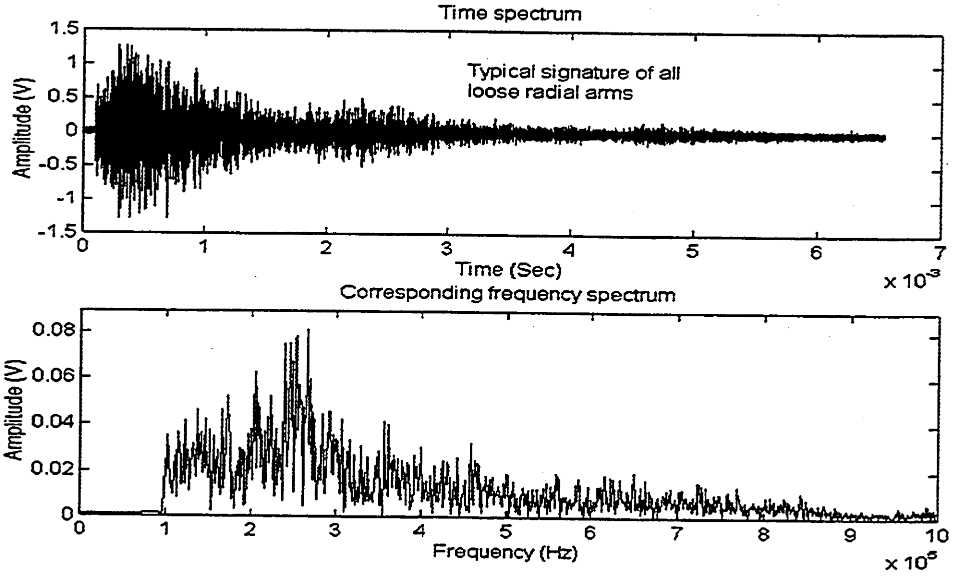

Figure 7.7 **Typical response to simulated frame looseness.**

7.4.2 Broken support-rod rubbing

A typical stress wave signature sampled at 5MHz, with its corresponding frequency spectrum, can be seen in figure 7.8.

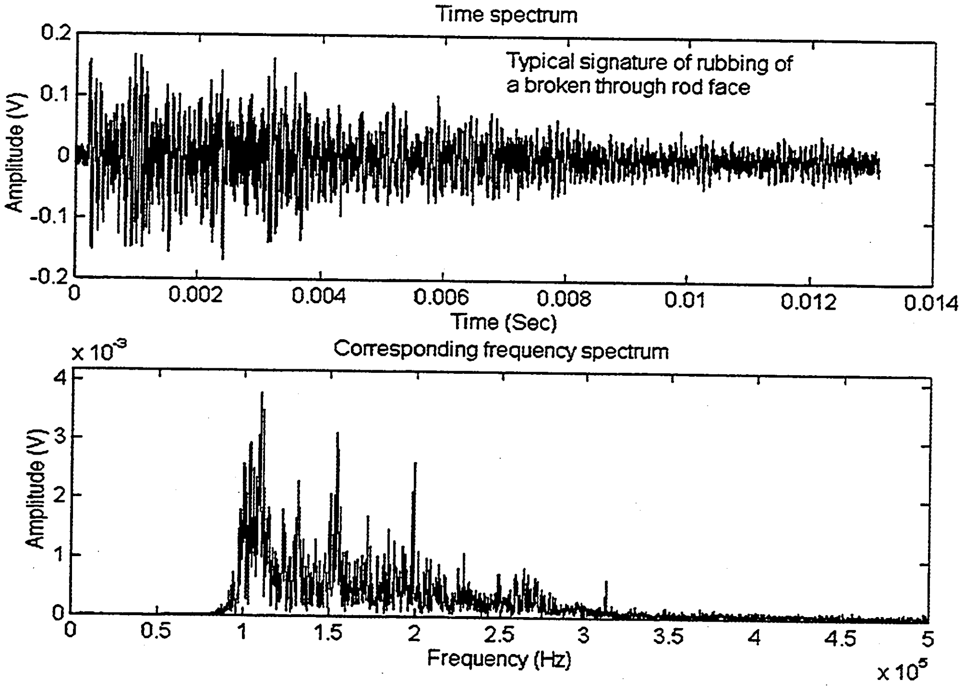

Figure 7.8 Typical response to broken through-rod simulations.

7.4.3 Media movement

Stress waves as a result of media rubbing on the support rod were not detected. This is attributed to the physical nature of plastics and was not unexpected. The impingement of the polymer onto a steel through rod will produce large impact time constants, thereby generating low frequency signatures.

7.5 Classification for identification

The predetermined positions of figure 7.1 were selected to provide as many varied transmission paths as possible. Therefore, it provided an adequate test to any classification algorithm to be employed.

7.6 AR model order determination

Determining the correct model is an important decision. As stated in section 6.3, the shape of a stress wave signature can be represented by AR coefficients as long as the model order is sufficiently large. Selecting a model order lower than the correct order will result in coefficients that do not completely represent the shape of the signature. When the model order is initially unknown, the correct model order can be determined by observing changes in the variance of the minimum mean-squared error. The point where the variance of the minimum squared-error remains constant indicates the correct model order, see section 6.3.1.

Stress waves generated by the Nielson source technique on the test-rig were used to determine the optimum model order. An inherent problem with the auto-correlation method to AR parameter estimation is that the time domain signature has to be truncated (windowing) [109], and this drawback is more pronounced if the signature used for estimation is a portion of an impulse response. Therefore, AR parameter estimation was based on the complete length of the stress wave response, i.e., from the beginning of the burst until a point where most of the decay has already occurred. A 40th model order was used to compute the successive variances of the minimum mean-squared error. A plot of this variance against model order, for two different stress waves, is shown in figure 7.9.

Results of analysis on the various stress waves generated on the test-rig showed that a 14th order model was sufficient for characterisation. No relatively significant decrease in the variance occurred after this model order, indicating that a higher model order was not worth the additional computation. This model order was used for characterisation of stress wave signatures from the test-rig and operational RBCs. A 9th order model was used for diagnosis on bearing defect signatures, as this reduced order was adequate for characterisation of the shorter bursts (chapter 9).

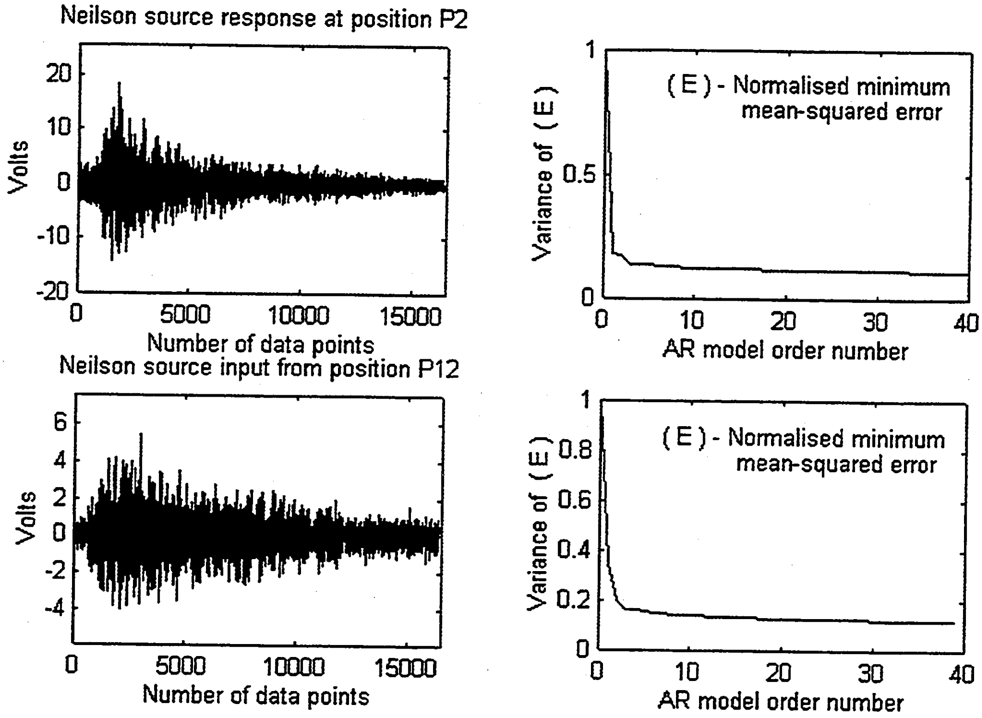
Neilson source response at position P2

Neilson source input from position P12

Figure 7.9 AR model order determination

7.7 Effective source classification parameter

The initial development of a feature extraction and classification algorithm was based on stress waves generated on the test-rig. Computation of classification features was applied on averaged signatures (see section 6.6) generated from the eighteen predetermined positions by the Nielson source. The signatures used for all analysis consisted of the initial burst with all its accompanying reflections, i.e., from the time the signature rose above background noise to the moment it decayed to background noise level. The computed time/frequency features and AR coefficients were passed through a cluster algorithm (see section 6.6) to provide an indication of their classification efficiencies. The results are displayed in figures 7.10 and 7.11. All features were extracted from 16384 data points and AR coefficients were based on a 14th order model.

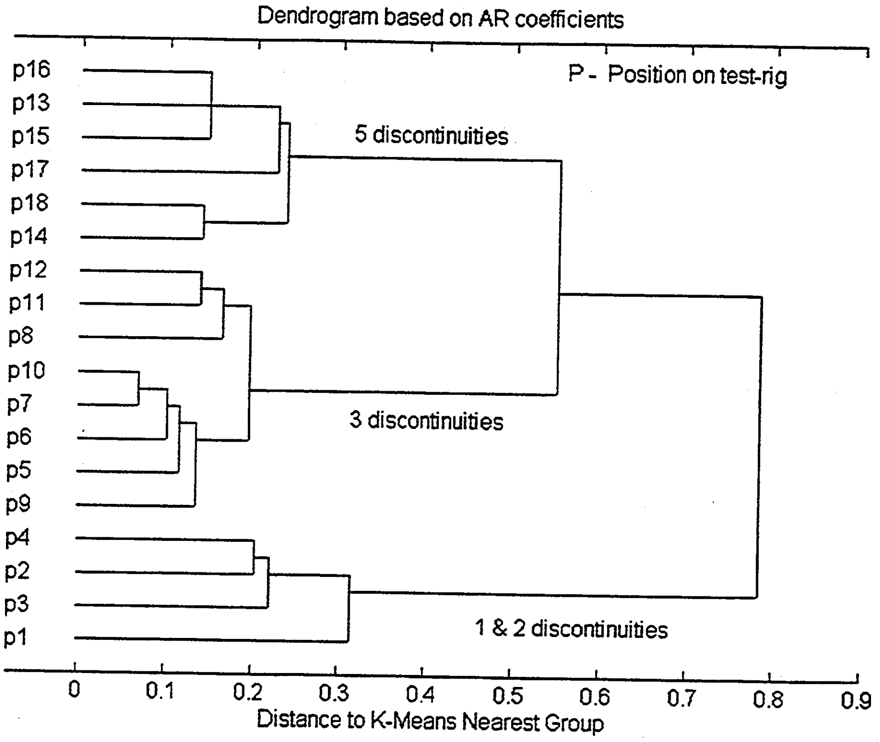

Figure 7.10 Classification based on AR coefficients

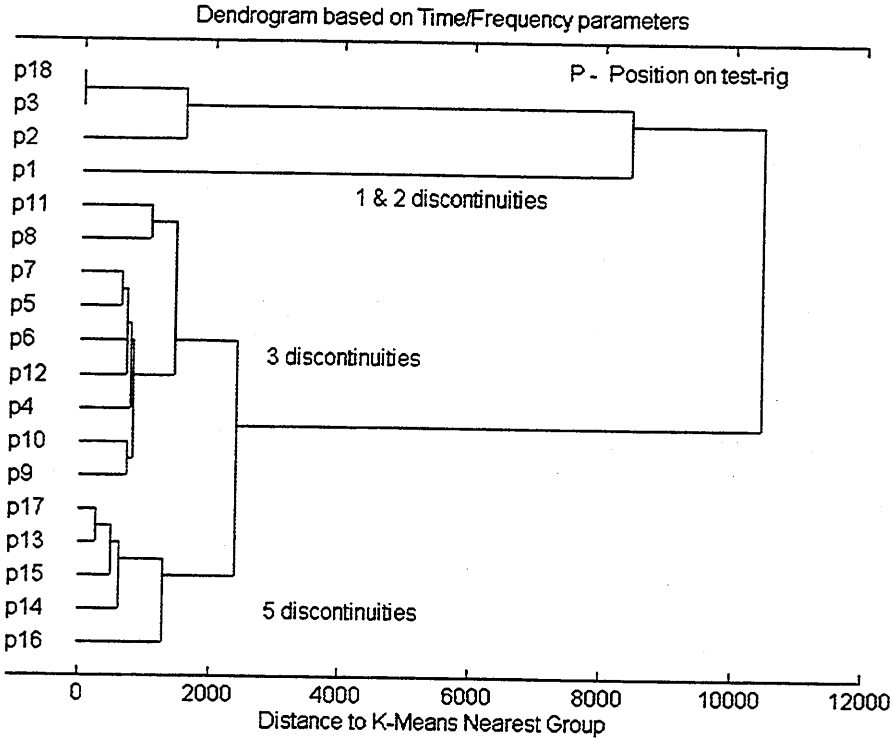

Figure 7.11 Classification based of time and frequency characteristics.

It was evident that both features could classify the signatures into groups of discontinuities, with the AR coefficients showing an improved performance. This is emphasised by the unsuccessful classification of positions P18 and P4 with time/frequency parameters see figure 7.11. Position P18 had 5-discontinuities but was clustered with 1 & 2 discontinuities while position P4 had 2-discontinuities but was clustered with 3-discontinuities. The successful classification with AR coefficients suggests that the shape of signatures associated with the same number of discontinuities was distinct. Furthermore, it emphasises that the transfer function characteristics, between the source and the receiving transducer, was the significant factor for classification. Figure 7.12 displays three signatures with differing discontinuities, highlighting distinct patterns.

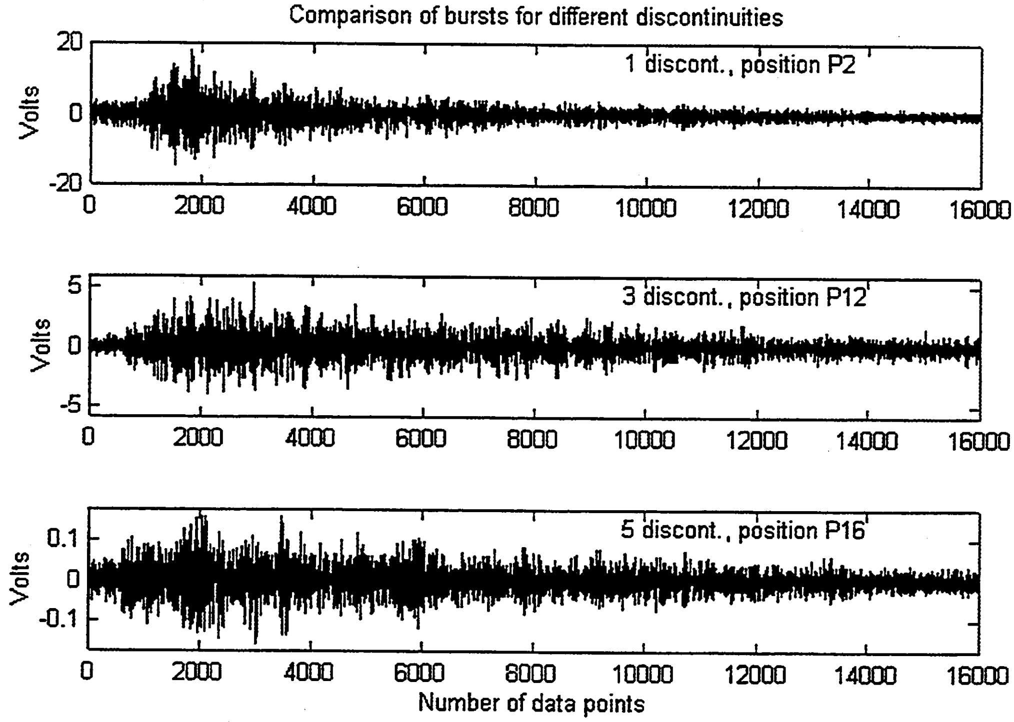

Figure 7.12 Bursts generated at three different positions on the test-rig.

7.8 Severity classification

As severity of rubbing increases, the strength of the burst will also increase, assuming a constant duration of rubbing activity. To test the effectiveness of both time/frequency and AR cluster parameters as a function of severity, simulations of pulse inputs with varying amplitudes was undertaken at five positions, P2, P3, P4, P8 and P12. The pulse was set at 100 nano-secs for five different amplitudes, 16.67V (a1), 13V (a2), 10V (a3), 7V (a4) and 4V (a5). The feature extraction and classification algorithms were applied to these sets of averaged data and the results are shown in figures 7.13 and 7.14.

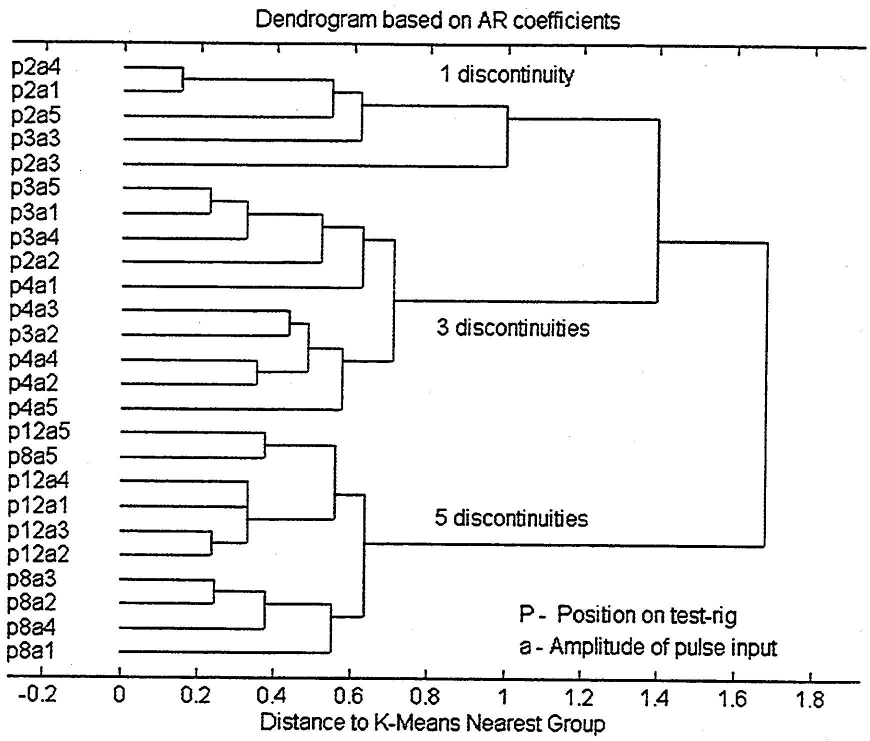

Figure 7.13 **Severity classification based on AR coefficients**

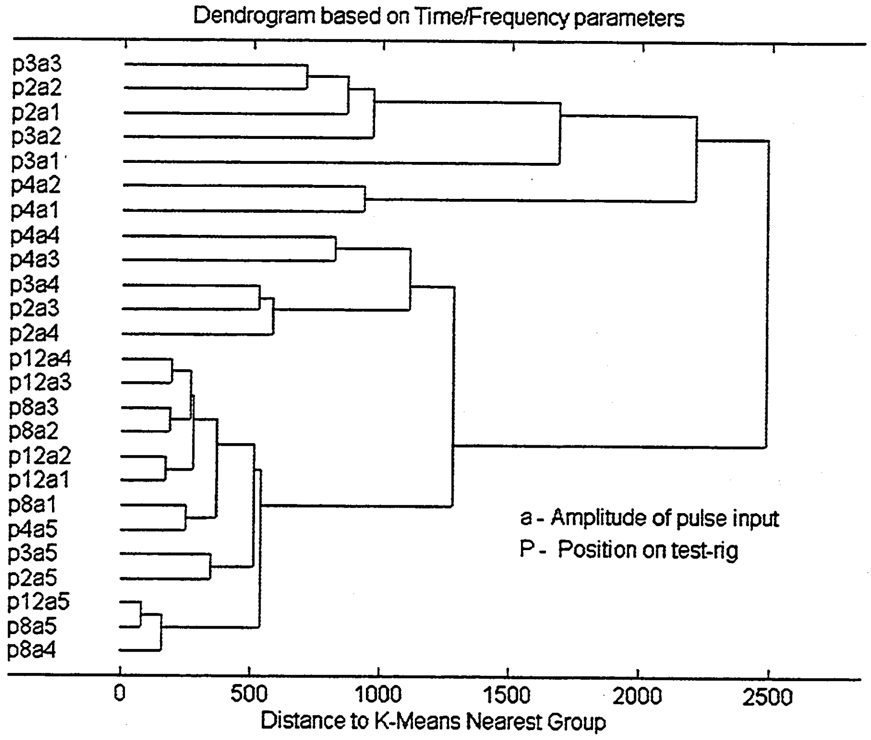

Figure 7.14 **Severity classification based on Time/Freq. parameters.**

Classification with AR coefficients showed an improved performance in relation to time/frequency parameters. This suggests that classification with AR coefficients are not affected by a variation in severity. This phenomena can be explained by observing the severity responses at one of the measured positions, P8, see figure 7.15.

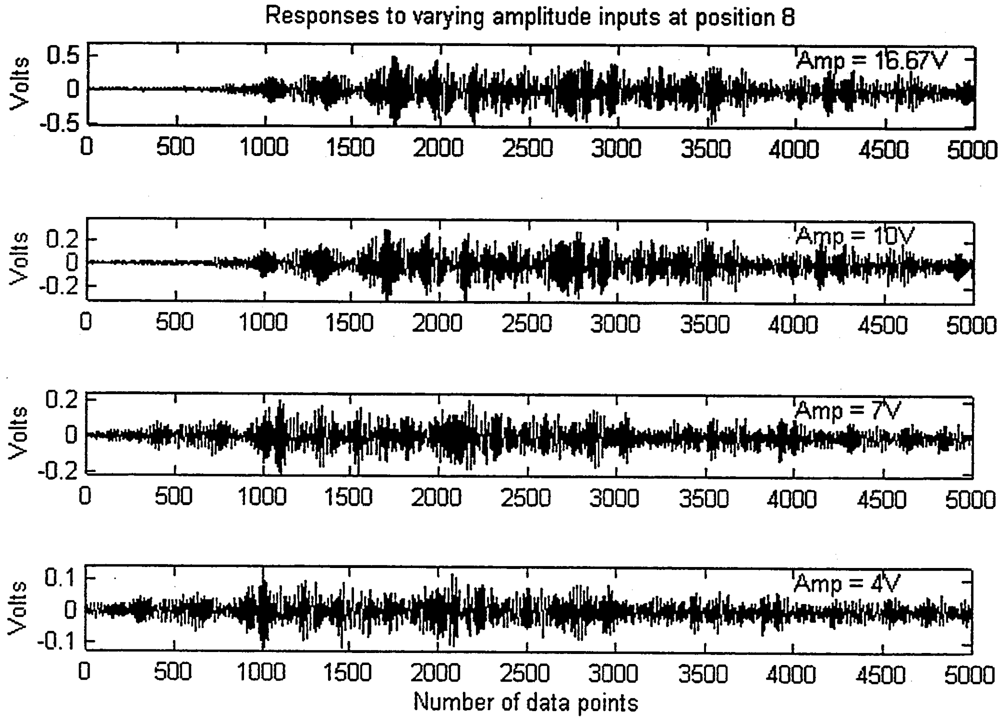

Figure 7.15 Responses to varying amplitudes at position P8.

Whilst the amplitude and rise time of the entire burst decreases with decreasing severity, the wave form still remains very similar, and therefore, its AR coefficients remained similar. This implies that given a cluster of events, their relative severity can be compared by observing time domain features such as maximum amplitude with total energy. By extracting these features and plotting them against each other, relative levels of severity could be determined, see figure 7.16.

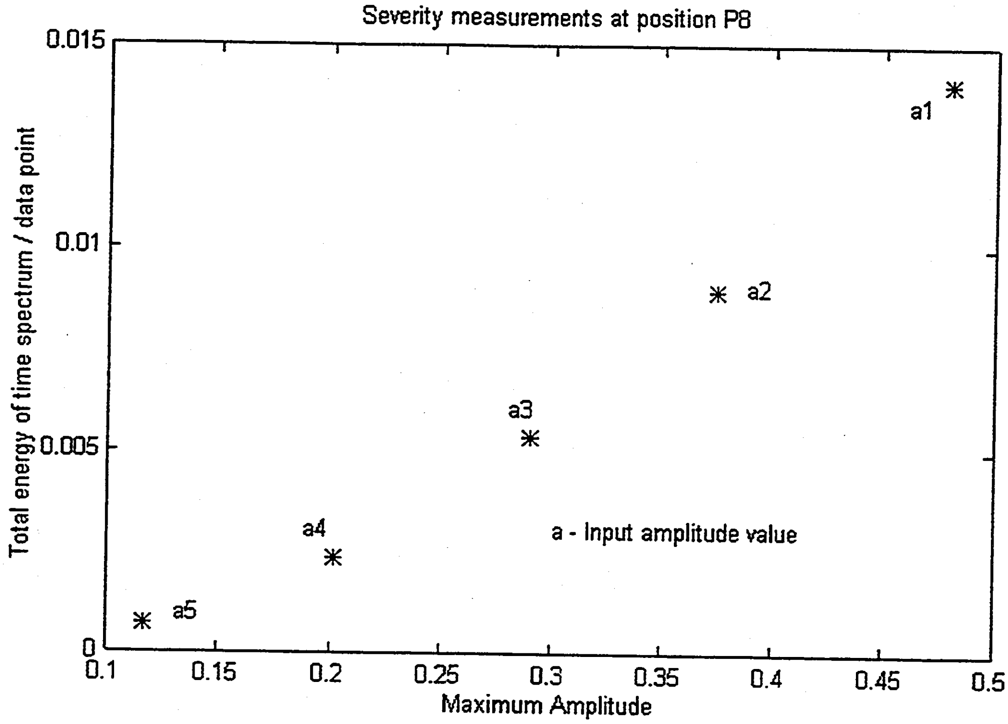

Figure 7.16 Severity measurements at position P8.

Earlier it was assumed that the duration of the burst will remain equal whilst severity increases. This is purely an 'ideal' case and would not always apply as the mechanisms for stress wave generation could vary. The effectiveness of both time/frequency and AR cluster parameters to variation in the duration of burst inputs was undertaken. The same input positions, P2, P3, P4, P8 and P12, were used. Bursts with a fixed amplitude of 16.67 volts and varying duration's of, 100 nano-secs (b1), 1000 nano-secs (b2), 10 micro-sec (b3), 100 micro-sec (b4) and 1000 micro-sec (b5), were applied to the test-rig. Results of these tests are shown in figures 7.17 and 7.18.

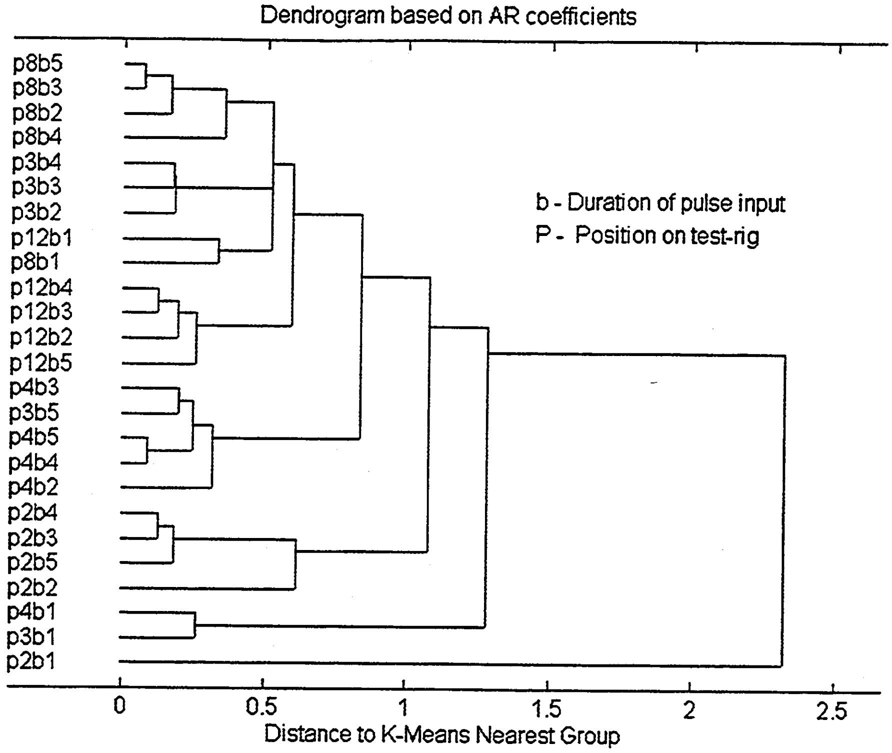

Figure 7.17 Classification based on AR coefficients

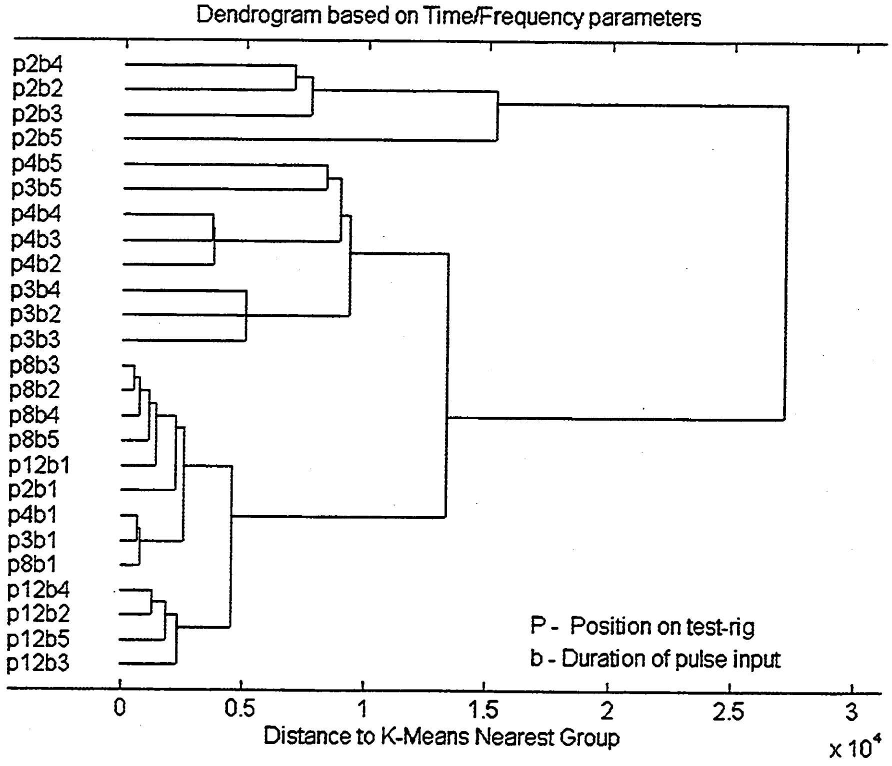

Figure 7.18 **Classification based of time and frequency characteristics.**

Whilst neither algorithm could effectively classify all simulated signatures into their discontinuities, both techniques attempted to cluster signatures generated from the same position. From figures 7.17 and 7.18 it is apparent that signatures generated with 'b1' burst inputs were separated from their anticipated cluster positions, suggesting that they are of distinct wave patterns to other stress waves generated from the same source. From figure 7.19a, the detected stress wave response for a 100 nano-sec ('b1') burst input did not show a markedly distinction from bursts 'b2' (1000 nano-sec) and 'b3' (10micro-sec). The reason that the responses to pulse inputs 'b1' were distinct becomes apparent by observing the frequency response to the various input pulses, see figure 7.19b.

The pulse 'b1' (100ns) had a flat frequency response over the frequency range of the transducer employed, whilst bursts 'b2' and 'b3' show a steep roll-off to 1000KHz. Therefore, the relative influence of these frequencies on the time signatures will result in variations in the pattern of the signature. Bursts 'b4' and 'b5' also showed this steep roll-off characteristic. Therefore, it was not surprising that signatures generated from pulses 'b2 to b5' were clustered together. Stress wave signatures generated from position P8, with corresponding frequency spectrums, highlight the variation in frequency content, see figures 7.19c and 7.19d. The rippling effect of pulse 'b3' is clearly evident in the frequency spectrum shown on the bottom of figure 7.19c. The frequency spectrums in figure 7.19d are very similar; however, the rippling effect was not clearly evident. The peak at 300KHz on the frequency spectrums of figures 7.19c and 7.19d was attributed to the resonance of the structure.

Clearly, the signatures generated with 'b1' pulses had more distinct features due the to influence of higher frequencies. This influence was masked by the structural resonance frequency, thereby making the time spectrum of burst 'b1' less distinct from others.

Based on time/frequency features, the responses to 'b1' burst inputs were held in the same group, see figure 7.18. However, there was no pattern to the group structure. In comparison, classification of the same responses with AR coefficients showed the relationship between their relative discontinuities, i.e., the bursts from positions P8b1 and P12b1 were clustered together, as were positions P3b1 and P4b1, see figure 7.17. Furthermore, the hierarchical structure of classification by AR coefficients suggests that they were clearly grouped by their discontinuities. On the whole, the time/frequency features were more successful in attempting to classify signatures by their discontinuities.

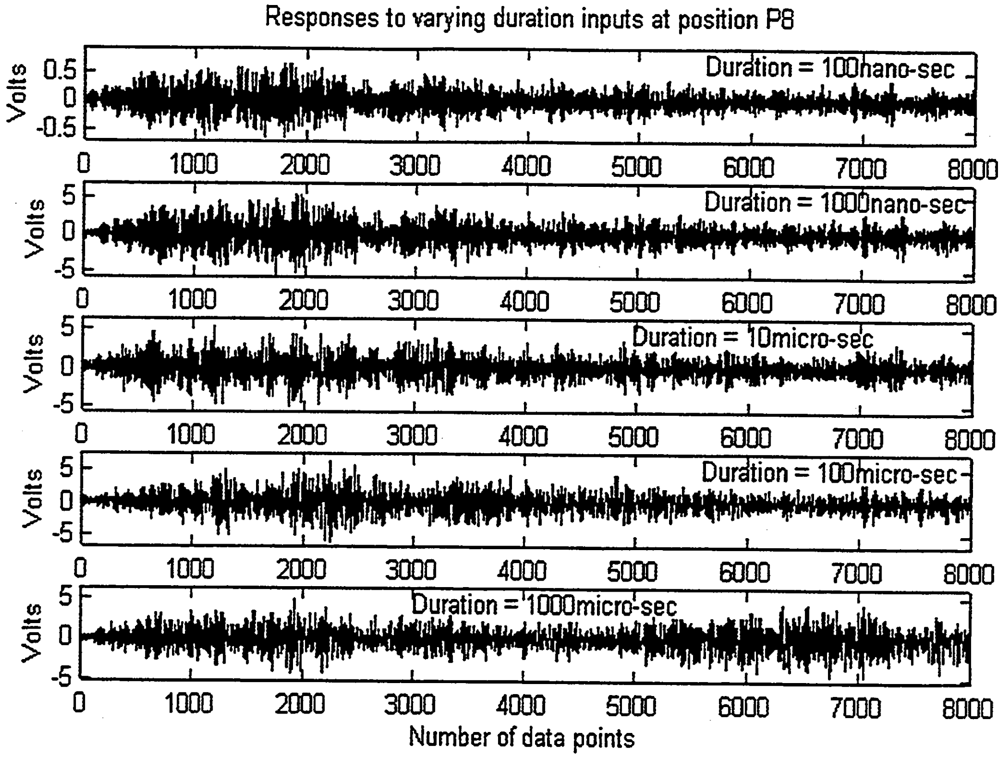

Figure 7.19a Responses to varying pulse input durations at position P8.

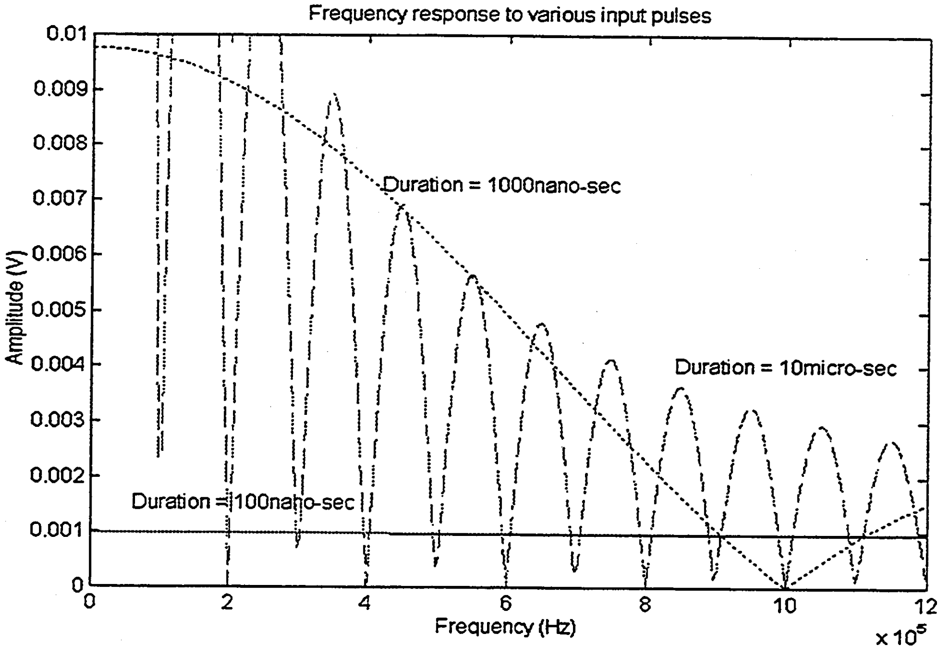

Figure 7.19b Frequency responses of various pulse-input durations.

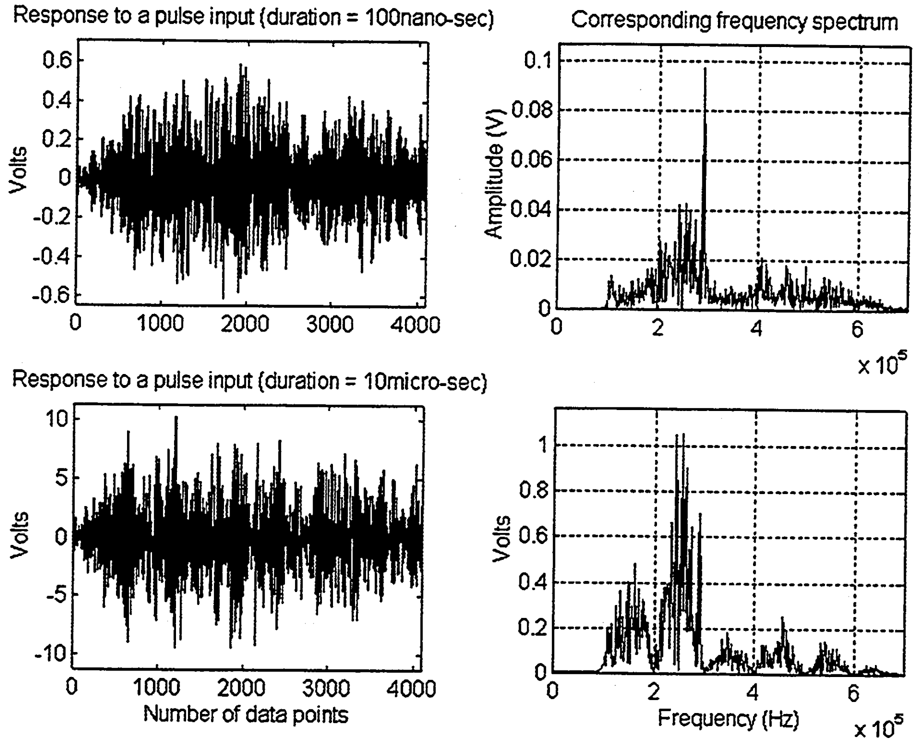

Figure 7.19c Signatures generated at position P8 with different pulse durations

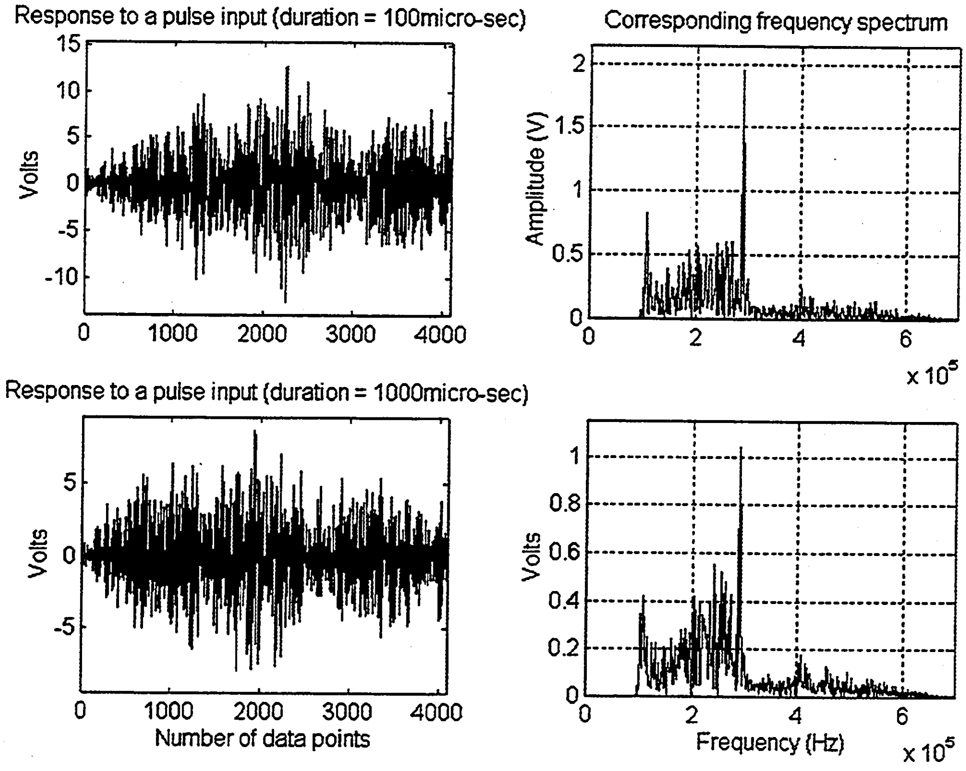

Figure 7.19d Signatures generated at position P8 with different pulse durations

7.9 Classification of simulations arising from mechanical faults to the test-rig.

Stress waves generated from simulations were classified with AR coefficients. The stress waves used consisted of eight through rod faults signatures, each consisting of three averaged signatures, seven single loose radial arm distress signatures, each averaged four times, eleven signatures of loose paired radial arms and six signatures of entire looseness. Five of the seven single loose signatures were obtained from rubbing at position P3, while two signatures were obtained from position P4. Double loose radial arms were simulated in pairs, six distress signatures were used for the first pair while five were used for the second pair. The mixture of varying number of distress signatures was intended to simulate likely conditions on real RBCs. From the clustering results, displayed in figure 7.20a, the following is evident:

i) Through rod distress signatures are clearly distinguishable, cluster 1 of figure 7.20a.

ii) Stress wave signatures of single, double and entire radial arm looseness were held in cluster 'X' of figure 7.20a. The reason that the double and entire frame looseness signatures were not separable from single arm looseness signatures was because the burst associated with double/entire looseness could have been generated from one of two sources. These sources are the shaft clamps, positions P3 and P4 on figure 7.1.

Further observations showed that the sources of stress wave generation for double and entire arm looseness were clearly separable, clusters 2 and 3 in figure 7.20a. For instance, cluster 2 highlights double/entire looseness generated from position P4. This was concluded because single arm looseness from this source was held within this cluster. The same results also apply to position P3 and cluster 3. Comparisons were again made with the time/frequency feature classification algorithm and results are shown in figure 7.20b. These results showed time/frequency features to be relatively ineffective for classification.

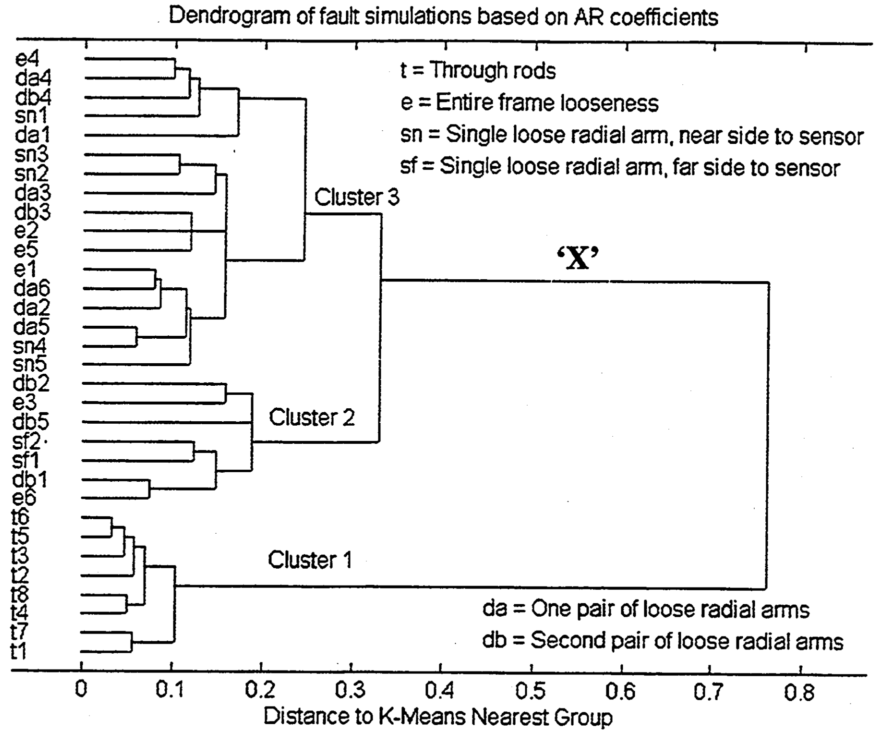

Figure 7.20a Classification of simulation results based on AR coefficients

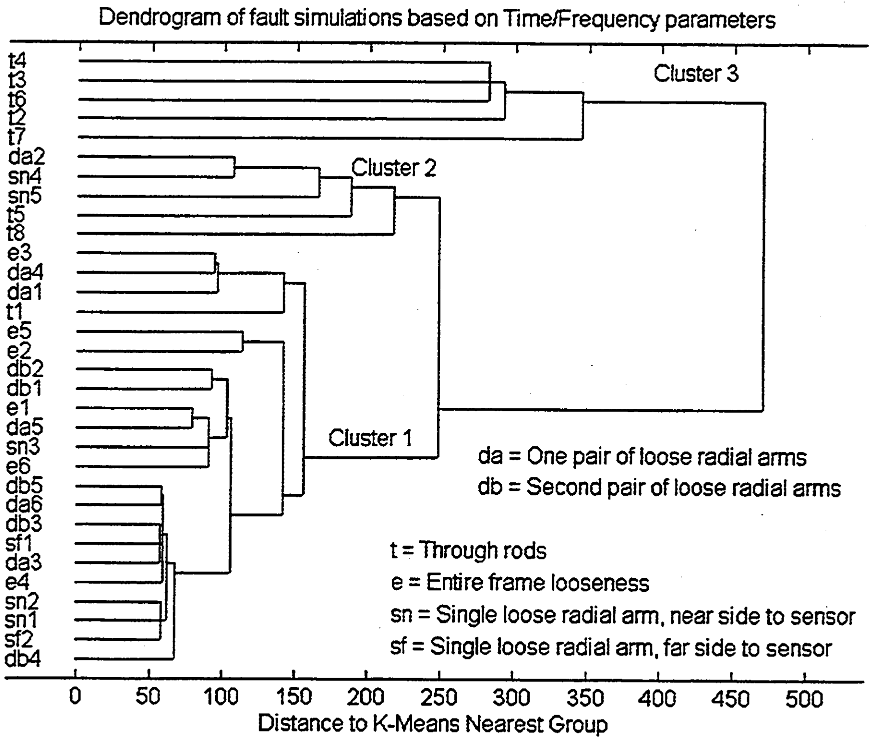

Figure 7.20b Classification of simulation based on Time/Freq. characteristics

7.10 Severity of simulations

Whilst it was not possible to clearly distinguish sources of stress wave generation for all forms of radial arm movement, the severity between single, double and entire arm movement was not evident. Therefore, the distress signatures associated with cluster 3 of figure 7.20a were passed through the severity algorithm, see figure 7.21.

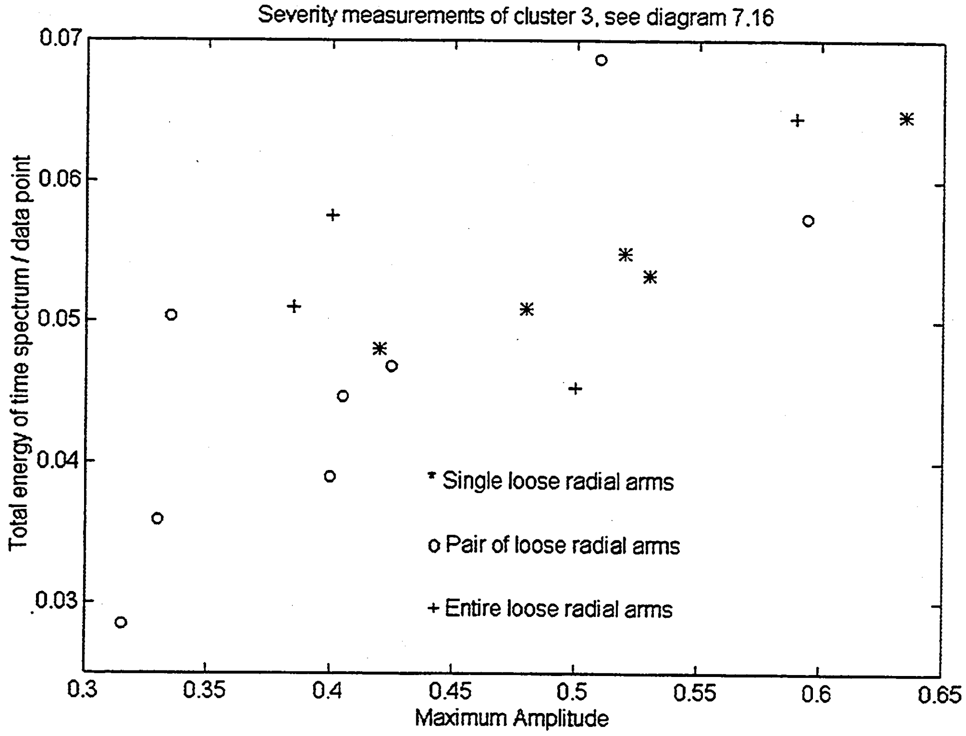

Figure 7.21 **Severity of simulations**

The results do not indicate an increased level of severity between single, double and entire looseness. This was not unexpected, as all simulations had the same degree of movement. During the experiment it was impossible to control the amount of movement for any simulation, therefore, a fixed amount of looseness was used for all simulations.

7.11 Other observations

Observations on long data lengths of generated stress waves showed two or more bursts to be evident, see figure 7.22. The second burst was attributed to the breaking of a second surface asperity during the sliding motion, or the breaking of another asperity from a different source, typical with double/entire radial arm looseness.

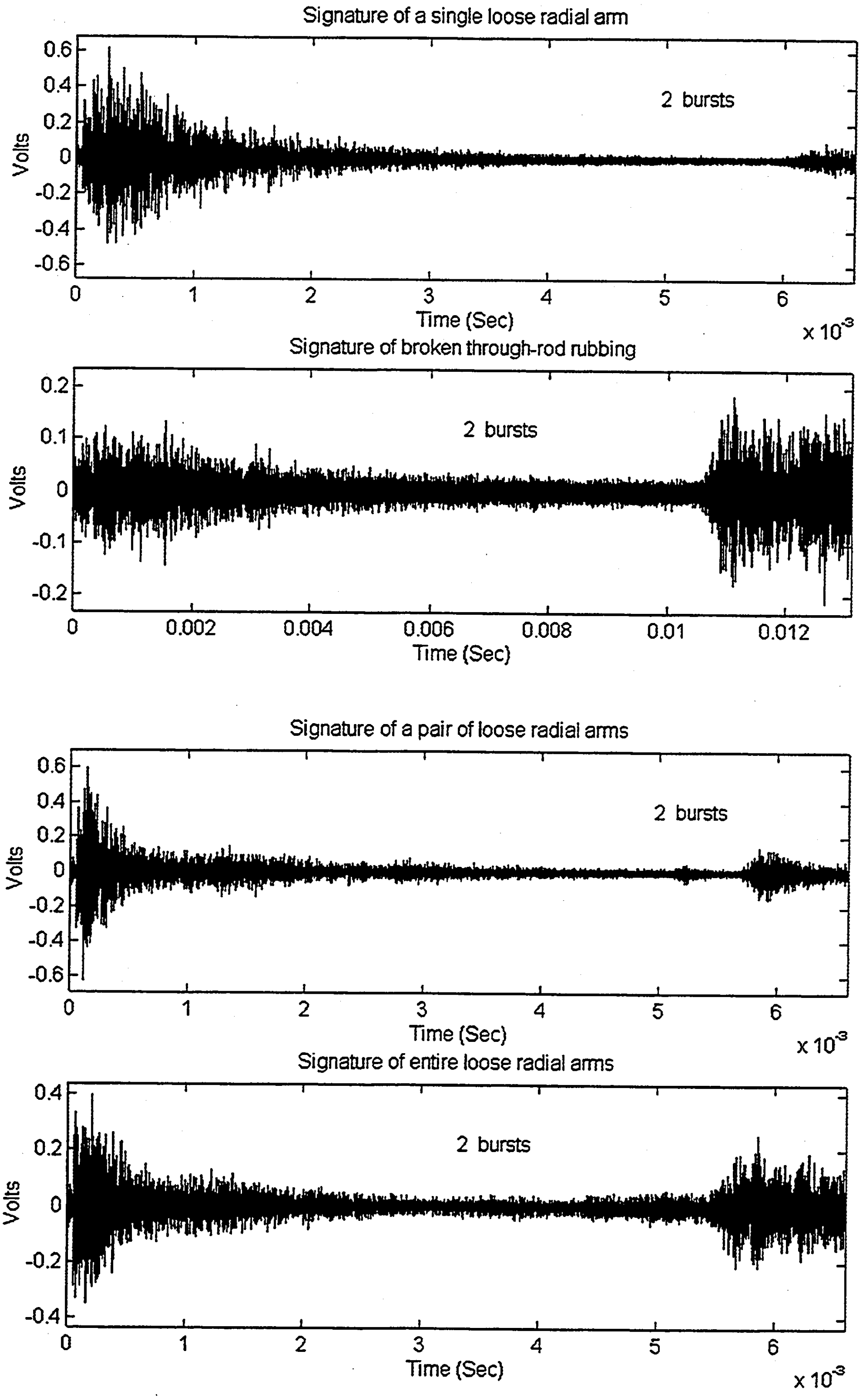

Figure 7.22 Bursts indicative of continued rubbing/sliding of mating parts.

CHAPTER 8

RBC SITE RECORDINGS

8.1 Introduction

The successful operation of an RBC relies on the performance of each component, i.e. bearing, shaft, media support structure and motor/gearbox unit. An effective approach to overall machine monitoring therefore requires a detailed understanding of the behaviour of these components and their interactions. This chapter details the successful application of stress waves to the monitoring of RBC support structures and shaft, while chapter 9 details its application to bearings. Together, **they detail application of stress waves to the condition monitoring of low-speed rotating machinery, the first of its kind.**

As with the experimental tests, the sensor was always placed on the stub shaft end, see photograph 8.1.

Photograph 8.1 Placement of sensor on stub shaft, STW Illmington

8.2 Attenuation tests on a real sized RBC

Attenuation tests were undertaken on a 3.6m diameter Cambridge RBC held in storage at STW Ladywood, see photograph 8.2. These tests, undertaken to provide a comparison between the test rig and a real-sized machine, was undertaken using the Neilson source technique. A lead, 0.5mm 2H, was pressed obliquely against the surface until fracture. Table 8.1 lists the number of discontinuities the stress wave must travel through, from varying positions, to reach the sensor.

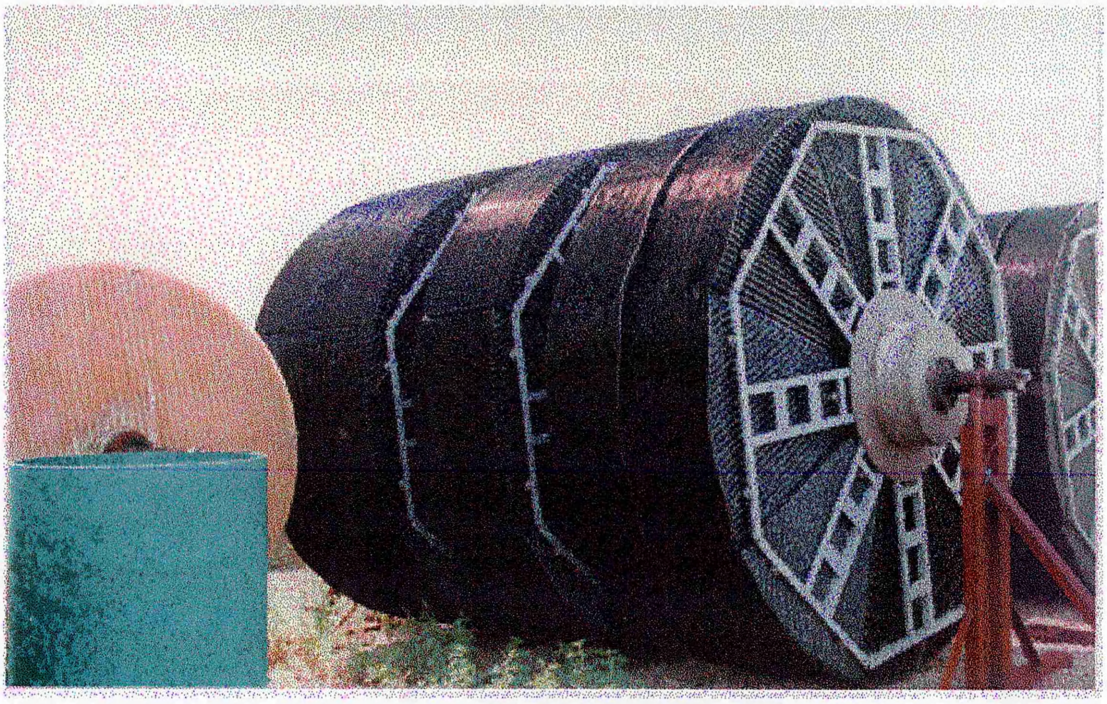

Photograph 8.2 **Cambridge 3.6 diameter RBC in storage depot, STW Ladywood**

Table 8.1 **List of discontinuities**

Discontinuity number	Interface positions at:
	Stub shaft
1	Stub shaft to transducer.
2	Shaft to stub shaft.
3	Radial arm (support structure) to shaft clamp.
4	Through-rods to support structure and/or 'U' bolts to support structure.

The results , showing relative attenuation to lead fracture 25mm from the sensor, are shown in figures 8.1 and 8.2

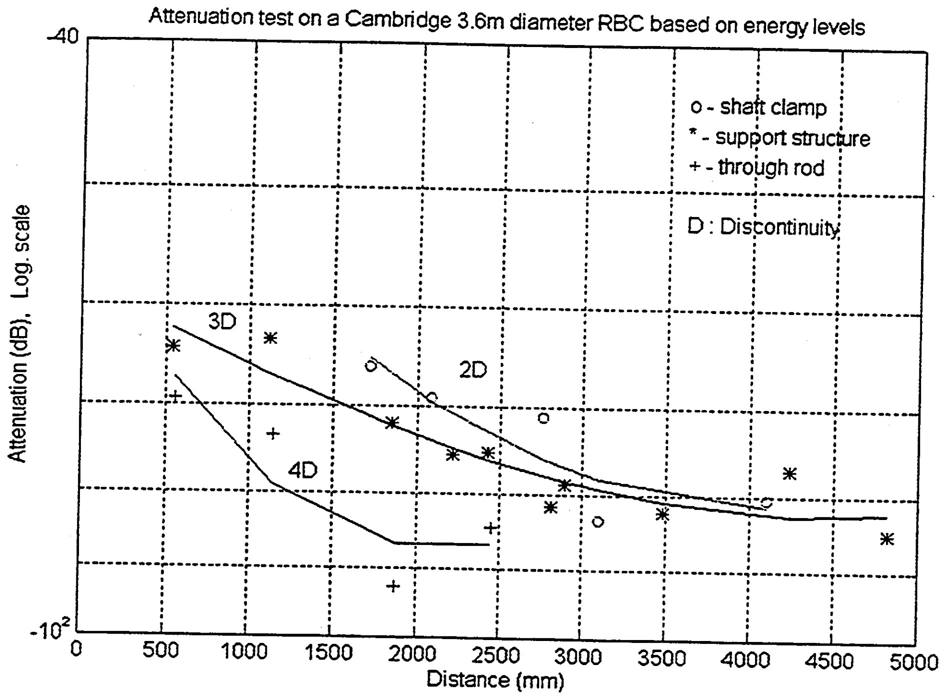

Figure 8.1 **Relative attenuation based on energy levels**

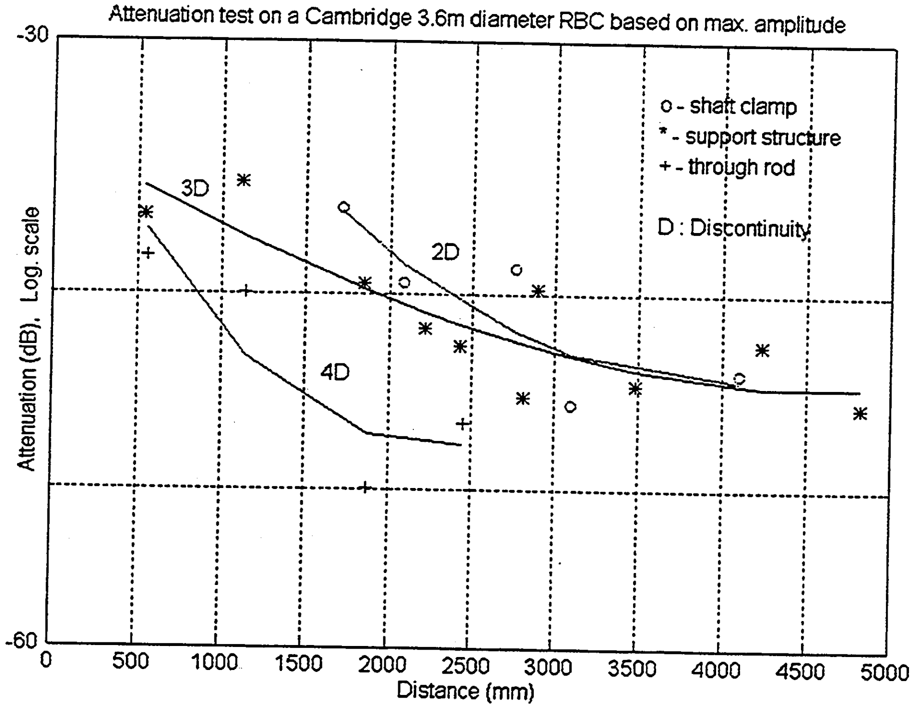

Figure 8.2 **Relative attenuation based on maximum amplitude**

Whilst the same lead type was used on the test rig, attenuation values for similar distances were markedly different. For instance, at a distance of 1000m, with 3-discontinuities, the test-rig showed an attenuation of 24dB for maximum amplitude levels, while on the real-sized machine an attenuation of 35dB was observed. These differences could be attributed to the different sized components and materials used, e.g. stainless steel support structure and galvanised steel shaft and shaft clamp plate were used on the real sized RBC. As these materials are of different impendences, some of the signal strength will be attenuated. Furthermore, since the structures are of larger size than the test-rig, surface attenuation (absorption) of the waves will also occur.

It was observed that stress waves could be detected at distances over 4.7m on the support structure. These findings were very encouraging prior to 'on-site' testing, as this is the largest RBC in operation. However, stress waves were not detected on the through-rods beyond the inlet media pack. This suggests that the rubbing between cracked faces of a through-rod might not be detected beyond the first pack. In view of the fact that all through-rod fractures have occurred on the inlet pack, the lack of stress wave detection beyond the inlet pack was not considered to be a serious drawback. Moreover, should the through-rods have fractured, rubbing between the loose through rods and the support structure will occur and generate stress wave activity of sufficient energy as to be easily detected.

8.3 Background noise measurements

Before attempting to monitor any RBCs, it was thought prudent to take background noise recordings, thereby allowing for development of software to eliminate these unwanted data. Two RBC's earmarked were:

i) STW Beckford, 3.2-meter diameter, manufactured by Klargester.
ii) STW Moreton Morrell, 3.6-meter diameter, manufactured by Cambridge.

As both RBCs had been operational for less than 24 months, it was thought that they would therefore be free of any mechanical deficiencies. Following inspections after site recordings, no visible mechanical deficiencies were detected. Typical background signatures, and corresponding frequency spectra, can be seen in figures 8.3 and 8.4.

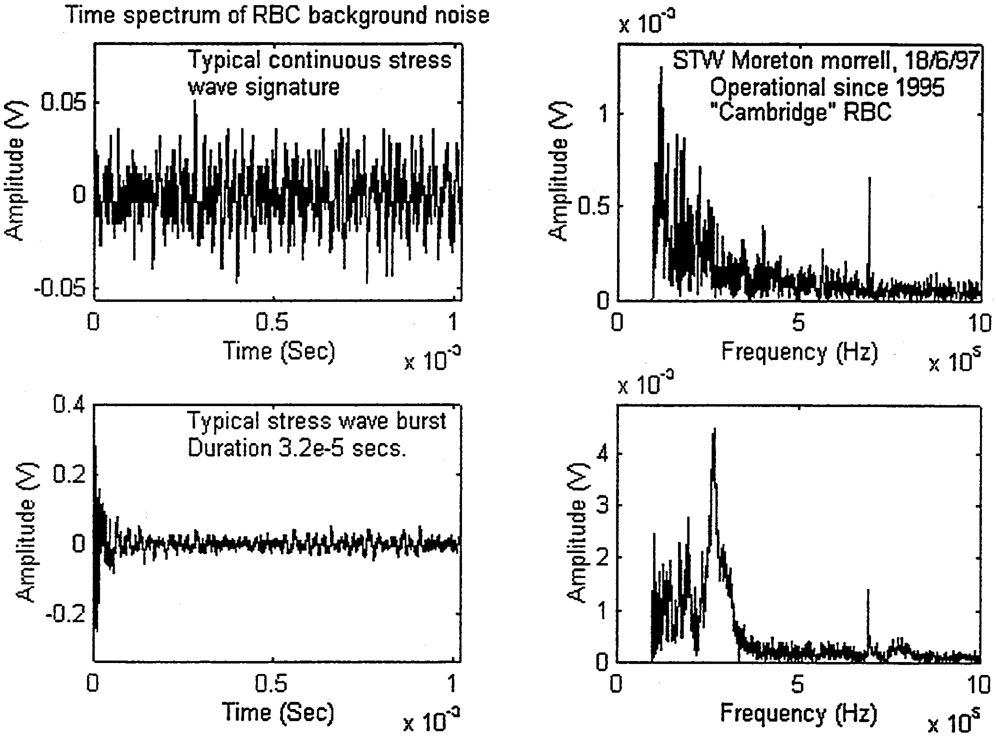

Figure 8.3 Background noise form STW Moreton Morrell

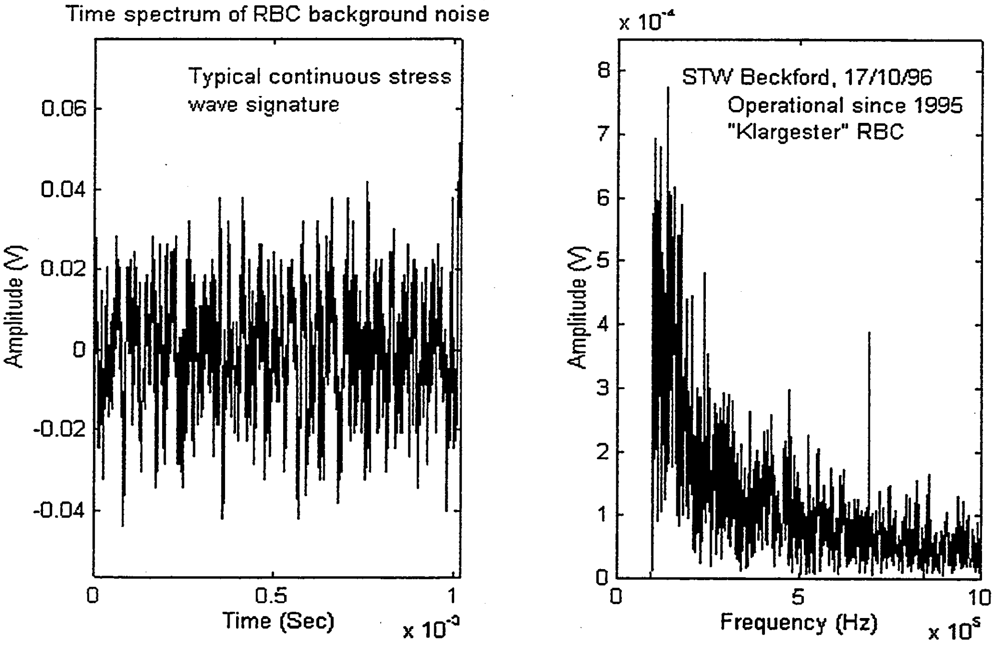

Figure 8.4 Background noise from STW Beckford

The tests on both sites showed stress wave burst generation to be negligible and the occasional bursts detected, as in figure 8.3, were of very short duration. Based on experimental results which showed stress wave bursts, generated from rubbing, to have duration's of over 1.5msec. and of complex pattern, these above-mentioned bursts were discarded as background noise. The amplitude of the continuous stress waves detected was comparable to the electronic noise of the recording system, at 60dB. This suggests that background noise consists of frequency components below 100KHz. Also, Liu [1] found background noise to consist of frequency components below 100KHz on large gas turbine generators. Therefore for all future site recordings, a trigger level of 75mV was set. This level was above the background noise. Should no bursts be detected at this level, the acquisition system will be set to continuous mode, allowing for a continuous intake of data.

Application of the classification algorithm to the continuous stress wave showed no appreciable changes in level, indicating that the data had no group structure and could therefore be attributed to random background noise, see figure 8.5. The algorithm was based on a 14th order AR model applied to 8192 data points

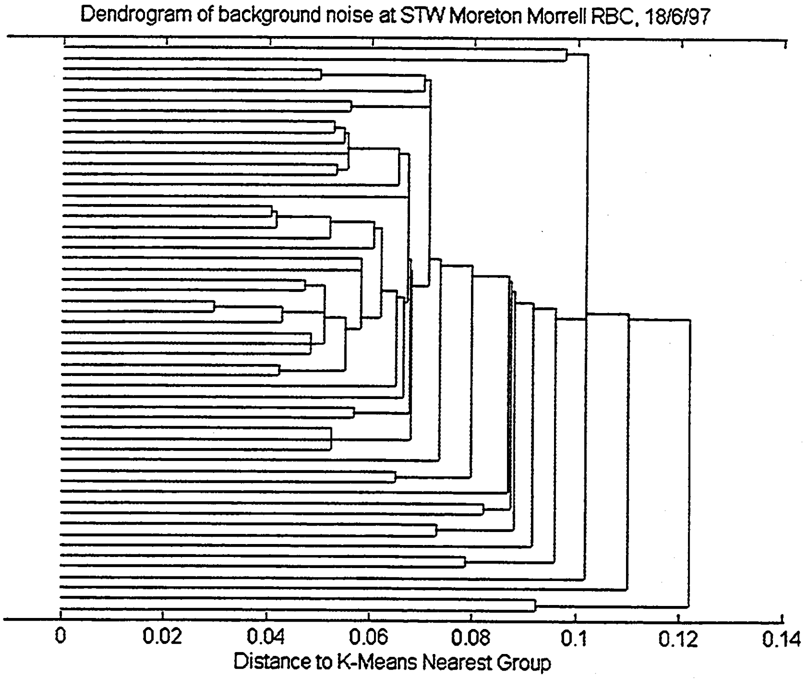

Figure 8.5 Dendrogram of background noise at STW Moreton Morrell

8.4 On-site RBC fault detection

This section highlights some of the successful applications of stress waves to the monitoring of RBCs within the Severn Trent Water region. Table 8.2 in section 8.5 details other successful investigations.

8.4.1 STW Billesdon

The two RBCs operational at this site were manufactured by Klargester both having a diameter of 3.0m. One of the RBCs monitored produced a considerable amount of stress wave activity and ninety-six data files were recorded over four revolutions. Classification analysis of these bursts are shown in figure 8.6, and were based on a 14th order AR model applied to 16384 data points.

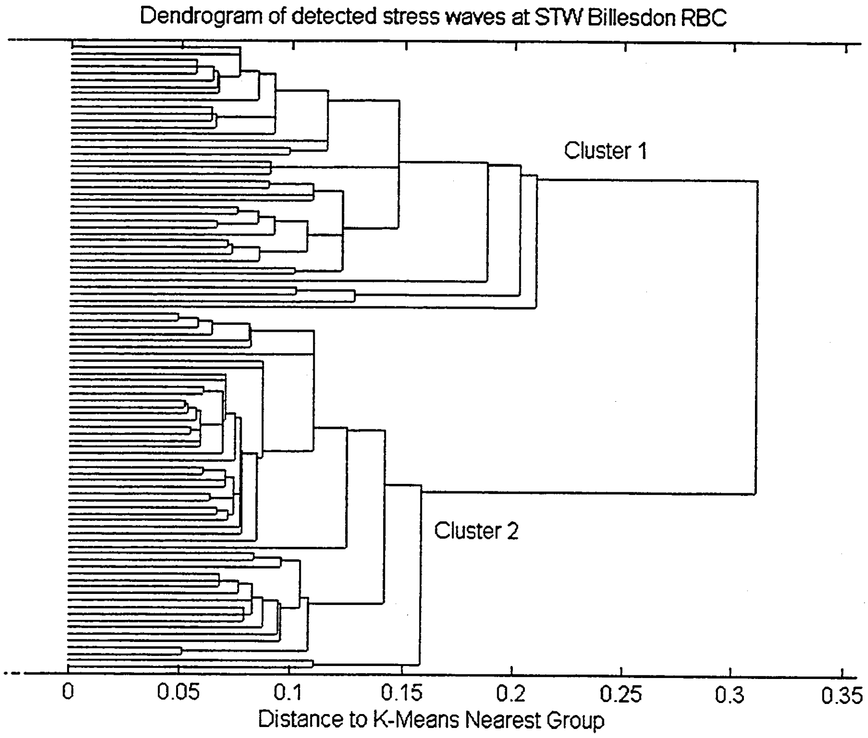

Figure 8.6 Classification of stress waves at STW Billesdon, 3/12/97

Two main groups emerged and their typical time signatures, with corresponding frequency spectra, are shown in figure 8.7.

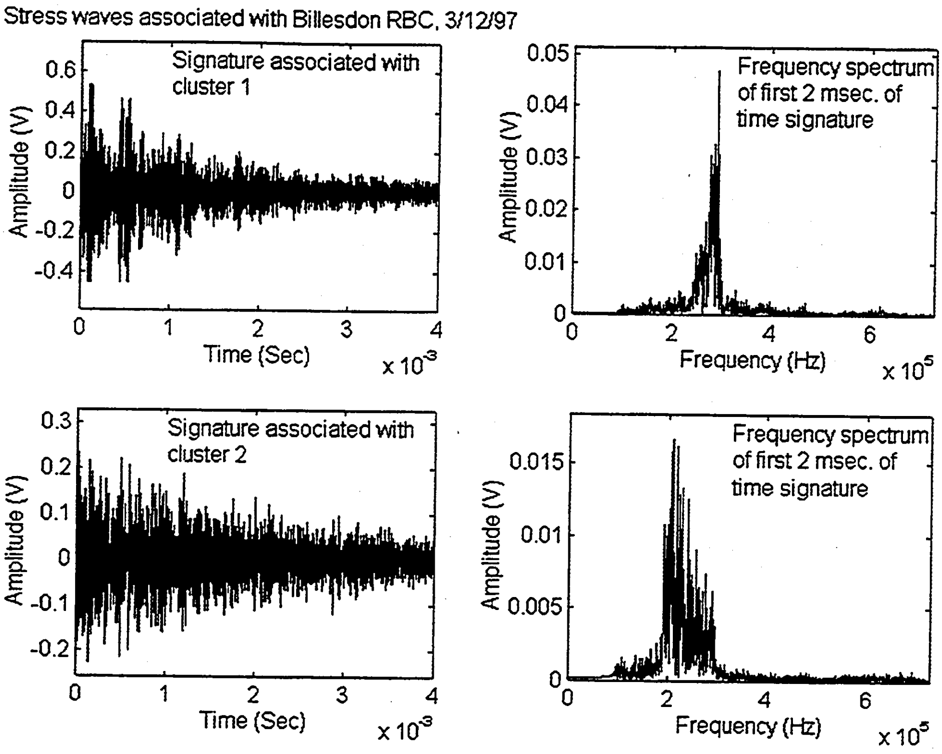
Stress waves associated with Billesdon RBC, 3/12/97

Figure 8.7 Stress waves detected at STW Billesdon

The bursts displayed in figure 8.7 show clearly two different waveform patterns, whose dominating frequencies are also different. The duration of these bursts was in excess of 1.5ms and their shape was of a complex pattern, similar to results from the test-rig and indicative of a complex transmission path burst reflections. Furthermore, it was observed on some data files that several bursts had been generated within the short time span, indicative of the continuous breaking/rubbing of two faces, see figures 8.8 and 8.9. This phenomenon was also observed on stress waves generated with the test-rig, see section 7.4.4.

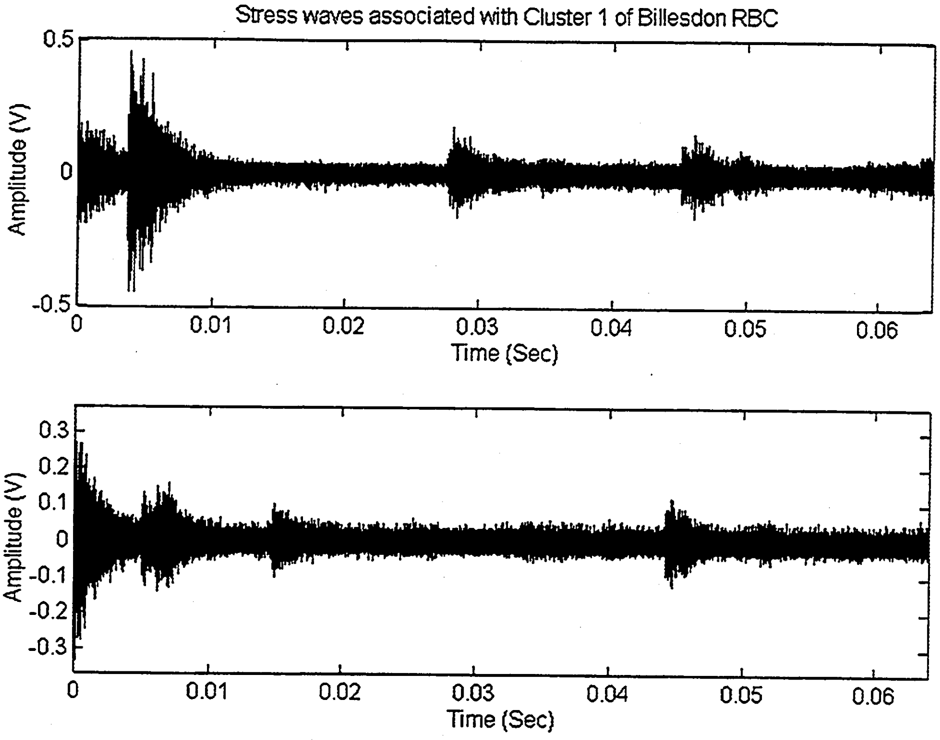

Figure 8.8 Stress wave bursts associated with cluster 1

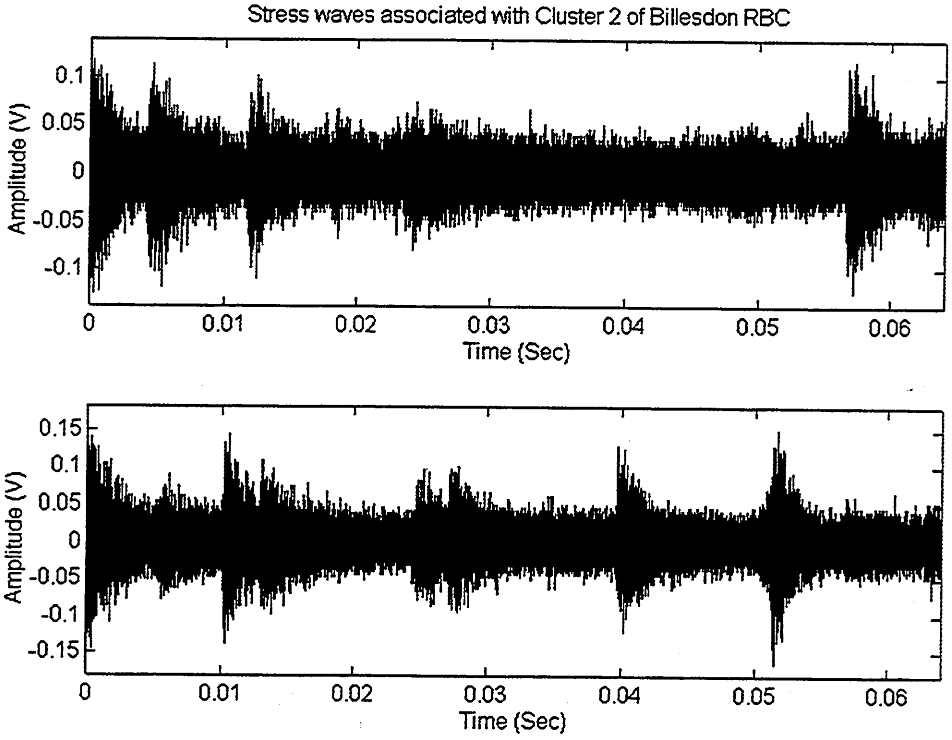

Figure 8.9 Stress wave bursts associated with cluster 2

Based on these results, it was concluded that rubbing between mating components was occurring. The RBC covers were removed by STW engineers and the following mechanical deficiencies were observed :

i Rubbing between the shaft clamp plate and the radial arms was occurring as a result of loss of tightening torque, see photograph 8.3.
ii Rubbing between the outer circumferential rim and the radial arms was also observed, again due to loss of tightening torque, see photograph 8.4.
iii Media movement was evident and was attributed to the inadequate clamping arrangement of the inner through rod. This caused rubbing between the inner through rods and radial arms.

The relative movement of the above-mentioned components inevitably generates stress wave activity. It is probable that deficiencies (i) and (iii) could be held in the same cluster, as waves generated from these regions share very similar transmission paths and discontinuities.

Photograph 8.3 Radial arm/shaft clamp movement

Photograph 8.4 Radial arm/outer-rim movement

8.4.2 STW Illmington

The two RBCs operational at the Illmington site were manufactured by Klargester and had a diameter of 3.6 meters. Both RBCs were monitored and produced a considerable amount of stress wave activity. A total of eighty-two bursts were detected over three revolutions, of which twenty were rejected, either they were of very short duration, and attributed to background noise, or they were severely chipped in the voltage domain. A typical burst, rejected and attributed to background noise is shown below in figure 8.10.

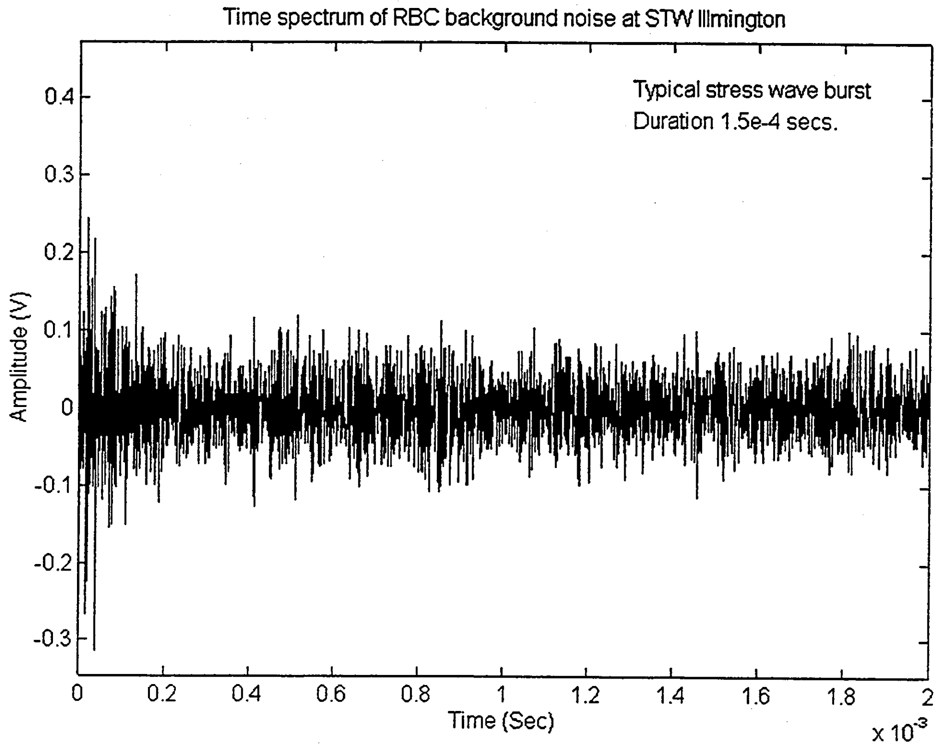

Figure 8.10 Background noise from STW Illmington

Classification analysis of the accepted bursts is shown in figure 8.11, and was based on a 14th order AR model applied to 16384 data points.

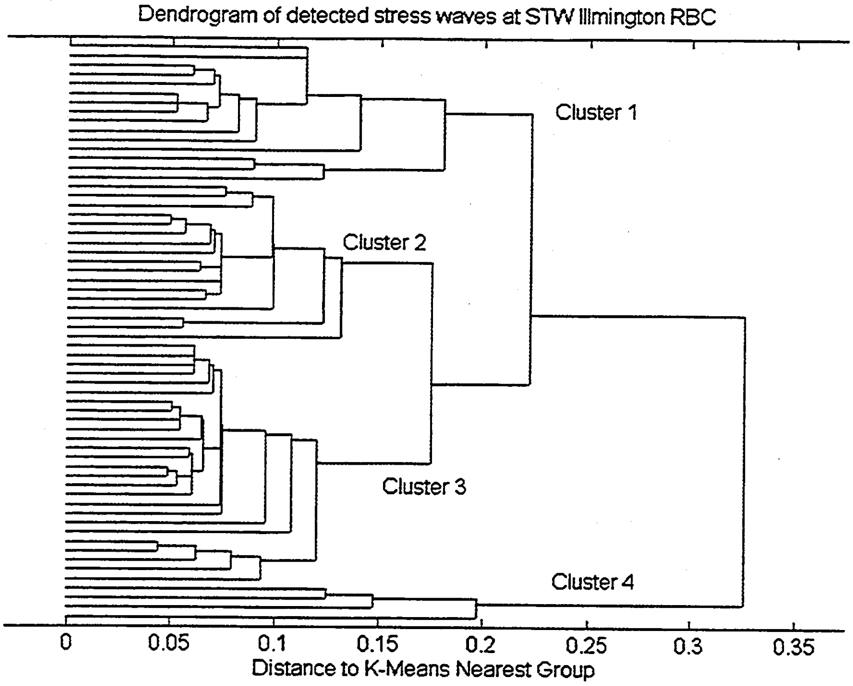

Figure 8.11 Classification of stress wave bursts at STW Illmington, 31/10/96

Four groups emerged and their typical time signatures, with corresponding frequency spectrums, are shown in figures 8.12 and 8.13. The signatures are of different patterns, as to be expected.

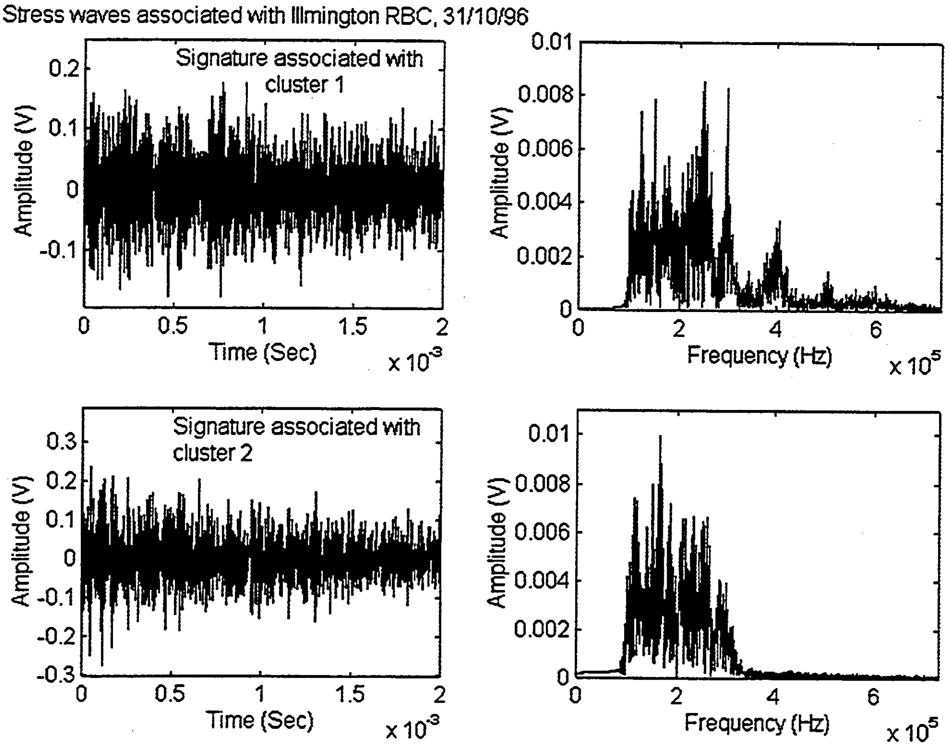

Figure 8.12 Stress waves detected at STW Illmington

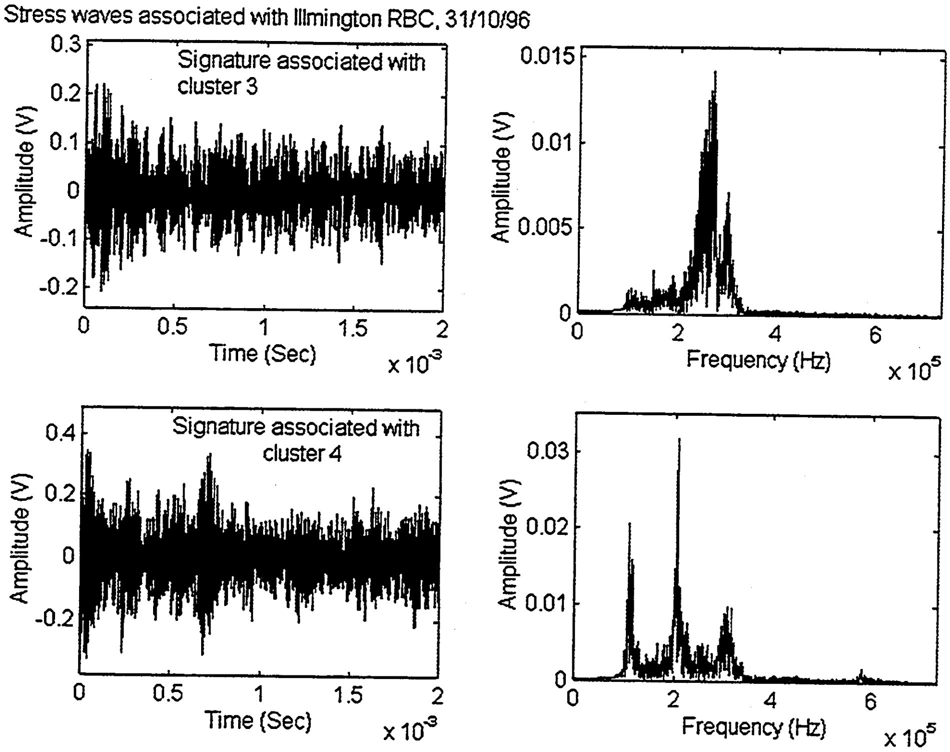
Stress waves associated with Illmington RBC, 31/10/96

Figure 8.13 Stress waves detected at STW Illmington

The duration of these bursts was over 2msec, and of complex pattern. Furthermore, on a few acquisitions several bursts were generated, indicative of continuous breaking/rubbing of two faces, see figure 8.14.

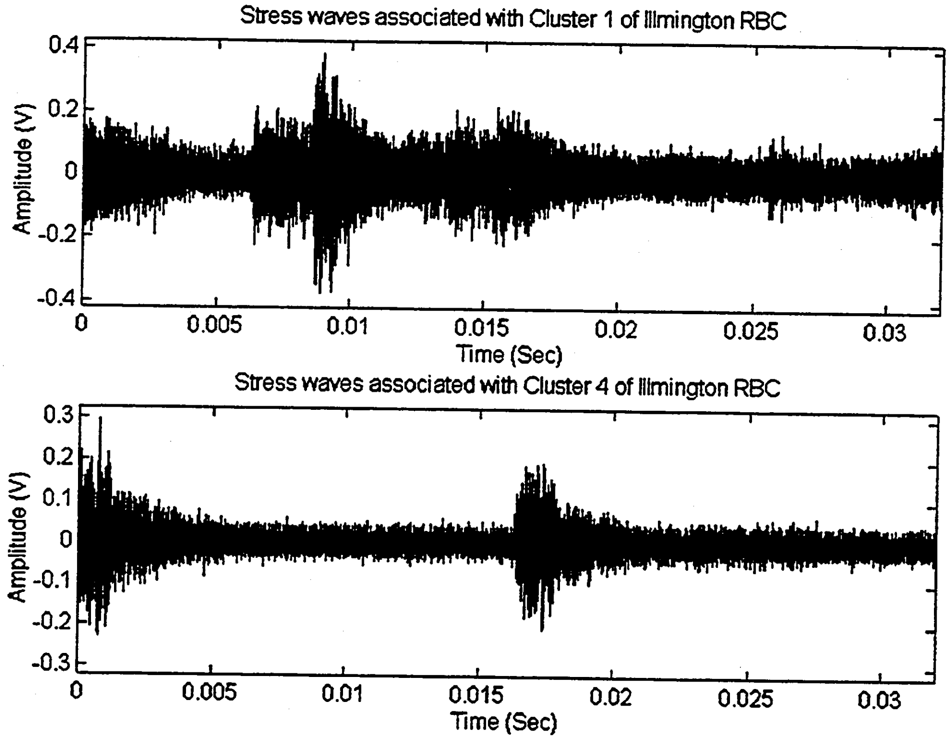
Stress waves associated with Cluster 1 of Illmington RBC

Stress waves associated with Cluster 4 of Illmington RBC

Figure 8.14 Stress waves detected at STW Illmington

Based on these results, it was concluded that rubbing between mating components was occurring. The RBC covers were removed and the following mechanical deficiencies were observed :

i Media movement was visible and was attributed to the inadequate clamping arrangement of the inner through-rod. This caused rubbing between the inner through-rods and radial arms, see photograph 8.5.

ii The outer through-rods were loose due to an inadequate clamping arrangement and were cutting grooves into their end location plates, see photograph 8.6. These plates, fixed onto the outer circumferential rim, prevent axial movement of the through-rods. The continuous cutting by the through-rod ends into their end location plates was considered responsible for generating the stress wave activity.

Mechanical deficiency (i) can be attributed to one cluster group, while deficiency (ii) could be responsible for two closely related cluster groups. This would result from stress wave generation in the end location plate and generation due to rubbing between the loose 'U' strap and the though-rods. No visible mechanical deficiencies can be attributed to the fourth cluster. It is of interest that these deficiencies were generated over a distance of 7 meters from the receiving transducer, **indicative of the enormous potential of stress wave detection for machine health monitoring.**

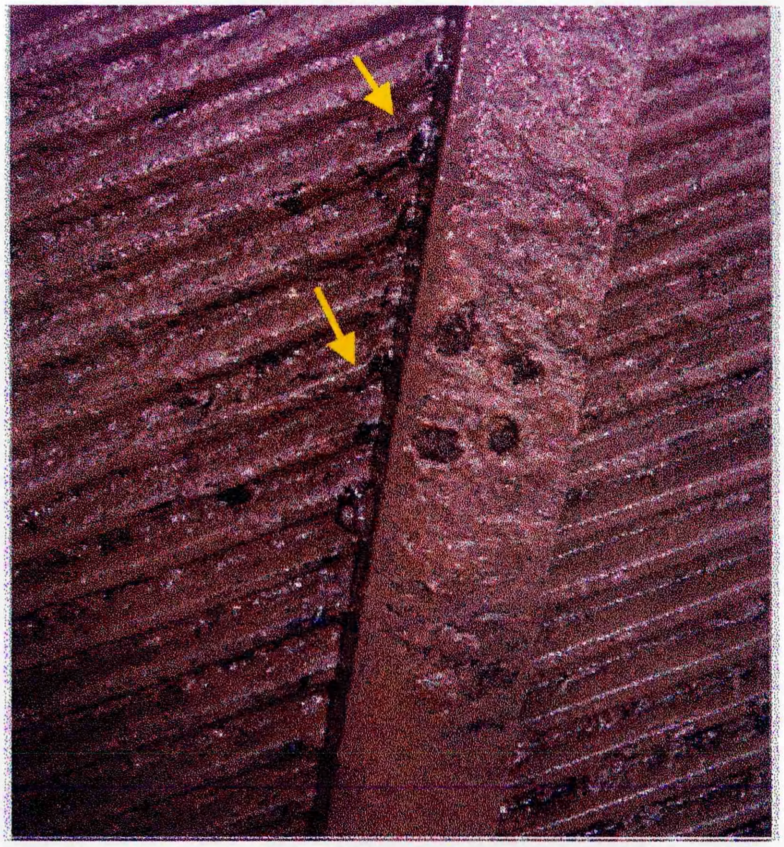

Photograph 8.5 Media segment movement

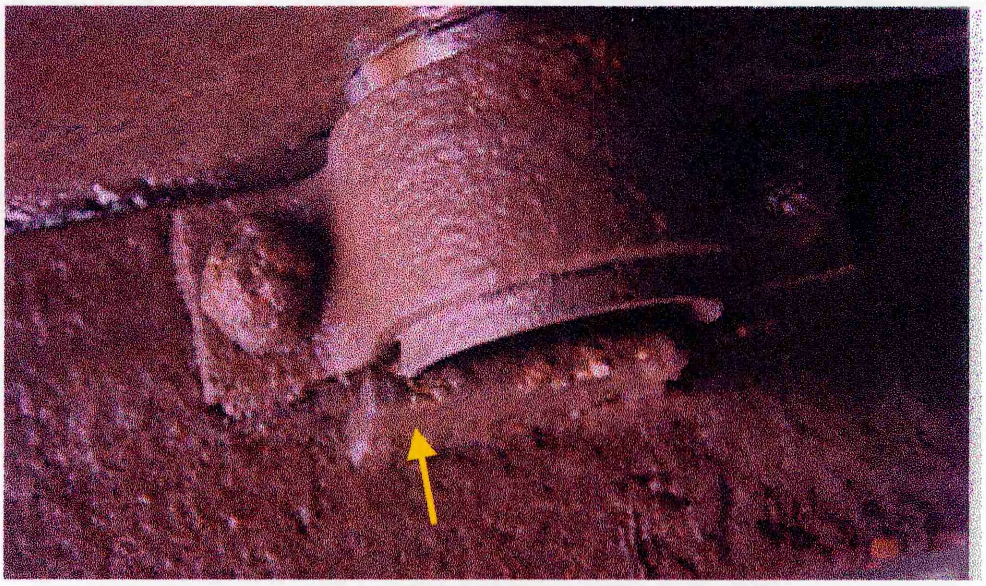

Photograph 8.6 Rotational and axial through rod movement

8.4.3 STW Hamstall Ridware

RBC : Cambridge 3.0-meter diameter.

Date visited : 3/6/97

Classification: 14th order AR model applied to 8192 data points.

Number of data files recorded : Eighty-five data files over three revolutions, twenty-five of which were rejected as spurious electronic spikes or bursts of short duration, see figure 8.15.

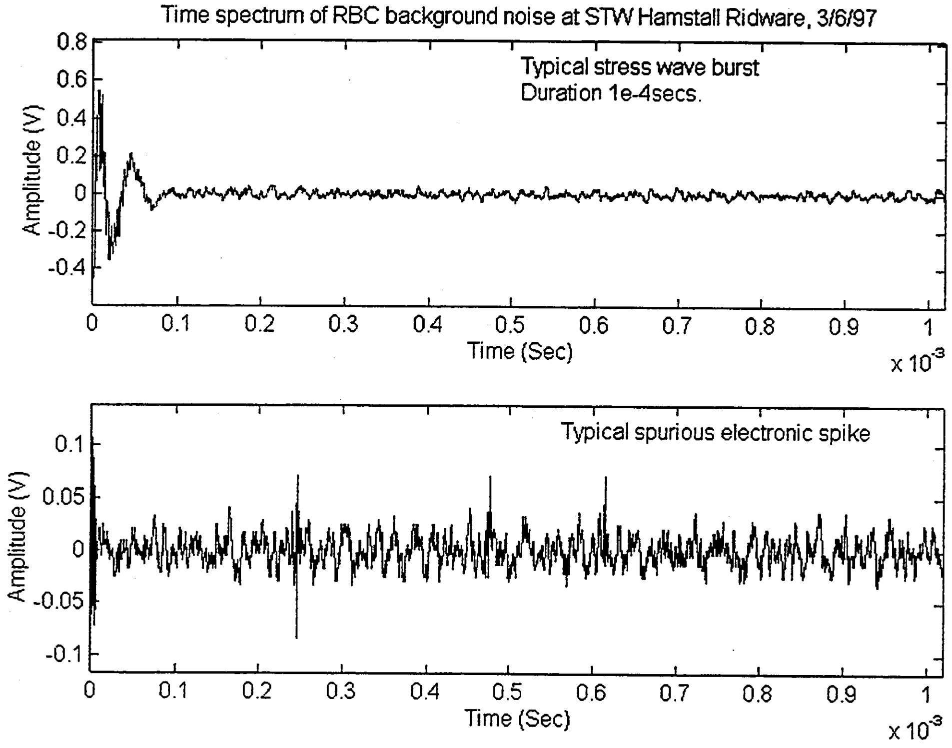

Figure 8.15 Rejected stress wave bursts at STW Hamstall Ridware.

From the classification results shown in figure 8.16, four possible groups emerged. Typical bursts, with corresponding frequency spectra, can be seen in figures 8.17 and 8.18. Again, the duration and pattern of these bursts are consistent with rubbing of mating components. Some data files had several bursts, indicative of the continuous breaking/rubbing of two faces, see figure 8.19.

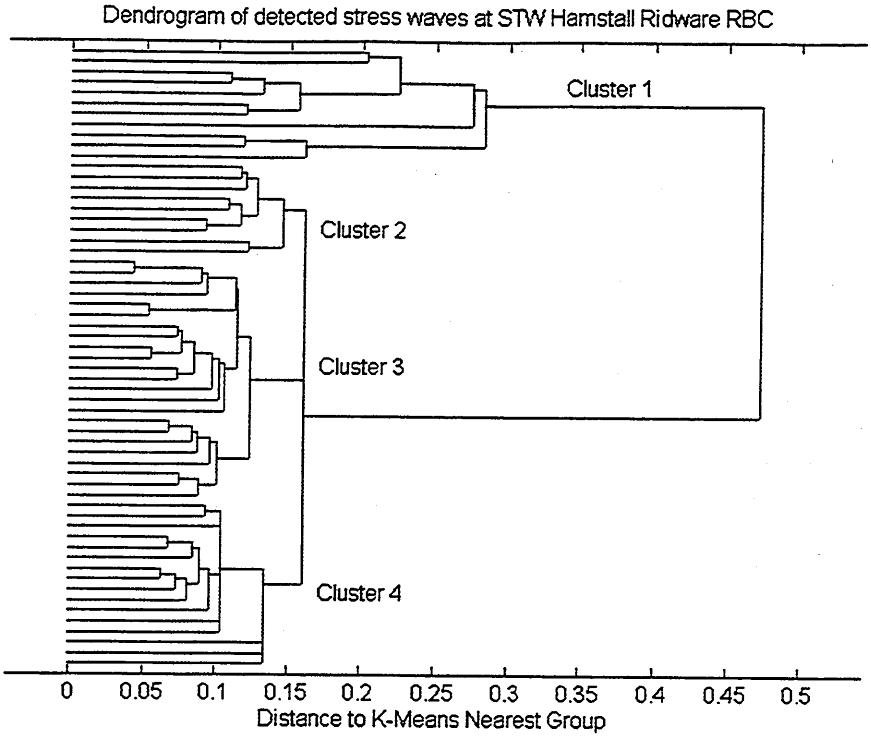

Figure 8.16 Results of classification to stress waves detected at STW 'Hamstall Ridware'

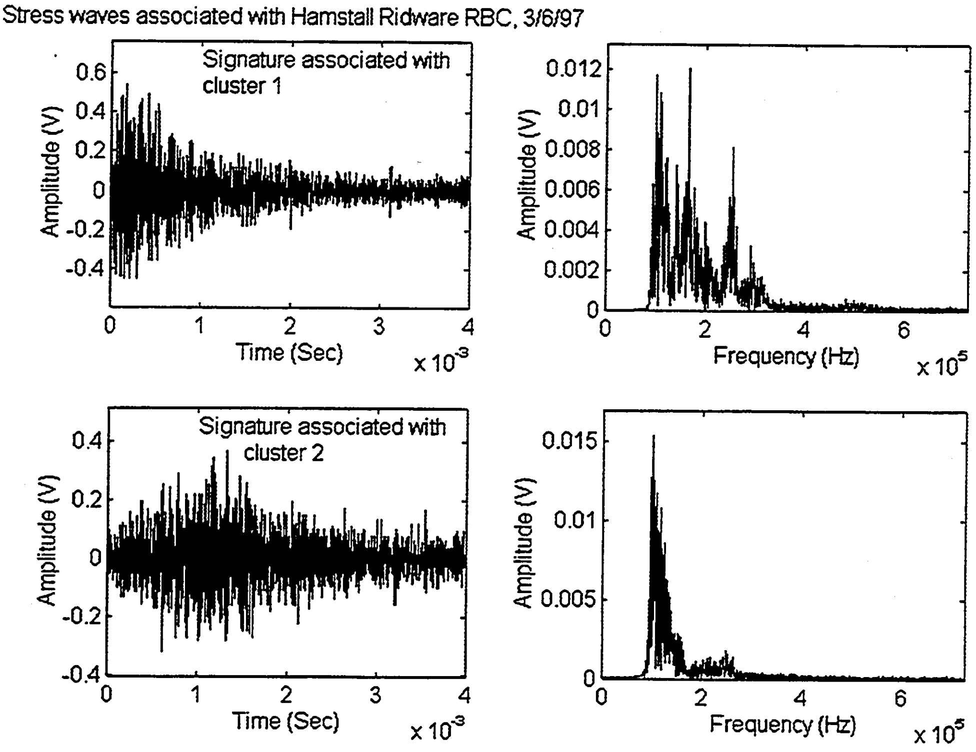

Figure 8.17 Stress waves detected at STW Hamstall Ridware

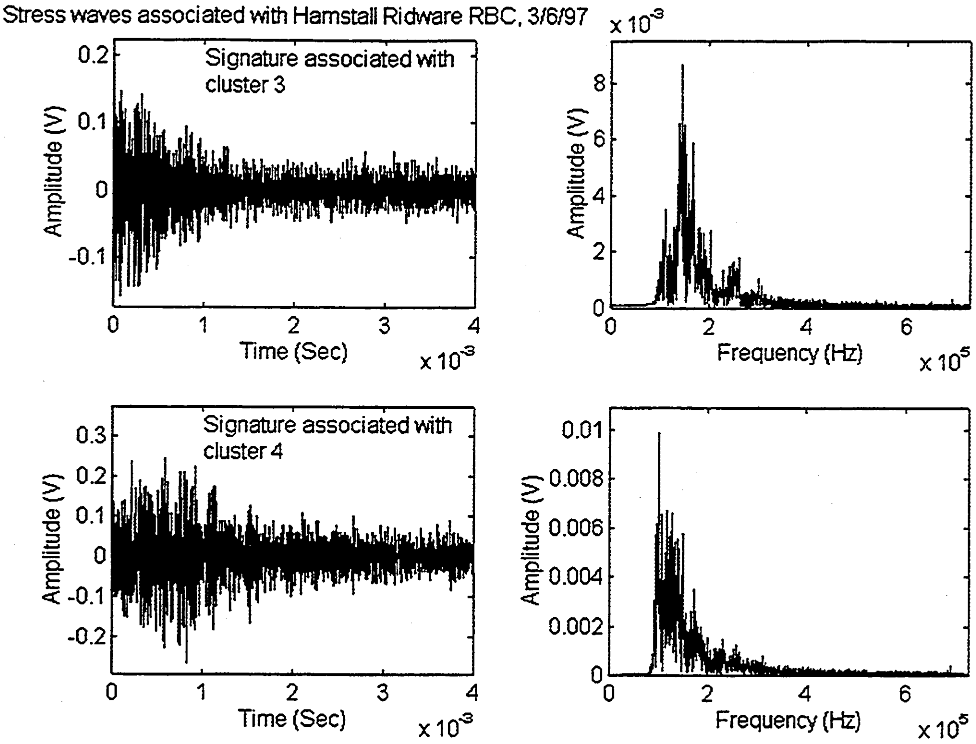

Figure 8.18 Stress waves detected at STW Hamstall Ridware

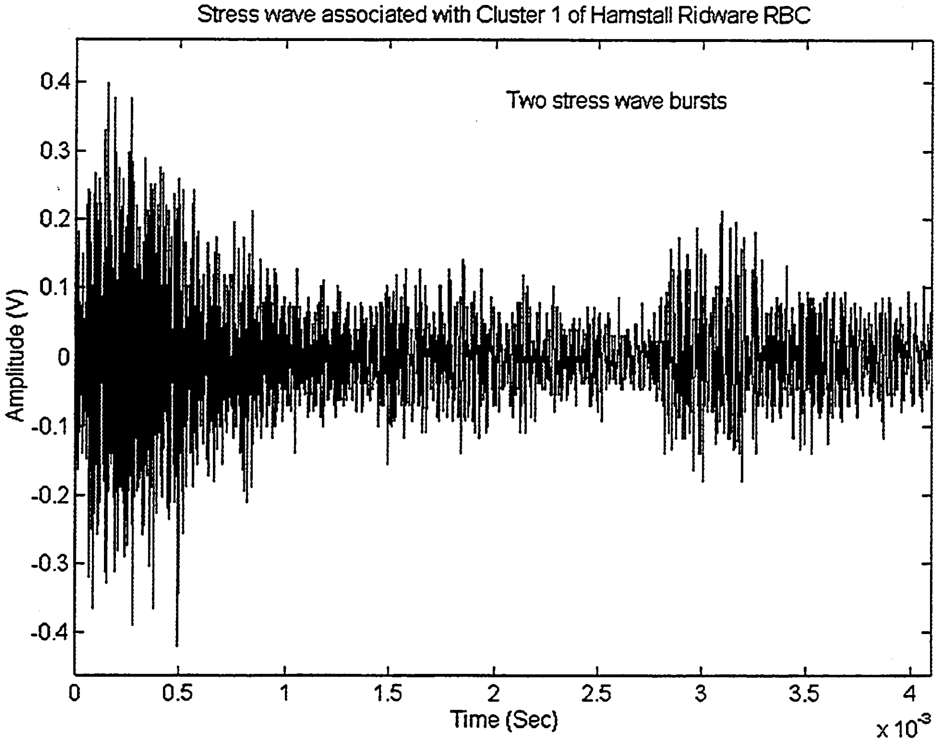

Figure 8.19 Stress wave detected at STW Hamstall Ridware

Based on these results, it was concluded that rubbing between mating components was occurring. The RBC covers were removed and it was observed that a few 'U' bolts were loose, allowing movement of the through-rods against the support structure. Rubbing was also occurring between the 'U' bolts and the through-rods, see photograph 8.7. Whilst it could be assumed that the bursts or cluster groups associated with theses faults can represent two possible emission sources, faults associated with the other two groups were not visually detectable.

Subsequently, on 13/01/98, it emerged that the shaft had moved axially due to a loose tapered locking nut in the bearing. This fault inevitably generates stress wave activity, as the stub shaft, and tapered locking nut, would have been experiencing minute movements at the time of recording. Relative movement between the stub shaft and the bearing inner race, a result of a loose tapered locking nut, will certainly generate stress wave activity.

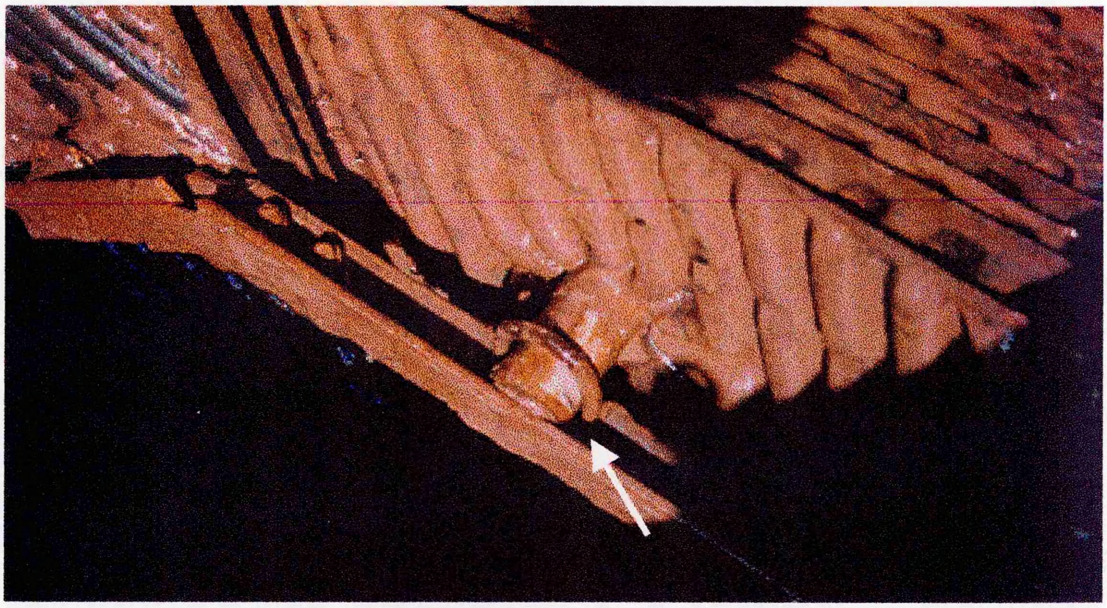

Photograph 8.7 Loose 'U' bolt detected at STW Hamstall Ridware, 3/6/97

8.4.4 STW Defford

RBC : Cambridge 3.0-meter diameter

Date visited : 20/5/97

Classification: 14th order AR model applied to 8192 data points.

Number of data files recorded : One hundred and sixteen data files over three revolutions, thirty-six of which were rejected as spurious electronic spikes or bursts of short duration.

Results of classification, shown in figure 8.20, indicate four possible cluster groups and typical bursts, with corresponding frequency spectra, can be seen in figures 8.21 and 8.22. Whilst there is no clear change of level between clusters 3 and 4, it is evident that two groups are independent.

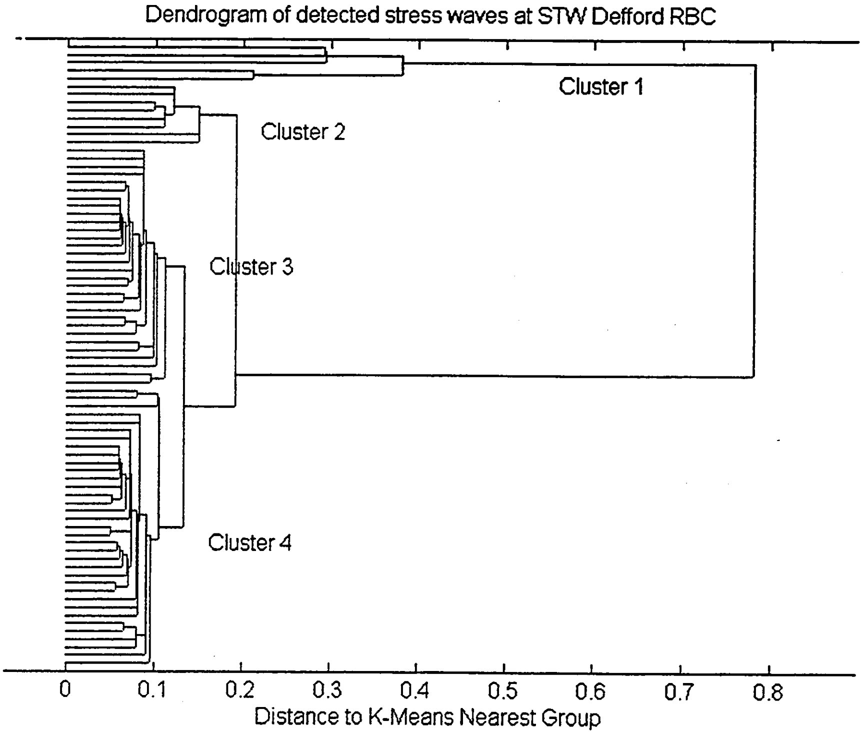

Figure 8.20 Results of classification to stress waves detected at STW 'Defford'

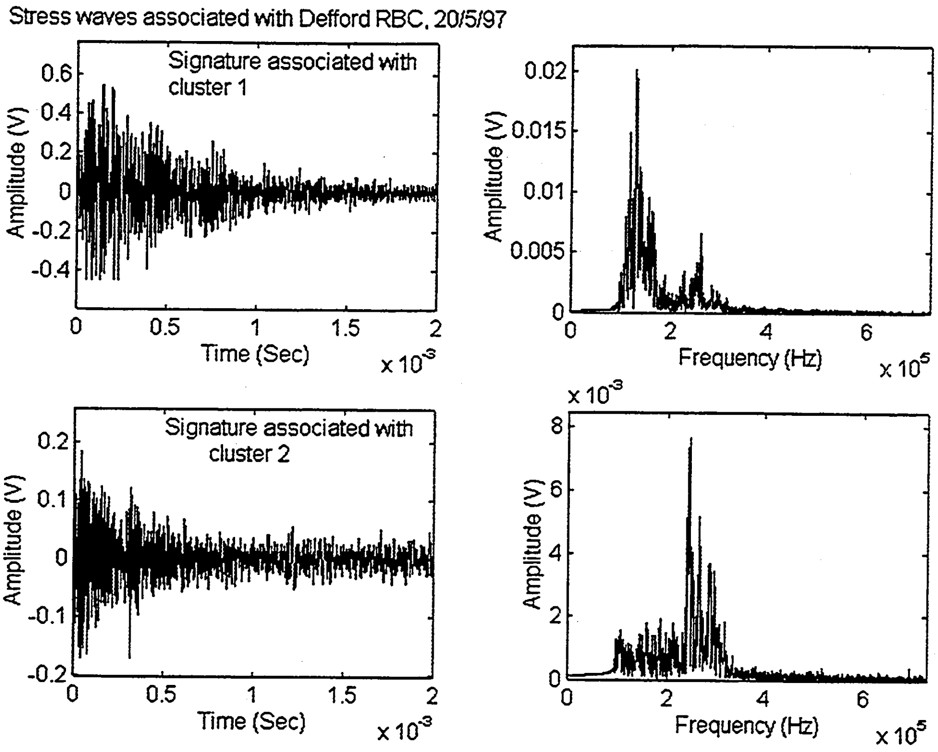
Stress waves associated with Defford RBC, 20/5/97

Figure 8.21 Stress waves detected at STW Defford.

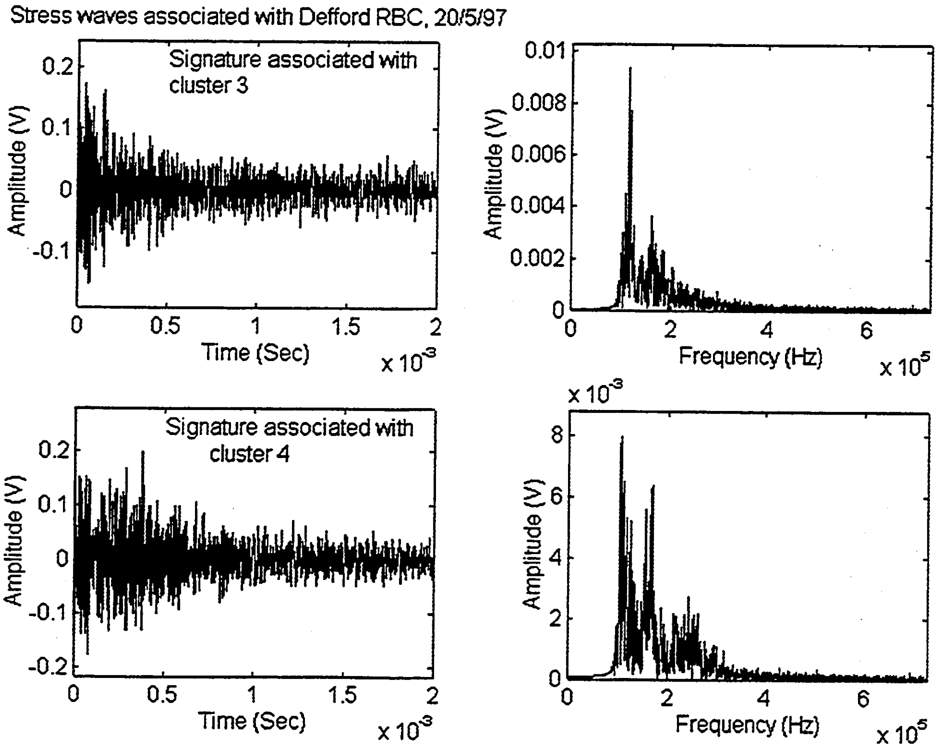
Stress waves associated with Defford RBC, 20/5/97

Figure 8.22 Stress waves detected at STW Defford.

Again it was concluded that rubbing between mating components was occurring. The RBC covers were removed and the following were observed:

i Rubbing between the radial arms and the shaft clamp plate, see photograph 8.8.
ii Rubbing between fractured parts of the outer circumferential rim, see photograph 8.9.
iii Rubbing between fractured parts of the radial arm, see photograph 8.10.
iv Rubbing between the inner through rods and the support structure, a result of fractured 'U' bolts, see photograph 8.10.

It is feasible that cluster groups 3 and 4 are of similar emission source, i.e., deficiencies (i) and (iii), which share similar transmission paths. Other cluster groups could be associated with the other mechanical deficiencies.

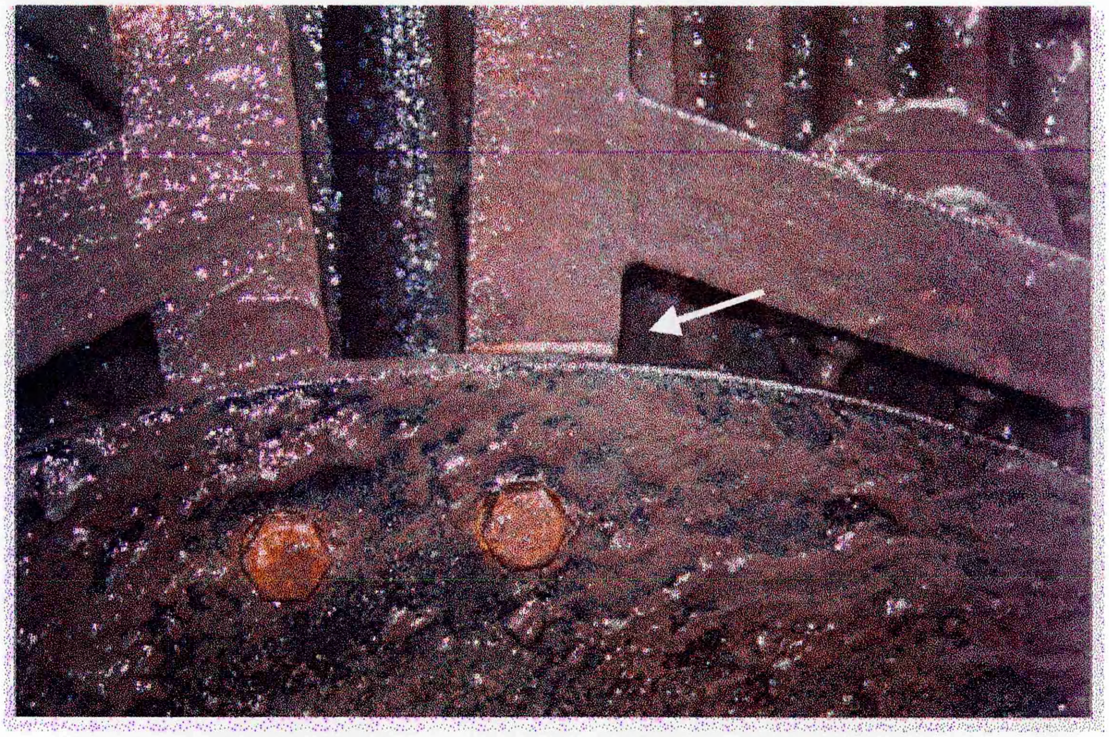

Photograph 8.8 **Movement of the radial arms**

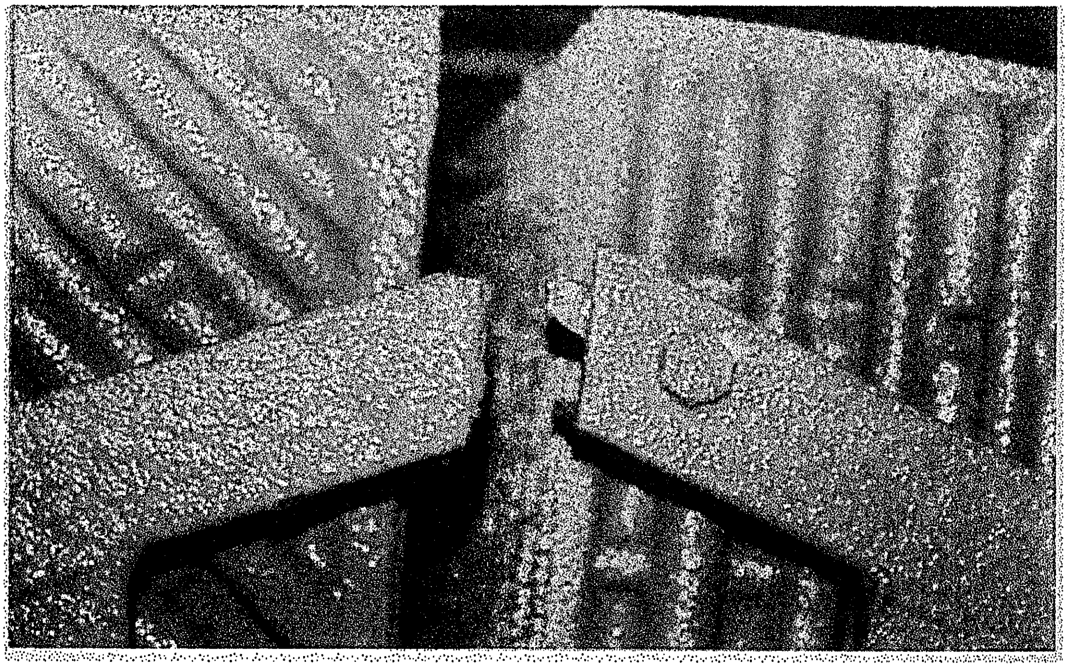

Photograph 8.9 Fractured section of the outer circumferential rim

Photograph 8.10 Fractured radial arm and 'U' bolt

8.4.5 STW Flyford Flavell

RBC : Cambridge 3.0-meter diameter
Date visited : 20/5/97
Classification: 14th order AR model applied to 8192 data points.
Number of data files recorded : Fifty data files were recorded over three revolutions, sampled at 4MHz.

Results of classification, shown in figure 8.23. No group formation, therefore the detected bursts were attributed to background noise. On inspection of the unit, there were no visible mechanical deficiencies. The result of the visual inspection was expected as typical bursts, displayed in figure 8.24, were not of the same complex pattern as stress wave bursts associated with mechanical faults on the test-rig and the previously discussed operational RBCs. Furthermore, two or more bursts were not detected in any single acquisition.

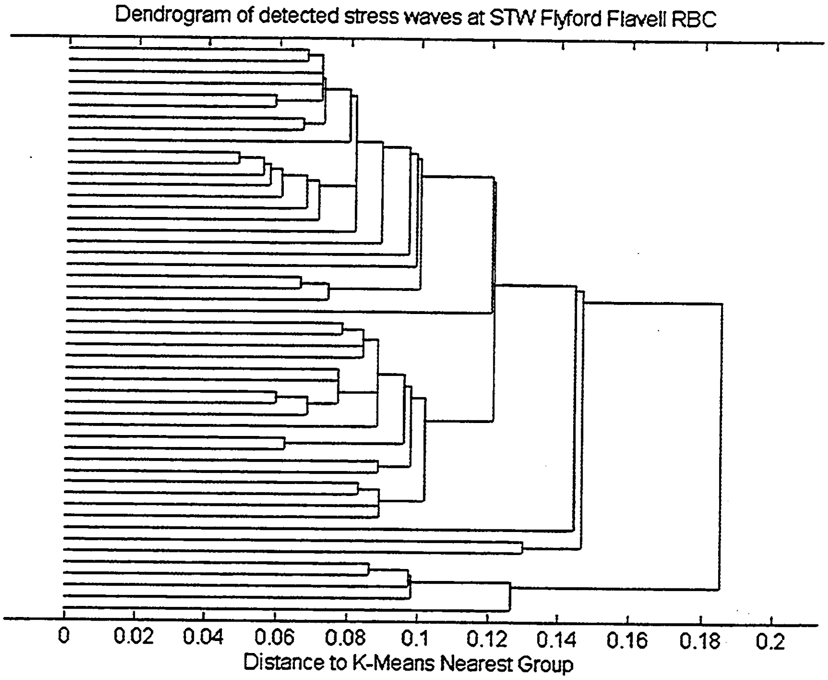

Figure 8.23 Stress waves detected at STW Flyford Flavell

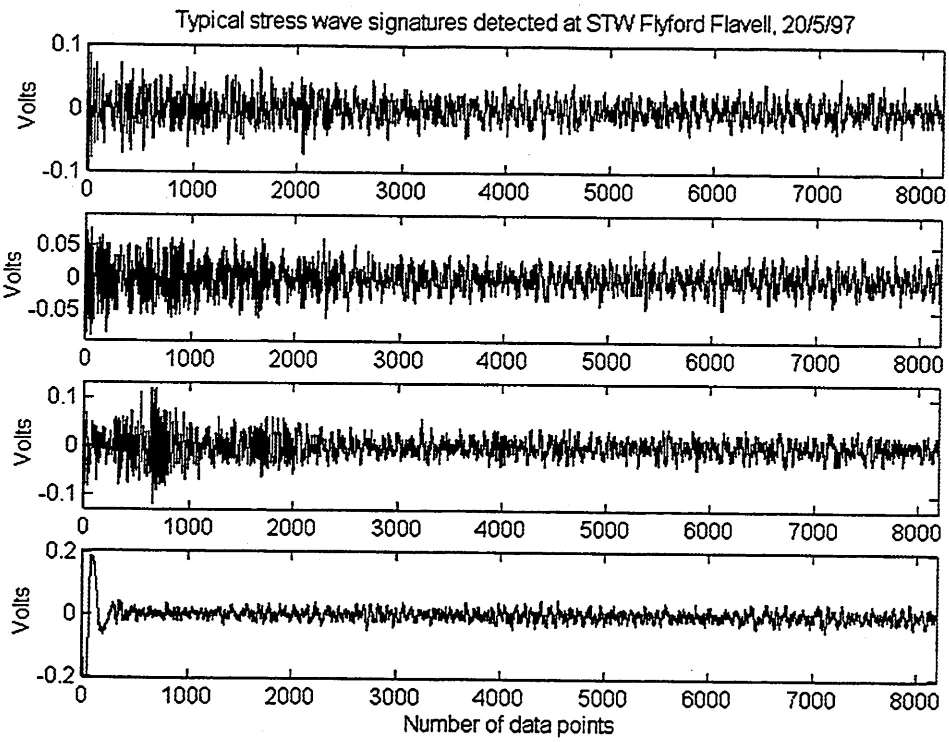

Figure 8.24 Typical stress waves at STW Flyford Flavell

8.5 List of other RBC's monitored with results

Table 8.2

No.	Site	Date visited	RBC manufacturer	Operational since	No. of clusters formed	Other comments
1	Longdon	10/22/96	Klargester	1992	-	No detectable stress wave bursts Inspection revealed no visible mechanical deficiencies
2	Moreton Morrell	6/18/97	Cambridge	1995	-	No detectable stress wave bursts Inspection revealed no visible mechanical deficiencies
3	Honiley	5/1/97	Klargester	1993	-	No detectable stress wave bursts Inspection revealed no visible mechanical deficiencies
4	Beckford	10/17/96	Klargester	1995	-	No detectable stress wave bursts Inspection revealed no visible mechanical deficiencies
5	Rous Lench	5/9/97	Cambridge	1993	-	No detectable stress wave bursts Inspection revealed no visible mechanical deficiencies
6	Flyford Flavell	5/20/97	Cambridge	1995	-	No detectable stress wave bursts Inspection revealed no visible mechanical deficiencies
7	West Felton	5/21/97	Cambridge	1992	-	No detectable stress wave bursts Inspection revealed no visible mechanical deficiencies
8	Condover	10/2/96	Cambridge	1992	4	Inspection revealed fractured 'U' bolts and movement of inner and outer through rods.
9	Ashover	8/21/96	Klargester	1988	4	Inspection revealed damaged bearing
10	Ashford Carbonell	4/22/97	Cambridge	1993	3	Inspection revealed fractured 'U' bolts and movement of inner and outer through rods.

CHAPTER 9

RBC BEARINGS

9.1 Introduction

The conditions of the bearings are vital to maintaining uninterrupted operation of the RBC. There are numerous bearing types available to the engineer, such as ball, cylindrical, spherical, tapered, needle etc., and selection is dependent on the type of application. Numerous textbooks can aid the engineer in selection.

There are several reasons for premature bearing failures [99,100,101] such as sparse lubrication, corrosion, contaminates such as dirt, defective seal, scoring, fatigue spalls, misalignment, excessive looseness, tight fittings, creep, vibration etc. STW have experienced numerous bearing failures on their RBCs resulting in loss of operation. The most severe form of bearing damage will result in scoring of the stub shaft. Under such a condition the stub shaft might be replaced leading to prolonged loss of operation. **This chapter provides evidence of successful application of stress waves to monitoring of low speed bearings, the first of its kind**, and outlines the foundation on which future work might be based. All the data analysed were based on actual operational RBC bearings as no experimental tests were undertaken, therefore, **assumptions reached were derived from a process of elimination.**

9.2 Condition monitoring of bearings

Condition monitoring of bearings has largely been accomplished with vibration analysis and there are many techniques to aid detection of incipient faults in rolling element bearings at medium to high speeds. These include measuring r.m.s. , peak levels, shock pulse monitoring, crest factor and kurtosis analysis, spectrum analysis, envelop spectral analysis and high-frequency resonance analysis. All these established techniques have been widely discussed, and therefore, only a summary is presented in this thesis to acquaint the diagnostician. The high-frequency resonance technique is best suited to vibration monitoring in noisy environments and analysis by enveloping is commonly used for this technique [102]. However, the interpretation of the envelop spectrum is not straight-forward and requires considerable experience for interpretation. For instance, the envelop spectrum could contain a large number of other components, such as harmonics of defect and characteristic frequencies, as well as modulated sidebands of any of these frequencies.

Vibration measurements of bearings are usually collected from the housing. There are three main signature sources [103]: bearing element passing frequencies, resonance of bearing elements and supports, and acoustic emissions.

9.2.1 Bearing element passing frequencies

The main bearing elements, inner race, outer race, rolling elements and cage, each have characteristic rotational frequencies at which vibration energy is produced when the bearing has a defect. The theoretical estimates of these frequencies are given as:

1 Rotating unit Frequency, RF, (RPM/60) Hz
Defect :Un-balance, excessive internal looseness, loose fit between bearing and shaft, etc..

2 Fundamental Train Frequency, FTF, $\frac{RF}{2}\left(1 - \frac{Bd}{Pd}\cos\varnothing\right)$ Hz
Defect : Cage, rollers and /or raceway.

3 Ball Pass Frequency of the Inner race, BPFI, $\frac{RF * Nb}{2}\left(1 + \frac{Bd}{Pd}\cos\varnothing\right)$ Hz
Defect : Inner race

4 Ball Pass Frequency of the Outer race, BPFO, $\frac{RF * Nb}{2}\left(1 - \frac{Bd}{Pd}\cos\varnothing\right)$ Hz
Defect : Outer race

5 Ball Spin Frequency, BSF, $\frac{Pd * RF}{2 * Bd}\left(1 - ((Bd)^2/Pd)\cos^2\varnothing\right)$ Hz

6 Natural Frequency of Bearing
Defect: Inadequate lubrication.

$\varnothing$ = contact angle Nb = number of rollers Bd = roller diameter, Pd = pitch diameter

A disadvantage with the interpretation of bearing element rotational frequencies [104], r.m.s., and peak values is that they are dependent on baseline information. With increasing bearing damage the magnitude of rotational frequencies, r.m.s. and peak values will increase. Furthermore, the measured values of r.m.s., peak and power spectra are dependent on bearing load, speed, housing tightness, quality of lubricant and bearing clearance. It is therefore difficult to define the condition of a bearing from a single measurement except where substantial background information is available, moreover it makes it difficult to relate wear on identical bearings unless the assembly of these bearings can be guaranteed to be exactly the same.

Kurtosis has been shown [103] to assess the extent of bearing damage with minimum recourse to historical information. The kurtosis value for a Gaussian distribution of amplitudes, characteristic of the random noise generated by a new bearing, is 3. Dyer [103] assessed the extent of damage from the distribution of this parameter in selected frequency ranges and observed that early indication of damage was found in the lower frequency range, 3Hz - 5KHz, whilst advanced damage was evident in the higher frequency range, 10KHz to 20KHz. This technique was developed to overcome the drawback with kurtosis, being that the kurtosis value will return to 3 as the damage increases. The Crest Factor, i.e., peak acceleration/r.m.s. acceleration, has also been shown [103,104] to require minimum recourse to historical data.

The above techniques can be applied successfully to medium and high-speed bearings. Due to the known problems associated with low-speed vibration analysis (see chapter 4) monitoring through vibration will be fraught with difficulties. For instance, an RBC manufactured by 'Tuke & Bell' would normally employ a Split Cooper spherical rolling element bearing with a bore diameter of between 90 to 130mm, depending on the size of RBC. The defect frequencies for this type of bearing, at 1 revolution per minute and a bore diameter of 125mm are:

RF = 0.01667 Hz, BPFI = 0.1515 Hz
FTF = 0.0072 Hz, BPFO = 0.1151 Hz

Source : Cooper Rolling Bearings Ltd.

Whilst RBCs manufactured by Klargester or Cambridge would normally have an SKF or FAG self-aligning double spherical roller bearings. The defect frequencies of two types employed on operational RBCs are detailed below (assuming a contact angle of 0^0) :

Type	**22222EK** (Hz)	**23028CC** (Hz)
RF	0.102	0.1675
FTF	0.007	0.0075
BPFI	0.174	0.247
BPFO	0.126	0.203

Source : SKF bearings Ltd., Milton Keynes

The author is not aware of any commercially available sensor, nor data collector/analysis unit, that can measure vibration defects as low as 0.007Hz.

9.2.2 Resonance of bearing elements

An alternative to bearing element frequency analysis is the resonant technique, which involves measurement of bearing component natural frequencies initiated by shock excitation associated with minor structural irregularities. These resonant frequencies are a function of the mass configuration and type of material involved. The frequencies and amplitudes at resonance are much higher than bearing element rotations, so they are ideal under conditions of high background noise. Moreover, the resonant frequencies are independent of rotational speed, however, their amplitudes will vary directly with rotational speed, as will the impact energy.

Resonant frequencies can be as high as 300KHz for ball rollers, and up to 140KHz for the inner race, depending on the mode of vibration [105]. Balderstone [105] suggested that the 'free' resonant frequencies of the individual components were not changed significantly after assembly, though, the assembly created a damping effect. He also suggested that because of the interaction between the components of a bearing, a defect in any component would cause resonant frequency ringing in all components, making interpretation difficult. Moreover, at low rotational speeds the impact energy generated will be very low and this might explain why there have been limited applications of this technique to low-speed bearings.

The principal of the shock pulse meter (SPM) is similar to the resonant technique as both respond to minute transient pressure waves generated from fault impacts in regions of contact though, the SPM resonates itself. Ray [106] investigated the use of the Shock Pulse Meter (SPM) to monitor low-speed bearings (25rpm). He concluded that the SPM failed to register defects at speeds below 750 rpm.

9.2.3 Acoustic emissions

The natural progression from the resonant technique is acoustic emission. A few authors have claimed successful application of AE to the detection of incipient damage in rolling element bearings at low speeds, though, evidence of success has not been conclusive. These have been detailed in chapter 4. The application of stress waves to monitoring low-speed bearings, highlighted in this chapter, is the first of its kind. Moreover, the applicability of source identification makes its use even more attractive.

9.3 'On-site' measurements of stress waves from operational RBC bearings

It was important that possible sources of stress wave generation were identified before 'on-site' measurements were taken. These could be caused by mechanical rubbing between :

i a loose inner raceway and the stub shaft.
ii the rollers and the inner race.
iii the rollers and the outer race.
iv a loose outer race and the bearing housing.
v the cage and the rollers
vi the 'swivel cartridge' and the housing, applicable to Split Cooper bearings.

Stress wave emissions from any of these sources should contain certain characteristics to aid classification.

9.3.1 Position of sensor

Due to the internal configuration of most roller bearings, internal radial clearance values will vary for different applications, classification and size of bearing. Under these conditions it is possible to place a sensor on the bearing housing where **no** contact exists between the rolling elements and the outer ring, i.e., at 180^0 from the load zone, resulting in poor transmission from the source of the fault to the receiving transducer. Thus, the sensor should be placed near to the load zone, i.e., on the bottom of the housing. There are two bearing housing configurations used on all RBCs, and in both types the sensor was positioned, as shown in photographs 9.1 and 9.2, on the bottom of the housing.

Photograph 9.1 Split Cooper housing

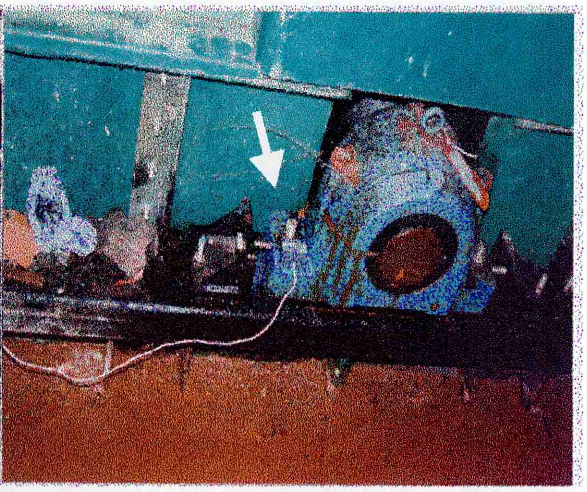

Photograph 9.2 SKF housing

9.3.2 Background noise

Before attempting to monitor RBC bearings, it was thought prudent to take background noise recordings, thereby allowing for development of software to eliminate these unwanted data. Three bearings were earmarked, two manufactured by SKF and the third a Split Cooper bearing. The SKF bearings had been in operation for less than 24 months, while the Split Cooper had been operational for approximately 40 months. It was thought that these bearings would be free of any deficiencies at this stage of their operational life. Furthermore, because of the high attenuation across the bearing, at least 30dB in terms of amplitude, any background noise from the RBC would be severely attenuated. Typical background signatures and corresponding frequency spectra can be seen in figures 9.1 and 9.2.

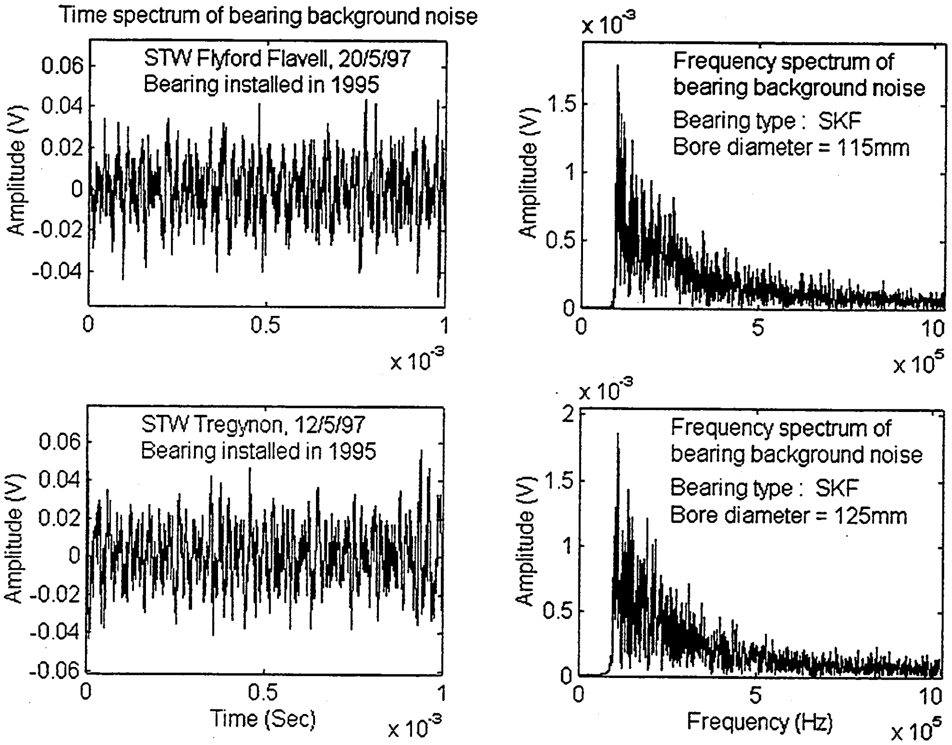

Figure 9.1 **Background noise of SKF bearings**

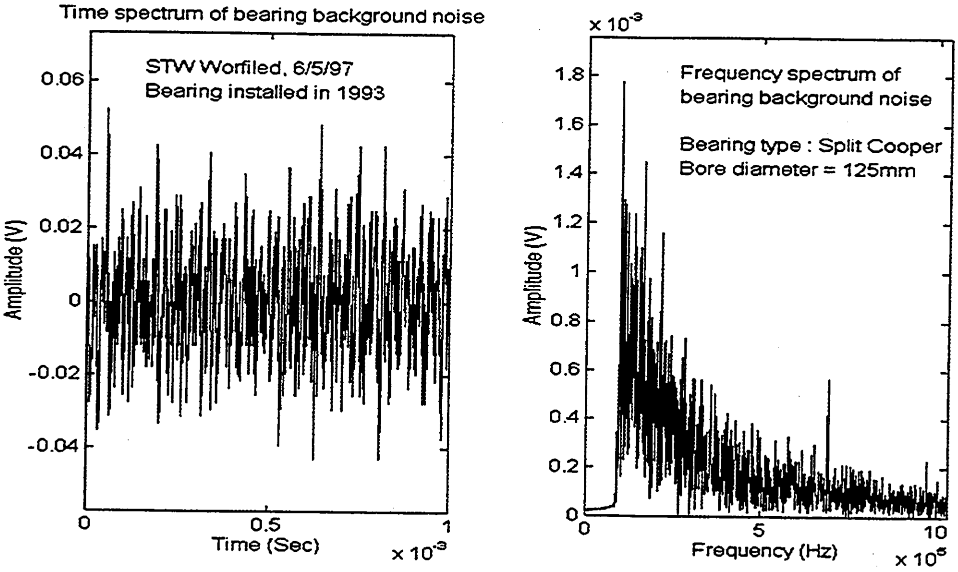

Figure 9.2 **Background noise of Split Cooper bearing**

Over several revolutions no stress wave bursts were detectable at these three sites. At a gain of 60dB the amplitude of the continuous waves detected at these sites was comparable to the electronic noise of the recording system. Therefore, for all subsequent site recordings, a trigger level of 75mV was set. This level was above the background noise.

It was not surprising that stress waves were not detected on the above-mentioned bearings. In a new and well-lubricated bearing there should not exist any metal-to-metal contact resulting in appreciable wear on the bearing components. Application of the developed classification algorithm to the background signatures at STW Tregynon showed no changes in level, indicating that the data had no group structure, see figure 9.3. Classification was applied to 47 data files captured at various positions within one revolution. The same classification trend was noted at STW Flydord Flavell and Worfield.

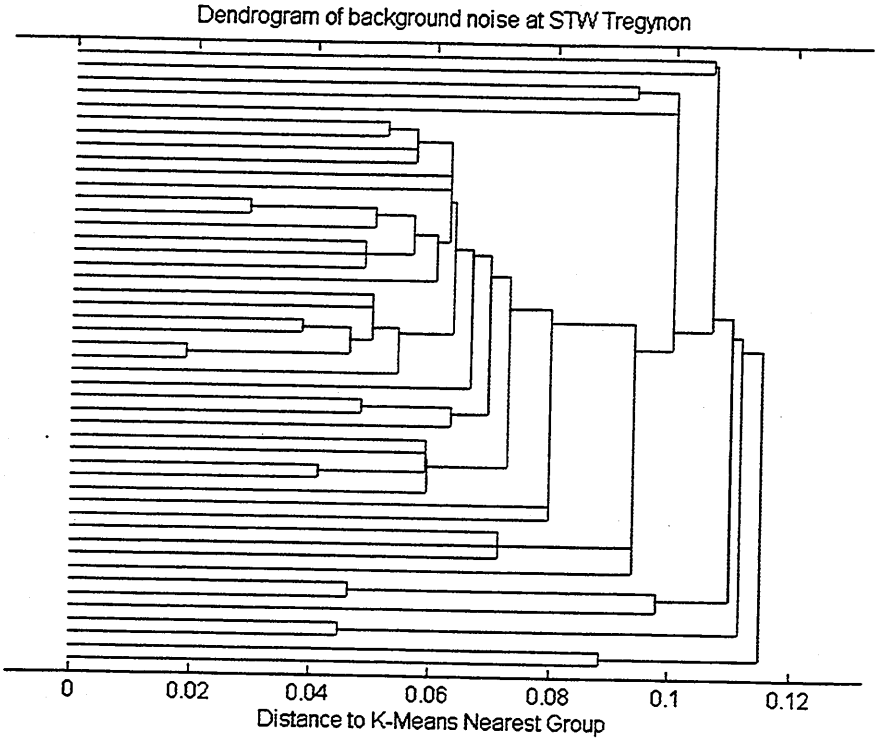

Figure 9.3 **Dendogram of background noise at STW Tregynon**

9.4 'On-site' bearing fault detection

This section highlights some of the successful applications of stress waves to the monitoring of bearings within the Severn Trent Water region. Table 9.1 in section 9.5 details other successful investigations.

9.4.1 STW Willoughby

Three RBCs manufactured by Bi-Water were operational at this site and used SKF double roller bearings, with a bore diameter of 120mm. Because of the restricted access to the bearings, only the drive end bearings were monitored, i.e., the bearings at the highly loaded end of the RBC. For the same reason, the sensor could only be placed on the top half of the bearing housing, see photographs 9.3 and 9.4. The sensor could not be rested squarely on the top housing owing to its curved structure, though it was held firmly.

Photograph 9.3 Willoughby RBC

Photograph 9.4 Placement of sensor

Three bearings on different RBCs were monitored . There were no detectable stress wave bursts on two of the bearings, but stress wave bursts were detected on the third bearing. A total of 40 bursts were detected over three revolutions, nineteen of which were rejected as the acquisition system was triggered by spurious electronic spikes, as shown in figure 9.4. It was interesting to not that a majority of stress waves detected were generated at a particular position during rotation.

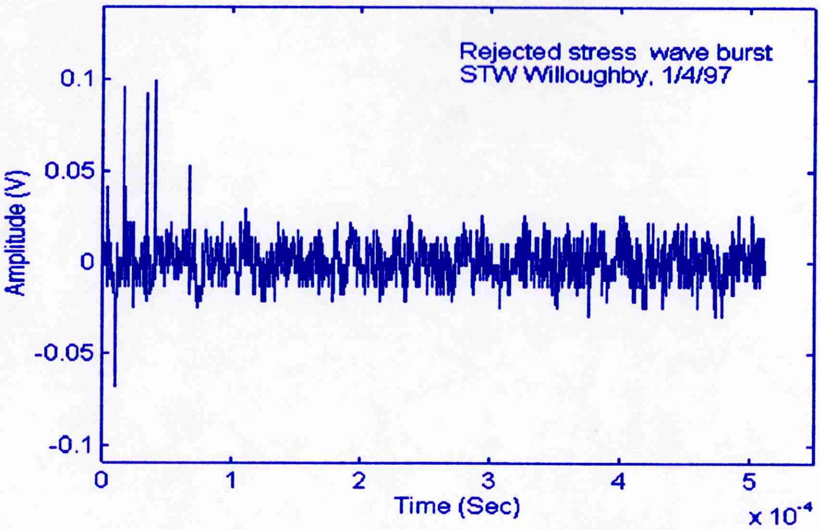

Figure 9.4 Typical signature of rejected stress wave bursts

The classification algorithm was applied to bursts thought to contain information describing the fault condition, the results are shown in figure 9.5. Classification was based on a 9th order AR model applied to 2048 data points. Four cluster groups were observed, indicating clearly that the stress waves could have been emitted from four different sources. Each group had a distinct stress wave signature.

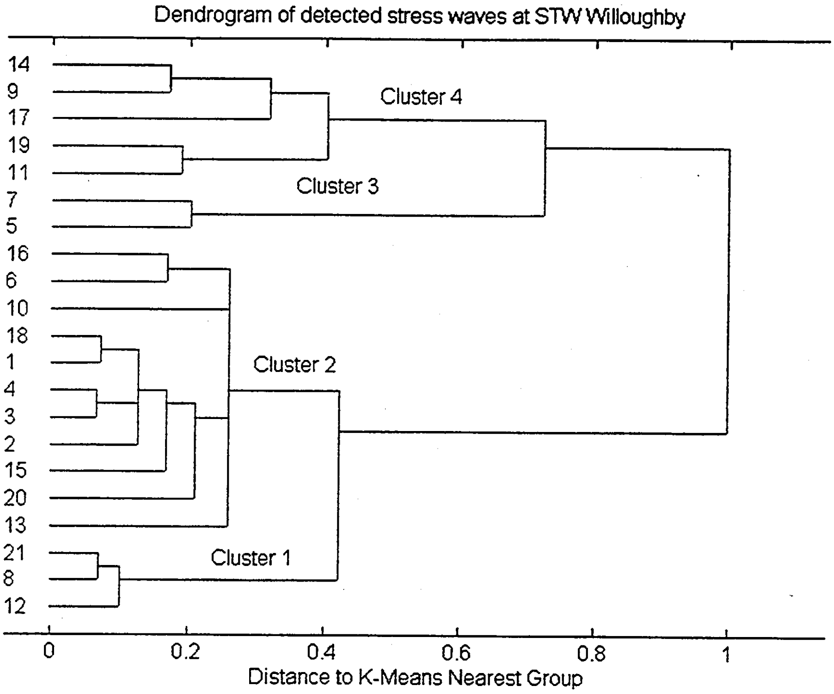

Figure 9.5 Classification of stress waves at STW Willoughby, 1/4/97

Typical signatures of these cluster groups, with corresponding frequency spectra, are shown in figure 9.6 and 9.7.

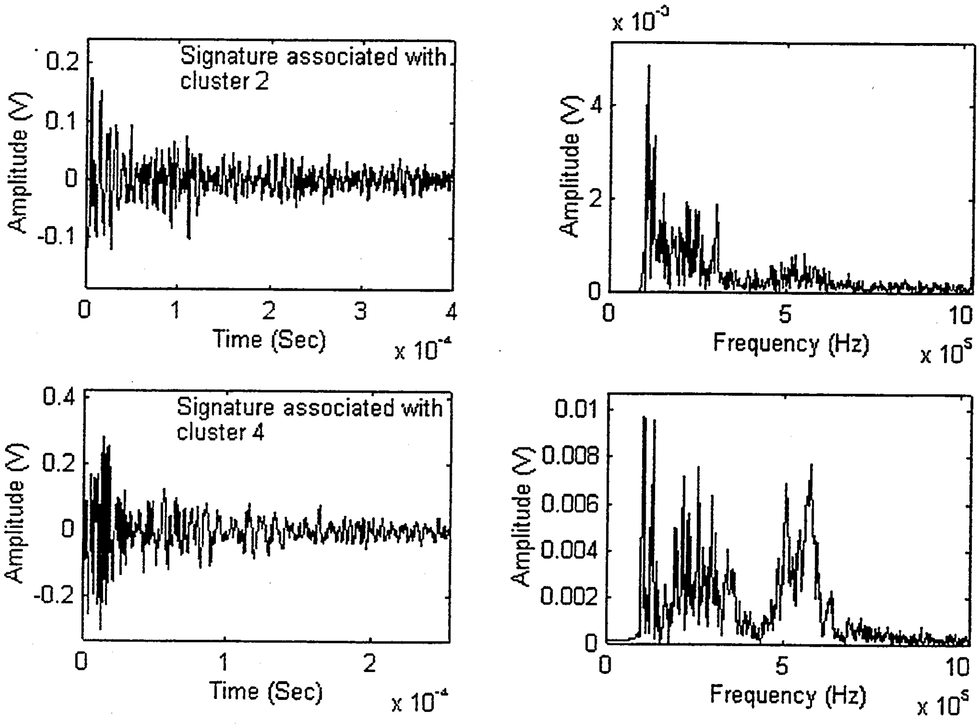

Figure 9.6 Stress waves detected at STW Willoughby.

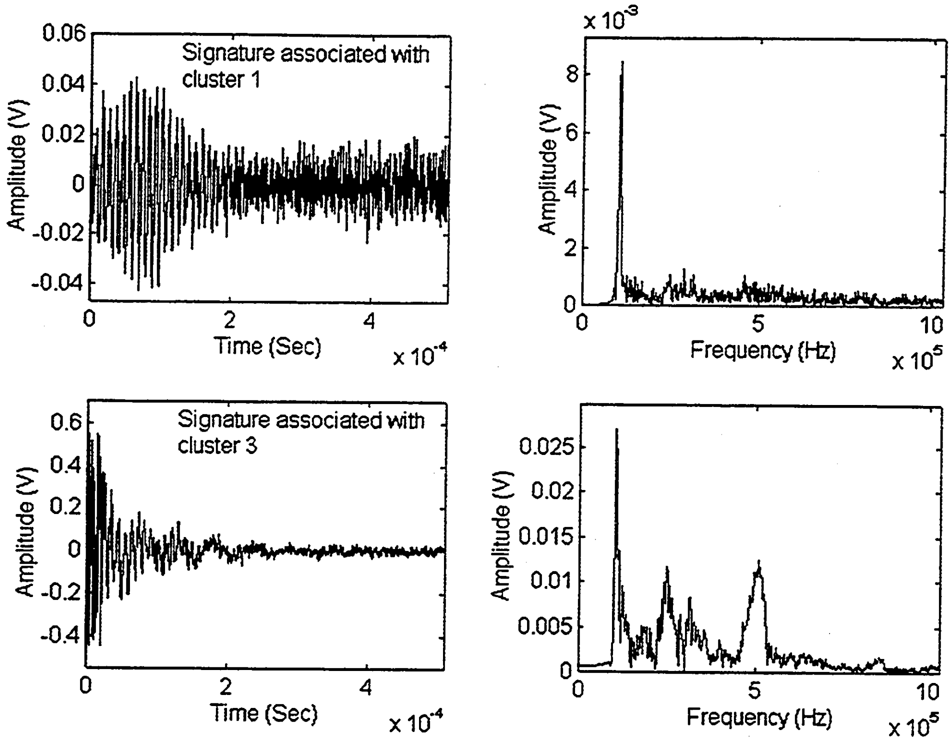

Figure 9.7 Stress waves detected at STW Willoughby.

Based on these results, STW were informed of a potential bearing deficiency. On the 2/4/97, a team of STW engineers removed the top housing of the suspect bearing for further inspection and the following were observed :

i Water had contaminated the lubricant, so there was a high probability that an elastohydrodyamic film did not exist between the rollers and races. This would result in metal-to-metal contact.

ii Close inspection of the grease revealed metal fragments, which would appear to be part of the cage. This is highlighted in photographs 9.5 and 9.6.

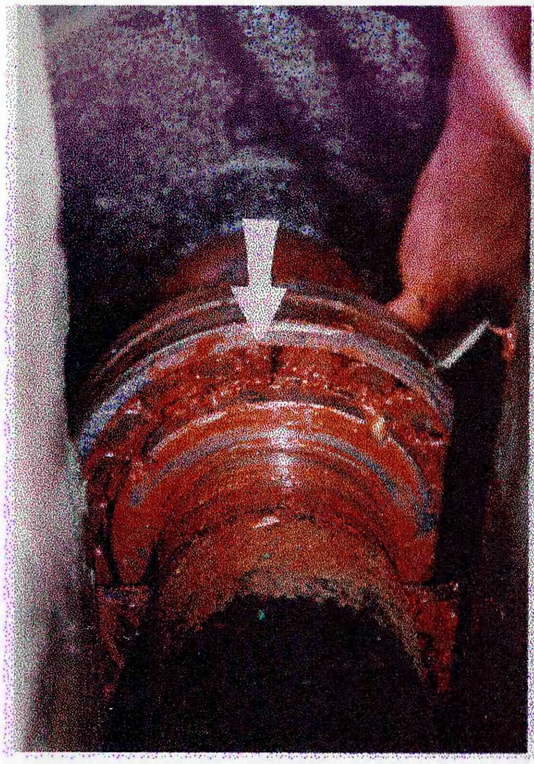

Photograph 9.5 **Excessive gap between rollers**

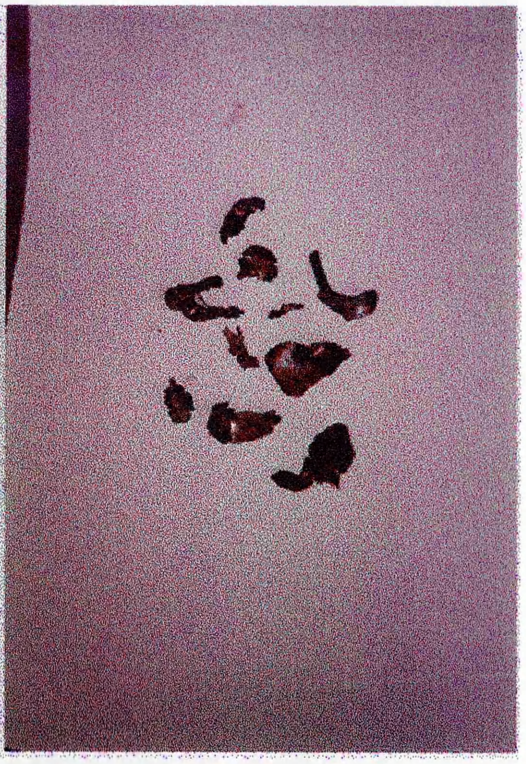

Photograph 9.6 **Cage fragments**

The arrow on figure 9.12 shows the excessive gap between two adjacent rollers, confirming cage fracture. It is highly probable that the stress waves detected were emitted from :

i roller/roller contact due to the fractured separation cage.
ii trapped cage fragments between the inner race and the rollers.
iii trapped cage fragments between the outer race and the rollers.
iv skidding of the rollers against the raceways due to an ineffective elastohydrodynamic film.

9.4.2 STW Stiperstone

The RBC at Stiperstone was manufactured by Tuke & Bell and used Split Cooper roller bearings, with a bore diameter of 125mm. The bearing at the highly loaded end was monitored and a total of 56 bursts were detected over two revolutions. The classification algorithm was applied to the bursts and the results are displayed in figure 9.8. Classification was based on a 9th order AR model applied to 2048 data points.

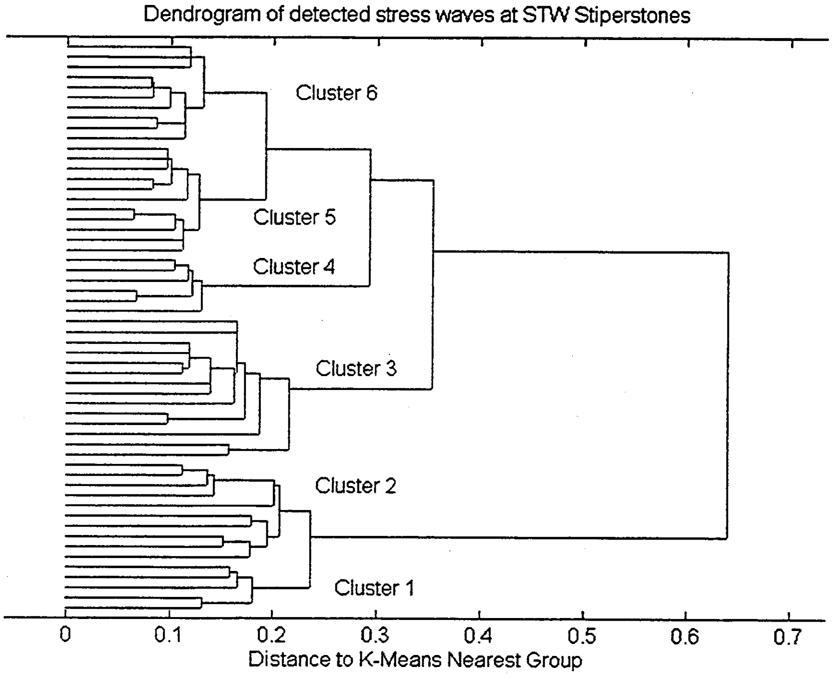

Figure 9.8 Classification of stress waves at STW Stiperstone, 18/8/97

Six clusters could clearly be identified and typical signatures of these cluster groups, with corresponding frequency spectra, are shown in figures 9.9, 9.10 and 9.11.

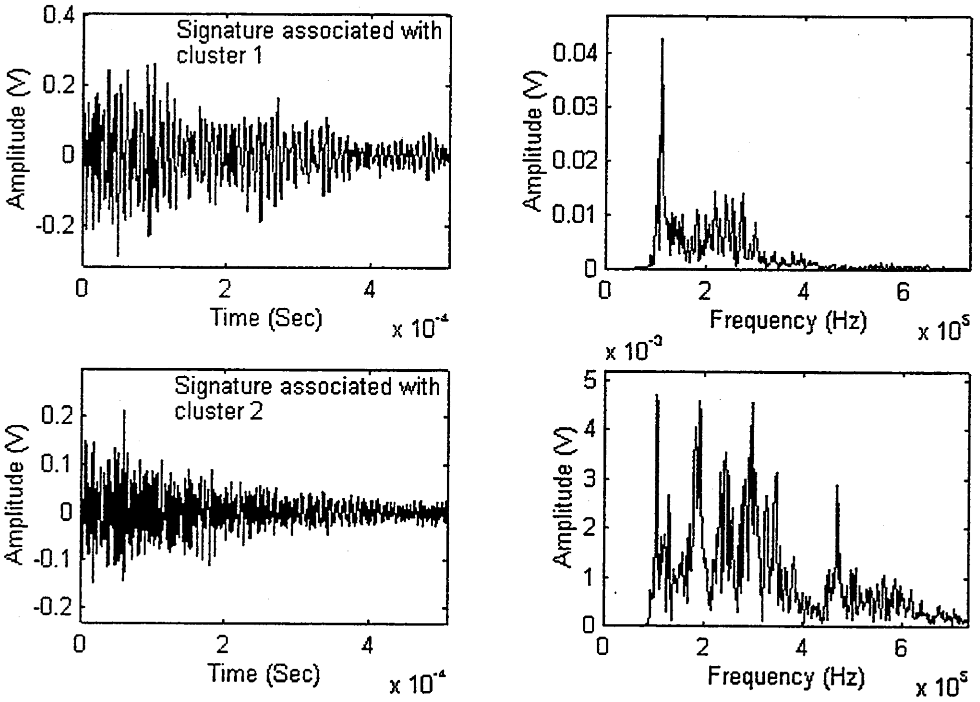

Figure 9.9 Stress waves detected at STW Stiperstone

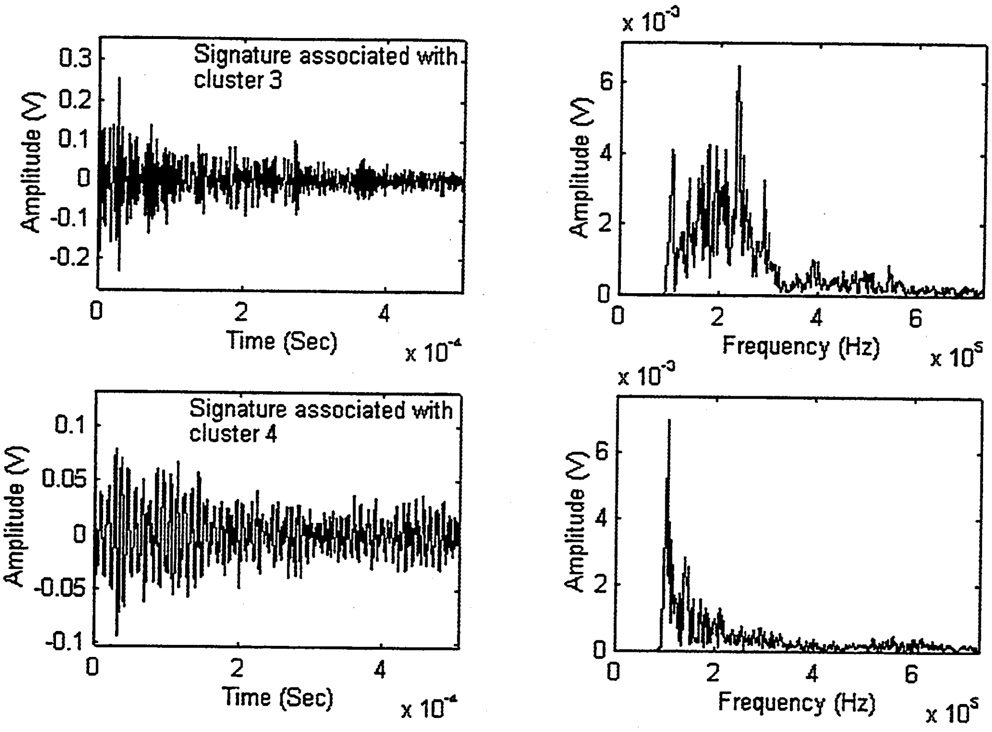

Figure 9.10 Stress waves detected at STW Stiperstone

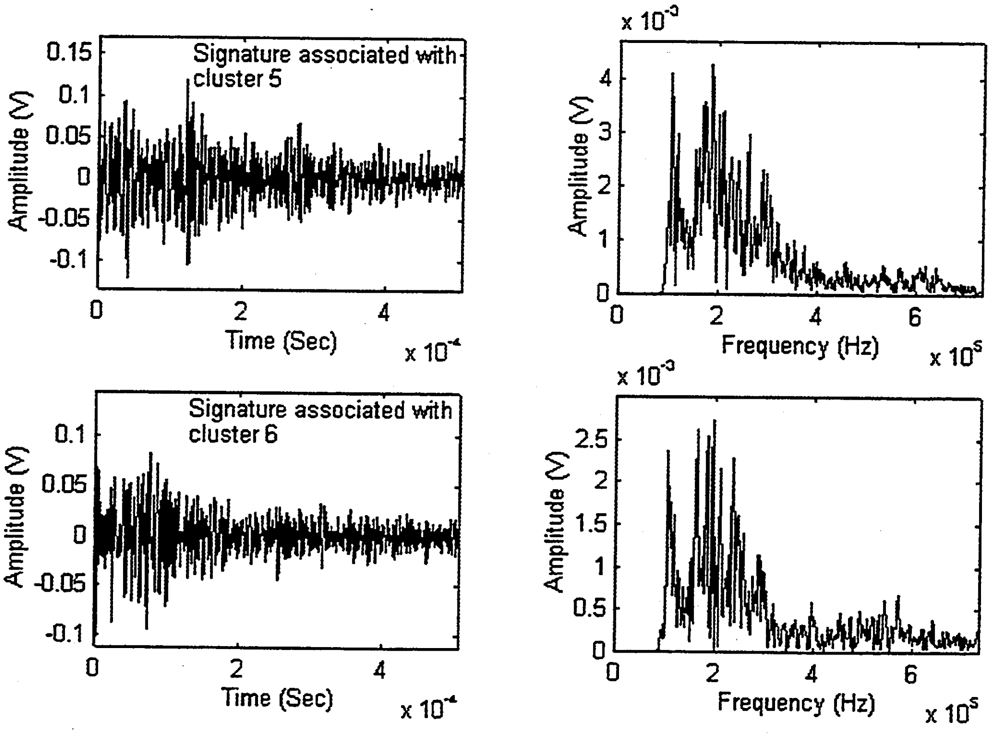

Figure 9.11 Stress waves detected at STW Stiperstone

Based on these findings STW were informed of a potential bearing deficiency. On the 25/8/97, a team of STW engineers split the bearing for further inspection. On inspection the following were observed :

i The stub shaft was scored as the weight of the RBC unit was been supported by the bearing housing, see photograph 9.7.

ii Part of the cage had fractured, see photograph 9.8.

iii The rollers were severely worn, probably as a result of skidding due to inadequate lubrication, see photograph 9.9.

It is highly probable that the stress waves detected were emitted from :

i Rubbing between the stub shaft and the bearing housing causing the breaking of surface asperities on the stub shaft and the bearing housing.

ii Rubbing between the inner race and the damaged rollers.

iii Contact between worn metal fragments and rotating parts of the bearing.

Further investigations showed that a few signatures held in clusters 3 and 5 contained two bursts, see figure 9.12. This is thought to be related to the continuous breaking of surface asperities that will be synonymous with the continuous rubbing between the stub shaft and the housing, and also, as a result of the skidding of the rollers. It may be concluded that clusters 3 and 5 are related to these sources.

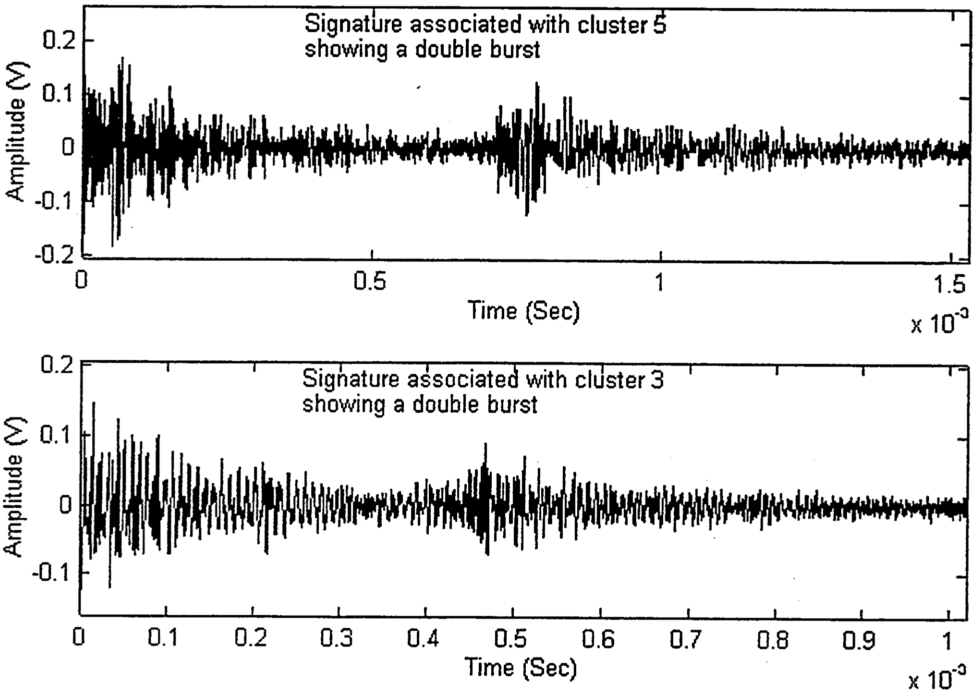
Signature associated with cluster 5 showing a double burst

Signature associated with cluster 3 showing a double burst

Figure 9.12 Stress waves detected at STW Stiperstone

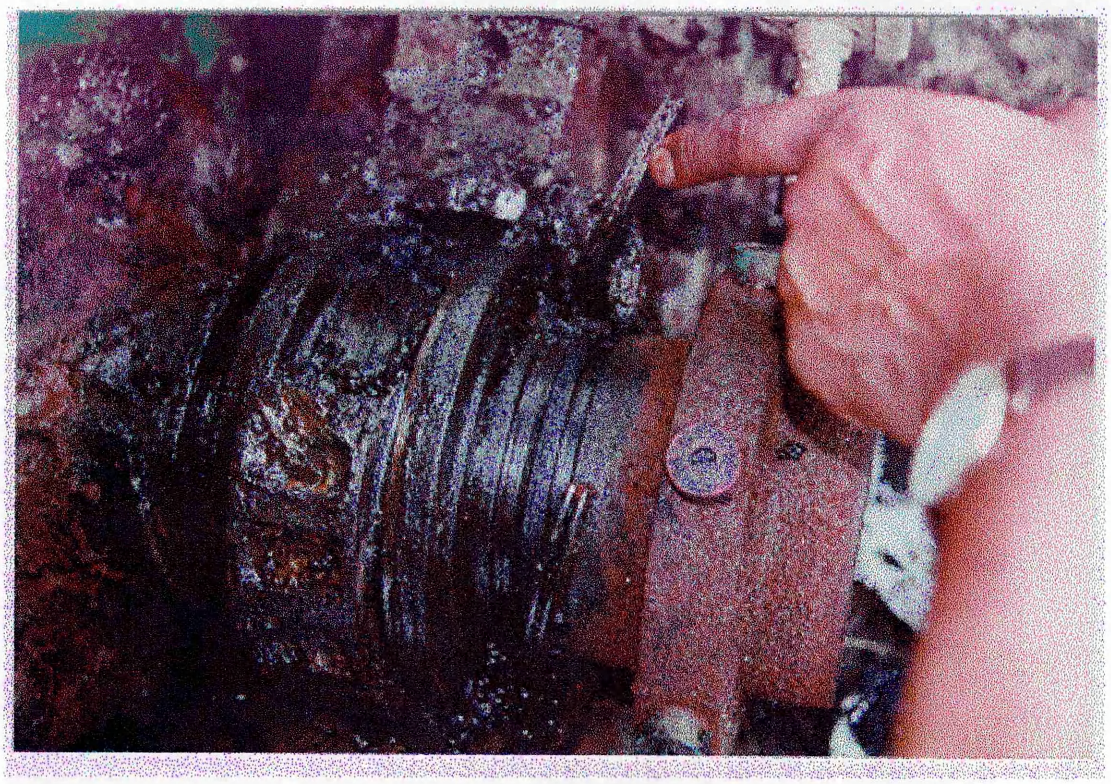

Photograph 9.7 Scored stub shaft

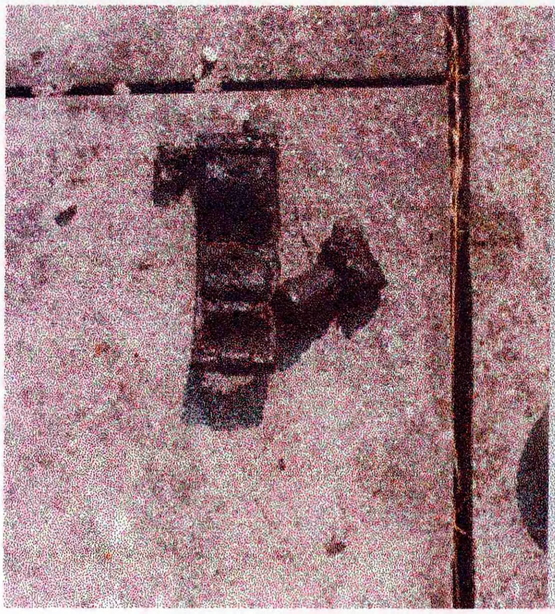

Photograph 9.8 Part of fractured cage

Photograph 9.9 Severely worn roller

9.4.3 STW Ashover

The RBCs at Ashover were manufactured by Klargester and used SKF roller bearings, with a bore diameter of 110mm. Two of the four bearings monitored produced a considerable amount of stress wave activity: for instance, seventy-seven data files were recorded over one revolution for the drive end bearing. Classification analysis of these bursts are shown in figure 9.13 based on a 14th order AR model applied to 8192 data points.

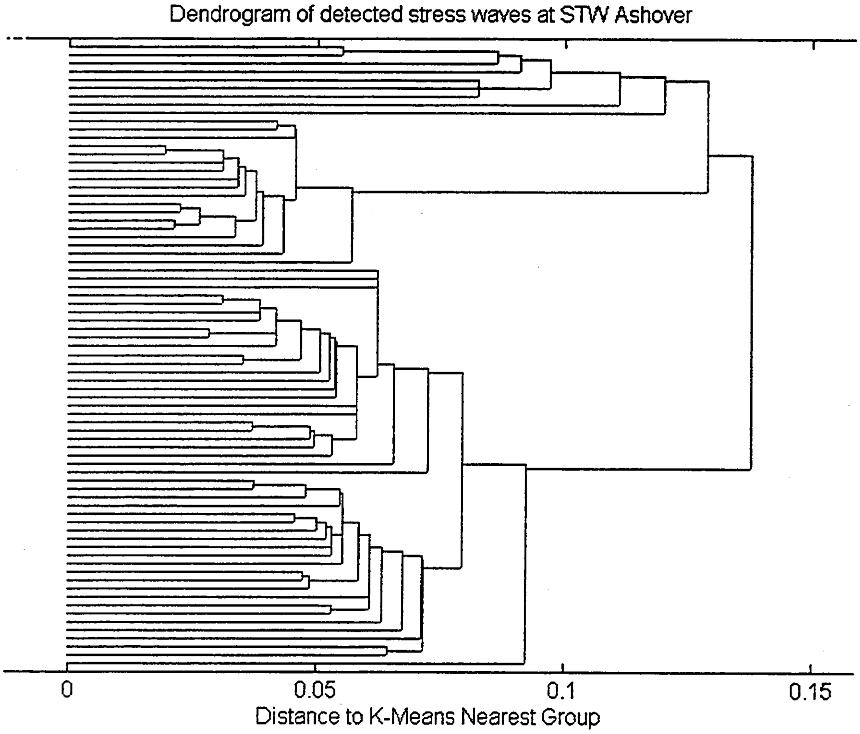

Figure 9.13 Classification of stress waves at STW Ashover, 16/10/97

Whilst it was observed that no cluster or group patterns emerged, the signatures detected were unique. The time domain signature of bearing-one (drive end), shown in the top of figure 9.14, was probably caused by the resonance of a component of the bearing and/or the stub shaft. The strength of this signature was such that it overcame the high-pass filtering built into the pre-amplifier. It was therefore thought prudent to undertake further investigations. Signals were band-pass filtered between 100KHz and 1000KHz using an Elliptical filter. A typical time signature after filtering is shown in figure 9.14. The classification algorithm was applied to the filtered data and the classification results are shown in figure 9.15.

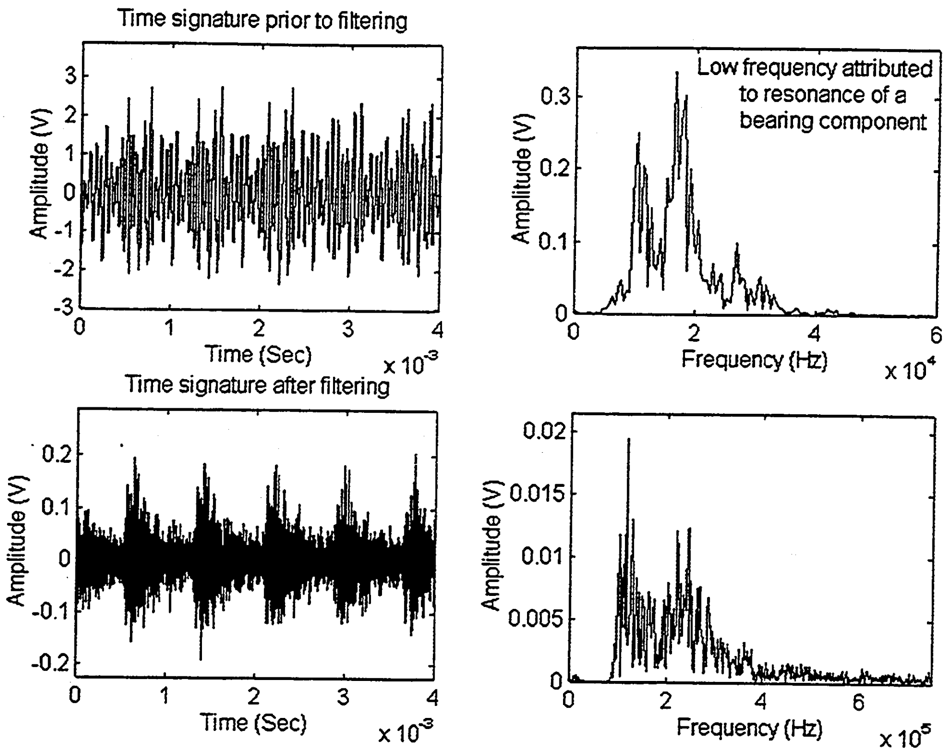

Figure 9.14 Typical stress waves at STW Ashover, before and after filtering

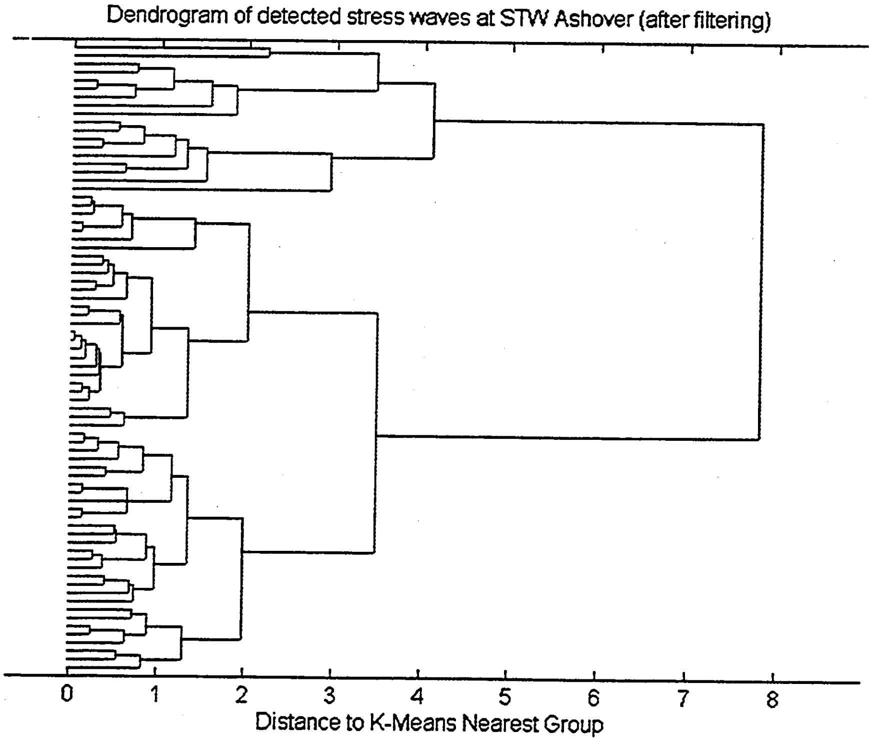

Figure 9.15 Classification of stress waves at STW Ashover, after filtering

The results shown in figure 9.15 indicate that there are three or four sources of stress wave emission. Moreover, the typical time signature, shown in figure 9.14, had a multiple of bursts within a short span and was probably due to the breaking of surface asperities during a sliding/rubbing motion. This indicated a severe form of rubbing, consequently STW was informed of a defective bearing and investigations revealed that the rollers were badly worn, moreover, the stub shaft was severely scored. This failure mechanism is very similar to that highlighted at STW Stiperstone.

The bearing at the non-drive end of the RBC which was eight meters from the drive end, was also monitored. The measured time signature was also similar to that detected at the drive end bearing, but at a magnitude of 20dB less. This would suggest that the signatures at bearing-two were generated from the defective bearing at the drive end. The main source of stress wave emission was attributed to the rubbing between the stub shaft and the bearing housing. The reduction in magnitude of the time signature can be attributed to attenuation.

9.4.4 STW Snailbeach

This Tuke & Bell RBC used Split Cooper roller bearings with a bore diameter of 125mm. The classification algorithm was applied to stress wave bursts at the non-drive end bearing for a time period equal to four revolutions of the rotor. Results of the classification are shown in figure 9.16. Classification was based on a 9th order AR model applied to 2048 data points.

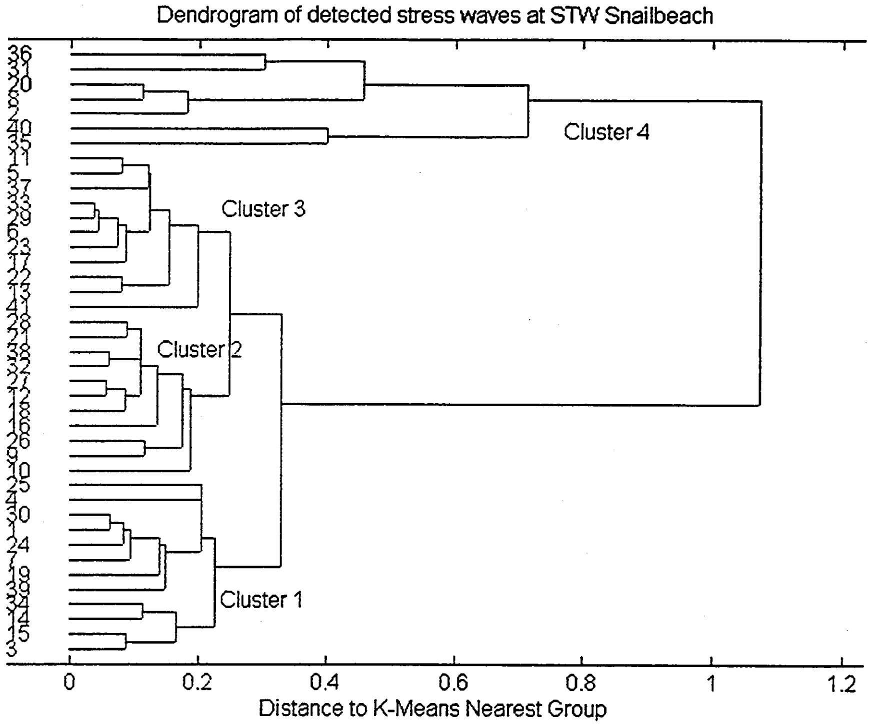

Figure 9.16 Classification of stress waves at STW Snailbeach, 18/8/97

Four groups emerged and typical signatures, with corresponding frequency spectra, are shown in figure 9.17 and 9.18.

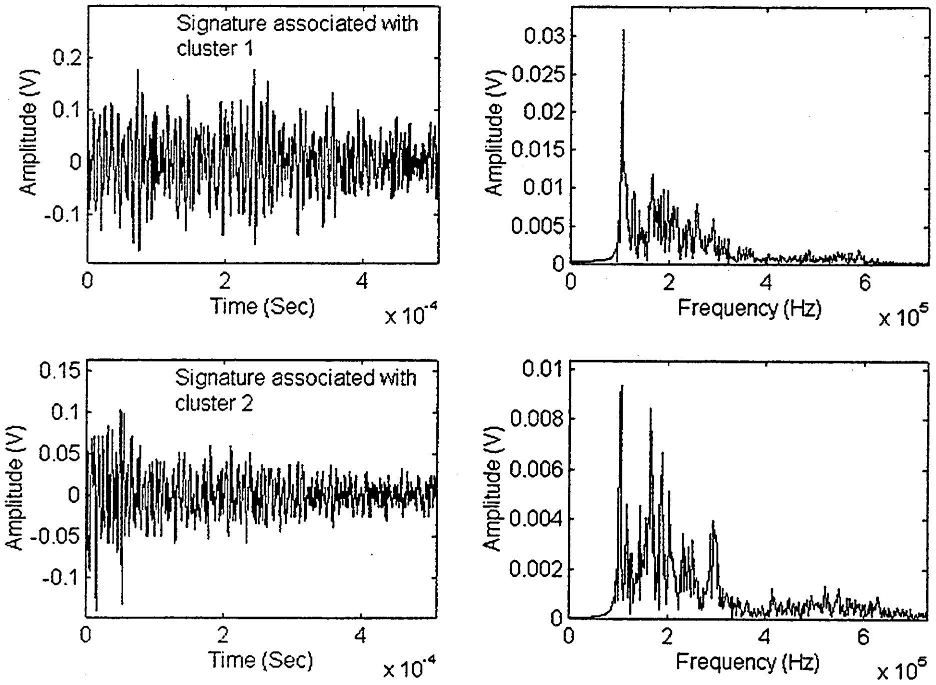

Figure 9.17 Stress waves detected at STW Snailbeach

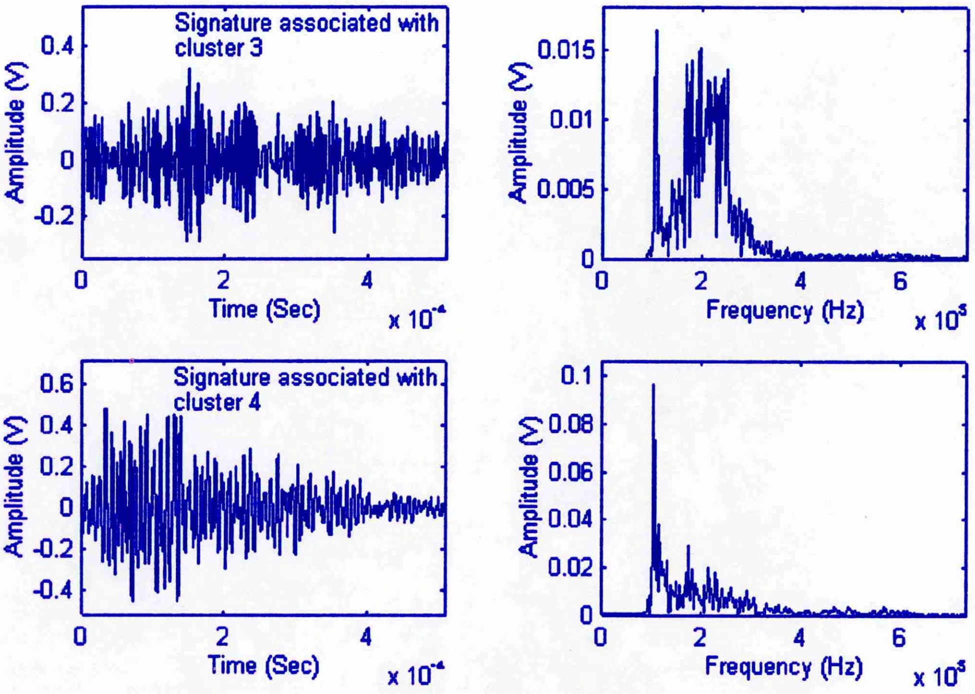

Figure 9.18 Stress waves detected at STW Snailbeach

Inspection of the bearings revealed uneven wear across the rollers, see photograph 9.10, moverover, it appeared that the rollers were not square with the outer raceway, see roller entry in photograph 9.11. This is probably the result of misalignment, which will be taken up by the rollers and movement of the swivel cartridge. Misalignment will also result in minute movements of the swivel cartridge about the housing, producing metal-to-metal rubbing and thus generating stress wave activity. It can be concluded that the fault condition was related to misalignment.

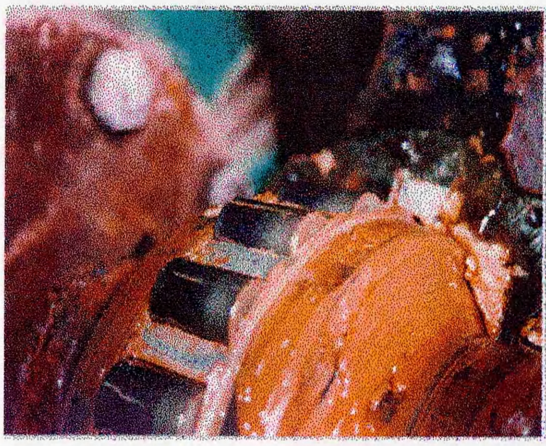

Photograph 9.10 Uneven wear across rollers

Photograph 9.11 Misalignment

9.4.5 STW Penybontfawr

This Tuke & Bell RBC used Split Cooper roller bearings with a bore diameter of 125mm. Both bearings on the unit were monitored over five revolutions. Stress wave activity was detected on the bearing at the non-drive end. Minimal activity was detected on the second bearing. The classification algorithm was applied to the stress wave bursts detected on the non-drive end bearing and the results are shown in figure 9.19. Classification was based on a 9th order AR model applied to 2048 data points.

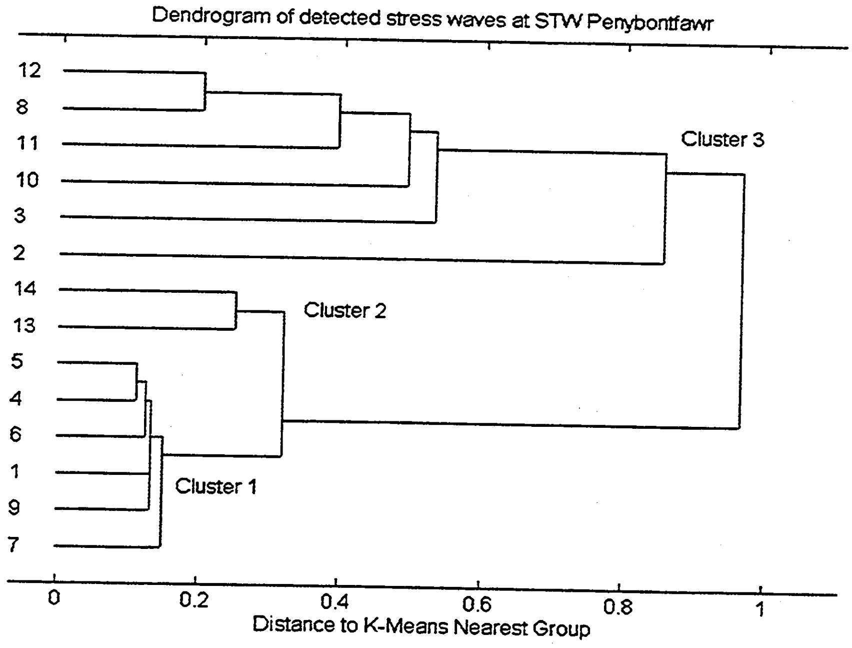

Figure 9.19 Classification of stress waves at STW Penybontfawr, 13/5/97

Three groups emerged and typical time signatures, with corresponding frequency spectrums, are shown in figure 9.20 and 9.21.

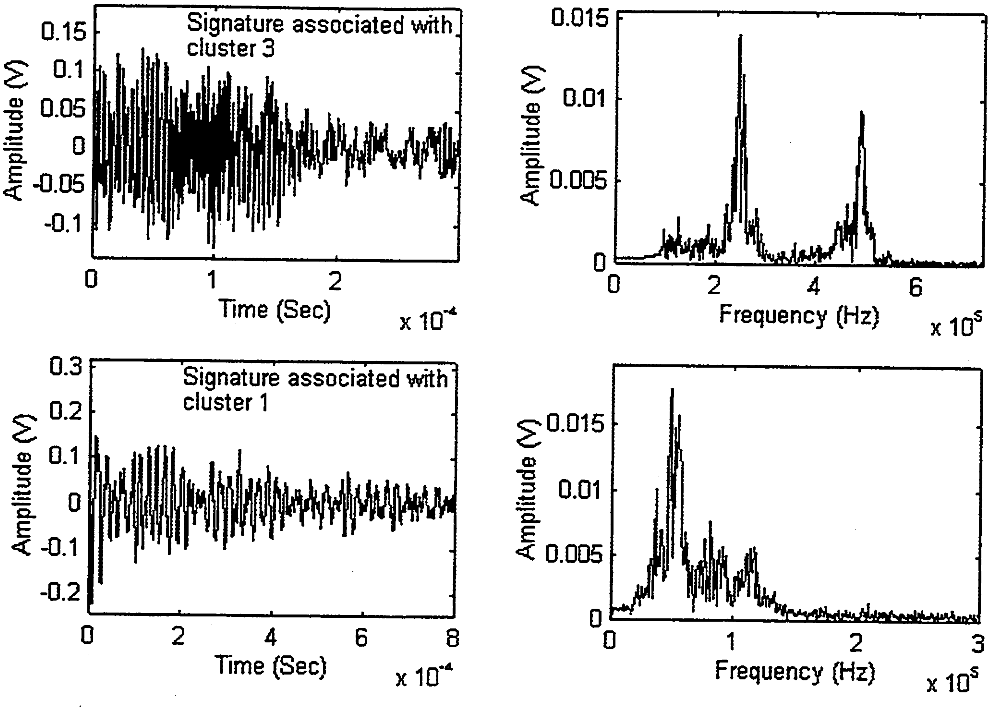

Figure 9.20 Stress waves detected at STW Penybontfawr

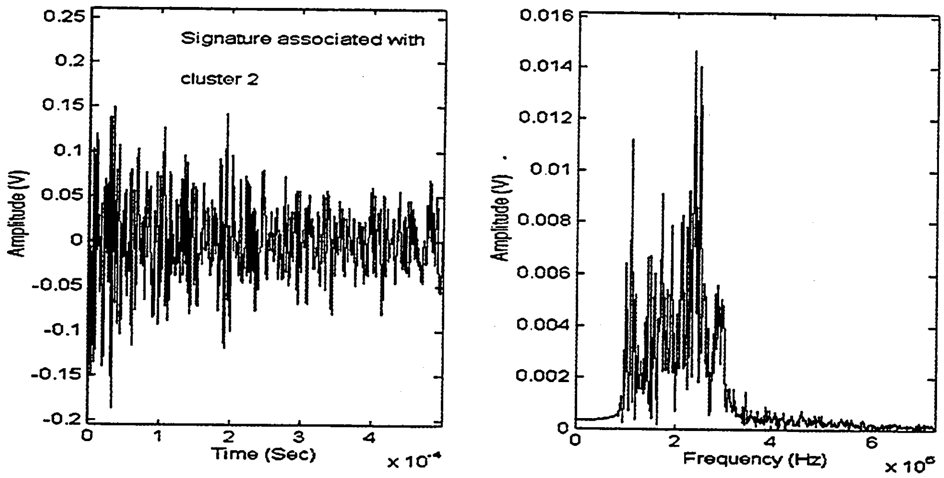

Figure 9.21 Stress waves detected at STW Penybontfawr

Inspection of the bearings revealed wear of the bearing roller cage, see photographs 9.12 and 9.13. The arrows on these figures point to regions were surface cracks can be seen. Observations of the clustered time signatures indicate that signatures associated with cluster 1 are in the low frequency range, 30KHz to 150KHz. This could be associated with the resonance of a component within the bearing. A tenable conclusion would be that;

i) One of these clusters resulted from resonance of a component within the bearing.
ii) A second cluster could be attributed to cage wear.
iii) The final cluster could be attributed to relative movement between the swivel cartridge and the bearing housing, a consequence of misalignment. However, if this were the case, the author would have expected considerable more acoustic activity. Furthermore, there wasn't evidence of uneven wear across the rollers.

It is the opinion of the author of this thesis that because of the amount of stress wave activity, the diagnosis of this bearing could result in a false alarm.

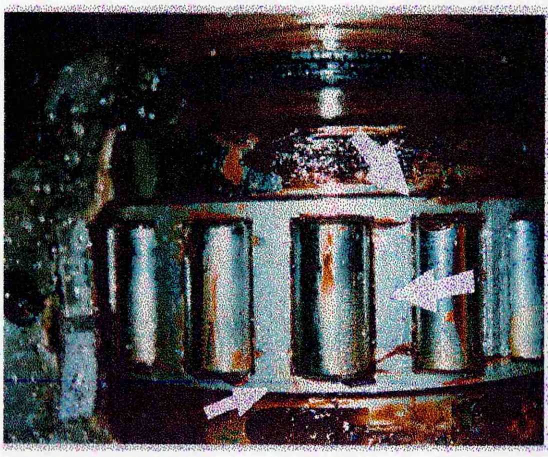

Photograph 9.12 Cage wear

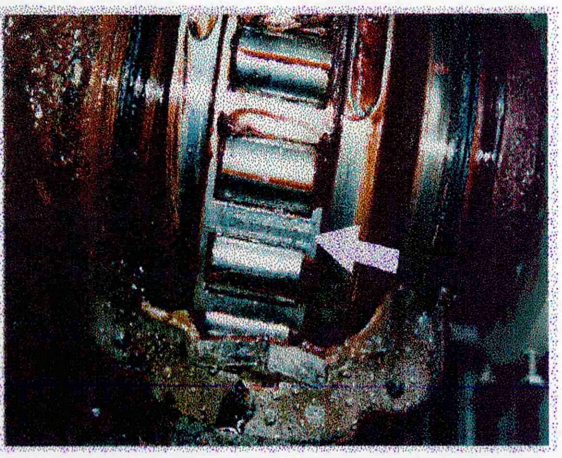

Photograph 9.13 Cage wear

9.4.6 STW Hamstall Ridware

RBC : Cambridge
Bearing type : SKF, non-drive end.
Date visited : 3/6/97
Classification : 9th order model applied to 4096 data points.
Number of data files recorded : 25 data files were recorded over 5 revolutions, 8 of which were rejected due to spurious electronic spikes.

Results of classification are shown in figure 9.22, whilst typical signatures, with corresponding frequency spectrums, associated with the formed clusters are shown in figure 9.23.

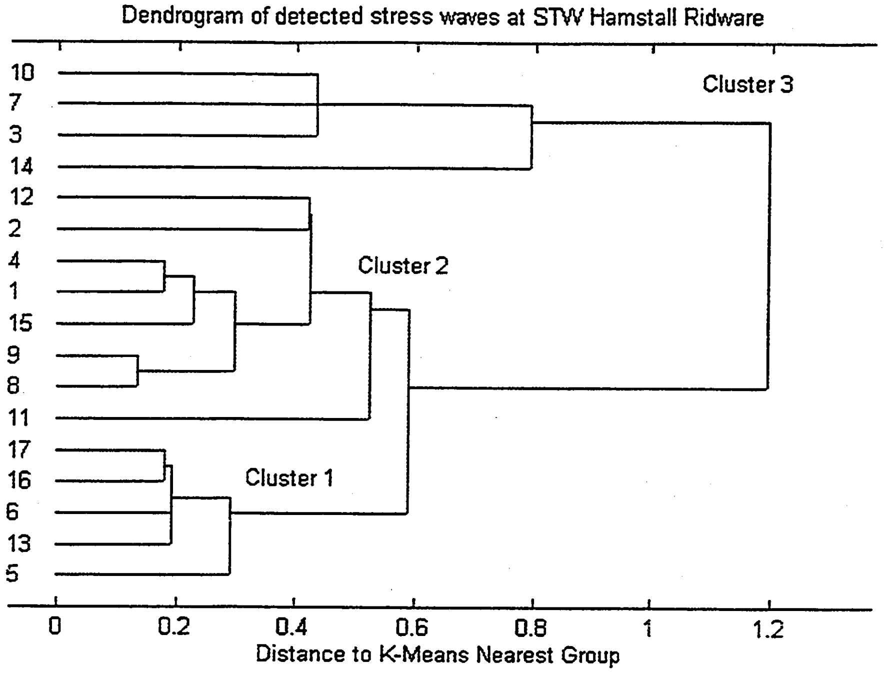

Figure 9.22 Classification of stress waves at STW Hamstall Ridware, 3/6/97

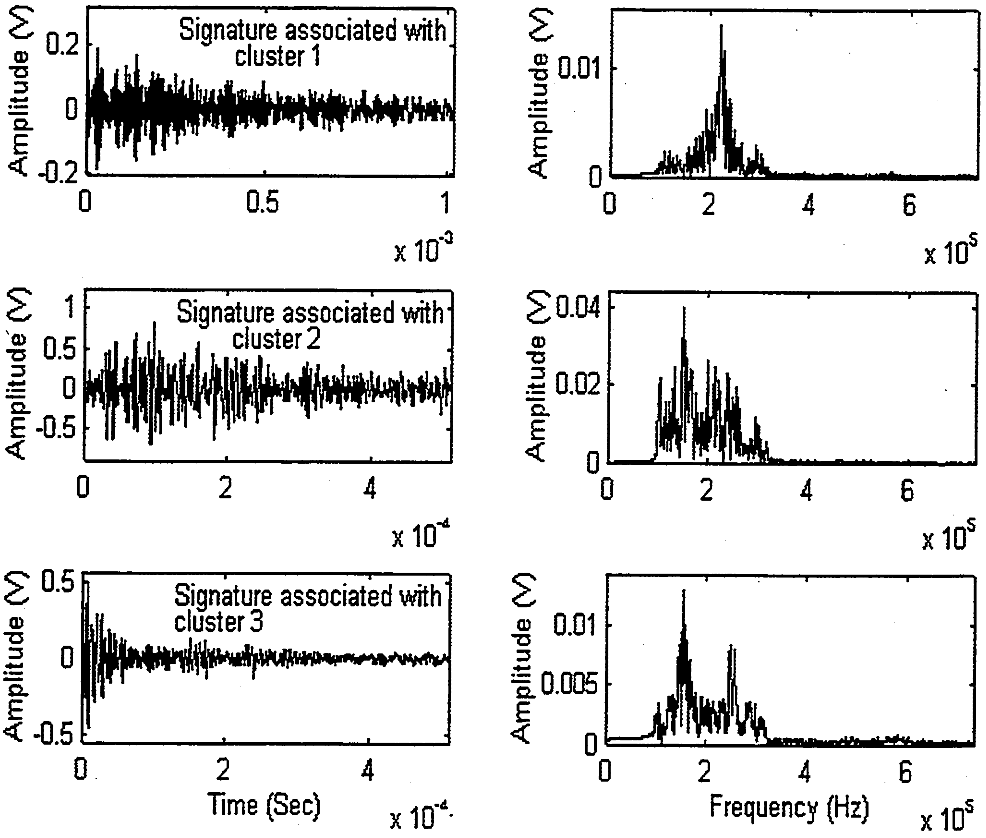

Figure 7.23 Stress waves detected at STW Hamstall Ridware

Based on these results, it was concluded the bearing had a mechanical defect. At the time of writing this thesis the bearing had not been inspected, however, STW engineers discovered that the tapered locking nut was loose, see section 8.4.3.

9.4.7 Other RBC locations

Several other RBC bearings were monitored and a detailed list of the results of investigations is given in table 9.1. Over sixteen of the sites monitored did not produce any stress wave activity. It was therefore concluded that at these RBC sites the bearings were in good operational condition at the time of monitoring. Bearings as old as 10 years were found to be in good condition, authenticating this method of monitoring.

Sites at STW 'Rous Lench' and 'Hamstall Ridware' had not been inspected at the time of writing this thesis. Clusters detected at STW 'Rushbury' and 'Kirk Langley' were attributed to uneven wear on the rollers due to misalignment; for instance, see photograph 9.14.

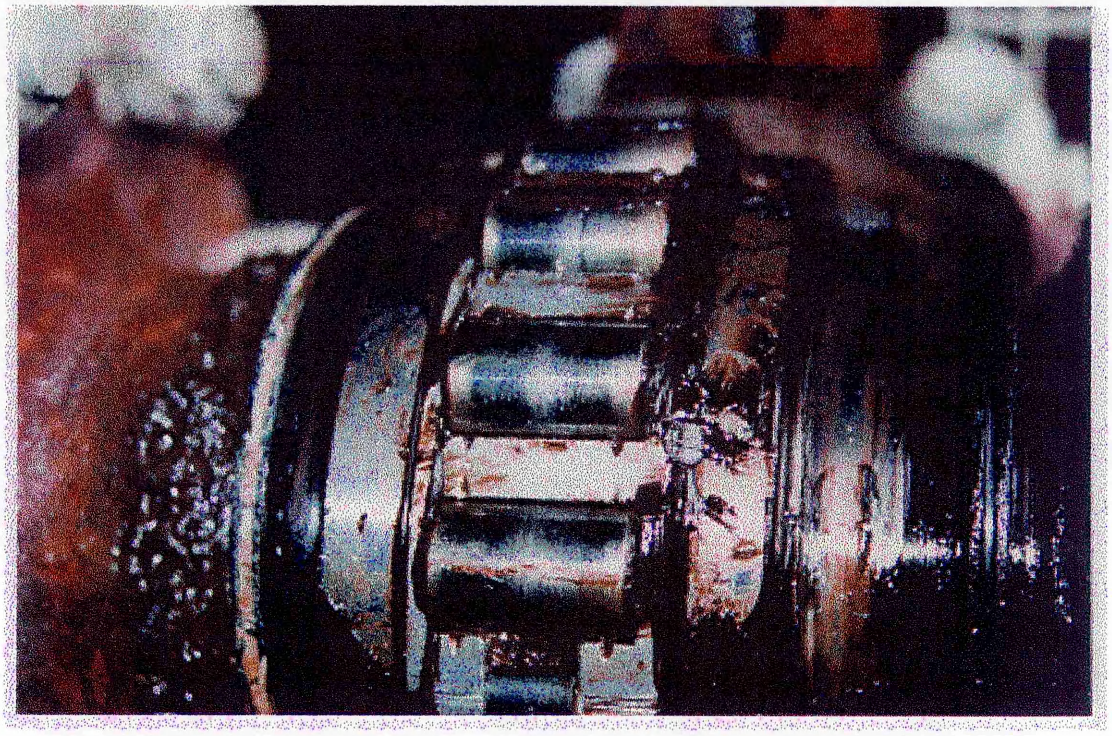

Photograph 9.14 Uneven wear on rollers at STW Rushbury, 23/4/97.

9.5 List of other bearings monitored

See table 9.1.

9.5 List of other bearings monitored with results

Table 9.1

No.	Site	Date visited	Bearing type	Operational since	No. of bearings monitored	No. of clusters formed	Other comments
1	Caynham	4/22/97	Split cooper	1986	1	-	No detectable stress wave bursts
2	Ditton Prior	4/30/97	Split cooper	1986	1	-	No detectable stress wave bursts
3	Honiley	5/1/97	SKF	1993	2	-	No detectable stress wave bursts
4	Worfield	5/6/97	Split cooper	1993	1	-	No detectable stress wave bursts
5	Hilton	5/6/97	FAG	1993	1	-	No detectable stress wave bursts
6	Tregynon	5/12/97	SKF	1995	2	-	No detectable stress wave bursts
7	Hognaston	5/13/97	SKF	1992	8	-	No detectable stress wave bursts
8	Defford	5/20/97	SKF	1995	2	-	No detectable stress wave bursts
9	Flyford Flavell	5/20/97	SKF	1995	1	-	No detectable stress wave bursts
10	West Felton	5/21/97	SKF	1992	2	-	No detectable stress wave bursts
11	Llanfair Caereinion	6/4/97	SKF	1992	1	-	No detectable stress wave bursts
12	Dorsington	6/12/97	SKF	1990	1	-	No detectable stress wave bursts
13	Hinton-on-the-Green	7/7/97	SKF	1993	1	-	No detectable stress wave bursts
14	Clifton Campville	6/2/97	SKF	1995	2	-	No detectable stress wave bursts
15	Hamstall Ridware	6/3/97	SKF	1995	1	3	Not yet inspected On the 13th Jan. 1998, it emerged that the shaft had moved axially as a result of a loose tapered locking nut.
16	Rous Lench	5/9/97	SKF	1993	2	bearing 1, 2	Not yet inspected
						bearing 2, 0	No detectable stress wave bursts
17	Rushbury	4/23/97	Split Cooper	1993	2	bearing 1, 3	Inspection revealed uneven wear on the roller, indicative of mis-alignment and therefore, swivel cartridge movement, see photo. 9.14
						bearing 2, 0	No detectable stress wave bursts
18	Kirk Langley	8/13/97	Split Cooper	1993	6	RBC 2, bearing 1, 4 RBC 2, bearing 2, 4	Inspection revealed uneven wear on the roller, indicative of mis-alignment and therefore, swivel cartridge movement. Also, there was early indication of cage wear.
19	Napton	10/27/97	SKF	1992	6	-	No detectable stress wave bursts Inspection revealed no visible mechanical deficiencies

CHAPTER 10

DISCUSSIONS

Application of the stress wave technique to condition monitoring of RBCs and their bearings has proven extremely successful. This is the first application of its kind and contributes a significant advance to monitoring of low-speed machinery.

Prior to obtaining 'on-site' measurements, attenuation tests were undertaken on the test-rig in order to obtain an understanding of the various transmission paths. Stress waves were generated at various positions on the test-rig using the Nielson source technique and Dirac pulse inputs. It was evident that these stress waves were of distinct shapes, representative of their different source positions. Furthermore, the attenuation tests showed stress waves to be detectable at considerable distances with several discontinuities. Attenuation tests on a real size RBC reinforced the above statement.

Results of attenuation tests on the test-rig showed the best position for placement of the transducer to be on the stub shaft. Furthermore, there was access to this position on almost all-operational RBCs and the receiving transducer was attached to the stub shaft using a magnetic clamp. During mechanical deficiency simulations and 'on-site' measurements, the transducer cable had to be unwound after five revolutions, this was because twisting of the cable triggered the acquisition system. Other methods of attaching the sensor to the stub shaft are possible, for example, slip rings, or the use of a telemetric system. However, both are impractical for on-site recordings, moreover, each will be accompanied by additional background noise. Experimental results for placement of the receiving transducer showed attenuation across the bearing of 30dB and 57dB in terms of amplitude and energy levels respectively.

Stress waves generated from fault conditions associated with the low speed test-rig were found to be suitable for monitoring the mechanical integrity of a rotating frame. Therefore, it was concluded that **the detection of these stress waves was a landmark for its applicability as a monitoring tool.** The stress waves generated were attributed to the relative movements, in the order of 0.002m/sec, between mating components. However, the rate of wear and relative movement between mating components could not be controlled, therefore, no relationship between severity and stress wave activity was established.

Experimental results of simulated mechanical faults showed the frequency range of stress waves associated with frame looseness was between 100KHz and 750KHz.

Simulations of broken through-rod rubbing showed a much reduced frequency range of between 100KHz and 300KHz. This reduction in frequency range was attributed to attenuation with increased discontinuity. The frequencies associated with frame looseness and through-rod rubbing were much greater than typical background noise, thus overcoming the major drawback with conventional vibration monitoring systems.

Media movement simulations did not generate any stress wave activity. This was not unexpected, as the impingement of a plastic sheet on a metal surface will not produce any appreciable wear on the metal surface. However, the continuous impingement of the media panels on the through-rods will eventually result in minute movement between the through-rods, the through-rod clamps and the supporting structure. With the passage of time these movements will increase, eventually causing looseness between mating components, i.e., the through-rod and its clamps, or, the through-rod and the supporting structure. Therefore, the inability to detect media movement was not considered a drawback to the proposed monitoring system.

During experimental tests for frame looseness, it was observed that further reductions in tightening torque resulted in a reduction of stress wave emission. This was attributed to gaps that appeared between the interfaces. Stress waves released with this further reduction in torque were associated with the twisting of the radial arm about the bolts, ensuring some contact between interfaces. This reinforces the author's belief of the existence of a 'Kasier' effect, see section 4.4.1. Typical stress waves detected from mechanical faults on the test-rig were of complex pattern with a duration of up to 3 milli-seconds. In some instances two-stress wave bursts were evident within one acquisition, indicative of the breaking of a second surface asperity. As two-stress wave bursts were not evident on all recorded data files, the possibility that the second burst was a reflection of the first burst was eliminated. Furthermore, acquisitions of the Neilson source test and Dirac pulse inputs did not contain more than one stress wave burst.

Extracting optimal characteristics from stress waves is fundamental to classification and source identification. Classification parameters for time/frequency domain features were obtained within a frequency range of 100KHz and 1000KHz. Whilst more features could have been extracted at varying frequency bands, i.e., 100KHz to 200KHz, 200KHz to 300KHz, ... etc, it was thought unwise as:

i) The specification of frequency bands with dominating classification features on the test-rig might have been inappropriate to operational RBCs and their bearings. This is because operational units have different sized component members, materials, initial assembly conditions and loading.

ii) Computational times will be increased by a factor dependent on the number of frequency bands of interest. This could result in lengthy delays before any decisions are reached, defeating our philosophy of simplicity

An alternative to time/frequency domain features were auto-regressive (AR) coefficients, see section 6.3. The approiate model order was selected by observing changes in the variance of minimum mean-squared value, see section 6.3.1. At the point when a constant variance was reached, the corresponding model order was selected. The use of AR coefficients resulted in a reduced number of features and computational times. The computational times could be reduced by a factor of twenty in some instances. The recursive Levinson algorithm was employed for computation of the AR coefficients.

Classification of Nielson source tests, Dirac pulse inputs and mechanical looseness simulations on the test-rig showed the centriod value of AR coefficients provided efficient and robust parameters for classification. Furthermore, it was shown that AR coefficients provided sufficient characterisation properties for the cluster algorithm to differentiate stress waves from various sources. Results of mechanical looseness on the test-rig clearly differentiated between rubbing of the through-rods and looseness of the radial arms. This marked difference in signature pattern was attributed to the increased number of discontinuities and thus, different transfer functions.

The presented case studies in chapter 8 and 9 represent the broad range of mechanical defects evident on RBCs and their bearings, while tables 8.1 and 9.1 detail more results. Background noise recordings for RBCs and bearings showed the operational noise to be less than 100KHz. On numerous operational RBCs and bearings, stress wave activity above the electronic noise of the data acquisition system was undetectable. At these sites, the health of the RBCs and bearings were deemed good as no mechanical faults were detected at the time of data acquisition. To date, none of these units have been diagnosed as defective. The above comment reinforces the fact that background noise was below 100KHz.

Whilst RBC signatures were taken from the stub shaft, bearing signatures were taken from the housing. This was because of the attenuation across the bearing, i.e., signatures from the outer race of the bearing will be attenuated before it reaches the stub shaft. Similarly, faults on the RBC will be attenuated across the bearing. The maximum amplitude of stress wave detected on defective RBCs was 0.6V, and a 30dB attenuation across the bearing (section 7.2) will result in amplitude of 0.019V. This is far below the set trigger level, moreover, this signature will be embedded in the electronic noise of the recording system. Therefore, any signatures taken from the bearing housing will be void of RBC distress signatures, e.g., STW Defford (section 8.4.4 and table 9.1). However, it is probable that distress signatures from the bearing could be detected on the stub shaft, particularly if the fault is on the inner race or tapered sleeve. Under this circumstance, attenuation of the stress wave signature across the inner race to the stub shaft will be insufficient as to be undetectable. A typical example was encountered at STW Hamstall Ridware, see section 8.4.3.

A variety of mechanical deficiencies were detected with the application of AR coefficients to classification of stress waves generated from operational RBC units and their bearings. The AR coefficients provided a robust system for identification of RBC/bearing deficiencies without prior knowledge of the characteristics of the unit. The time signatures for the various clusters formed at each site were of distinct waveform pattern. Typically, the frequency spectrums of these signatures were also different. Whilst the frequency ranges might have been similar, the dominating frequency/ices were different. Frequencies of stress waves generated ranged from 100KHz to 400KHz for RBC deficiencies and 100KHz to 700KHz for bearing deficiencies. Further observations on defective RBCs and bearings showed two or more bursts to be evident per acquisition. This was synonymous with rubbing between mating components as proved with experimental results on the test-rig. Generally, stress waves resulting from bearing defects were of shorter duration than RBC distress waves, typically 0.4 milli-seconds.

Stress wave signatures from different defective RBCs and bearings were not correlated for the following reasons:

i) The variation in materials and loading conditions between RBCs of identical sizes.

ii) A variety of mechanical faults can exist on identical units. This implies that different mechanisms for the generation of stress waves can exist on identical machines, and in turn, would lead to different shaped stress waves, even though the emitting source positions could be identical.

iii) The different grease types will have different transmission properties resulting from the difference in elastohyrodymanic lubrication properties across the rolling elements.

There were no 'false alarms' on the RBCs monitored. This was because of three stringent conditions that had to be satisfied during diagnosis, namely; a duration of over 1 milli-second, a complex pattern representative of the transmission path and evidence of two or more stress wave bursts on some of the acquisitions. Bearing diagnosis at STW Snailbeach (section 9.4.4), Penybontfawr (section 9.4.5) and Rushbury (section 9.4.6) clearly suggested rubbing activity, however, inspection of these bearings revealed no major defect that could result in early loss of operation, though, there was evidence of misalignment. It is interesting to note that all three sites named above employed the Split Cooper bearing, and, a characteristic of this bearing is that misalignment is taken-up by the swivel cartridge that seats on the bearing housing. Consequently, to compensate for misalignment, the cartridge will move about the housing, generating stress wave activity. This design of bearings is intended to compensate for misalignment, but the question that arises is: When will the misalignment have reached a stage to be of concern to the integrity of the bearing ? Experimental investigations are required to aid differentiation of stress waves associated with misalignment and those associated with bearing defects. Therefore, at present, diagnosis of this type of bearing could lead to false alarms, however, it does bring to attention of the operators those bearings that are misaligned. This present restriction in use of the stress wave technique to diagnosis on Split Cooper bearings shows **a further application of stress waves as a Quality Control tool**. In this particular instance, the use of stress waves could be applied to reduce the amount of misalignment. There were no false alarms on SKF and FAG bearing types.

Fundamental to the philosophy behind the condition monitoring system for RBCs is, that at the time of data acquisition, relative movements between any loose components remain fairly constant. Although slight variations in amplitude and duration of stress waves generated can be expected, these variations were assumed insignificant to the classification algorithms employed. The classification of these distinct stress waves offers the opportunity to diagnose the health of the RBC unit at that time of diagnosis. It is probable that a second diagnosis at a later date would produce stress waves that are distinct from those generated in the first diagnosis. This could be as a result of the Kaiser effect, see section 4.4.1, and increased deterioration of the RBC unit. Since the mechanical integrity of a machine deteriorates as a function of time, the measured signature will also change. This is due to the change in slip characteristics, i.e., the surface of the slip area may become smooth, or, the contact pressure in the slip region may reduce, and is a major drawback of the monitoring system. Therefore, the idea that severity of structural looseness could be ascertained by observing the duration and strength of stress waves at subsequent inspections was dropped.

However, the monitoring system proposed offers the ability to ascertain the health of an RBC, and its bearings, irrespective of the stage of mechanical deficiency. Furthermore, a decision on the health of an RBC unit can be reached without prior knowledge of any characteristics, as long as the transmission path to the stub shaft is guaranteed.

CHAPTER 11

CONCLUSIONS

The loss of mechanical integrity that has resulted in operational problems with RBCs have been detailed, and, substantiated with significant evidence from RBCs operated within the Severn Trent Water region. The reasons for such deficiencies have been discussed, furthermore, relevant technical information has been presented to improve the readers understanding.

Present day limitations of vibration analysis to slow-speed rotating machinery has resulted in the progression to high frequency stress waves, in the order of 1 Mega-Hertz. The application of stress waves as a monitoring tool presented in this thesis is the first of its kind and contributes to the advancement of condition monitoring of slow-speed machinery. The monitoring system proposed has been authenticated by numerous tests on operational RBCs, furthermore, the application of the stress wave technique to bearing health monitoring, and, as a quality control tool have been presented, proposed and discussed.

Results of the seeded mechanical fault on the test-rig showed that stress waves generated from rubbing of mating components were of complex pattern, indicative of their different transmission paths. Furthermore, in some instances two or more bursts could be detected per acquisition. This phenomenon was also evident during tests on operational RBCs and their bearings, and, is attributed to the breaking of a second surface asperity and/or stress wave generation from another source. Classification of stress wave signatures from the test-rig showed that the centriod value of Auto-Regressive (AR) coefficients, associated with each stress wave, provided a more efficient and robust parameter for diagnosis than traditional time/frequency domain features. This particular technique has its strength in the ability to represent the shape of a stress wave by a few AR coefficients; furthermore, this technique has not been used for analysis of stress wave signatures.

Prior to 'on-site' tests, a computer program written to control the 'Kiethley' ADC board thereby allowing stress wave signatures to be collected over an entire revolution. Early 'on-site' tests encompassed this but it soon became evident that large amounts of data storage would be required. Typically an acquisition of 256,000 data points required over

2,000,000 bytes for storage, based on double floating points. Also evident during diagnosis were vast amounts of uninformative data, therefore, the application of trigger levels was intended to reduce the amount of storage required and, more importantly, reduced the amount of unwanted data. The setting of trigger levels for data acquisition was established after background noise measurements on operational RBCs and bearings were investigated. It emerged that background noise was less that 100KHz, and therefore, below the frequency range of interest (100KHz to 1Mega-Hertz).

Application of signal processing algorithms developed to assess the mechanical integrity of RBCs and their bearings were extremely successful. On several RBC sites, mechanical deficiencies were detected using the stress wave technique and appropriate action was taken by STW engineers to alleviate potential operational problems. The frequency range of mechanical deficiencies associated with RBCs ranged from 100KHz to 400KHz, whilst deficiencies associated with bearing defects ranged from 100KHz to 700KHz. Case studies presented in this thesis authenticate the applicability of stress waves to monitoring of slow-speed rotating machinery, furthermore, it **highlights savings in maintenance cost that have already been made as a direct consequence of this research.**

From recordings on the laboratory test-rig and also the 'on-site' measurements, the author could not find a direct relationship, which allowed the degree (magnitude) of stress wave activity to correlate with the severity of the mechanical looseness. Therefore, increased mechanical looseness would not necessarily manifest itself with increased stress wave activity. Whilst severity on RBCs could not be ascertained, bearing diagnosis of SKF bearings showed that the rate of stress wave activity was an indication of the severity of damage. For instance, at STW Ashover, the rate of stress wave activity on the bearings was much greater than at STW Willoughby, indicative of the more severe damage (section 9.4). Furthermore, the number of stress wave bursts per acquisition was also an indication of the severity. The use of stress wave activity for monitoring Split Cooper bearings could result in a false diagnosis. This is because signatures resulting from bearing misalignment are similar to those signatures measured from failing rolling elements.

During 'on-site' data acquisition, it was impossible to relate the stress wave burst to the rotational position of the RBC. Since structural members in each segment undergo maximum straining at different stages during one complete revolution, the onset of looseness, and accompanied straining of other structural members, will result in stress wave generation from various positions. Therefore, a stress wave burst detected at a particular rotational position cannot be related to any particular segment. However, the information relating stress wave burst to rotational position can be informative for bearing diagnosis, e.g., a cracked outer or inner raceway. For instance, at STW Willoughby (section 9.4.1), stress wave activity was detected at a particular interval within one revolution.

To provide an effective monitoring system with stress waves, the author proposes that the system should employ an ADC with the longest data recording capacity possible (buffer memory). From the author's experience, a minimum value of 512 Kbytes per acquisition is acceptable, furthermore, the electronic noise level of the acquisition system, with a 60dB gain, should be as low as possible. A value of less than 10milli-volts would be ideal, though the author is unaware of its practicality. Pre-amplification above 60dB is not required. Since the frequency range of mechanical deficiencies on RBCs and their bearings ranged from 100KHz to 750KHz, a sampling rate of 5MHz will be sufficient, furthermore, to overcome background noise, the receiving transducer and/or pre-amplifier should have a cut-off frequency of 100KHz.

An 8-bit ADC board was used throughout investigations presented in this thesis and was found to be adequate in overcoming quantisation. However, an increase to a 16-bit ADC will improve the quality of signatures, especially if the signatures are comparable in amplitude to the electronic noise level of the monitoring system, therefore, it would be prudent to use as high a bit capability as is economically feasible.

The receiving transducer to be employed should have, as far as possible, a flat frequency response between 100KHz to 800KHz. The method of attachment of the receiving transducer to the stub shaft means that only a few revolutions can be investigated before twisting of the cable becomes a problem. For the experienced hand, these few revolutions can be adequate. The author has recently carried out preliminary investigations on a 'new material' as a possible couplant between the receiving transducer and the rotating machine. This would allow direct contact between the rotating machine and the transducer, irrespective of the contact position on the machine. The new material, developed at Cranfield University and is in the process of been patented, is extremely ductile and flexible. The initial results were extremely promising and could go further in revolutionising the application of acoustic emissions and stress waves to all types of rotating machinery. For now, the twisting of the transducer cable cannot be avoided.

Evident on several 'on-site' acquisitions was the presence of spurious electronic spikes, which resulted in several false acquisitions. Consequently, it is imperative that the monitoring system has a means of overcoming these spikes, one such method is by the use of the median filter (section 6.7.2).

In conclusion, the proposed monitoring system can be summarised as follows: Classification of stress waves generated from mechanical deficient RBCs, by the use of AR coefficients, provides sufficient information that **a decision on the RBC health can be made immediately,** however, severity levels cannot be ascertained at present. Condition monitoring with the proposed system must go hand-in-hand with general maintenance procedures. The GRP covers on RBCs make routine mechanical and electrical inspections almost impossible, and suggest that the manufacturers/suppliers of RBCs have portrayed a maintenance free system, which is nonsense. The problem can be overcome by ensuring that the covers on RBCs are easily removed, allowing total access to the unit. It would be prudent for purchasers to assess the long-term costs of RBC units rather than just capital costs.

The objectives of this research have been accomplished, namely:

i. To demonstrate that stress wave activity was generated from rubbing of mating surfaces.
ii. Develop signal-processing techniques to aid decision making on the health of RBCs, and, to verify its applicability to operational units.
iii. Finally, the proposed system meets the demand for simplicity and availability. All hardware used are commercially available and the processing techniques can be applied without the interference of a third party, thereby removing any training required for site personnel. The software used for processing all signatures was written with MATLAB, a commercially available package.

A further accomplishment of this research program was that, at relatively low cost, STW have been able to recommend a design standard of RBC that would guarantee a 20 year life of the metal assembly, thereby putting RBCs in a unique position in comparison to other small sewage treatment processes. The condition monitoring system, developed by the author, will only be used by STW when the RBCs that have been recently refurbished are approaching the end of their useful life (2017), or to check the condition of those RBCs where the biomass growth is over the consistent level.

However, STW have identified the commercial opportunity to assist other water companies in checking the mechanical integrity of their RBCs, and, have licensed the use of this device to Cranfield University. A recently published article on this has resulted in a substantial world-wide response about the improved RBC design and condition monitoring system. With Cranfield University's involvement, maintenance costs are now greatly reduced and STW plan to cut back on RBC operational visits to one-day/fortnight, resulting in further savings.

CHAPTER 12

RECOMMENDATIONS

Several operational RBCs and bearings were void of stress wave activity and assumed to be free of any mechanical faults. Whilst visual inspections revealed no defects, these units could have been experiencing looseness that was undetectable by the acquisition system and the ‘experienced’ human eye. Therefore, it would be prudent to establish the amount of looseness required for the onset of stress wave activity. This can be accomplished by making improvements to the test-rig so that measured looseness can be seeded. Furthermore, measurement of the rate of stress wave activity, for a fixed clamping force and relative velocity, would determine if the authors belief of a 'Kaiser effect’ exists, and provide a relationship between the rate of wear and stress wave activity.

Changes to the test-rig can also aid in determining a relationship between the surface finish and stress wave activity. This would be beneficial in making the monitoring system more robust, as the surface finish on RBCs varies from manufacturer, size and materials used. It would also be interesting to determine if changes in surface roughness affect the shape of the stress wave signature generated, for the same relative velocity.

Experimental tests on bearings are required to validate the findings of this thesis. It would be prudent to use an acquisition system that can relate stress wave bursts to the circumferential position of the bearing, as this could aid diagnosis under certain fault conditions, for instance, a cracked inner race. The association of burst to circumferential position is essential because of the varying rotational frequencies of the elements. Furthermore, tests on Split Cooper bearings are required to help differentiate stress waves associated with misalignment from bearing defects, thereby overcoming a drawback discovered whilst monitoring operational bearings of this type, see chapter 10.

A thorough investigation of the 'new couplant' proposed by the author is essential, as this has enormous potential in improving, and increasing, the applicability of stress wave detection to monitoring of all types of machinery. The author hopes to pursue this possibility vigorously.

REFERENCES

1. Findlay, G. E., The selection and design of rotating biological contactors and reed beds for small sewage treatment plants, Proc. Institute of Civil Engrs Wat., and Energy, Vol. 101, pp 237-246, Water Board paper 10249, Dec. 1993.

2. ASCE Manual on Engineering practice, Waste water Treatment Plant design, No. 36, p309- 312,1977, USA.

3. Tchobanoglous,G., Burton,F.L., Wastewater Engineering treatment, disposal and refuse, METCALF & EDDY, INC., p418-430.

4. Lumbers, J. P., Rotating Biological Contactors: Current problems and potential developments in design and control. The Public Health Engineer, Vol. 11, No. 3, pp 41-45, July 1983.

5. Brenner,R.C., Opaken, E.J., Design information on Rotating Biological Contactors Design, Technical report data, Municipal environmental research laboratory, Cincinnati, Ohio, USA

6. Greaves, F.E., Throp, B., and Critchley, R.F., Operational performance of package sewage treatment plants in North West England. Water Science Technology, Vol. 22, No. 3/4, pp 25-32, 1990.

7 Bannister, R. H., Kriacou, S., Stress analysis on RBC structures. 1995/1996. RESTRICTED.

8 Komai, K., Minoshima, K., and Kinoshita, S., Corrosion fatigue crack initiation behaviour of high tensile strength in synthetic seawater, JSME International journal, Vol. 31, No. 3, July 1988, pp612.

9 Szklarska-Simalowska, Z., Corrosion science.

10 Parkins, R. N., Aqueous environmental influences in corrosion fatigue [paper edited in ref 9]

11 Komai, K., Corrosion fatigue crack growth retardation and enhancement in structural steels, Current Japanese materials research, Vol. 1.

12 USA-Japan seminar on passivity and its breakdown on iron base alloys Honolulu, 1975

13 Oriani, R.A. Hydrogen – The versatile Embrittler, Corrosion, Vol. 43, No. 7, pp 390 – 453, July 1998.

14 Vosikovsky, O., Fatigue crack growth in an X-65 line pipe steel at low frequencies in an aqueous environment, Engineering materials and technology, Vol. 10, pp298-304, 1975.

15 Speidel, M. O., Corrosion fatigue in Fe-Ni-Cr alloys. Stress corrosion cracking and hydrogen embrittlement of iron base alloys. NACE, pp 1071, 1977.

16 Parkins, R. N., Aqueous enviromental influences in corrosion fatigue. Edited in reference no. 9.

17 Gabetta , G., A model for environmentally assisted crack growth rates. ASTM STP 1049, pp267, 1990.

18 Nibbering, J. J. W., Behaviour of mild steels under very low frequency in seawater. 1982

19 McEvily, A. J. Jr. Atlas of stress corrosion fatigue curves. 1990.

20 Corrosion fatigue : chemistry, mechanics and mircostructure. NACE - 2, 1971.

21 Komai, K., Stress corrosion cracking of high strength steels under dynamic loading conditions. Current Japanese materials research, Vol. 4, 1988.

22 Corrosion fatigue data for carbon and alloy steels. Corrosion of metals in marine environments, Battelles Columbus labortaries, 1981.

23 Corrosion fatigue failures - the effects of frequency. Metals handbook, Vol. 13.

24 Endo, K., Goto, H., and Nakamura, T., Effects of cycle frequency on fretting fatigue life of carbon steel. Bulletin of JSME, Vol. 12, No. 54, 1969.

25 Masuda, C., Abe, T., Hirukawa, H., Corrosion fatigue life prediction for SUS403 stainless steel in 3% NaCl aqueous solution, Trans. Jpn. soc. mech. eng. Vol.52, no.480, pp1764, 1986.

26 Swanger and France, Effect of zinc coatings on the endurance properties of steel. Proceedings of the American Society for Testing Materials, Vol. 32, p 430, 1932.

27 Dolan, J. T. and Benniner, H. H., The effect of protective coatings on the corrosion-fatigue strength of steel.pp 658-666.

28 Watt, D.G., Fatigue tests on zinc-coated steel wire. pp 717-732.

29 Forsman, O.,Lundin, E., The influence of different surface coatings on the fatigue strength of steel. Proceedings of the 1st world Metallugists congress of American Society of Metallugists, p 606-612, 1951.

30 Harvey, W.E., Zinc as a protective coating against corrosion fatigue of steel. Metals and Alloys, Vol. 1, No. 10, p 458-461, 1930.

31 Trulear, M. G., and Characklis, W.G., Dynamics of biofilm processes. Journal WPCF, Vol. 54, No. 9, pp 1288, Sept. 1982.

32 Kornegay, B. H. and Andrews, J. F. Characteristics and Kinetics of Biological Fixed Film Reactors. FWPCA-17050-00/70, NTIS PB-199 834/BE, 1970.

33 Hynek, R. J. and Chou, C. C. Development and performance of Air-Driven Rotating Biological Contactors. In: Proceedings of the 34th Industrial Waste Conference, Purdue University, West Lafayette, Indiana, May 8-10, 1979.

34 Kornegayo, B. and Andrews, J. Kinetics of fixed film biological reactors, Journal of Water Pollut. Control Fed., p R46, 1968.

35 Harris, N. P. and Hansford, G.S. A study of substrate removal in a microbial film reactor. Water Res. 10, 935, 1976.

36 Trulear, M. G. and Characklis, W. G. Dynamics of biofilm processes. J. Water Pollut. Control Fed., 54, 226, 1982.

37 Surampalli, R.Y.,Tekippe,R.J. and Baumann, E. R. Value of Supplemental Air in improving RBC performance, Water Poll. Res. J., Vol. 29, No. 1, 53-73, Canada, 1994.

38 Chesner, W.H., Iannone, J.J. Review of current RBC performance and design procedures. Report prepared for U.S. EPA under contract No. 68-02-2775, 1968.

39 Hitdlebaugh, J.A., Miller, R. D. Full-scale biological rotating contactor for secondary treatment and nitrification. Proceedings of the first National Symposium on RBC technology, Champion, PA, 1980.

40 U.S. EPA. A nation-wide RBC teleconference, Cincinnati, Ohio, USA 1983.

41 Surampalli, R.Y., and Baumann, E. R., RBC Kinetics in Treating Domestic and Industrial Dairy Wastewater under low and high organic loading conditions , Water Poll. Res. Jou., Vol. 27, No. 4, pp 665-691, 1992, Canada.

42 Hamilton,W. A., The sulphate reducing bacteria: their physiology and consequent ecology, Proceedings of the conference sponsored and organised jointly by The National Physical Laboratory and The Metals Society, Teddington, 8-10 March 1983, pp 1-5.

43 Sanders,P.F, and Maxwell,S., Microfouling, macrofouling and corrosion of metal test specimens in seawater, Proceedings of the conference sponsored and organised jointly by The National Physical Laboratory and The Metals Society, Teddington, 8-10 March 1983, pp 74-83.

44 Wilkinson,T.G., Biological Mechanisms Leading to Potential Corrosion Problems, In Corrosion and Marine Growth on Offshore Structures, Ed. Lewis, JR. & Mercer, A.D, 1983, pp 117-122.

45 Ringas,C. and Robinson, F.P.A., Corrosion of Stainless Steel by Sulfate-Reducing Bacteria- Total Immersion Test Results. The Journal of Science and Engineering Corrosion, Vol. 44, No. 9, pp 671, Sept. 1988.

46 Ringas,C. and Robinson, F.P.A., Corrosion of Stainless Steel by Sulfate-Reducing Bacteria-Electroochemical Techniques. The Journal of Science and Engineering Corrosion, Vol. 44, No. 6, pp 386, June 1987.

47 Wagner,P.A., and Ray,R.I., “Surface analytical techniques for microbiologically influenced corrosion-A review”, Microbiologically Influenced Corrosion Testing, ASTM STP 1232, Philadelphia, pp 153-169, 1994.

48 Borenstein, S.W,” Why does Microbiologically Influenced Corrosion occur preferentially at welds?”, Proceedings, Corrosion/91, Paper 286, National Association of Corrosion Engineers, Houston, Texas, USA, 1991.

49 Kilgallon, P.J., The effect of sulphate Reducing bacteria on the hydrogen absorption of cathodically protected high strength low alloy steels, PhD Thesis 1993-94, Cranfield University.

50 Hoyt, S. L., Metals and alloys data book, 1943.

51 Fysh, S.D., Oravec, E.M., and Medley, J.B. An experimental simulation of the tribology of large spherical roller bearings in paper machines. Tribology International, Vol. 23, No. 5, pp 317-327, Oct. 1990.

52 Robinson, J.C, Canada, R.G., and Piety, R.G. Vibration Monitoring on Slow speed Machinery: New Methodologies covering Machinery from 0.5 to 600rpm. 5th international Conference on Profitable Condition Monitoring - Fluids and Machinery Performance Monitoring, pp 169-182, bHr Group Ltd., Publication 22, 3-4 Dec. 1996, Harrogate, UK.

53 Berry, P.E. Required vibration analysis techniques and instrumentation on low speed machines. Techincal associates of Charlotte, Inc. 1992.

54 Murphy, T.J., The development of a data collector for low-speed machinery. 4th international Conference on Profitable Condition Monitoring, bHr Group Ltd., 8-10 Dec. 1992, Stratford-upon-Avon, UK.

55 Berry, J. E., Required vibration analysis techniques and instrumentation on low speed machines (particularly 30 to 300 RPM machinery), Technical Associates of Charlotte Inc.,Advanced Vibration Diagnostic and Reduction Techniques, 1992.

56 Weavesr, m., Prof., Fundamentals of Acoustic Emission, 22nd European Conference on Acoustic Emission Testing, EWGAE, 29-31 May 1996, The Robert Gordon University, Aberdeen, pp 1- 11.

57 Kuboyama, K., Development of Low Speed Bearing Diagnosis Technique, NKK Fukuyama Works, Fukuyama City, Hiroshima, Japan.

58 Penter, A. Vibration monitoring of low speed machinery as found in the mining industry. Condition Monitoring of Machinery and Plant.

59 Canada, R.G., and Robinson, J.C., Vibration measurements on slow speed machinery. P/PM Technology, Vol. 8, no. 6, pp 33-37, Dec. 1995.

60 Mechefskse, C. F., and Mathew, J., Fault detection and diagnosis in low speed rolling element bearings. Part II: The use of Parametric spectra. Mechanical systems and signal processing, Vol. 6, No. 4, pp 297-307, 1992.

61 Sato, I., Rotating machinery diagnosis with acoustic emission techniques, Electrical engineering in Japan, Vol. 110, No. 2,pp 115-127, 1990.

62 Mathews, J. R., Acoustic emission, Gordon and Breach science publishers, NewYork, 1983.

63 Boness, R.J., McBride, S.L., and Sobczyk, M. Wear studies using acoustic emission techniques. Tribology International, Vol, 23, No. 5, pp 291-295, Oct. 1990.

64 Sarychev, G.A., and Shchavelin, V.M. Acoustic emission method for research and control of friction pairs. tribology International, Vol. 24, No. 1, pp 11-16, Feb. 1991.

65 Singh, B.R. Study of critical velocity of stick-slip sliding. Journal of Engineering for Industry, pp 393-398, Nov. 1960.

66 Bell, R., and Burdekin, M. A study of the stick-slip motion of machine tool feed drives. Proceedings of the Institute of Mechanical Engineers. Vol. 184, No. 30, pp 543-555, 1969-1970.

67 Halmshaw, R. Non-destructive testing. ISBN 0-7131-3634-0, 1987.

68 McGonnagle, W.J. Non-destructive testing. 1961, Gordon and Breach science publisher, New York, USA.

69 Gorman, M.R. Plate wave acoustic emission. Journal of Acoustic society of America, Vol. 90, No. 1, pp 358-364, July 1991.

70 Beattie, A.G. Acoustic emission, Principles and Instrumentation. Journal of acoustic emission, Vol. 2, No. 1/2, pp 95-128, 1983.

71 Whittaker, J.W., Brosey, W.D., Burenko, O., and Waldrop, D.A. Acoustic emission wave propagation and source location in small, spherical composite test specimens. Journal of Acoustic emission, Vol. 7, No. 1, pp 31-40, 1988.

72 Liu, H., The use of stress waves for detecting shaft seal rubbing and source location, PhD thesis, 1996, Cranfield University, RESTRICTED.

73 Roger, L. M., The application of vibration analysis and acoustic emission source location to on-line condition monitoring of anti-friction bearings. Tribology International, pp 51-59, April 1979,.

74 Balderstone, H, The detection of incipient failure in bearings, Materials evaluation, Vol. 27, No. 6, pp 121 - 128, June 1969.

75 McFadden, P. D., and Smith, J. D., Acoustic emission tranducers for the vibration monitoring of bearings at low speeds, Report no. CUED/C-Mech/TR29, 1983.

76 Smith, J.D., Vibration monitoring of bearings at low speeds, Tribiology International, pp 139-144, June 1982.

77 Xinh,.T, 'The use of ultrasound measurement system to monitor the mechanical integrity of rolling element bearings and gears'. PhD. Thesis. Cranfield Institute of Technology, 1992.

78 Belchamber, R.M., Betteridge, D., Chow, T.Y., Lilley, T., Cudby, M.E.A., and Wood, D.G.M. Evaluation of Pattern Recognition Analysis of Acoustic Emission from stressed polymers and composite. Journal of Acoustic emission, Vol. 4, No. 4, pp 71-83, 1985.

79 Chan, R.W.Y, Hay, R.D., Caron, V., Hone, M., and Sharp, R.D. Classification of acoustic emission signals generated during welding. Journal of Acoustic emission, Vol. 4, No. 4, pp 115-123, 1985.

80 Murthy, C.R.L., Dattaguru, B., and Rao, A.K. Application of Pattern recognition concepts to Acoustic emission signal analysis. Journal of Acoustic emission, Vol. 6, No. 1, pp 19-28, 1987.

81 Liang, S.Y., and Dornfeld, D.A. Punch stretching process monitoring using Acoustic Emission signal analysis-Part 1: Basic Concepts. Journal of Acoustic emission, Vol. 6, No. 1, pp 29-36, 1987.

82 Oksa, G. and Bahna, J. Matched predictive filter enhancement recognition of bursts. Proceedings on the Symposium on Nuclear Reactor surveillance and diagnostics. Session 10, 19-23 June, 1995, Avignon, France.

83 Haykin, S. Introduction to adaptive filters. Macmillan publishing company. ISBN 0 - 02 - 949460 - 5.

84 Kay, S.M, and Marple, S.L Jr. Spectrum analysis - A modern perspective. Proceedings of the IEEE, Vol. 69, No. 11, pp 1380-1419, Nov. 1981

85 Chen,C.H., Recognition of underwater transient patterns. Pattern Recognition, Vol. 18, No. 6, pp 485-490, 1985.

86 Chen, C.H. On segmentation algorithm for seismic signal analysis. Geoexploration, Vol. 23, pp 35-40, 1984/85.

87 Bodenstein, G., and Praetorius, M. Feature extraction from the electroencephalogram by adaptive segmentation. Proceedings of the IEEE, Vol. 65, No. 5, pp 642-652, May 1977.

88 Zhuge, Q., Yongxiang, L., and Yang, S. Non-stationary modelling of vibration signals for monitoring the condition of machinery. Mechanical systems and signal processing, Vol. 4, No. 5, pp 355-365, 1990.

89 Charbonnier, R., Barlaud, M., Alengrin, G., and Menez, J., Results on AR-modelling of non-stationary signals. Signal processing, Vol. 12, pp 143-151, 1987.

90 Alengrin, G., Barlaud, M., and Menez, J. Unbiased parameter estimation of non-stationary signals in noise. IEEE transactions on Acoustics, Speech and Signal Processing, Vol. ASSP-3, No. 5, pp1319-1322, Oct. 1986.

91 Masayasu, O., and Kanji, O. Pattern Recognition analysis of Acoustic emission from unidirectional carbon fibre-epoxy composites by using Autoregressive modelling. Journal of Acoustic emission, Vol. 6, No. 1, pp 61-71, 1987.

92 Everitt, B. Cluster analysis. ISBN 0 435 82297 7, 1974.

93 Green, Paul, E., Analyzing Multivariant Data.

94 Daultery, S. Principal Component Analysis, 1976. ISBN 0 902246 56 9. ISSN 0306 - 6142.

95 Signal Processing Toolbox, MATLAB.

96 K.G. Beauchamp, Signal processing using Analog and Digital Techniques, 1973

97 Olli Yli-Harja, Medial Filters: Extensions, Anaylsis and Design. Lappeenrannan Research Papers, Paper 13, 1989

98 Liu, H., The use of stress waves for detecting shaft seal rubbing and source location, PhD thesis, 1996, Cranfield University, RESTRICTED.

99 Riddle, J., Ball bearing maintenance, University of Oklahoma Press, First edition, 1955.

100 Wilcock, D. F.,, and Booser, E. R., Bearing design and application, First edition, McGraw-Hill Book Company, ISBN 07-070197-0, 1957.

101 Nisbet, T. S., and Mullett, G. W., Rolling bearings in service - Interpretations of types of damage, ISBN 0 09 129880 6, 1978.

102 McFadden, P. D., and Smith, J. D., Vibration monitoring of rolling element bearings by high-frequency resonance technique- a review. Tribology International, Vol. 17, No. 1, pp 3-10, Feb. 1984.

103 Dyer, D., Stewart, R. M., Detection of rolling element bearing damage by statistical vibration analysis, Journal of Mechanical Design, Vol. 100, p 229 - 235, April 1978.

104 Taylor, J. L., Identification of bearing defects by spectral analysis, Journal of Mechanical Design, Vol. 102, p 199-204, April 1980.

105 Balderstone, H, The dtection of incipient failure in bearings, Materials evaluation, Vol. 27, No. 6, pp 121 - 128, June 1969.

106 Ray, A.G., Monitoring rolling contact bearings under adverse conditions, I of Mechanical Engineers conference on vibrations in rotating machinery, Churchill college, Cambridge, pp 187-194, 1980.

107 Tatnal, R. E., Case histories: Bacteria-influeneced corrosion. Proceedings Corrosion/81, papre 130, National Association of Corrosion Engineers, Huston, Texas, USA, 1981.

108 Szrom, D. B., Low speed bearing analysis. Proceedings of the 10th annual meeting ..., the vibration Institute, Las Vegas, USA, pp 183-188, Jun 24-46 1986.

109 Makhoul, J., Linear prediction: A tutorial review. Proceedings of the IEEE, Vol. 63, No. 4, pp 561-581, April 1975.

APPENDIX

A

Attenuation tests for placement of recieving transducer

Position	Lead fracture tests						Pulse tests					
	Energy (Vs)			Amplitude (V)			Energy (Vs)			Amplitude (V)		
	Bearing	Stub shaft	Relative attenuation (dB)	Bearing	Stub shaft	Relative attenuation (dB)	Bearing	Stub shaft	Relative attenuation (dB)	Bearing	Stub shaft	Relative attenuation (dB)
	* 1e-4						* 1e-6	* 1e-3				
P1	2.73E-01	0.04310	-63.97	0.5300	20.600	-31.79	-	-		-	-	
P2	1.94E-01	0.01640	-58.56	0.4550	18.200	-32.04	0.5192	1.40300	-68.63	0.08	9.3000	-41.31
P3	1.15E-01	0.01200	-60.35	0.4800	17.600	-31.29	0.6261	0.63360	-60.10	0.102	3.4000	-30.46
P4	5.10E-02	0.01610	-69.98	0.1980	13.400	-36.61	0.399	0.44200	-60.89	0.062	2.4000	-31.76
P5	6.10E-02	0.00190	-49.87	0.2320	3.650	-23.94	NR	0.04700		NR	0.7100	
P6	3.66E-02	0.00150	-52.26	0.1800	3.500	-25.78	NR	0.01700		NR	0.4000	
P7	2.92E-02	0.00170	-55.30	0.1580	4.350	-28.80	NR	0.01600		NR	0.5100	
P8	1.79E-02	0.00150	-58.49	0.1220	4.550	-31.43	NR	0.01900		NR	0.5300	
P9	1.82E-02	0.00310	-64.61	0.1160	4.000	-30.75	NR	0.03650		NR	0.5500	
P10	1.73E-02	0.00180	-60.35	0.1200	3.400	-29.05	NR	0.03120		NR	0.4600	
P11	2.71E-02	0.00220	-58.18	0.1540	4.000	-28.29	NR	0.02860		NR	0.5300	
P12	2.81E-02	0.00260	-59.32	0.1560	5.400	-30.79	NR	0.04480		NR	0.5800	
P13	1.06E-02	0.00140	-62.39	0.1000	2.593	-28.27	NR	0.00220		NR	0.1460	
P14	7.59E-03	0.00020	-48.41	0.0780	1.020	-22.33	NR	0.00540		NR	0.1620	
P15	4.01E-03	0.00040	-59.98	0.0740	1.580	-26.59	NR	0.00365		NR	0.1500	
P16	3.02E-03	0.00030	-59.95	0.0640	1.600	-27.96	NR	NR		NR	NR	
P17	9.28E-03	0.00080	-58.71	0.0960	2.080	-26.72	-	-		-	-	
P18	7.99E-03	0.00020	-47.97	0.0920	1.080	-21.39	-	-		-	-	
	Average		-58.26			-28.54			-63.21			-34.51

NR - No detectable response

Table 7.3

Attenuation of test-rig

Position	P0	P1	P2	P3	P4	P5	P6	P7	P8	P9	P10	P11	P12	P13	P14	P15	P16	P17	P18	Average
No. of discontinuities	1	1	1	2	2	3	3	3	3	3	3	3	3	5	5	5	5	5	5	
Frequency range					Signal energy within specified frequency bands (Vs), sensor on stub shaft															
															*1e-3	*1e-3	*1e-3	*1e-3	*1e-3	
100-1000 KHz	0.1175222	0.0431318	0.0163656	0.0120329	0.0160796	0.0018779	0.0014581	0.0017166	0.0015450	0.0031381	0.0018038	0.0021990	0.0025744	0.0014462	0.2074700	0.4302000	0.3080100	0.8236000	0.2127000	
Attenuation (dB)	0.00	-8.71	-17.12	-19.80	-17.28	-35.93	-38.13	-36.71	-37.62	-31.47	-36.28	-34.56	-33.19	-38.20	-55.06	-48.73	-51.63	-43.09	-54.85	-35.46
100-200 KHz	0.0482298	0.0177107	0.0039738	0.0032229	0.0058526	0.0005317	0.0004127	0.0004136	0.0007299	0.0008860	0.0003340	0.0004059	0.0011667	0.0003836	0.0953067	0.1695347	0.1024900	0.1931067	0.0664788	
Attenuation (dB)	0.00	-8.70	-21.68	-23.50	-18.32	-39.15	-41.35	-41.33	-36.40	-34.72	-43.19	-41.50	-32.33	-41.99	-54.08	-49.08	-53.45	-47.95	-57.21	-38.11
200-300 KHz	0.0328354	0.0145661	0.0069320	0.0043504	0.0052448	0.0006821	0.0005938	0.0007997	0.0003804	0.0012867	0.0008836	0.0011747	0.0007335	0.0003366	0.0500200	0.1247682	0.1112432	0.4945053	0.0981452	
Attenuation (dB)	0.00	-7.06	-13.51	-17.56	-15.93	-33.65	-34.85	-32.27	-38.72	-28.14	-31.40	-28.93	-33.02	-39.78	-56.34	-48.40	-49.40	-36.44	-50.49	-33.11
300-400 KHz	0.0044743	0.0019744	0.0007801	0.0005951	0.0006075	0.0000867	0.0000560	0.0000596	0.0000690	0.0001040	0.0001087	0.0000586	0.0001345	0.0000176	0.0057877	0.0155185	0.0120845	0.0297758	0.0063426	
Attenuation (dB)	0.00	-7.11	-15.17	-17.52	-17.34	-34.26	-38.05	-37.51	-36.24	-32.67	-32.29	-37.66	-30.44	-48.08	-57.76	-49.20	-51.37	-43.54	-56.97	-35.73
400-500 KHz	0.0007067	0.0006256	0.0003469	0.0003486	0.0002148	0.0000379	0.0000258	0.0000205	0.0000163	0.0000489	0.0000253	0.0000195	0.0000187	0.0000060	0.0007608	0.0025608	0.0017153	0.0021104	0.0010535	
Attenuation (dB)	0.00	-1.06	-6.18	-6.14	-10.34	-25.41	-28.76	-30.74	-32.75	-23.20	-28.92	-31.18	-31.54		-59.36	-48.82	-52.30	-50.50	-56.53	-29.10
500-600 KHz	0.0001862	0.0002346	0.0001162	0.0001753	0.0000932	0.0000103	0.0000087	0.0000054	0.0000047	0.0000086	0.0000067	0.0000048	0.0000046	0.0000025	0.0001962	0.0005430	0.0003960	0.0004002	0.0002236	
Attenuation (dB)	0.00	2.01	-4.10	-0.52	-6.02	-25.16	-26.61	-30.74	-31.96	-26.69	-28.83	-31.80	-32.08	-37.47	-59.54	-50.70	-53.44	-53.35	-58.41	-30.86
600-700 KHz	0.0000833	0.0000720	0.0000295	0.0000458	0.0000325	0.0000025	0.0000025	0.0000019	0.0000014	0.0000035	0.0000020	0.0000015	0.0000014	0.0000014	0.0001822	0.0003783	0.0002298	0.0003096	0.0001719	
Attenuation (dB)	0.00	-1.27	-9.02	-5.21	-8.17	-30.35	-30.60	-33.05	-35.30	-27.48	-32.39	-34.63	-35.66	-35.68	-53.21	-46.86	-51.19	-48.60	-53.71	-31.80
700-800 KHz	0.0000774	0.0000392	0.0000099	0.0000353	0.0000208	0.0000013	0.0000011	0.0000009	0.0000006	0.0000020	0.0000011	0.0000010	0.0000007	0.0000008	0.0001160	0.0001924	0.0001482	0.0002934	0.0001278	
Attenuation (dB)	0.00	-5.91	-17.86	-6.81	-11.40	-35.42	-37.22	-38.25	-42.44	-31.79	-37.17	-37.73	-41.08	-40.08	-56.48	-52.08	-54.35	-48.42	-55.64	-36.12
800-1000 KHz	0.0000547	0.0000270	0.0000106	0.0000182	0.0000118	0.0000011	0.0000011	0.0000010	0.0000008	0.0000014	0.0000011	0.0000011	0.0000011	0.0000010	0.0002104	0.0002954	0.0002310	0.0004108	0.0002321	
Attenuation (dB)	0.00	-6.14	-14.27	-9.58	-13.34	-33.57	-34.24	-34.75	-36.89	-31.63	-33.62	-34.14	-34.22	-34.60	-48.30	-45.36	-47.49	-42.49	-47.45	-32.34

Table 7.4

Attenuation of test-rig

Position	P0	P1	P2	P3	P4	P5	P6	P7	P8	P9	P10	P11	P12	P13	P14	P15	P16	P17	P18	Average
No. of discontinuities	1	1	1	2	2	3	3	3	3	3	3	3	3	5	5	5	5	5	5	
Distance (mm)	10	1000	2000	425	1325	800	1000	1420	1670	1620	1800	2280	2450	1000	1810	1725	2490	1400	2220	
					Signal maximum amplitude within specified frequency bands (Vs), sensor on stub shaft															
100-1000 KHz	56.00000	20.60000	18.20000	17.60000	13.40000	3.65000	3.50000	4.35000	4.55000	4.00000	3.40000	4.00000	5.40000	2.59250	1.02000	1.58000	1.60000	2.08000	1.08000	
Attenuation (dB)	0.00	-8.69	-9.76	-10.05	-12.42	-23.72	-24.08	-22.19	-21.80	-22.92	-24.33	-22.92	-20.32	-26.69	-34.79	-30.99	-30.88	-28.60	-34.30	-22.75
100-200 KHz	36.69730	16.90590	5.97740	7.74900	7.16660	2.14590	1.49310	2.16430	2.37120	2.02520	0.98040	1.68880	3.16020	1.75590	0.62820	0.91970	0.80640	0.82750	0.51550	
Attenuation (dB)	0.00	-6.73	-15.76	-13.51	-14.19	-24.66	-27.81	-24.59	-23.79	-25.16	-31.46	-26.74	-21.30	-26.40	-35.33	-32.02	-33.16	-32.94	-37.05	-25.14
200-300 KHz	37.52020	11.70580	11.06810	10.97440	6.78840	2.45460	2.19240	2.41250	2.03550	2.66190	2.56450	3.39230	2.26070	2.75560	0.52490	0.91560	0.84600	1.58770	0.79050	
Attenuation (dB)	0.00	-10.12	-10.60	-10.68	-14.85	-23.69	-24.67	-23.84	-25.31	-22.98	-23.31	-20.88	-24.40	-22.68	-37.08	-32.25	-32.94	-27.58	-33.53	-23.41
300-400 KHz	16.45860	4.42960	3.23270	3.57850	2.60480	0.87810	0.77130	0.81940	0.83790	0.82790	1.03070	0.66330	1.18000	0.41580	0.21240	0.40990	0.32370	0.29990	0.19690	
Attenuation (dB)	0.00	-11.40	-14.14	-13.25	-16.01	-25.46	-26.58	-26.06	-25.86	-25.97	-24.07	-27.89	-22.89	-31.95	-37.78	-32.07	-34.13	-34.79	-38.44	-26.04
400-500 KHz	8.21730	4.04360	3.16230	2.55050	1.63190	1.03200	0.62150	0.50180	0.49460	0.60150	0.50660	0.46900	0.36570	0.32660	0.07820	0.15920	0.16470	0.09340	0.08480	
Attenuation (dB)	0.00	-6.16	-8.29	-10.16	-14.04	-18.02	-22.43	-24.28	-24.41	-22.71	-24.20	-24.87	-27.03	-28.01	-40.43	-34.26	-33.96	-38.89	-39.73	-24.55
500-600 KHz	2.78040	3.19950	1.69610	2.79490	1.26020	0.46590	0.42160	0.28330	0.32480	0.31300	0.26370	0.24090	0.23610	0.24030	0.03060	0.06640	0.05330	0.04750	0.03580	
Attenuation (dB)	0.00	1.22	-4.29	0.05	-6.87	-15.52	-16.38	-19.84	-18.65	-18.97	-20.46	-21.25	-21.42	-21.27	-39.17	-32.44	-34.35	-35.35	-37.80	-20.15
600-700 KHz	2.45770	1.64660	0.85650	1.30280	0.65880	0.18870	0.24700	0.16020	0.17800	0.24680	0.18620	0.12940	0.11030	0.21960	0.02840	0.07000	0.03390	0.03070	0.02830	
Attenuation (dB)	0.00	-3.48	-9.16	-5.51	-11.44	-22.30	-19.96	-23.72	-22.80	-19.96	-22.41	-25.57	-26.96	-20.98	-38.74	-30.91	-37.21	-38.07	-38.77	-23.22
700-800 KHz	2.05750	1.10790	0.45120	1.27340	0.56770	0.14030	0.14510	0.09130	0.07370	0.15260	0.11020	0.07630	0.06870	0.10770	0.03050	0.04030	0.02600	0.02340	0.02500	
Attenuation (dB)	0.00	-5.38	-13.18	-4.17	-11.18	-23.33	-23.03	-27.06	-28.92	-22.60	-25.42	-28.62	-29.53	-25.62	-36.58	-34.16	-37.97	-38.88	-38.31	-25.22
800-1000 KHz	2.17970	0.71780	0.35940	0.85870	0.42830	0.08290	0.08320	0.07270	0.06670	0.09640	0.09170	0.06210	0.05810	0.11790	0.04790	0.05050	0.03690	0.04180	0.03750	
	0.00	-9.65	-15.66	-8.09	-14.13	-28.40	-28.37	-29.54	-30.29	-27.09	-27.52	-30.91	-31.48	-25.34	-33.16	-32.70	-35.43	-34.34	-35.29	-26.52

Table 7.5

APPENDIX B : SIGNAL PROCESSING ALGORITHMS EMPLOYED

1. % Time/Frequency domain feature extraction algorithm %

This algorithm was modified to suit the various applications. In the example detailed below, it was employed to extract features from signatures generated with the Nielson technique. The receiving transducer, in this instance, was placed on the stub shaft.

```
%                         class4.m                         %

function [C] =class4(pt)
%
%
%       If x=1, kietley card
%       If x = 2 SCOPE 2000
%
axe=1e6;
fs=5e6;          % Sampling rate
%pt = number of data points

%%    Classification tests on rig with Nielson technique input

%%% Tests with sensor on stub shaft

x=2;
for i=1:18
        if i<10
        fname=[’d:\exper\rigatten\pencil\ls’ int2str(i) ’.dat’];
        %pause
        elseif i>=10 & i<100
        fname=[’d:\exper\rigatten\pencil\ls’ int2str(i) ’.dat’];
        %pause
        end

if x==1
        fid=fopen(fname,’r’);
        A=fread(fid,pt,’float64’);
        fclose(fid);
        A=A-mean(A);
        A=A*2;
        %figure(1);clf;gcf;
        %plot(A);
```

```
        %A=medfilt1(A,5);

elseif x==2
        fid=fopen(fname,'r');
        status=fseek(fid,321+1000,'bof');
        A=fread(fid,pt);
        A=(A-128)*0.001;    %for a gain 0f 0.256 Volts
%plot(A);pause
        A=medfilt1(A,5);
        A=filtfilt(b,a,A);
        B(:,i)=A;
        fclose(fid);

end

end

G=[20 20 20 20 5 5 5 5 5 5 5 5 5 2 2 2 2 2]*10;    %    Gain factors , for
                                                         40db and gain/0.256

for j=1:18
        D(:,j)=B(:,j)*G(j);
end

for jj=1:18
        C(:,jj)=tt5xx(D(:,jj)); %    Extact time/frequency domain features

end
```

……………………………………………………………………………………

2. % AR coefficient extraction algorithm %

This algorithm was modified to suit the various applications. In the example detailed below, it was employed to extract features from signatures generated with the Nielson technique. The receiving transducer, in this instance, was placed on the stub shaft.

```
%                        class2.m                        %

function [C,D] =class2(pt)

%

%

%    If x=1, kietley card
```

```
%       If x = 2 SCOPE 2000
%

axe=1e6;
fs=5e6;         % Sampling rate

%%***           Attenuation tests on rig with Nielson technique input


%%%%            Tests with sensor on stub shaft


x=2;

for i=1:18

        if i<10

        fname=['d:\data\rigatten\ls' int2str(i) '.dat'];
        %pause
        elseif i>=10 & i<100
        fname=['d:\data\rigatten\ls' int2str(i) '.dat'];
        %pause
        end

if x==1
        fid=fopen(fname,'r');
        A=fread(fid,pt,'float64');
        fclose(fid);
        A=A-mean(A);
        A=A*2;
        %figure(1);clf;gcf;
        %plot(A);
        %A=medfilt1(A,5);


elseif x==2
        fid=fopen(fname,'r');
        status=fseek(fid,321+1000,'bof');
        A=fread(fid,pt);
        A=(A-128)*0.001;        %for a gain Of 0.256 Volts
%plot(A);pause
        A=medfilt1(A,5);
        A=filtfilt(b,a,A);
        B(:,i)=A;
```

```
        fclose(fid);

 end

 end

 G=[20 20 20 20 5 5 5 5 5 5 5 5 5 5 2 2 2 2 2]*10;      %      Gain factors , for
                                                               40db and gain/0.256

 for j=1:18
        D(:,j)=B(:,j)*G(j);
        %max(D(:,j));
        %pause
 end

 for jj=1:18

        C(jj,:)=lpc2(D(:,jj),14);

 end
```

……

3. % Sub-routine program for time/frequency domain feature extraction algorithm

```
%                          tt5xx.m                              %

function [AA]=tt5xx(x)



%     Modified version of TTT2.m for n number of files   %

%     Used for feature extraction  in time/freq.  domain

%

%wind=512*1;         % for 8192 points
wind=1024            %  for 16384 data points

noverlap=0;
```

```
x = x(:);                                    % Make sure x and y are column
vectors

n = max(size(x));                            % Number of data points

k = fix((n-noverlap)/(wind-noverlap));       % Number of windows



index = 1:wind;

format long;

for i=1:k
        xw = detrend(x(index));
        index = index + (wind - noverlap);
        %xww=medfilt1(xw,5);            % Median  filter, already done
        A(:,i)=carter(xw);


end

[m,n]=size(A);

AA=[A(:,1);A(:,2);A(:,3);A(:,4);A(:,5);A(:,6);A(:,7);A(:,8);...
A(:,9);A(:,10);A(:,11);A(:,12);A(:,13);A(:,14);A(:,15);A(:,16)];
```

……

3.1 % **Sub-routine program of tt5xx.m** %

% **carter.m** %

Feature extraction algorithm for time/freq. domain

```
function [A] = carter(x)
%
%
%% This program computes the characteristics of a signal in the time/freq. domain
%% for further analysis.
%
```

```
 pt=length(x);
 fs=5e6;

 %%%%%%%%          Time domain features

 c1=mean(x);                          % Mean
 c2=std(x);                           % STD
 c3=cov(x);                           % Variance
 c4=abs(max(x));                      % Max amplitude
 c5=rms(x);                           % RMS  value
 c6=abs(median(x));                   % Median
 c7=c4/c5;                            % Crest factor
 c8=abs(trapz(abs(x)));               % Area of time spectrum
 c9=top(x);                           % Area of positive valuse of x, for 10 thresholds
 c10=bot(x);                          % Area of negative values of x, for 10 thresholds
 c11=dskew(x,pt);                     % Skewness
 c12=dkurt(x,pt);                     % Kurtosis
 c13=count(x);                        % Number of counts at 9 specified thresholds
 c13=c13./pt;
 [c14,c15]=pickpeak(x,3,5);           % 5 peaks of x with their position on the x-axis
 c14=c14./fs;                         % Time to these peaks, RISE TIME


 %%%%%            Frequency domain feature

 [a,f]=field3(x,pt,fs);
 f=f./max(f);
 f1=trapz(abs(f),abs(a));             % Area of frequency spectrum, from 0 to 0.5fs
 f2=mefre(f,a);                       % Median frequency
 f3=frepeak(f,a,3);              % 3 peaks on the spectrum, with respective freq. position.
 f4=top(a);                           % Area of amplitude of spectrum for 10 thresholds


 A=[c1;c2;c3;c4;c5;c6;c7;c8;c9;c10;c11;c12;c13;c14;c15;f1;f2;f3;f4];
```

……………………………………………………………………………………

***   Listing of most routines used in computing carter.m   ***

3.1.1 %   **Sub-routine program of carter.m**   %

i. %   **count.m**   %

```
%            Counts for 9 multiples of x
```

```
 function c = count(x)
 %
 % This program counts the number of counts of a burst
 %
 %
 cunt=0;
 m=max(x);
 y=[0.1*m;0.2*m;0.3*m;0.4*m;0.5*m;0.6*m;0.7*m;0.8*m;0.9*m];
 [my,ny]=size(y);
 [m,n]=size(x);
 for j=1:my
         for i=1:m-1
                 if x(i)>y(j) & x(i+1)<y(j)
                         cunt=cunt+1;
                         c(j,:)=cunt;
                 else
                         cunt=cunt+0;
                         c(j,:)=cunt;
                 end
        end
cunt=0;
end;
```

……

ii. % **bot.m** %

```
function t = bot(x)
%
%
%% This program computes the area for 9 steps of the maximun amplitude
%% of x. This is performed for negative values of x.
%
%
x=x(:);

for i=1:length(x)
        if x(i) <0
                x(i)=x(i);
        else
                x(i)=0;
        end
end

t1=trapz(x);
```

```
mm=max(abs(x))*(-1);

for i=1:length(x)
        if x(i) <0.1*mm
                x(i)=x(i);
        else
                x(i)=0;
        end
end

t2=trapz(x);

for i=1:length(x)
        if x(i) <0.2*mm
                x(i)=x(i);
        else
                x(i)=0;
        end
end

t3=trapz(x);

for i=1:length(x)
        if x(i) <0.3*mm
                x(i)=x(i);
        else
                x(i)=0;
        end
end

t4=trapz(x);

for i=1:length(x)
        if x(i) <0.4*mm
                x(i)=x(i);
        else
                x(i)=0;
        end
end

t5=trapz(x);


for i=1:length(x)
        if x(i) <0.5*mm
```

```
                x(i)=x(i);
            else
                x(i)=0;
            end
    end

    t6=trapz(x);


    for i=1:length(x)
            if x(i) <0.6*mm
                x(i)=x(i);
            else
                x(i)=0;
            end
    end

    t7=trapz(x);

    for i=1:length(x)
            if x(i) <0.7*mm
                x(i)=x(i);
            else
                x(i)=0;
            end
    end

    t8=trapz(x);

    for i=1:length(x)
            if x(i) <0.8*mm
                x(i)=x(i);
            else
                x(i)=0;
            end
    end

    t9=trapz(x);

    for i=1:length(x)
            if x(i) <0.9*mm
                x(i)=x(i);
            else
                x(i)=0;
            end
```

```
end

t10=trapz(x);

t=[t1 t2 t3 t4 t5 t6 t7 t8 t9 t10]';
t=abs(t);
```

……

iii. % **top.m** %

```
function t = top(x)
%
%
%% This program computes the area for 9 steps of the maximun amplitude
%% of x. This is performed for positive values of x.
%
%
x=x(:);
mm=max(x);
for i=1:length(x)
        if x(i) >0
                x(i)=x(i);
        else
                x(i)=0;
        end
end

t1=trapz(x);

for i=1:length(x)
        if x(i) >0.1*mm
                x(i)=x(i);
        else
                x(i)=0;
        end
end

t2=trapz(x);

for i=1:length(x)
        if x(i) >0.2*mm
                x(i)=x(i);
        else
```

```
                x(i)=0;
        end
end

t3=trapz(x);

for i=1:length(x)
        if x(i) >0.3*mm
                x(i)=x(i);
        else
                x(i)=0;
        end
end

t4=trapz(x);

for i=1:length(x)
        if x(i) >0.4*mm
                x(i)=x(i);
        else
                x(i)=0;
        end
end

t5=trapz(x);


for i=1:length(x)
        if x(i) >0.5*mm
                x(i)=x(i);
        else
                x(i)=0;
        end
end

t6=trapz(x);


for i=1:length(x)
        if x(i) >0.6*mm
                x(i)=x(i);
        else
                x(i)=0;
        end
end
```

```
t7=trapz(x);

for i=1:length(x)
        if x(i) >0.7*mm
                x(i)=x(i);
        else
                x(i)=0;
        end
end

t8=trapz(x);

for i=1:length(x)
        if x(i) >0.8*mm
                x(i)=x(i);
        else
                x(i)=0;
        end
end

t9=trapz(x);

for i=1:length(x)
        if x(i) >0.9*mm
                x(i)=x(i);
        else
                x(i)=0;
        end
end

t10=trapz(x);

t=[t1 t2 t3 t4 t5 t6 t7 t8 t9 t10]';
```

……………………………………………………………………………………

```
iv. %                    dkurt.m                    %


%       Kurtosis value

function K=dkurt(x,pt)

%       This program calculates the kurtosis of x
%        pt- number of data points %
```

```
a=mean(x);
s=std(x);

K=(1/pt*sum(((x-a)/s).^4));
```

……

v. % **dskew.m** %

```
%      Skew  value

function K=dskew(x,pt)

%      This program calculates the skewness of x
%      pt- number of data points        %

a=mean(x);
s=std(x);
K=abs(1/pt*sum(((x-a)/s).^3));
```

……

v. % **rms.m** %

```
%      RMS   value

function y = rms(x)
%   ROOT MEAN SQUARED value
%   For vectors, RMS(x) returns the rms value.
%   For matrices, RMS(x) is a row vector
%   containing a the rms value of each column.
%
[m,n] = size(x);
if m == 1
   m = n;
end
for i = 1:m;
   sq(i) = x(i) * x(i);
end
s = sum(sq)/m;
y = sqrt(s);
```

……

vi. %   cov.m [95]   %

```
%              Variance

function xy = cov(x,y)
%COV Covariance matrix.
%      COV(X), if X is a vector, returns the variance. For matrices,
%      where each row is an observation, and each column a variable,
%      COV(X) is the covariance matrix. DIAG(COV(X)) is a vector of
%      variances for each column, and SQRT(DIAG(COV(X))) is a vector
%      of standard deviations.  COV(X,Y) is COV([X Y]).

[m,n] = size(x);
if nargin > 1
   [my,ny] = size(y);
   if m ~= my | n ~= ny
      error('X and Y must be the same size.');
   end
   x = [x(:) y(:)];
elseif min(size(x)) == 1
   x = x(:);
end
[m, n] = size(x);
x = x - ones(m,1) * (sum(x)/m);
if m == 1
   xy = 0;
else
   xy = x' * x / (m-1);
end
```

……………………………………………………………………………………………

vi. %   median.m   [95]   %

```
**********  Median (absolute value only)

function y = median(x)
%MEDIAN    Median value.
%      For vectors,  MEDIAN(X)  is the median value of the elements in X.
%      For matrices, MEDIAN(X) is a row vector containing the median value
%      of each column.
%
[m,n] = size(x);
x = sort(x);
if (m==1)
   if isnan(x(1)) | isnan(x(n))
```

```
        y = nan;
        return
     end
     if rem(n,2)        % n is odd
        y = x((n+1)/2);
     else          % n is even
        y = (x(n/2) + x(n/2+1))/2;
     end
  else
     if rem(m,2)        % m is odd
        y = x((m+1)/2,:);
     else          % m is even
        y = (x(m/2,:) + x(m/2+1,:))/2;
     end
     nn = find( isnan(x(1,:)) | isnan(x(m,:)) );
     y(nn) = nan*ones(size(nn));
  end
```

……

vii. %   mefre.m   %

```
%              Median frequency

function z = mefre(x,y)
%
%       This program computes the *median freq.* frequency %%
%       Using PSD, x= frequency vector ( axis ), y= frequency amplitude ( strength )
%
%       Median freq. divides the area of the amplitude spectrum by two
%
% Make sure x and y are column vectors, or y is a matrix.
if nargin < 2, y = x; end
[m,n] = size(y);
if m == 1, y = y(:); m = n; end
if nargin < 2, x = 1:m; end
x = x(:);

% Trapezoid sum computed with vector-matrix multiply.

yy=y(1:m-1,:);
yyy=y(2:m,:);
yyyy=(yyy+yy)/2;
zz=sum(yyyy);
x=x;
xx=((x(1:m-1,:) + x(2:m,:))/2);
```

```
num=sum(yyyy.*xx);
z=num/zz;
```

……

viii. % **frepeak.m** %

```
**********    Number of freq. paeks

function z = frepeak(x,y,nopeaks)
%
%       This program extracts up 3 peaks with their corresponding frequency
%       values
%
%
format long;
x=x(:);
y=y(:);           %       Amplitude

[m,n]=pickpeaks(y,nopeaks,3);

for i=1:length(m)
        ff(i)=x(m(i));
end
z=[ff';n];
```

……

4. % Sub-routine program for AR coefficient extraction algorithm %

% **lpc2.m** [95] %

```
%       *LPC algorithm has been modifed by the author of this thesis*

function [a,vv]=lpc2(h,N);

%LPC Linear Predictive Coefficients.
%       A = LPC2(X,N) finds the coefficients of an Nth order auto-regressive
%       process that models the time series X as follows:
%         X(n) = -A(2)*X(n-1) - A(3)*X(n-2) - ... - A(N+1)*X(n-N-1)
%       Here, X is the real input time series (a vector), and N is the order of
%       denominator polynomial A(z), i.e. A = [ 1 A(2) ... A(N+1) ].
```

```
%
%       LPC uses the autocorrelation method

%       R is the auto correlation vector, R(1) = E(h(t)h*(t)),
%               R(2) = E(h(t+1)h*(t)),...

   error(nargchk(1,2,nargin))
   if nargin<2, N = length(h)-1; end

   if (N>length(h)-1),
      % disp(‘Warning: zero-padding short input sequence’)
      h(N+1)=0;
   end
   R = xcorr(h);

   M=length(h);
   R(1:M-1) = [];

      [a,vv] = lev2(R,N);
```

……

4.1.1 % **Sub-routine program of lpc2.m** %

```
%                       xcorr.m     [95]                %

%       Auto / Cross correlation        %

function c = xcorr(a, b, option)
%       XCORR(A), when A is a vector, is the auto-correlation sequence.

%       The zeroth lag of the output correlation is in the middle of the
%       sequence, at element or row M.

onearray = 1;
if nargin == 1
        option = 'none';
        if min(size(a)) == 1    % a is a vector
                a = [a(:) a(:)];
        else
                onearray = 0;
        end
elseif nargin == 2
        if isstr(b)
                option = b; clear b
```

```
        na = max(size(a));
        if min(size(a)) == 1    % a is a vector
            a = [a(:) a(:)];
        else    % a is a matrix
            onearray = 0;
            [m,n] = size(a);
        end
  else % b is truly a second arg
        if min(size(a)) ~= 1 & min(size(b)) ~= 1
            error('You may only specify 2 vector arrays.')
        end
        option = 'none';
        onearray = 2;
    end
else
    if max(size(a)) ~= max(size(b)) & ~strcmp(option,'none')
        error('OPTION must be "none" for different length vectors A and B')
    end
    onearray = 2;
end
if onearray == 2
    [ar,ac] = size(a);
    na = max([ar ac]);
    nb = max(size(b));
    if na > nb
        b(na) = 0;
    elseif na < nb
        a(nb) = 0;
    end
    a = [a(:) b(:)];
end
[nr, nc] = size(a);
nsq  = nc^2;
mr = 2 * nr - 1;
c = zeros(mr,nsq);
ci = zeros(1,nsq);
cj = ci;
nfft = 2^nextpow2(2*nr);
for i = 1:nc
    atmpi = a(:,i);
    if ~any(any(atmpi))
        real1 = 1;
    else
        real1 = 0;
    end
```

```
        atmpi = fft([atmpi(:); zeros(nfft-nr,1)]);
        for j = 1:i
                col = (i-1)*nc+j;
                colaux = (j-1)*nc+i;
                tmp = fft([a(:,j); zeros(nfft-nr,1)]); % pad with zeros for fft
                tmp = fftshift(ifft(atmpi.*conj(tmp)));
                c(:,colaux) = tmp((1:mr)+nfft/2-nr+1);
                ci(col) = i;
                cj(col) = j;
                ci(colaux) = j;
                cj(colaux) = i;
                if ~any(any(imag(a(:,j)))) & real1
                        c(:,colaux) = real(c(:,colaux));
                end
                if i~= j
                        c(:,col) = conj(c(mr:-1:1,colaux));
                end
        end
end
if nopt == 1    % return normalized by sqrt of each autocorrelation at 0 lag
% do column arithmetic to get correct autocorrelations
        cdiv = ones(mr,1)*sqrt(c(nr,1+(ci-1)*(nc+1)).*c(nr,1+(cj-1)*(nc+1)));
        c = c ./ cdiv;
elseif nopt == 2        % biased result, i.e. divide by nr for each element
        c = c / nr;
elseif nopt == 3        % unbiased result, i.e. divide by nr-abs(lag)
        c = c ./ ([1:nr (nr-1):-1:1]' * ones(1,nsq));
end
if onearray == 1
        c = c(:,1);     % just want the autocorrelation
        [am, an] = size(a);
        if am == 1
                c = c.';
        end
elseif onearray == 2    % produce only cross-correlation
        c = c(:,2);
        if ar == 1
                c = c.';
        end
end
if ~any(any(imag(a)))
        c = real(c);
end
```

4.1.2 % Sub-routine program of lpc2.m %

```
%                         Lev2.m        [95]                  %

%    Levinson-Durbin Recursion algorithm has been modifed by the author of this
     thesis*


function [a,vv]=levinson(R,N);
%LEVINSON  Levinson-Durbin Recursion.
%     A = LEVINSON(R,N) solves a symmetric toeplitz system of equations using
%     the Levinson-Durbin recursion.  R is a vector of autocorrelation
%     coefficients, starting with lag 0 as the first element. N is the
%     order of the recursion; A will be a length N+1 row, with A(1) = 1.
%
%     The equations solved are of the form:
%       [ R(1)   R(2)  ... R(N)  ] [ A(2)  ]  = [ -R(2) ]
%       [ R(2)   R(1)  ... R(N-1)] [ A(3)  ]  = [ -R(3) ]
%       [ .      .        .      ] [ .     ]  = [ .     ]
%       [ R(N-1) R(N-2)... R(2)  ] [ A(N)  ]  = [ -R(N) ]
%       [ R(N)   R(N-1)... R(1)  ] [ A(N+1)]  = [ -R(N+1) ]

%     R is the auto correlation vector, R(1) = E(h(t)h*(t)),
%             R(2) = E(h(t+1)h*(t)),...

  error(nargchk(1,2,nargin))
  if nargin < 2, N = length(R)-1; end
  if length(R)<(N+1), error('Correlation vector too short.'), end

    a = -R(2)/R(1);
    V = R(1) - R(2)^2/R(1);
      v1=V;
    for n = 1:N-1,
      alfa = [1 a.']*R(n+2:-1:2);
      rho = -alfa / V;
      V = V + rho*alfa;
      vv(n,:)=V;
      a = [ a + rho*flipud(a); rho ];
      %pause
    end
    a = [1; a].';              % AR coefficients
      vv=[v1;vv];              % vector of all variances
      l=1:1:N;
      %clf;plot(l,vv,'r');
```

……………………………………………………………………………………

5. % Algorithms used for computation of attenuation characteristics of test-rig

% akiet44a.m %

```
%       Extraction of maximum amplitude values for the various stress wave signatures at
        the specified frequency ranges.

function [Z,ZZ] = akiet44a(pt)
%
%
%       If x=1, kietley card
%       If x = 2 SCOPE 2000
%       Amplitude
%
axe=1e6;
fs=5e6;          % Sampling rate

%       Band-pass filter design, ELLIP Filter, 100KHz to 1000KHz.

wp=[1e5 1e6]*2/fs;ws=[0.75e5 1.1e6]*2/fs;rp=1;rs=30;
[n,wn]=ellipord(wp,ws,rp,rs);
[b,a]=ellip(n,rp,rs,wn);         %  Filter coefficients.
%freqz(b,a);pause

%       Attenuation tests on rig with Nielson source  input, with sensor on stub shaft

[D]=class2x(pt);   %  Matrix of all stress waves, similar to class4.m detailed earlier, but
                      in this instance no computations on data files are undertaken. The
                      data files, D, are the output of this algorithm, class2x.m

Z=gentha(D,b,a);     %      Max. amplitude valuse at all specified frequency bands


%       Reference for attenuation calculations, position P0 on test-rig        %

fid=fopen(’c:\exper\lead2.dat’,’r’);
        status=fseek(fid,(321),’bof’);
        A=fread(fid,pt);
        A=(A-128)*0.256/256*(12.8/.256);          %for a gain 0f 0.256 Volts * factor
of gain used
        fclose(fid);
        AA=medfilt1(A,5);
        AA=A*10;    % 40dB compensation
```

```
        AA=filtfilt(b,a,AA);

ZZ=gentha(AA,b,a);  %       Max. amplitude valuse at all specified frequency bands
```

NOTE: The values Z and ZZ wer used to compute attenuation values (dB). The procedure described above was also used to calculated energy values at specified frequency bands.

……………………………………………………………………………………

5.1.1 % Sub-routine program of akiet44a2.m %

i. % gentha.m %

```
function [E] = gentha(x,b,a)
%
%
%       This function computes the max. amplitude value of the signals at different
%%      frequency  bands.
%
%
%%% This filter passes all frequencies above 20KHz.  %%%%%%%%%
%
fs=5e6;

x1=x;           %       Already bandpass filtered

%wp=[1e5 1e6]*2/fs;ws=[0.75e5 1.1e6]*2/fs;
%[n,wn]=ellipord(wp,ws,rp,rs);
%[b,a]=ellip(n,rp,rs,wn);
%freqz(b,a);pause

[m,n]=size(x1);
%pause

for i=1:n
rp=1;rs=30;
%max(x1(:,i))
%x55=filtfilt(b,a,x1(:,i));
x55=x1(:,i);
%clf;plot(x1(:,i));pause
e0(:,i)=max((x55));

rp=1;rs=30;
```

```
%            Frequencies  between 100 - 200 KHz.        %%%%%%%
%
p1=100e3*2/fs;
p2=200e3*2/fs;
p3=p1-(10e3*2)/fs;
p4=p2+(10e3*2)/fs;
wp1=[p1 p2];ws1=[p3 p4];
[n1,wn1]=ellipord(wp1,ws1,rp,rs);
[b1,a1]=ellip(n1,rp,rs,wn1);
%freqz(b1,a1);pause;
x2=filtfilt(b1,a1,x1(:,i));
e1(:,i)=max((x2));

%size(e1)

%            Frequencies  between 200 - 300 KHz.        %%%%%%%
%
v1=200e3*2/fs;
v2=300e3*2/fs;
v3=v1-(5e3*2)/fs;
v4=v2+(5e3*2)/fs;
wp8=[v1 v2];ws8=[v3 v4];
[n8,wn8]=ellipord(wp8,ws8,rp,rs);
[b8,a8]=ellip(n8,rp,rs,wn8);
%freqz(b8,a8);pause;
x9=filtfilt(b8,a8,x1(:,i));
e2(:,i)=max((x9));

%            Frequencies  between 300 - 400 KHz.        %%%%%%%
%
rp=1;rs=40;

vv1=300e3*2/fs;
vv2=400e3*2/fs;
vv3=vv1-(5e3*2)/fs;
vv4=vv2+(5e3*2)/fs;
wp9=[vv1 vv2];ws9=[vv3 vv4];
[n9,wn9]=ellipord(wp9,ws9,rp,rs);
[b9,a9]=ellip(n9,rp,rs,wn9);
%freqz(b9,a9);pause;
x10=filtfilt(b9,a9,x1(:,i));
e3(:,i)=max((x10));

%            Frequencies  between 400 - 500 KHz.        %%%%%%%
%
```

```
pp1=400e3*2/fs;
pp2=500e3*2/fs;
pp3=pp1-(2*5e3)/fs;
pp4=pp2+(5e3*2)/fs;
wp2=[pp1 pp2];ws2=[pp3 pp4];
[n2,wn2]=ellipord(wp2,ws2,rp,rs);
[b2,a2]=ellip(n2,rp,rs,wn2);
%freqz(b2,a2);pause;
x3=filtfilt(b2,a2,x1(:,i));
e4(:,i)=max((x3));

%               Frequencies  between 500 - 600 KHz.          %%%%%%%
%
ppp1=500e3*2/fs;
ppp2=600e3*2/fs;
ppp3=ppp1-(5e3*2)/fs;
ppp4=ppp2+(5e3*2)/fs;
wp3=[ppp1 ppp2];ws3=[ppp3 ppp4];
[n3,wn3]=ellipord(wp3,ws3,rp,rs);
[b3,a3]=ellip(n3,rp,rs,wn3);
%freqz(b3,a3);pause;
x4=filtfilt(b3,a3,x1(:,i));
e5(:,i)=max((x4));

%               Frequencies  between 600 - 700 KHz.          %%%%%%%
%

pppp1=600e3*2/fs;
pppp2=700e3*2/fs;
pppp3=pppp1-(5e3*2)/fs;
pppp4=pppp2+(5e3*2)/fs;
wp4=[pppp1 pppp2];ws4=[pppp3 pppp4];
[n4,wn4]=ellipord(wp4,ws4,rp,rs);
[b4,a4]=ellip(n4,rp,rs,wn4);
%freqz(b4,a4);pause;
x5=filtfilt(b4,a4,x1(:,i));
e6(:,i)=max((x5));

%%%%%%          Freqencies  between 700 - 800 KHz.  %%%%%%%
%

ss1=700e3*2/fs;
ss2=800e3*2/fs;
ss3=ss1-(5e3*2)/fs;
ss4=ss2+(5e3*2)/fs;
```

```
 wp6=[ss1 ss2];ws6=[ss3 ss4];
 [n6,wn6]=ellipord(wp6,ws6,rp,rs);
 [b6,a6]=ellip(n6,rp,rs,wn6);
 %freqz(b6,a6);pause;
 x7=filtfilt(b6,a6,x1(:,i));
 e7(:,i)=max((x7));

 %%%%%%          Freqencies  between 800 - 1000 KHz.          %%%%%%%
 %

s1=800e3*2/fs;
s2=1000e3*2/fs;
s3=s1-(5e3*2)/fs;
s4=s2+(5e3*2)/fs;
 wp5=[s1 s2];ws5=[s3 s4];
[n5,wn5]=ellipord(wp5,ws5,rp,rs);
[b5,a5]=ellip(n5,rp,rs,wn5);
%freqz(b5,a5);
x6=filtfilt(b5,a5,x1(:,i));
e8(:,i)=max((x6));

%A=[x55,x2,x9,x10,x3,x4,x5,x7,x6];

end

E=[e0;e1;e2;e3;e4;e5;e6;e7;e8];
```

……

ii. %   **genthe.m**   %

```
function [E] = genthe(x,b,a)
%
%%   This function computes the energy value of the signals at different
%%   frequency  bands.
%
%
%%% This filter passes all frequencies above 20KHz. %%%%%%%%%
fs=5e6;

x1=x;        %      Already bandpass filtered
```

```
%wp=[1e5 1e6]*2/fs;ws=[0.75e5 1.1e6]*2/fs;
%[n,wn]=ellipord(wp,ws,rp,rs);
%[b,a]=ellip(n,rp,rs,wn);
%freqz(b,a);pause

[m,n]=size(x1);
%pause

for i=1:n
rp=1;rs=30;
%x55=filtfilt(b,a,x1(:,i));
x55=x1(:,i);
e0(:,i)=sum(x55.^2)/fs;

%clf;plot(x1(:,i));pause
i
rp=1;rs=30;
%%%%%%          Frequencies  between 100 - 200 KHz.          %%%%%%%
%
p1=100e3*2/fs;
p2=200e3*2/fs;
p3=p1-(10e3*2)/fs;
p4=p2+(10e3*2)/fs;
wp1=[p1 p2];ws1=[p3 p4];
[n1,wn1]=ellipord(wp1,ws1,rp,rs);
[b1,a1]=ellip(n1,rp,rs,wn1);
%freqz(b1,a1);pause;
x2=filtfilt(b1,a1,x1(:,i));
e1(:,i)=sum(x2.^2)/fs;

%size(e1)

%%%%%%          Frequencies  between 200 - 300 KHz.          %%%%%%%
%
v1=200e3*2/fs;
v2=300e3*2/fs;
v3=v1-(5e3*2)/fs;
v4=v2+(5e3*2)/fs;
wp8=[v1 v2];ws8=[v3 v4];
[n8,wn8]=ellipord(wp8,ws8,rp,rs);
[b8,a8]=ellip(n8,rp,rs,wn8);
%freqz(b8,a8);pause;
x9=filtfilt(b8,a8,x1(:,i));
e2(:,i)=sum(x9.^2)/fs;
```

```
%%%%%%          Frequencies  between 300 - 400 KHz.          %%%%%%%
%
rp=1;rs=40;

vv1=300e3*2/fs;
vv2=400e3*2/fs;
vv3=vv1-(5e3*2)/fs;
vv4=vv2+(5e3*2)/fs;
wp9=[vv1 vv2];ws9=[vv3 vv4];
[n9,wn9]=ellipord(wp9,ws9,rp,rs);
[b9,a9]=ellip(n9,rp,rs,wn9);
%freqz(b9,a9);pause;
x10=filtfilt(b9,a9,x1(:,i));
e3(:,i)=sum(x10.^2)/fs;

%%%%%%          Frequencies  between 400 - 500 KHz.          %%%%%%%
%
pp1=400e3*2/fs;
pp2=500e3*2/fs;
pp3=pp1-(2*5e3)/fs;
pp4=pp2+(5e3*2)/fs;
wp2=[pp1 pp2];ws2=[pp3 pp4];
[n2,wn2]=ellipord(wp2,ws2,rp,rs);
[b2,a2]=ellip(n2,rp,rs,wn2);
%freqz(b2,a2);pause;
x3=filtfilt(b2,a2,x1(:,i));
e4(:,i)=sum(x3.^2)/fs;

%%%%%%          Frequencies  between 500 - 600 KHz.          %%%%%%%
%
ppp1=500e3*2/fs;
ppp2=600e3*2/fs;
ppp3=ppp1-(5e3*2)/fs;
ppp4=ppp2+(5e3*2)/fs;
wp3=[ppp1 ppp2];ws3=[ppp3 ppp4];
[n3,wn3]=ellipord(wp3,ws3,rp,rs);
[b3,a3]=ellip(n3,rp,rs,wn3);
%freqz(b3,a3);pause;
x4=filtfilt(b3,a3,x1(:,i));
e5(:,i)=sum(x4.^2)/fs;

%%%%%%          Frequencies  between 600 - 700 KHz.          %%%%%%%
%

pppp1=600e3*2/fs;
```

```
pppp2=700e3*2/fs;
pppp3=pppp1-(5e3*2)/fs;
pppp4=pppp2+(5e3*2)/fs;
wp4=[pppp1 pppp2];ws4=[pppp3 pppp4];
[n4,wn4]=ellipord(wp4,ws4,rp,rs);
[b4,a4]=ellip(n4,rp,rs,wn4);
%freqz(b4,a4);pause;
x5=filtfilt(b4,a4,x1(:,i));
e6(:,i)=sum(x5.^2)/fs;

%%%%%%        Frequencies  between 700 - 800 KHz.        %%%%%%%
%

ss1=700e3*2/fs;
ss2=800e3*2/fs;
ss3=ss1-(5e3*2)/fs;
ss4=ss2+(5e3*2)/fs;
wp6=[ss1 ss2];ws6=[ss3 ss4];
[n6,wn6]=ellipord(wp6,ws6,rp,rs);
[b6,a6]=ellip(n6,rp,rs,wn6);
%freqz(b6,a6);pause;
x7=filtfilt(b6,a6,x1(:,i));
e7(:,i)=sum(x7.^2)/fs;

%%%%%%        Frequencies  between 800 - 1000 KHz.        %%%%%%%
%

s1=800e3*2/fs;
s2=1000e3*2/fs;
s3=s1-(5e3*2)/fs;
s4=s2+(5e3*2)/fs;
wp5=[s1 s2];ws5=[s3 s4];
[n5,wn5]=ellipord(wp5,ws5,rp,rs);
[b5,a5]=ellip(n5,rp,rs,wn5);
%freqz(b5,a5);
x6=filtfilt(b5,a5,x1(:,i));
e8(:,i)=sum(x6.^2)/fs;

%A=[x55,x2,x9,x10,x3,x4,x5,x7,x6];

end

E=[e0;e1;e2;e3;e4;e5;e6;e7;e8];
```

……………………………………………………………………………………

6. % Cluster algorithm used for classification of features %

% clustxxx.m %

* This program has been modified by the author of this thesis to allow for computation of K-means distances only . *

```
function clustxxx(dat,labels,fig00)
%CLUSTER KNN and K-means cluster analysis with dendrograms

%       Used for classification of of simulations


labels=['t1 ';'t2 ';'t3 ';'t4 ';'t5 ';...
 't6 ';'t7 ';'t8 ';'sf1';'sf2';...
't6 ';'t7 ';'t8 ';'sf1';'sf2';...
'sn1';'sn2';'sn3';'sn4';'sn5';'da1';'da2';'da3';...
'da4';'da5';'da6';'e1 ';'e2 ';...                    5'];
'e3 ';'e4 ';'e5 ';'e6 ';'db1';'db2';'db3';'db4';'db5'];
%labels=[];
```

<u>NOTE:</u> Labels will vary with application

```
if nargin<3
 fig00 = 0;
 %disp(' ')
 %disp('Would you like knn or k-means clustering?')
 %input('knn = 1, k-means = 2 ');
 ans=2;
 copt = ans;
 %disp(' ')
 %disp('Would you like to autoscale or mean center the data?')
 %input('autoscale = 1, mean center = 2 ');
 anss=2;
 f1 = anss;

else
 handl = get(fig00,'userdata');
 if get(handl(3,1),'Value')==1
  copt  = 1;
 else
  copt  = 2;
```

```
  end
  f1   = handl(1,2);
 end
 if f1 == 1
  dat = auto(dat);
 elseif f1 == 2
  dat = mncn(dat);
 end

[m,n] = size(dat);
adat = [(1:m)’ zeros(m,m) dat];
ins = zeros((m-1)*2,m+2);
clc
for k = 1:m-1
  if copt == 2
    dist = ones(m-k,m-k)*inf;
    for i = 2:m-k+1
      for j = 1:i-1
        dist(i-1,j) = sqrt(sum((adat(i,m+2:m+n+1) - adat(j,m+2:m+n+1)).^2));
      end
    end
    [mind,yind] = min(dist);
    [mind,xind] = min(mind);
    yind = yind(xind);
    home
    s = sprintf('Link %g connects the following samples’,k);
    disp(s)
    [i1,i2] = size(find(adat(yind+1,1:m)));
    [i3,i4] = size(find(adat(xind,1:m)));
    disp(adat([xind yind+1]’,1:max([i2 i4])))
    ins(k*2-1:k*2,1:m) = adat([xind yind+1]’,1:m);
    ins(k*2-1:k*2,m+1) = [1 1]*mind;
    nsamp = zeros(1,m+n+1);
    sampvect = [adat(xind,1:m) adat(yind+1,1:m)];
    samplocs = find(sampvect);
    sampnos = sampvect(samplocs);
    [d,ns] = size(sampnos);
    nsamp(1,m+2:m+n+1) = sum(dat(sampnos’,:))/ns;
    nsamp(1,1:ns) = sampnos;
    nsamp(1,m+1) = mind;
    ins(k*2-1,m) = adat(xind,m+1);
    ins(k*2,m) = adat(yind+1,m+1);
    adat = delsamps(adat,[xind yind+1]);
    adat = [adat; nsamp];
  else
```

```
if k == 1
  dist = zeros(m,m);
  for i = 1:m
    for j = 1:i
      if j == i
        dist(i,j) = inf;
      else
        dist(i,j) = sqrt(sum((dat(i,:)-dat(j,:)).^2));
        dist(j,i) = dist(i,j);
      end
    end
  end
end
[min1,ind1] = min(dist);
[min2,ind2] = min(min1);
r = ind1(ind2);
c = ind2;
home
s = sprintf(‘Link %g connects sample %g to sample %g’,k,r,c);
disp(s)
ins(k*2-1:k*2,1) = [c r]’;
ins(k*2-1:k*2,m+1) = [1 1]*min2;
% Segment to order samples here
if k == 1
  groups = zeros(round(m/2),m);
  groups(1,1:2) = [c r]; gi = 1;
else
  % does r belong to an existing group?
  [zr1,zr2] = find(groups==r);
  % does c belong to an existing group?
  [zc1,zc2] = find(groups==c);
  % If neither c nor r belong to a group they form their own
  if zr1 == []; %r doesn’t belong to a group
    if zc1 == []; %c doesn’t belong to a group
      gi = gi+1;
      groups(gi,1:2) = [c r];
    else  % r doesn’t belong by c does, add r to group c
      sgc = size(find(groups(zc1(1),:))); %how big is group c
      groups(zc1(1),sgc(2)+1) = r;
    end
  else  %r does belong to a group
    if zc1 == []; %c doesn’t belong to a group, add c to group r
      sgr = size(find(groups(zr1(1),:))); %how big is group r
      groups(zr1(1),sgr(2)+1) = c;
    else  %both c and r belong to groups, add group c to group r
```

```
     sgr = size(find(groups(zr1(1),:)));  %size of group r
     sgc = size(find(groups(zc1(1),:)));  %size of group c
     groups(zr1(1),sgr(2)+1:sgr(2)+sgc(2)) = groups(zc1,1:sgc(2));
     groups(zc1,:) = zeros(1,m);
    end
   end
  end
  dist(r,c) = inf;
  dist(c,r) = inf;
  z1 = find(dist(r,:)==inf);
  z2 = find(dist(c,:)==inf);
  z1n = z1(find(z1~=r));
  z1n = z1n(find(z1n~=c));
  z2n = z2(find(z2~=c));
  z2n = z2n(find(z2n~=r));
  ins(k*2-1,2:1+max(size(z2n))) = z2n;
  ins(k*2,2:1+max(size(z1n))) = z1n;
  if max(size(z2n)) >= 1
   [zbi,zbj] = find(ins(1:k*2-2,1:m-1)==ins(k*2-1,1));
   zb = max(zbi);
   ins(k*2-1,m) = ins(zb,m+1);
  end
  if max(size(z1n)) >= 1
   [zbi,zbj] = find(ins(1:k*2-2,1:m-1)==ins(k*2,1));
   zb = max(zbi);
   ins(k*2,m) = ins(zb,m+1);
  end
  z = [z1 z2];
  sz = size(z);
  for j = 1:max(sz);
   for k = 1:max(sz);
    dist(z(j),z(k)) = inf;
   end
  end
 end
end
if copt == 2
 order = adat(1,1:m);
else
 [z1,z2] = find(groups(:,1));
 order = groups(z1,:); clear groups
end
for i = 1:2*(m-1)
 ind = find(ins(i,1:m-1));  %Find non-zero elements of in
 [mi,ni] = size(ind);       %Determine the number of elements
```

```
  if ni == 1             %  If the number = 0
   ins(i,m+2) = find(order==ins(i,1));  %set yval equal to its order
  else                   % Otherwise
   subords = zeros(1,ni);
   for j = 1:ni
    subords(j) = find(order==ins(i,j));
   end
   ins(i,m+2) = (min(subords)+max(subords))/2;
  end
 end
 maxdist = max(ins(:,m+1))*1.15;
 if isempty(labels)
 %if nargin == 1
  mindist = -maxdist*0.08;
 else
  [mn,mm] = size(labels);
  mindist = -maxdist*0.03*mm;
 end
 if fig00~=0
  figure(handl(1,1));
 else
  figure
 end

 set(gcf,'Color',[1,1,1]);          % White background

 for i = 1:m-1
  if ins(2*i-1,m) > ins(2*i-1,m+1);
   rind = find(ins(:,m) == ins(2*i-1,m+1));
   ins(2*i-1:2*i,m+1) = max([ins(2*i-1,m) ins(2*i,m)])*[1 1]';
   if rind > 0
    ins(rind,m) = max([ins(2*i-1,m) ins(2*i,m)]);
   end
  elseif ins(2*i,m) > ins(2*i,m+1)
   rind = find(ins(:,m) == ins(2*i,m+1));
   ins(2*i-1:2*i,m+1) = max([ins(2*i-1,m) ins(2*i,m)])*[1 1]';
   if rind > 0
    ins(rind,m) = max([ins(2*i-1,m) ins(2*i,m)]);
   end
  end
  plot([ins(2*i-1,m) ins(2*i-1,m+1)],ins(2*i-1,m+2)*[1 1],'-b')
  hold on
  plot([ins(2*i,m) ins(2*i,m+1)],ins(2*i,m+2)*[1 1],'-b')
  plot(ins(2*i-1,m+1)*[1 1],[ins(2*i,m+2) ins(2*i-1,m+2)],'-b')
end
```

```
 for i = 1:m
  ind = find(order==i);
  if isempty(labels)
% if nargin < 2
    s = int2str(i);
    text(mindist,ind,s,'Color','b')
  else
    text(mindist,ind,labels(i,:),'Color','b')
  end
end
axis([mindist maxdist 0 m+1]);                %       always use
%hold off
```

NOTE :   Text will be dependent on application

```
text('Units','normalized','Position',[0.45 0.95],'Color','b','String','t = Through rods');
text('Units','normalized','Position',[0.45 0.85],'Color','b','String','sn = Single loose radial
arm, near side to sensor');
text('Units','normalized','Position',[0.45 0.80],'Color','b','String','sf = Single loose radial
arm, far side to sensor');
text('Units','normalized','Position',[0.55 0.1],'Color','b','String','da = One pair of loose
radial arms');
text('Units','normalized','Position',[0.55 0.05],'Color','b','String','db = Second pair of loose
radial arms');
text('Units','normalized','Position',[0.45 0.9],'Color','b','String','e = Entire frame
looseness');

text('Units','normalized','Position',[0.35 0.75],'Color','b','String','Cluster 3');
text('Units','normalized','Position',[0.3 0.4],'Color','b','String','Cluster 2');
text('Units','normalized','Position',[0.3 0.175],'Color','b','String','Cluster 1');


set(gca,'XColor','b');
set(gca,'YColor','w');

hold off
% xlabel('Distance to K-Nearest Neighbor')  % if ans=1
xlabel('Distance to K-Means Nearest Group','Color','b')        % If ans=2

title('Dendrogram of fault simulations based on AR coefficients','Color','b');

%gtext(' p -  Position on test-rig');
%gtext(' a -  Amplitude of pulse input');
```

```
%zc = get(gcf,'Color');
%set(gca,'YColor',zc);
```

……

7. % The median filter algorithm [95] %

% medfilt1.m %

This filter was used to remove spurious electronic spikes from stress wave signatures.

```
function y = medfilt1(x,n,blksz)
%MEDFILT1  One dimensional median filter.
%       Y = MEDFILT1(X,N) returns the output of the order N, one dimensional
%       median filtering of vector X.  Y is the same length as X; for the edge
%       points, zeros are assumed to the left and right of X.
%
%       For N odd, Y(k) is the median of X( k-(N-1)/2 : k+(N-1)/2 ).
%       For N even, Y(k) is the median of X( k-N/2 : k+N/2-1 ).
%

if nargin < 2
  n = 3;
end
if all(size(x) > 1)
   nx = size(x,1);
   if nargin < 3
      blksz = nx;   % default: one big block (block size = length(x))
   end
   y = zeros(size(x));
   for i = 1:size(x,2)
      y(:,i) = medfilt1(x(:,i),n,blksz);
   end
   return
end
nx = length(x);
if nargin < 3
   blksz = nx;   % default: one big block (block size = length(x))
end
if rem(n,2)~=1    % n even
   m = n/2;
else
   m = (n-1)/2;
end
X = [zeros(1,m) x(:)' zeros(1,m)];
```

```
y = zeros(1,nx);
% Work in chunks to save memory
indr = (0:n-1)’;
indc = 1:nx;
for i=1:blksz:nx
   ind = indc(ones(1,n),i:min(i+blksz-1,nx)) + ...
        indr(:,ones(1,min(i+blksz-1,nx)-i+1));
   xx = reshape(X(ind),n,min(i+blksz-1,nx)-i+1);
   y(i:min(i+blksz-1,nx)) = median(xx);
end

% transpose if necessary
if size(x,2) == 1  % if x is a column vector ...
   y = y.’;
end
```

……